IMPULSE BREAKDOWN OF LIQUID-SOLID INTERFACES

Thesis presented for the degree of

Doctor of Philosophy

in the

Department of Electronic & Electrical Engineering

University of Strathclyde

2011

Mark Peter Wilson, BEng (Hons), MPhil

Department of Electronic & Electrical Engineering

University of Strathclyde

Glasgow, U.K.

DECLARATION OF AUTHENTICITY AND AUTHOR'S RIGHTS

This thesis is the result of the author's original research. It has been composed by the author and has not been previously submitted for examination which has led to the award of a degree.

Signed:
Date:

ABSTRACT

The interface between different dielectric media often proves to be the weakest link in a composite high-voltage insulation system, and this study has focused on experimental determination of the breakdown characteristics associated with discharges along polymer surfaces immersed in mineral oil. The materials tested were polypropylene, low-density polyethylene, ultra-high molecular weight polyethylene, Rexolite, and Torlon. Two applied voltage wave-shapes were studied under three different electrode geometries, with inter-electrode gap lengths of up to 10 mm. Breakdown voltage, time to breakdown, and implied average streamer propagation velocity are compared and discussed.

The results show that the time to breakdown for composite liquid-solid gaps is shorter than that for oil gaps without a solid spacer. Shorter times to breakdown were measured with increasing rate of voltage rise. Ultra-high molecular weight polyethylene consistently showed the longest times to breakdown. Weibull statistical analysis of the results suggests an ageing process for Rexolite samples, resulting in an increase of implied streamer propagation velocity from 11 km/s to over 200 km/s in non-uniform fields. Different sample geometries were tested, and the results show that the average breakdown voltage can be raised by up to 26% by introducing a 'shoulder' at the end of the solid sample in contact with the high-voltage electrode.

In uniform fields, the critical applied field required to initiate surface breakdown events was higher for materials with relative permittivity closely matched to that of the surrounding oil. Breakdown events were initiated at lower applied fields for materials of higher permittivity. Of the materials investigated, polypropylene and low-density polyethylene are concluded as being the most appropriate choice for use as mineral-oil immersed mechanical supports in high-voltage, pulsed-power systems, operating with similar voltage wave-shapes to those reported herein. The results and discussion will be of interest to designers of high-voltage and pulsed-power systems.

CONTENTS

Chapter 1

INTRODUCTION

The interface between different dielectric media often proves to be the weakest link in a composite high-voltage insulation system; usually comprising a solid dielectric immersed in either atmospheric air, vacuum, a compressed gas, or a dielectric liquid.

For three of these media – air, vacuum and compressed gas – dielectric performance under different conditions of applied voltage are fairly well documented, and reliable test procedures and design criteria have been established. On the other hand, less information is available on the behaviour of solid dielectrics immersed in dielectric liquids; an area of high-voltage engineering that has become increasingly important in recent years with the development of industrial-scale pulsed-power machines using multi-megavolt power supplies.

The present study is a contribution to this area of high-voltage pulsed-power engineering, and involves a detailed investigation of the flashover performance of five different dielectric materials immersed in insulating oil.

In multi-megavolt regimes associated with industrial-scale pulsed-power machines, sub-systems are commonly completely immersed in a dielectric liquid such as insulating oil; the external insulation provided by the oil allowing for the production of compact machines when the use of atmospheric air would result in unfeasibly large components and systems. Many liquid-solid interfaces are introduced into the insulation system under these circumstances, such as those between the liquid and cylindrical plastic legs/supports/stand-offs used to provide mechanical support, or high-voltage lead-through. Furthermore, industrial demands for increasing levels of output voltage and current, combined with a simultaneous drive for more compact systems, mean that experimental data on the flashover performance of solid dielectric materials that are immersed in dielectric fluids such as insulating oil and water are increasingly required by designers of pulsed-power systems and components.

Unwanted surface flashover of such interfaces during operation means the loss of the output data relating to the shot, and can result in catastrophic failure if allowed to persist. Even in the situation where insulation degradation begins to manifest itself in changes to the output voltage wave-form, problems with accessibility inherent to physically large systems immersed in oil-tight vessels mean that detection of the problematic interface can be difficult. This can lead to costly system downtime as oil-immersed sub-systems are drained and disassembled to facilitate the location and replacement of damaged dielectric components.

Studies of flashover associated with both lightning- and switching-impulse regimes (typically 1.2/50 μs and 250/2500 μs, respectively), for example refs. [1]-[5], are abundant, but the insulating properties of oil gaps bridged with solid dielectrics under pulsed-power conditions are not well documented, and there exists a distinct lack of published data pertaining to the breakdown characteristics of gaps bridged with solids greater than a few millimetres in length. Experimental data are therefore required on the behaviour of such composite insulating systems when subjected to short-duration impulses, in order to facilitate the proper design of insulators to be used in pulsed-power applications, and for the development of robust selection criteria.

Previous studies of flashover in the nanosecond regime have assessed the behaviour of one or two materials, analysing the breakdown voltages of liquid-solid interfaces subjected to a single flashover event under uniform-field conditions [6], [7]. In the present study, a detailed investigation of the flashover performance of five different materials immersed in insulating oil has been undertaken. The materials investigated were:

- polypropylene (PP);
- low-density polyethylene (LDPE);
- ultra-high molecular weight polyethylene (UHMWPE);
- Rexolite (a cross-linked polystyrene); and
- Torlon (a polyamide-imide).

Experiments were performed under non-uniform field conditions with different electrode configurations and sample topologies, and with a plane-parallel electrode configuration to provide uniform-field conditions. Data on the pre-breakdown delay times and breakdown voltages were gathered in order to provide a comparison between the performance of the different materials when the composite insulation system was subjected to over-voltages. Applied voltage wave-forms were chosen to replicate the electric-field conditions encountered in pulsed-power systems, and the changes in breakdown voltage and time to breakdown were monitored with increasing number of applied impulses. Furthermore, in addition to the standard approach of subjecting the gap to an over-voltage and recording the breakdown voltage, measurements have included the application of impulses that did not result in a breakdown event. This was done in order to determine the minimum voltages/fields required to initiate the flashover process. Gap lengths of up to 1 cm have been characterised compared to the gaps of 1-2 mm usually studied.

The ultimate goal is the development of reliable design rules and test procedures – similar to those presently used in the power industry – for oil-immersed dielectrics subjected to faster-rising impulses. Levels of electric field that lead to breakdown for different electrode/sample geometries, applied voltage wave-forms, and test procedures are presented herein. The results will provide data for high-voltage system designers to assist in the choice of dielectric materials.

The subsequent chapters of the thesis are presented as follows:

A literature review covering pulsed-power technology, industrial-scale systems and their underpinning insulation requirements; impulse generation techniques; and breakdown of liquid, solid, and composite liquid-solid insulation systems, is presented in Chapter 2.

Chapter 3 provides information on the experimental equipment and arrangements that have been utilised throughout the study, including high-voltage generation circuitry, test cells, liquid and solid samples, pneumatic control, and diagnostics.

Chapter 4 presents breakdown characteristics of the selected oil under three different electrode configurations: these data are utilised in the subsequent characterisation of composite liquid-solid gaps.

Chapter 5 details experimental results pertaining to characterisation of composite liquid-solid insulation systems when subjected to fast-rising impulse voltages, with breakdown occurring on the falling edge of the applied impulse. Two different types of measurement were performed in both uniform and non-uniform fields. For the first type, the insulation system was subjected to repeated over-voltages, such that breakdown occurred for every shot. The second type of measurement involved finding the average applied electric field required to initiate surface breakdown of the dielectric, by first applying lower voltages that did not result in breakdown, and then increasing the applied voltage until a breakdown event occurred. Weibull statistical analysis of the breakdown initiation data is presented and discussed.

The rise-time of the applied impulses was increased to produce the experimental results presented in Chapter 6, eradicating the variable falling-edge pre-breakdown delay time, and allowing comparison of the performance of the different materials with breakdown occurring on the rising edge. Composite gaps were further analysed under both uniform and non-uniform field conditions, and a detailed Weibull statistical analysis of the various data sets of results is presented and discussed.

Whereas the results presented in Chapters 5 and 6 are associated with determining applied voltage/field levels at which breakdown of the insulation system would occur, the results in Chapter 7 portray the levels of applied electric field below which breakdown will not occur for each material between plane-parallel electrodes. An open oil gap without solid spacer was also characterised for each set of test conditions in order to provide reference data. The probability of breakdown for increasing levels of applied field and rate of voltage rise is then discussed, to provide system designers with confidence intervals within which a given electric field can be applied to an insulation system without resulting in a breakdown event.

Finally, conclusions and recommendations for future work are discussed in Chapter 8, including recommendations on how the results should be interpreted and deployed by system designers, and how the study fits within the overall aim of developing reliable design rules, tests, and selection criteria for insulation systems to be used in high-voltage, pulsed-power machines.

Chapter 2

BACKGROUND AND LITERATURE REVIEW

2.0 INTRODUCTION

In a composite liquid-solid insulation system there are three types of electrical breakdown event that can occur, with each resulting in an unwanted collapse of the system voltage as a current flow is established through a normally insulating path. The different breakdown events that can occur are:

- bulk breakdown of the liquid dielectric;
- bulk breakdown of the solid dielectric; or
- surface flashover of the liquid-solid interface.

Of these types of breakdown event, bulk breakdown of the liquid dielectric is least damaging to an insulation system, since liquids have 'self-healing' properties [8] – that is, the liquid will regain close to its original breakdown strength after a relatively short period of time has elapsed [9].

Both of the other types of breakdown event can be catastrophic to a composite insulation system, since they may cause irreversible damage to the solid insulation. Once a breakdown path has been established, either through the bulk of the solid or along the liquid-solid interface, breakdown events can occur more readily at these weakened sites upon re-application of an impulse voltage to the system [10].

In terms of the design of a composite liquid-solid insulation system, there are therefore three major important parameters: the bulk breakdown strength of the liquid; the bulk breakdown strength of the solid; and the breakdown strength associated with flashover of the liquid-solid interface. Local field enhancements at the interfaces between materials of differing permittivity mean that 'triple junctions'

[11]-[14] are often the weakest links in electrical insulation systems, and experimental determination of the voltages and times associated with breakdown events on or around the surfaces of liquid-immersed solids is the focus of the present study.

Within this chapter, pulsed-power technology is initially reviewed, with an emphasis on industrial-scale systems, their applications, and their underpinning insulation requirements. Methods of generating impulse voltages of sufficient amplitude to induce surface discharges in insulating oil are discussed. Previous studies of impulse breakdown of liquids, insulating oil in particular, solid polymers, and liquid-solid interfaces are then reviewed.

2.1 PULSED-POWER TECHNOLOGY

Pulsed power involves the 'compression' of electrical energy with time and/or space, with pulses being dissipated in the load on a timescale of ps-μs. This compression means that output impulses with peak power in the range of GW can be generated with low average power consumption in the kW regime or less.

The types of energy-storage circuit deployed in pulsed-power applications can be broadly divided into two categories: inductive and capacitive. The major components of a simple inductive energy-storage circuit are shown in Figure 2.1. A high-current supply charges the energy-storage inductor, L, via the (normally-closed) opening switch, OS. The energy, E, stored in the magnetic field surrounding the inductor can be evaluated using equation (2.1):

$$E = \frac{1}{2} \cdot L \cdot I^2 \tag{2.1}$$

where L is the inductance (H) and I is the peak current value (A). The switch OS is opened at peak current, and the stored energy is delivered to the load. A fast opening

switch is required to rapidly interrupt the high current developed in the charging circuit, and this switch must withstand the full load voltage upon opening.

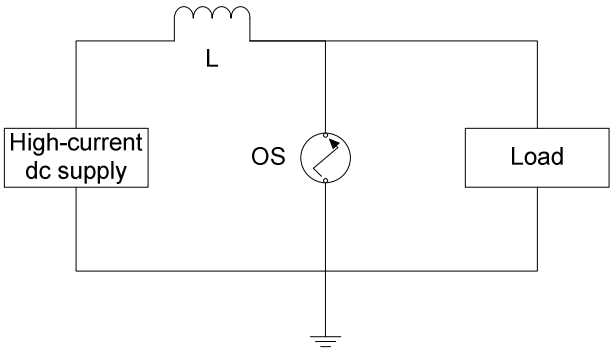

Figure 2.1. Schematic diagram of inductive energy storage circuit. L: energy-storage inductor; OS: opening switch.

While energy density of 50 J/cm^3 is readily achievable through inductive energy storage techniques, the self-discharge time constant is very short compared with a capacitive storage system, meaning that inductors need to be charged and discharged rapidly [15].

In order to remove the requirement for a high-current power supply, a primary energy-storage capacitor can first be charged to a high dc voltage via a charging resistor, R_{ch}. With reference to Figure 2.2, CS is closed when the capacitor is fully charged, and the stored energy is transferred to the inductor. The opening switch, OS, is then opened at peak current, and the stored energy is delivered to the load. Voltage multiplication is achieved in the load with this technique due to the rapidly decreasing current through L as OS is opened. The load voltage, V_L, is defined by equation (2.2):

$$V_L = L\frac{dI}{dt} \tag{2.2}$$

A high-current discharge capacitor, C, is required to supply the necessary large inductor-charging current [16].

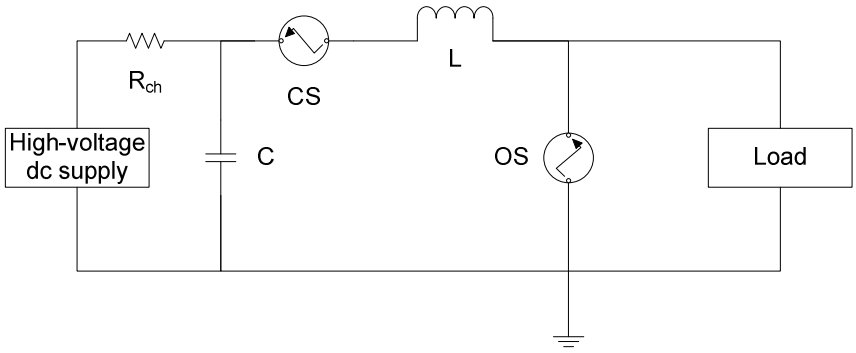

Figure 2.2. Schematic diagram of secondary inductive energy storage circuit (adapted from [16]). R_{ch}: charging resistor; C: primary energy-storage capacitor; CS: closing switch; L: secondary energy-storage inductor; OS: opening switch.

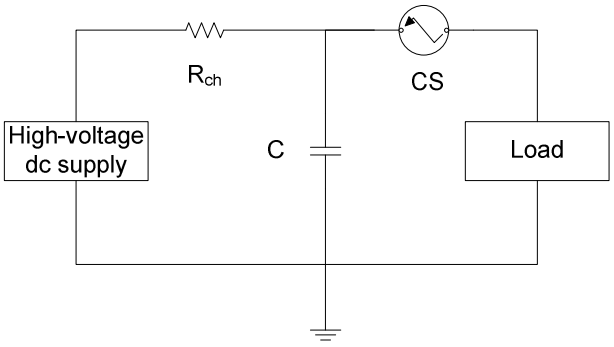

Figure 2.3. Schematic diagram of non-inverting capacitive energy storage circuit. R_{ch}: charging resistor; C: energy-storage capacitor; CS: closing switch.

Illustrated in Figure 2.3 are the basic components of a capacitive energy-storage circuit. The capacitor, C, is charged to a high dc voltage via R_{ch}, before CS either self-closes or breakdown is triggered, and the stored energy is delivered to the load. Figure 2.4 illustrates an alternative to this circuit, where the positions of C and CS are exchanged – analysis of this circuit reveals that when CS is closed, the charged

side of C is now connected to ground through the switch, and hence an impulse of inverted polarity is delivered to the load.

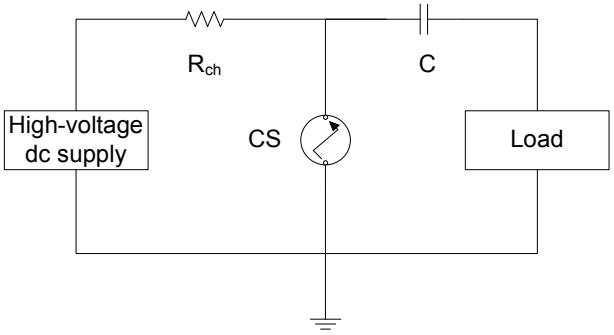

Figure 2.4. Schematic diagram of inverting capacitive energy storage circuit. R_{ch}: charging resistor; CS: closing switch; C: energy-storage capacitor.

The fact that the closed switch is in series with the charging circuitry during the discharge period in the non-inverting circuit of Figure 2.3 means that the primary power supply can be subjected to voltage reversal. This is of particular importance when a capacitor charging supply is deployed for the delivery of repetitive impulses, because reverse voltage may cause diode bridges at the supply output to conduct, leading to failure if proper protection is not deployed [17]. The inverting arrangement of Figure 2.4 offers the additional assurance that the primary power supply is completely decoupled from the load by the shorted switch during the discharge period.

The electrostatic energy stored in the dielectric between the plates of the capacitor can be evaluated using equation (2.3):

$$E = \frac{1}{2} \cdot C \cdot V^2 \tag{2.3}$$

where C is the capacitance (F), and V is the peak voltage across the capacitor (V). In repetitively triggered systems, the average power consumption can be calculated as the product of the pulse energy and the pulse repetition rate.

The instantaneous current, i (A), generated by capacitive energy-storage circuits can be evaluated using equation (2.4):

$$i = C\frac{dV}{dt} \tag{2.4}$$

analysis of which reveals that current multiplication can be achieved with capacitive-discharge circuits due to the rapidly decreasing voltage as the capacitor discharges. No voltage multiplication is achieved, however, with such single-stage capacitive circuits.

While the energy density achievable is much greater with inductive energy-storage systems [18], improvements in capacitor dielectric technology have seen the energy density offered by commercial capacitors improve by a factor of 60 over the last 25 years, increasing from 0.05 J/cm^3 in 1984 [16] to 3 J/cm^3 in 2009 [19].

2.1.1 Industrial Systems

Mogul-E [20] is an example of a large-scale industrial pulsed-power machine that is employed at AWE Aldermaston for flash X-ray radiography, and used for imaging of hydrodynamic experiments. Mogul-E weighs 280 tonnes, is 25 m long, and is the largest of AWE's X-ray machines. A simplified block diagram of the sub-systems used in the X-ray generation process is depicted in Figure 2.5. The Marx generator is utilised for voltage multiplication, and the Blumlein for pulse compression with time.

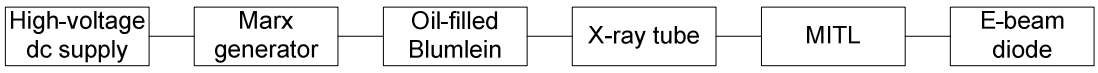

Figure 2.5. Simplified block diagram of typical AWE pulsed-power machine. MITL: magnetically-insulated transmission line.

Such machines are capable of simultaneously delivering multi-MV voltages and currents of the order of tens of kA depending upon the load. Again referring to Mogul-E, 84 × 700-nF storage capacitors are configured to form a 42-stage Marx generator. Each stage is initially charged to a high dc voltage, typically ±85 kV, via triggered spark-gap switches insulated with SF_6. The mid-plane trigger electrodes of the switches are initially resistively earthed to enable the ± charging regime. The output of the Marx generator is connected to an oil-filled Blumlein pulse-forming line, yielding an output pulse length of 70 ns. A self-closing switch discharges the Blumlein into a magnetically-insulated transmission line (MITL) via an X-ray tube, before reaching an electron-beam (e-beam) diode. The X-ray tube is an insulator stack, used to interface the oil-filled Blumlein and the vacuum-filled MITL [21]. In this manner, peak output voltages of 9.5 MV are attained, with a peak current of 40 kA delivered to the e-beam diode [22], providing a flash X-ray source. Typical diodes include paraxial diodes [23] and self-magnetic pinch diodes [24].

Voltage multiplication through Marx and Blumlein generators is discussed in section 2.1.2.

System Dielectric Requirements

In order to support the extremely high voltage levels of such systems, it is necessary to immerse the full Marx generator and Blumlein pulse-forming sections in insulating oil to allow a compact system design. This results in multiple liquid-solid interfaces within a machine.

The Blumlein is made up of three coaxial cylinders, forming an inner line and an outer line. The inner line of the Blumlein pulse-forming line is mechanically supported by large-diameter cylindrical solids, situated between a high-voltage conductor and an earthed external tank. This results in a liquid-solid interface that is subjected to fast-rising impulse voltages and electrical field levels of the order of hundreds of kV/cm. On Mogul-E, the inner-line support legs have been subject to tracking [22], and this type of liquid-solid interface will be investigated experimentally in the following chapters.

Load Characteristics

In order to select an appropriate method of impulse generation to provide the required electric-field stress and voltage wave-shape, the characteristics of the load presented by the composite insulation system must be considered. Assuming that the solid sample length is restricted to ≤1 cm, peak output voltages in the hundreds of kV range must be generated. Under such conditions, the dielectric system will represent a capacitive load of the order of hundreds of pF to the chosen impulse generator. Specific techniques for the generation of impulse voltages of hundreds of kV in magnitude are now reviewed.

2.1.2 Pulse Generation Techniques

Impulse voltages can be delivered to a load by a variety of different electrical circuit configurations. In each case, the primary energy-storage component is charged over a relatively long period (ms-s), and the energy is delivered rapidly to the load (ps-μs). The required voltage wave-shape dictates the choice of impulse generator, with the desired peak output voltage, rise-time, pulse duration, and fall-time providing the major selection criteria. The load characteristics are also important in determining the configuration of the chosen impulse generator. Described within this section are the main types of impulse generator, the inherent characteristics of each, and the operational advantages and disadvantages for use in different applications.

Coaxial and Stripline Generators

Fletcher showed in 1949 that coaxial generators are the most suitable for producing fast-rising impulses with minimum distortion, due to their low inherent stray capacitance and inductance [25]. Coaxial generators behave as transmission lines, and common arrangements include simple dc-charged coaxial cables (see Figure 2.6), switched at one end to produce an impulse of inverted polarity across the load, and Blumlein generators (see Figure 2.7), first demonstrated by Alan Blumlein in 1941 [26], where two such cables are charged in parallel and then discharged in series via a spark-gap switching only one of the cables.

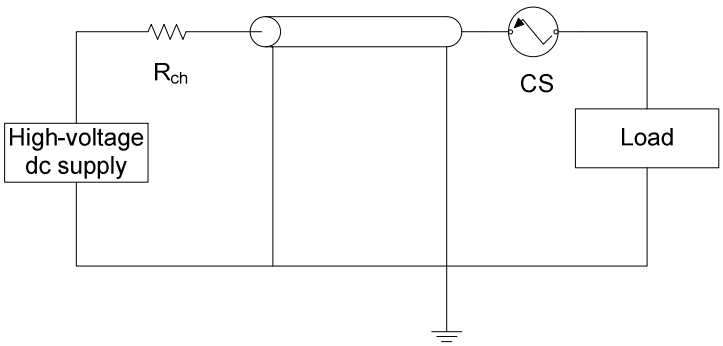

Figure 2.6. Simple dc-charged cable generator arrangement (adapted from [27]). R_{ch}: charging resistor; CS: closing switch.

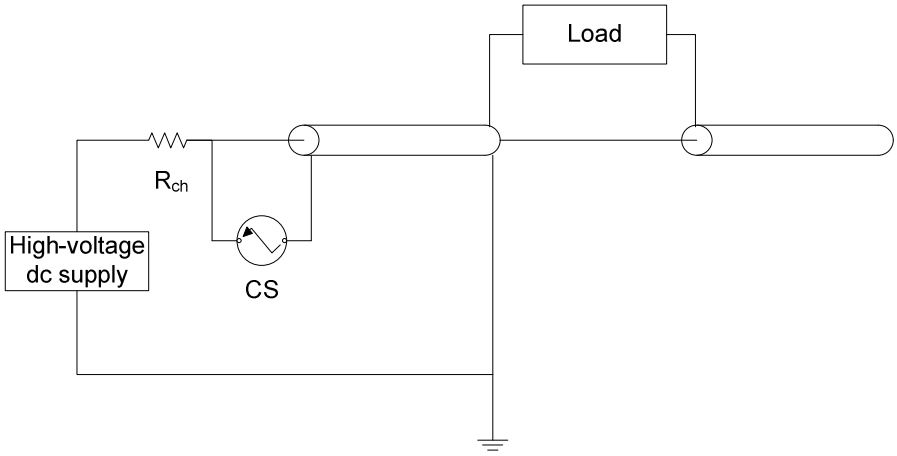

Figure 2.7. Blumlein cable generator arrangement (adapted from [27]). R_{ch}: charging resistor; CS: closing switch.

Impedance matching is an important concept in coaxial generators, and maximum energy transfer to the load is only achieved when the impedance of the load is equal to the output impedance of the impulse generator. Analysing the circuit of Figure 2.6, the theoretical voltage developed across the load can be calculated using equation (2.5):

$$V_L = V_S \cdot \frac{Z_L}{Z_{\text{OUT}} + Z_L} \tag{2.5}$$

where V_L is the load voltage (V); V_S is the charging voltage (V); Z_L is the impedance of the load (Ω); and Z_{OUT} is the output impedance of the impulse generator (Ω), which is equal to the characteristic impedance of the cable, Z_0. For equal Z_L and Z_{OUT}, the maximum load voltage is, therefore, half the charging voltage. Higher voltages, up to a maximum of V_S, can be developed across high-impedance loads, but this incurs multiple voltage reflections due to the impedance mismatch, resulting in energy being dissipated in parts of the circuit other than the load. This condition is generally undesirable and can result in switching problems in repetitive systems, where relatively high currents (mA) flow through the switch and the gas does not have sufficient time to recover its initial number density between pulses [28].

An impulse of magnitude equal to that of the charging voltage can be developed across a matched load, where $Z_L = 2Z_0$, through the Blumlein arrangement in Figure 2.7. For a high-impedance load, the maximum achievable voltage is, therefore, twice the charging voltage.

Blumlein stages can also be stacked to give voltage multiplication across a high-impedance load, the charging voltage being multiplied nominally by $2n$, where n is the number of stages. An elegant double-Blumlein arrangement, constructed from a single reel of high-voltage, coaxial cable is described in [27].

In such cable-generator arrangements, the input and output impedances are defined by the characteristic impedance of the coaxial cable. The output impedance is hence twice the input impedance for the Blumlein arrangement. For high-frequency signal components, the characteristic impedance can be approximated by equation (2.6):

$$Z_0 = \sqrt{\frac{L'}{C'}} \tag{2.6}$$

where L' is the inductance of the cable per unit length (H/m), and C' is the capacitance of the dielectric material between the two conductors per unit length (F/m).

The pulse duration is determined by the length of the transmission line and the properties of the dielectric material between the core and the braid. The propagation velocity, u_p (m/s), can be calculated via equation (2.7):

$$u_p = \frac{c}{\sqrt{\mu_r \cdot \varepsilon_r}} \tag{2.7}$$

where c is the speed of light in vacuum ($c \sim 3\times10^8$ m/s), and μ_r and ε_r are the relative magnetic permeability and the relative electrical permittivity of the dielectric material of the transmission line, respectively.

Analysing URM67 coaxial cable as a commonly-used example in pulsed-power applications, C' is 100 pF/m and L' is 250 nH/m, giving a characteristic impedance of 50 Ω. The dielectric material is polyethylene, which has $\mu_r \sim 1$, and $\varepsilon_r \sim 2.2$. This results in a propagation velocity of $\sim 2\times10^8$ m/s. For a charged line, the pulse duration will be equal to the two-way transit time of the transmission line – that is, 10 ns per metre of cable. For the Blumlein arrangement of Figure 2.7, an impulse of magnitude equal to the charging voltage will be developed across a matched load for the two-way transit time.

Coaxial generators are ideal for forming rectangular pulses with fast rise- and fall-times, and have found application in studies of solid dielectric breakdown [29], and of microbial inactivation in liquid foodstuffs [30]. The major disadvantage of cable generators is the limited charging voltage, and hence output voltage, achievable without resorting to expensive, bulky cables. The maximum dc charging voltage for URM67 cable is 40 kV for example, and the maximum energy-storage capability of a 100-m reel is hence only 8 J. The storage capacitance can be increased by charging several reels of cable in parallel, but this again increases the physical size of the impulse generator. The oil-filled Blumleins discussed above have to be physically large to support the multi-MV voltages. Pulse durations are limited by the physical properties of the insulation as described above.

In the planar geometry, stripline generators usually consist of a high-voltage electrode between two ground planes, separated by solid dielectric. Such geometries are used to achieve voltage multiplication in a similar manner to coaxial generators in that voltage doubling is achieved by the open-circuit reflection of fast transients [29]. The major advantage of this type of generator is in the development of sub-nanosecond rise-time impulses with minimum distortion, meeting the need for studies of the development of breakdown channels in solid dielectrics. Flashover issues usually limit the output voltage of single-stage stripline generators to the tens of kV range.

Fitch and Howell have described different geometries of stacked stripline generator, including vector-inversion generators and spiral generators, where voltage multiplication is achieved by "transient reversal of voltages in alternate units of series connected systems" [31]. The vector-inversion generator suffers from synchronisation problems with no capacitive coupling between the stages, while spiral generators can suffer from flashover problems and tend to be relatively low-energy systems used in switch-triggering applications [32].

Pulse Transformers

Pulse transformers work on the principle of a step-up voltage transformer, the level of voltage multiplication being determined by the turns ratio of the primary and secondary windings. With reference to Figure 2.8, a primary energy-storage capacitor is first charged to a relatively low dc voltage, before CS is closed. The mutual inductance of the two windings means that when the resulting impulse voltage is applied to the primary winding, the varying current results in a varying magnetic field in the secondary winding, inducing a voltage across the secondary. The energy transferred to the secondary storage capacitor is then dissipated in the load.

In the ideal case, with perfect coupling, no winding resistance, and negligible inter-turn capacitance, the secondary voltage and current can be defined as in equations (2.8) and (2.9), respectively [33]:

$$V_S = V_P \frac{N_S}{N_P} \tag{2.8}$$

$$I_S = I_P \frac{N_P}{N_S} \tag{2.9}$$

where V_P and V_S are the voltages on the primary and secondary coils respectively (V); N_P and N_S are the numbers of turns on the primary and secondary coils; and I_P and I_S are the primary and secondary currents (A).

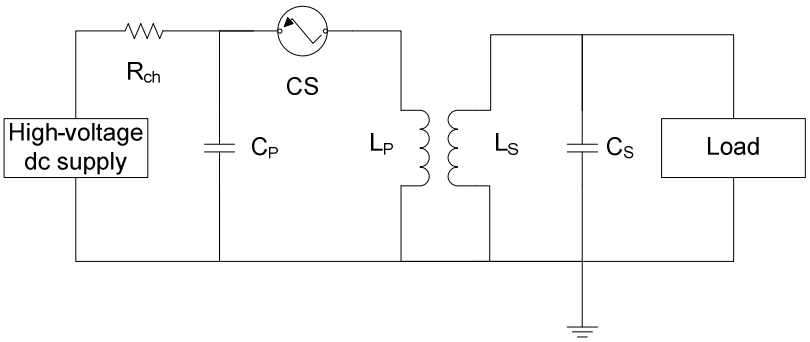

Figure 2.8. Schematic diagram of pulse transformer circuit (adapted from [33]). R_{ch}: charging resistor; C_P: primary energy-storage capacitor; CS: closing switch; L_P: primary winding inductance; L_S: secondary winding inductance; C_S: secondary energy-storage capacitor.

In conventional magnetically-cored high-voltage pulse transformers with large turn ratios, the output rise-time is limited by the combination of primary winding leakage inductance and secondary winding stray capacitance [34]. Restriction of the number of turns to reduce the stray capacitance associated with the secondary also acts to reduce the primary inductance, thus reducing the inductive isolation of the transformer input and output, and leading to distortion of the pulse shape [35].

A 100-kV, 100-A, magnetically-cored pulse transformer, utilised for plasma-based ion implantation is described in [36]. In [34], Graneau *et al*. describe a ten-stage, air-cored pulse transformer capable of generating 200-kV output voltages. Air-cored,

spiral-strip transformers have been operated at voltage levels up to 3 MV, with energy transfer efficiency from primary to secondary capacitor of 91% [37].

Practical issues associated with pulse transformers include turn-to-turn or inter-winding breakdown, and partial shorting between turns due to eddy currents induced in voltage-grading assemblies [33].

Magnetic Pulse Compression Generators

A magnetic pulse compression circuit capable of generating impulses of rise-time 200 ns and full-width at half-maximum (FWHM) pulse duration 500 ns, at a pulse repetition rate of up to 5 kHz, is described by Wang *et al*. in [38]. Such circuits utilise saturable inductors as magnetic compression switches, as illustrated in the circuit of Figure 2.9. The capacitor C_1 is the primary energy-storage component, and can represent the erected capacitance of, for example, a Marx generator. The stray inductance associated with the discharge loop is represented by L_1. When CS closes, the energy stored in C_1 is transferred to C_2; L_2 is unsaturated during this period, and as the inductance of L_2 is much larger than that of L_1, the current flowing through L_2 is low. The circuit is designed such that L_2 saturates when C_2 has fully charged, and the stored energy is then transferred to the load, since the inductance of the now saturated L_2 is much smaller than that of L_1. Through this technique, the maximum load voltage achieved in [38] was 20 kV.

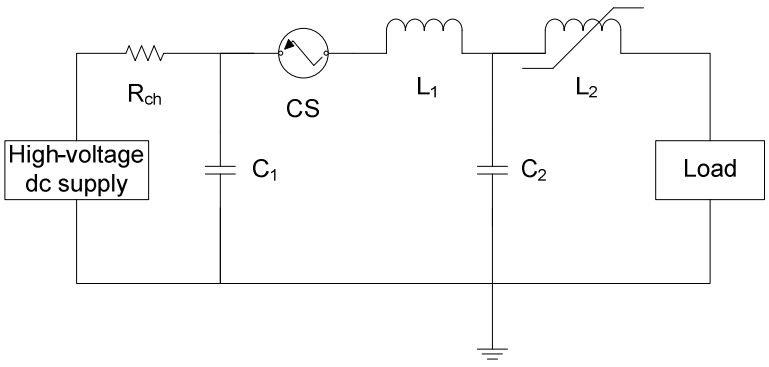

Figure 2.9. Schematic diagram of magnetic pulse compression circuit (adapted from [38]). R_{ch}: charging resistor; C_1: primary energy-storage capacitance; CS: closing switch; L_1: primary circuit inductance; L_2: saturable inductor; C_2: secondary energy-storage capacitor.

Sun Mok *et al*. describe a similar system capable of producing output voltage of up to 180 kV in [39], again with a rise-time of 200 ns. The maximum pulse repetition rate for the higher-voltage impulses in [39] was 200 Hz, and the application was removal of sulphur dioxide (SO_2) and nitrogen oxides (NO_x) from flue gas using corona discharges.

Magnetic *flux* compression generators have been widely utilised for military applications, due to the capability to deliver impulses of higher peak power than more conventional sources of greater size and weight. The principle of operation involves trapping magnetic flux in a conducting arrangement, before explosively deforming this arrangement to a smaller volume. In this manner magnetic flux compression is achieved, and the electromagnetic energy is delivered to the load [40]. A disk-type flux compression generator has been reported to deliver a pulse of energy in excess of 100 MJ into an inductive load of up to 10 nH [41]. The explosive deformation process renders the magnetic flux compression generator "a true one-time-use device," as stated by Neuber and Dickens in [40].

Marx Generators

Following an arrangement first demonstrated by Edwin Marx in 1923 [42], a series of high-voltage capacitors are charged in parallel to a high dc voltage, and then discharged in series via spark gaps. The gaps close almost instantaneously, a typical 10-stage Marx erecting in a time ~200 ns [43], and an impulse voltage of n times the charging voltage appears at the output for n stages.

The maximum available pulse energy from the system is therefore given by equation (2.10):

$$E = n \cdot \frac{1}{2} \cdot C \cdot V^2 \tag{2.10}$$

where n is the number of stages; C is the energy-storage capacitance of one stage (F); and V is the voltage to which each capacitor C is charged (V).

The major circuit components can be connected in two different ways, as illustrated by the single-stage equivalent circuits in Figure 2.10. Of the two configurations, the circuit shown in (b) is usually preferred for short fall-times or where the load capacitance is small, due to the higher obtainable efficiency [15]. As aforementioned in section 2.1.1, the loads in the present study are of a capacitive nature, and hence the parameter C_L has been introduced in the following discussion to represent the capacitance of the load. As previously discussed in relation to single-stage capacitive-discharge circuits, Marx generators can be configured in either inverting or non-inverting topology; the circuits in Figure 2.10 are representative of generators of the inverting type.

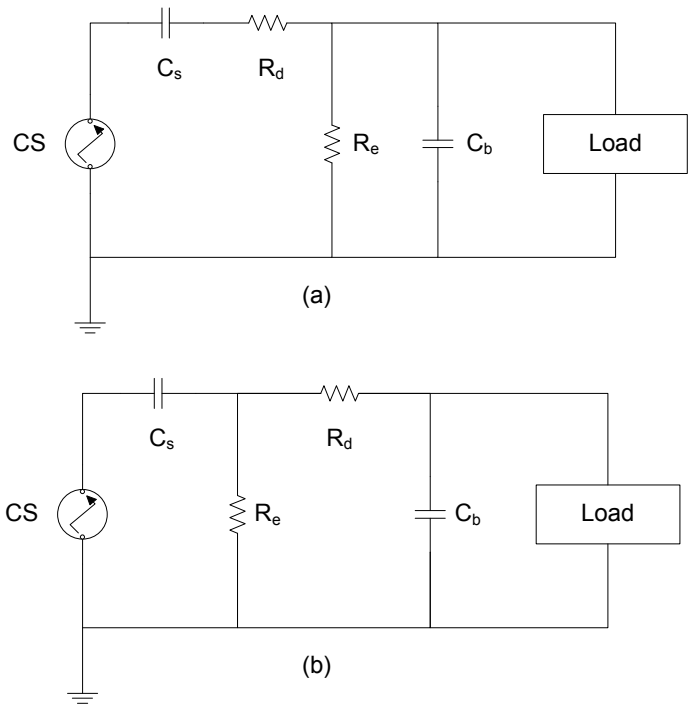

Figure 2.10. Single-stage equivalent schematic diagrams of inverting Marx generator circuit (adapted from [15]). CS: closing switch; C_s: energy-storage (discharge) capacitor; R_e: discharge/wave-tail resistor; R_d: damping/wave-front resistor; C_b: wave-front capacitor.

The output voltage wave-form with such an arrangement is described by the well-established double-exponential expression in equation (2.11) [15]:

$$v(t) = \frac{V_0}{R_d (C_b // C_L)} \cdot \frac{\tau_1 \tau_2}{\tau_1 - \tau_2} (e^{-t/\tau_1} - e^{-t/\tau_2}) \tag{2.11}$$

where V_0 is the output voltage magnitude (V); R_d is the wave-tail resistance (Ω); C_b is the wave-front capacitance (F); C_L is the load capacitance (F); τ_1 is the discharging time associated with the wave-tail (s); and τ_2 is the charging time associated with the wave-front (s). Providing that $R_e C_s \gg R_d(C_b//C_L)$, then the characteristic times τ_1 and τ_2 can be evaluated in terms of the circuit components in Figure 2.10b using equations (2.12) and (2.13), respectively:

$$\tau_1 \sim R_e (C_s + (C_b // C_L)) \tag{2.12}$$

$$\tau_2 \sim R_d \frac{C_s (C_b // C_L)}{C_s + (C_b // C_L)} \tag{2.13}$$

The major advantage of the Marx generator is the very high output voltage obtainable directly from a comparatively low dc charging voltage. Unlike with transmission-line based generators, the impulse wave-shape is controllable by changing the values of the resistors R_d and R_e. Disadvantages include the fact that wave-shaping resistors can require frequent maintenance and replacement. The self-inductance of capacitors has also traditionally placed a limit on the rate of current rise achievable from Marx generators, but capacitors with inductance <20 nH are now widely available [44].

Given the capability of the Marx generator to provide impulse voltages of hundreds of kV using charging voltages of tens of kV, its high efficiency for low-capacitance loads, and its capability for control of the impulse wave-shape, a Marx generator was the preferred method of impulse generation employed for this study. The Marx erection process is discussed in Chapter 3 (section 3.1) with reference to the generator used throughout the experimental phase of this study.

2.2 LIQUID INSULATION SYSTEMS

2.2.1 Dielectric Properties of Liquids

Dielectric liquids which are routinely subjected to impulse voltage stress should have the following electrical properties, as summarised by Ushakov [45]:

- high dielectric strength;
- high relative permittivity;
- low electrical conductivity;
- low rate of decomposition during electrical discharge; and
- fast restoration of dielectric properties following electrical breakdown.

Practical experience has shown that deionised or purified water and insulating oil best meet these selection criteria for use in pulsed-power systems, water particularly for its high relative permittivity (ε_r ~81) and oil for its high resistivity (10^{15}-10^{20} Ω.cm); for comparison, ε_r ~3 for insulating oils, and the resistivity of purified water is of the order of 10^7 Ω.cm [46].

2.2.2 Breakdown Mechanisms

Two general approaches to describing the mechanisms involved in liquid breakdown can be traced throughout the literature: bubble discharge theory, and ionisation discharge theory. In the former, discharges are assumed to form in gas cavities (bubbles) either pre-existing in the liquid and on the electrodes, or generated in the liquid under the action of an applied electric field [45]. Atrazhev *et al*. [47] discuss the formation of bubbles through localised Joule heating – local evaporation of the liquid starts to occur near the electrodes and around impurities, which act as nucleation centres for vapour bubbles generated as a result of boiling of the liquid. A percolation channel of bubbles can bridge the gap between the electrodes, the increased field strength in the low-permittivity vapour bubbles resulting in breakdown. Through development of a percolative model of liquid breakdown where the dielectric is treated as a network of resistors of random value, Qian *et al*.

[48] showed that breakdown is characterised by "successive breakdown of individual elements to finally form a percolation cluster."

In the ionisation discharge theory, electrons are accelerated due to an applied field and ionise molecules and atoms, with resultant boiling of the liquid leading to the formation of highly-conductive plasma channels [45]. In this case the discharge channel is in the form of an ionisation wave, or streamer. Atrazhev *et al*. [47] estimate this process as being dominant particularly for sub-microsecond impulse duration, with the formation of discharges inside gas cavities being more important for impulses of several microseconds duration.

During the past 40 years, an understanding of the processes leading to the electrical breakdown of liquid dielectrics has been derived through use of the following [49]-[56]:

- fast digitising oscilloscopes for voltage and current measurements;
- fast optical detecting systems for measurements of density gradients using shadowgraph/Schlieren photography with an image converter camera;
- electric field distributions produced using electric-field induced birefringence of the Kerr effect; and
- optical spectroscopy of emitted light.

The advent of fast optical diagnostics in particular has yielded evidence that streamer activity occurs in liquids prior to breakdown, with the streamers having a structure similar to that observed in gases and solids [57]. For liquids, the term streamer is used to describe a range of propagating pre-breakdown structures. Lesaint [58] suggests that streamers in liquids are gaseous in nature, with very high local fields of the order of MV/cm at the channel tips "able to induce intense and localised energy dissipation via charge injection and/or multiplication." This local energy dissipation facilitates the transition from liquid to gas phase.

Hebner [59] has shown that streamers are highly conducting through Kerr-effect electric-field measurements, with less than 10% of the total voltage across the electrodes being dropped across the streamer. The author also proposes that streamers can be separated into different modes, depending upon the voltage polarity and the velocity of the streamers.

Experiments conducted under dc conditions have shown that electron avalanches can occur in hydrocarbons when the high-voltage electrode is a negative point of diameter in the micrometer range [60], [61]. When the high-voltage electrode is a positive point, however, no fast initiating events are observed and the mechanisms leading to breakdown are less clear [61]-[63].

Butcher *et al*. [64] obtained results pertaining to the conduction and breakdown mechanisms in insulating oil with point-plane electrode geometry. The authors describe a 3-stage conduction process observed prior to dc breakdown. A low resistive current is initially witnessed at low fields ("stage 1"). When the applied field reaches approximately 40 kV/cm, a rapid rise in the injection current is observed as the effective barrier at the metal/oil interface is lowered and a "tunnelling" mechanism begins ("stage 2"). The current reaches space-charge saturation in "stage 3," just prior to breakdown.

Under impulse voltages, Top and Lesaint carried out experiments in semi-uniform fields in insulating oil, feeding a 100-µm-diameter tungsten wire through a 200-µm-diameter hole in the high-voltage electrode to mimic the effect of a protrusion on the electrode surface. It was shown through a combination of experiments and calculations that the local fields required to initiate streamers were similar to those determined for point-plane geometry [65]. With such a semi-uniform geometry (6 mm inter-electrode gap), a reduced threshold field value of around 50 kV/cm was found to cause filamentary, positive streamers to propagate to the point of breakdown [66].

Streamer Propagation

Streamer structures and characteristics in liquids depend especially upon the chemical composition of the liquid; the applied voltage in terms of wave-shape, magnitude, and polarity; the electrode arrangement; and the hydrostatic pressure. Furthermore, the current associated with fast streamers is always higher than that of slow streamers, independent of the liquid or the voltage polarity [57].

The concept of streamer modes, in highly divergent fields in insulating oil, is discussed by Beroual *et al*. in [57]. For positive polarity, measurements have shown the inception field for "1st mode" (primary) streamers to be around 2 MV/cm, and the streamers propagate with a constant velocity of 2-3 km/s. At higher voltages a decrease in the delay time to breakdown was observed, coinciding with the development of "2nd mode" (secondary) streamers. The inception field and propagation velocity for 2nd mode streamers were measured to be 12 MV/cm and 32 km/s, respectively. Tertiary or "3rd mode" streamers, with a velocity exceeding 100 km/s, were observed by "highly overstressing" the gap. Although positive streamers are normally up to 10 times faster than negative streamers, both polarities show more similar velocities in insulating oil. In the negative polarity, 1st mode streamers are initiated at fields above 2.5 MV/cm and propagate at ~1 km/s. Although no specific field levels are given in [57], Beroual *et al*. state that increasing the applied field results in the initiation of compact streamers with many branches, propagating at 1-3.5 km/s, and that at "very high fields," the propagation velocity can exceed 100 km/s as in the positive polarity. Secondary streamers were detected in gaps longer than 40 mm in the negative polarity.

Larger needle radii lead to lower streamer inception fields. For needle tips with radius of curvature <3 μm, the inception field is >10 MV/cm, falling to ~1 MV/cm for radius of curvature >100 μm [57].

Streamer propagation in liquids has been shown to be due to both electronic and gaseous processes depending upon the liquid composition; the former dominates when the liquid contains aromatic molecules. Devins *et al*. [53] found that negative

streamer velocity in naphthenic oil was increased through the addition of a non-ionic electron scavenger (SF_6 or ethyl chloride). Beroual and Tobazeon [67] showed a similar effect on negative streamer velocity in cyclohexane, but no effect on positive streamer velocity was found in either study.

The addition of a non-ionic, low ionization potential compound to naphthenic oil does not affect the negative streamer velocity, but increases positive streamer velocity by 2-3 times [53].

With increase in hydrostatic pressure, several effects are observed [68]:

- the breakdown strength generally increases;
- the number and amplitude of current and associated light pulses decreases;
- the streamer length decreases.

Above a threshold pressure, neither streamers nor the corresponding current/light pulses are observed [56], [69]. These findings support the theory that streamers are gaseous in nature. For fast streamers of velocity exceeding 10 km/s however, no such supporting evidence is available [58].

Bubble Development

The application of impulses of sufficiently high voltage to liquids results in the generation of pre-breakdown bubbles due to electromechanical forces. Such bubbles are usually considered as being filled with air and hence having $\varepsilon_r = 1$ for the purpose of calculations and modelling. Timoshkin *et al*. [70] present an analysis of the thermodynamic and electrostatic processes involved in dielectric liquids in highly-divergent fields. The authors calculate that higher critical electrical fields are required to form a stable pre-breakdown bubble, and that the critical bubble radius is larger in mineral oils compared with synthetic ester and silicone oil. This corresponds with lower measured breakdown voltages found for esters and silicone oils as compared with those found for mineral oils [71].

The Role of Impurities

Whereas higher concentration of particulate matter suspended in insulating oil can lead to reduced breakdown fields under ac voltage application [72], Lesaint and Top [73] state that experiments carried out on the breakdown of insulating oil in a uniform-field are not likely to be influenced by the particulate content of the oil or by space charge effects if impulse voltages, rather than dc or ac voltages, are applied. This is because the impulse duration is too short to allow breakdown to be triggered by particles moving towards the electrodes from the liquid volume. As already discussed, Atrazhev *et al*. [47] on the other hand state that impurities act as nucleation centres for vapour bubbles for impulses of duration longer than ~1 μs.

Volume and Surface Effects

In 1953, Wilson [74] stated that the primary factor determining the breakdown voltage of oils in different electrode geometries was the volume of oil subjected to an electrical field stress. This volume effect was also observed by Katahoire *et al*. [75], where it was shown that increasing the electrode surface area resulted in a decrease of the ac breakdown voltage of silicone oil. Increasing the electrode surface area results in a greater volume of the oil being electrically stressed, increasing the probability of breakdown and lowering the breakdown voltage accordingly.

Under impulse voltages, breakdown is more likely to be triggered by defects on the surfaces of the electrodes, or by particles adhering to the surfaces of the electrodes [73]. The impulse breakdown field of Shell Diala oil AX has been shown to fall from 1 MV/cm to 0.1 MV/cm when the electrode surface area is increased from 0.1 cm^2 to 10^5 cm^2 [76].

2.2.3 Measured Breakdown Voltages

Uniform Fields

It is known that both gases and liquids can withstand higher electrical stresses the shorter the pulse duration, and breakdown fields as high as 11 MV/cm have been measured in a plane-parallel electrode configuration by Lehr *et al*. [76], who subjected Shell Diala oil AX to single-shot impulses with a rise-time of 130 ps and a

FWHM pulse duration of 300 ps. It is understood that the reason behind this high breakdown field is the very short pulse duration, which limits the time available for streamer initiation and propagation, in turn reducing the probability of breakdown. When the oil was stressed at a pulse repetition rate of 100 pps, reduced breakdown strength of 5.8 MV/cm was measured. The planar, symmetric electrodes used in this case had a surface area of 12.5 cm^2.

Zheltov [77] reports a breakdown strength of 5 MV/cm for unnamed transformer oil when subjected to impulses of duration 1.5-3 ns. Also reported by Zheltov was a 2.5-fold increase in the breakdown strength of oils for a 10-fold decrease in the duration of the applied electric stress.

Martin reported a scaling law in [78], reproduced in equation (2.14), for impulse voltages of duration in the range 150-300 ns in insulating oil:

$$F^{3/2}t = 0.08 \tag{2.14}$$

where F is the electrical field in MV/cm, and t (μs) is the time from 63%-100% of the peak impulse voltage. Using this law, a 10-fold decrease in the impulse duration results in an increase in the strength of the oil of 4.6 times.

Jue *et al*. [79] have studied the uniform-field dielectric strength of insulating oil in the nanosecond pulse regime in very short gaps of length 0.15 mm to 1 mm. It was found that the breakdown field increased linearly from 1.75 MV/cm to 2.75 MV/cm for rates of voltage rise in the range 10-36 kV/ns. These fields were between 13 and 23 times greater than the corresponding dc breakdown field. All measurements were made on the rising edge of an impulse voltage wave-form of 300 kV peak magnitude and 10 ns rise-time. When the pulse duration was increased from 15 ns to 85 ns, with rate of voltage rise fixed at ~23 kV/ns, the breakdown field fell from 1.3 MV/cm to 0.6 MV/cm. This was found to be the case for both positive- and negative-polarity impulses.

Impulse voltages in the MV regime are required to produce ultra-wideband radiation, with rise-times of the order of hundreds of ps. Mankowski *et al*. [80] subjected unnamed transformer oil to impulse voltages in these regimes, with the oil located in a test cell between a pair of brass electrodes of radius 1 cm. The gaps used in the tests were in the range 0.4 mm to 0.8 mm, and the authors state that uniform-field conditions could be assumed for gap lengths of up to 5 mm. The highest measured breakdown fields were around 13 MV/cm, with breakdown occurring after 700 ps. The authors also suggest an empirical expression (equation (2.15)) relating the breakdown field, E (kV/cm), to the time to breakdown, t (s), for their own experimental data and for that of others from the literature for impulse durations less than 5 ns:

$$E = \frac{1}{44900} t^{-0.95} \tag{2.15}$$

Non-uniform Fields

The ASTM D 3300 [81] standard has been used to characterise the breakdown voltage of several oils. Negative-polarity, 1.2/50 μs lightning impulses are applied to a point-sphere electrode configuration, generating a highly-divergent electric field in the oil. The inter-electrode gap spacing is 25.4 mm.

Breakdown voltages for a range of oils measured using the D 3300 method are contained in Table 2.1. Using this method, the breakdown voltage of Shell Diala oil AX [82] is quoted as 197 kV minimum and 226 kV typical. Other available data for this method was for VOLTESSO 35 [83], with a minimum breakdown voltage of 225 kV; and for BIOTEMP (biodegradable vegetable oil) [84], with a minimum quoted breakdown voltage of 90 kV and a typical quoted breakdown voltage of 100 kV. The lower impulse breakdown strength of BIOTEMP compared to Shell Diala AX is in spite of the higher ac breakdown strength of BIOTEMP [85].

Also using the D 3300 method, Rouse [86] showed that the negative impulse breakdown strength of unnamed transformer oil decreased dramatically with

increasing aromatic hydrocarbon content. The measured breakdown voltage fell from over 300 kV for no aromatic hydrocarbon content, to 145 kV for a 25-30% concentration of aromatic hydrocarbons. Using the D 2300 standard, a corresponding decrease in the gassing tendency, from +50 µl/min to −10 µl/min, was measured with increasing concentration of aromatic hydrocarbons. A negative gassing tendency is undesirable, since this means that the liquid is gas absorbing, and trapped gases with a low relative permittivity in the liquid bulk can lead to field enhancement and breakdown, as evidenced by the decreasing breakdown voltages. Rouse also reported that the positive breakdown voltage of 120 kV did not depend on the concentration of aromatic hydrocarbons in the oil.

Table 2.1. Breakdown voltages of oils measured using D 3300 method. Percentage for "transformer oil" corresponds to aromatic hydrocarbon content.

Oil	Breakdown voltage (kV)	
	Minimum	*Typical*
Shell Diala AX [82]	197	226
VOLTESSO 35 [83]	225	-
BIOTEMP [84]	90	100
"Transformer oil" (0%) [86]	300	-
"Transformer oil" (25-30%) [86]	145	-

Table 2.2. Measured breakdown strength of oils [71] and calculated critical applied field to generate a stable pre-breakdown bubble and critical bubble radius that can lead to breakdown [70].

Oil	Measured Breakdown Strength (kV/cm) [71]	Calculated Critical Applied Field (kV/cm) [70]	Calculated Critical Bubble Radius (µm) [70]
Shell Diala	746	890	0.72
Midel 7131	706	810	0.60
Dow Corning	672	890	0.68

The impulse breakdown strength of various dielectric liquids in short gaps (1.5-3.5 mm) between spherical electrodes, giving a more uniform field distribution than the D 3300 method, is reported in [71]. With voltage rise-time ~60 ns, the measured breakdown strength for several oils is shown in Table 2.2. The critical applied field

required to form a critically-sized pre-breakdown bubble in a strongly non-uniform field, and the critical bubble radius, both calculated in [70], are also listed in Table 2.2. It can be seen that the combination of higher critical field and bubble radius calculated in [70] for Diala mineral oil compared to Midel synthetic ester and Dow Corning silicone liquid corresponds with higher measured breakdown strength in [71]. Dohnal and Frotscher [87] report that Midel 7131 has 26-30% lower breakdown voltage than Diala mineral oil when subjected to 1.2/50 μs lightning impulses.

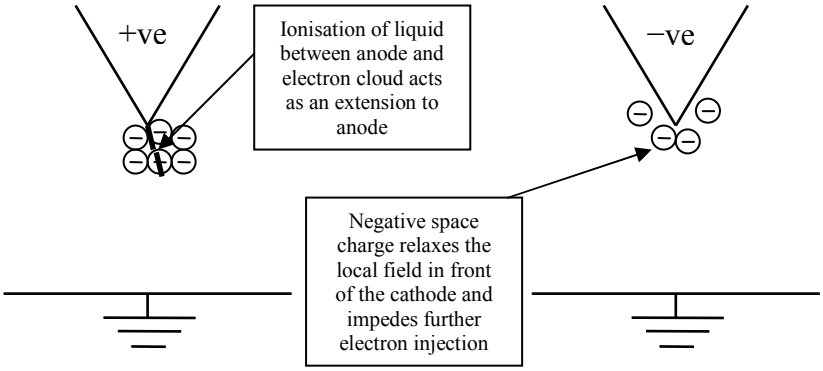

Figure 2.11. Sketch highlighting polarity effect in point-plane gaps in liquids. For positive points, ionisation between the point and electron clouds acts like an extension of the anode, reducing the gap length and resulting in lower breakdown voltages. For negative points, negative space charge surrounding the cathode relaxes the local field and impedes further electron injection, meaning that higher applied voltages are required to initiate breakdown.

A polarity effect on breakdown was observed in [80] when transformer oil was tested in a point-plane geometry. The breakdown strength was found to be ~50% higher for a negative point than a positive point at short breakdown times (1-2.5 ns). The polarity effect has been explained in [88]-[90] by an effective reduction in the inter-electrode gap length in the positive polarity, as electrons are generated in the liquid and attracted to the positive-point electrode, and the conducting channel formed as a result of ionisation of the liquid between the anode and the electron cloud acts as an extension of the needle electrode. In the negative polarity, a negative space charge is

formed in front of the needle, reducing the field gradient and impeding the injection of further electrons, meaning that higher applied voltages are required to cause breakdown or flashover. This argument is represented diagrammatically in Figure 2.11.

2.2.4 Selection of Liquid Dielectric

Several referenced studies have highlighted the higher breakdown voltage of mineral oils compared to esters and silicone oils. Mineral oils used in the literature vary from study to study, with several of the referenced works using unspecified oil simply named as "transformer oil". EOS Ltd (UK) L10B mineral oil, which meets the requirements of BS 148:2009 [91], was selected as the liquid dielectric for this study.

2.3 SOLID INSULATION SYSTEMS

Solid insulation systems have been developed in a variety of forms for the insulation of both power and pulsed-power systems. Porcelain, ceramic, and glass-ceramic insulation have found widespread use in the power industry, and reliable protection components have been developed and successfully deployed. Polymer insulation technology has also evolved steadily and found use in both power and pulsed-power applications, and the focus of this section is the dielectric properties of polymers relevant to pulsed-power systems.

2.3.1 Dielectric Properties of Solids

The selection criteria listed in section 2.2.1 with reference to liquids generally also apply to solids. Solids do not, however, possess the same self-healing capabilities as liquids, and the solid will not recover its insulating properties once a breakdown channel has been established in the bulk of the material. The important dielectric properties are:

- dielectric strength;
- relative permittivity;

- bulk/volume conductivity;
- surface conductivity; and
- tracking and arc resistance.

2.3.2 Breakdown Mechanisms

Several different mechanisms of solid breakdown have been identified as operating over a wide range of timescales, as indicated in Figure 2.12. The breakdown mechanism changes as the time of voltage application increases, and the measured breakdown strength can be much lower than the intrinsic breakdown strength (ns regime) for breakdown mechanisms which take a long time to develop, such as electro-chemical breakdown [92].

Under electric-field stress, breakdown of solids occurs when the magnitude of the field becomes high enough that free charge carriers acquire an excess of energy that cannot be dissipated by phonon/photon emission alone. As free charge carriers are not usually present, solid dielectric breakdown must follow the injection of charge carriers from the electrodes, and once the solid is stressed with an electric field of amplitude sufficient to cause charge-carrier injection, carriers are accelerated in the high field and breakdown ensues [93]. Processes of field-enhanced thermionic emission, as described by Schottky [94], and direct field emission, as described by Fowler and Nordheim [95], account for charge-carrier emission at different levels of applied field. The breakdown channel will become filled with a gas of low relative permittivity, causing local electric-field enhancement and increasing the probability of streamers forming and propagating to the point of breakdown upon application of subsequent voltage stress.

Contrary to gas and liquid breakdown where the applied electric fields required for breakdown often greatly exceed those for dc voltages, the impulse breakdown strength of solids can be lower than that for the application of dc voltages. Several studies in the 1960s [96]-[98] showed that the impulse breakdown strength of polyethylene was only 80% of the dc breakdown strength.

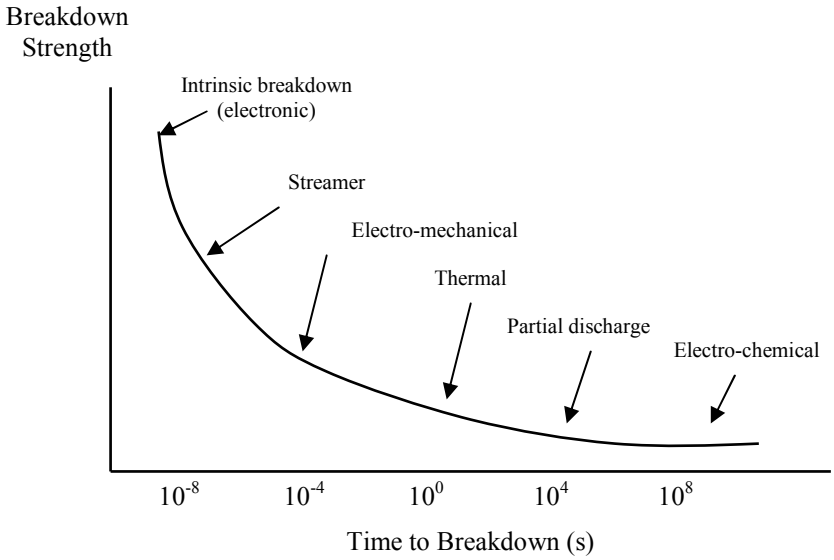

Figure 2.12. Sketch highlighting the relative breakdown strength versus time to breakdown for different solid breakdown mechanisms (adapted from [92]).

The Role of Impurities and Voids

Impurities and voids unavoidably introduced during the manufacturing process form the breakdown initiating sites in solids. Only where polymers could be produced and electrically tested without these undesirable inclusions, could the intrinsic breakdown strength associated with the material be measured. This has led to much research on thin-film polymer samples, where the small volume leads to a lower probability of breakdown being initiated by an impurity or void.

Gefle *et al*. [99] investigated the influence of inhomogeneities in low-density polyethylene on the breakdown field, applying positive-polarity, 3/10-μs impulses to 650-μm thick samples immersed in silicone oil. The applied electric-field strength was 750 kV/cm, with impulses applied at a repetition rate of 400 pps. In terms of dc pre-stressing, the authors found that an applied field in the range 200-400 kV/cm, applied for 1-15 minutes led to the accumulation of homo charges around the electrodes. When the dc pre-stressing field was raised to above 500 kV/cm, the field and charge distributions were found to be very inhomogeneous, with both homo and hetero charges accumulating around the electrodes. The volume charge density

increased by a factor of nine when the dc pre-stressing field was increased from 200 kV/cm to 450 kV/cm, and increased by a factor of two under negative pre-stress compared to positive. The impulse breakdown fields were shown to decrease, by up to eight times, following pre-stressing using the opposite polarity, and to increase by up to nine times following pre-stressing using the same polarity.

Space Charge

It is accepted that the injection of space charge into the bulk of solid dielectrics plays a major role in determining the impulse breakdown strength of solids, as demonstrated in various studies by pre-stressing thin-film polymer samples with dc voltages before impulse application. Bradwell *et al*. [100], for example, attributed variations in impulse breakdown strength to space charge in the vicinity of the electrodes, established by pre-stressing with dc voltages.

In an attempt to experimentally quantify the effects of space charge on solid breakdown, Suzuoki *et al*. [101] studied the behaviour of space charge in polyethylene and poly-p-phenylene sulphide (PPS) films utilising the laser-induced-pressure pulse (LIPP) technique. For 25-μm PPS samples, the impulse breakdown fields, relative to the case with no dc pre-stress, were found to decrease when a dc pre-stress of the opposite polarity to the impulse voltage was applied, and were not significantly affected when a dc pre-stress of the same polarity as the impulse voltage was applied. When the sample thickness was reduced to 6 μm however, decreases in the impulse breakdown fields were observed for both polarities of dc pre-stress. The authors suggest that the injected homo space charge penetrates the bulk of the sample close to the opposite electrode due to the very short inter-electrode gap, causing it to appear as a hetero space charge to the other electrode, and resulting in reduced breakdown voltages for both polarities of dc pre-stress. In this case, homo space charge refers to charge of the same polarity as that on the electrode, and hetero space charge refers to charge of the opposite polarity.

Modelling based on space-charge-limited conduction and the experimentally-determined impulse breakdown fields after pre-stressing indicated that the level of

space charge accumulated after a dc pre-stress of 1-2 MV/cm was ~100 nC/cm^2, with a charge penetration depth of ~10 μm. This theory was supported by LIPP measurements, where positive homo space charge was detected in the region of the anode soon after application of a dc pre-stress. The level of current detected remained almost unchanged for the duration of application of the pre-stressing dc voltage.

Accumulation of negative homo space charge around the cathode was observed in oxidised polyethylene, with detected charge levels in the range 10-50 nC/cm^2 at a distance of 5-15 μm from the cathode. Such accumulation of negative space charge was not witnessed in polyethylene samples that were not subjected to oxidation, correlating with the finding that oxidation enhances electron injection in polyethylene [102], [103]. When compared with the breakdown fields for samples not subjected to dc pre-stress, the breakdown fields in samples of oxidised polyethylene were found to increase with pre-stress of the same polarity, with the homo space charge acting to reduce the field at the cathode. In the case of opposite polarity pre-stress, the breakdown fields were lower than those for no pre-stress, with the negative space charge acting to enhance the field at the new anode.

Polarity Effect

Kitani and Arii [104] conducted experiments on thin-film polymer samples (20-500 μm) under point-plane geometry, and showed that the applied voltages required to achieve a 50% probability of breakdown were higher for negative impulses than for positive impulses. The authors credit the discovery of this polarity effect to Mason [105] in 1955, and propose that the differences in breakdown voltage are due to different breakdown mechanisms between polarities: positive streamers leading to breakdown for a positive point, as in gas breakdown; and electron avalanches leading to breakdown for a negative point. Space charge formed by electrons trapped in the polymer matrix reduces the field in the vicinity of the negative point, leading to a distribution that "seems to approach a uniform field," meaning that higher applied voltages are required to cause breakdown. Of five different thin-film materials tested (polyethylene; polyethylene terephthalate; polycarbonate; polystyrene; and

polymethyl methacrylate (PMMA)), Kitani and Arii found that although polystyrene had the highest breakdown strength in both polarities, the rank order of the other materials in terms of breakdown strength varied between polarities. The square-wave impulses applied were of short duration, with a rise-time of 1 ns and pulse duration of 100 ns. The voltage magnitudes were in the range 10-35 kV. It was also shown that the formative time lag, defined by the authors as "the minimum time lag under the same conditions," increased with increasing electrode separation, and decreased with increasing applied voltage. Apparent velocities associated with discharge-channel development, calculated simply by dividing the inter-electrode gap by the formative time lag, indicated that the channel developed much faster for the positive point than for the negative point, with similar differences having been reported in [106] for both liquids and gases.

Bradwell *et al*. [100] reported that pre-stressing polyethylene films with dc voltages and then applying impulse voltages of the same polarity resulted in an increase in the impulse breakdown voltage to a level closer to the dc breakdown strength. When impulses of the opposite polarity to the dc pre-stress were applied, the impulse breakdown voltage was found to be much reduced compared to the case when no pre-stressing dc field was applied.

Kitani and Arii [107] noted that the time lags to breakdown measured by Bradwell *et al*. [100] were very long (over 40 μs) for the case of opposite polarity pre-stress, and conducted a study of breakdown strength and time lags to breakdown in low-density polyethylene films (30 μm) with impulses of much shorter duration, again 1 ns rise-time and 100 ns pulse duration. Pre-stressing dc voltages were applied for one minute before the application of an impulse voltage in a plane-parallel configuration. As a reference point, the authors measured the dc breakdown strength as 5.8 MV/cm, and the impulse breakdown strength with no pre-stress as 4.9 MV/cm. Despite the short duration of the impulse voltages applied by Kitani and Arii, the ratio of 85% of impulse strength to dc strength is similar to prior studies with impulse durations in the range 1-8000 μs [96]-[98]. When compared with the impulse breakdown strength in the case of no pre-stress, the impulse breakdown

strength increased after pre-stressing with the same polarity, and decreased after pre-stressing with the opposite polarity.

The polarity effect reported in these studies was considered to be an anomaly of thermionic models where the electric field at the cathode dominates the breakdown process. To account for this, Pulfrey [93] proposed that in the situation where the work function of the electrode metal was lower than that of the solid dielectric, electrons could be emitted from the electrode into the solid dielectric upon contact of the two, and therefore negative space charge would pre-exist in the region of the cathode before application of an electric field.

More recently, Malec *et al*. [108] showed that the breakdown field of high-density polyethylene varies significantly with pressure.

Material Structure

Maeda and Yahagi [109] found that the impulse breakdown strength of 50 μm LDPE films was affected by the orientation of crystalline lamella in polyethylene, the orientation being changed via elongation of the film, and suggested that electrons liberated from traps in interfacial regions between amorphous and crystalline regions flow along the lamellae, transferring energy from the electric field to the bulk of the solid, with electronic thermal breakdown following due to the resultant increasing electron temperature.

Electrical tree initiation in LDPE was studied by Hozumi *et al*. [110], who applied 1.2/50 μs lightning impulses to samples of thickness 50-100 μm. The point-plane gap length was 1 mm, and it was found that tree-initiation voltages were lower and tree paths were thinner with positive impulses when compared with negative. Transmission electron microscope (TEM) photographs were utilised to study trees in the nanometre regime, and the trees were found to be less than 10 μm in length, with a diameter of ~100 nm at the point of initiation, growing in parallel with the lamellae. The authors concluded that the growth of trees initiated by the application of impulse voltages is a result of local dielectric breakdown events, occurring in a

filamentary form over several micrometres, with tree growth initiated when electrons are accelerated in the amorphous region or on the lamellar interface.

Following a period of extensive research into the breakdown behaviour of different types of polyethylene for use in high-voltage coaxial cables, Kawahigashi *et al*. [111] studied the impulse breakdown properties of polypropylene, with the motivation of finding a material that offered higher-voltage breakdown thresholds than polyethylene for the same cable dimensions. The authors concluded that there were three ways to increase the impulse breakdown strength of semi-crystalline insulating materials, each having the effect of removing boundaries between spherulites:

- the incorporation of a high-molecular-weight additive into the polymer matrix;
- the addition of a nucleating agent; and
- control of the crystallising temperature.

2.3.3 Selection of Solid Dielectrics

Given the widespread use of polyethylene in high-voltage, pulsed-power systems, two forms of this material were chosen for investigation as oil-immersed insulators in the present study: low-density polyethylene; and, given the conclusion of Kawahigashi *et al*. [111] that the addition of a high-molecular-weight additive into the polymer matrix can increase the breakdown strength, ultra-high molecular weight polyethylene. Polypropylene was found by the same authors to have desirable characteristics for resistance to impulse voltages, and this material was also investigated.

Two further materials with no published data for breakdown in oil were chosen for comparative purposes: Rexolite, a cross-linked polystyrene; and Torlon, a polyamide-imide. Rexolite is mechanically strong and has stable permittivity (ε_r ~2.5) over a wide frequency range, and is widely used in microwave applications [112]. Torlon has a higher relative permittivity than that of the other solid materials (ε_r ~3.9) – and also that of mineral oil (ε_r ~2.2) – and is used, for example, to form

"tie-rods" between ± dc-charged electrodes in the oil-immersed, pressurised spark-gap switches [113] discussed in section 2.1.1.

2.4 COMPOSITE LIQUID-SOLID INSULATION SYSTEMS

Most previous studies have focused mainly on dc, ac, and lightning-impulse (1.2/50 μs) stressing regimes, but more recently, the need for research into how dielectric materials respond to non-standard impulse voltage wave-forms has begun to be addressed. The dielectric properties and breakdown mechanisms of liquid-solid insulation systems when subjected to impulse voltages are considered in this section.

2.4.1 Dielectric Properties of Liquid-Immersed Solids

In a composite liquid-solid insulation system, breakdown is commonly initiated in the region of the liquid-solid interface. Therefore, in addition to the important dielectric properties listed in sections 2.2.1 for liquids and 2.3.1 for solids, the conductivity of the liquid layer immediately adjacent to the solid, and the processes by which this layer can obtain increased conductivity compared with the liquid bulk, are of major significance.

2.4.2 Breakdown Mechanisms

Cherney and Cross [114] investigated the effect of electro-hydrodynamic (EHD) flow on the breakdown of a liquid-solid interface, with a Teflon spacer immersed in unnamed insulating oil. The authors observed a transition from laminar to turbulent flow immediately prior to dc flashover, and suggested that the formation of a gas bubble in the turbulent flow led to breakdown. It was discovered that a dc voltage corresponding to 95% of the dc flashover level could be applied, and a 1/50 μs impulse of equal voltage magnitude to the dc stress subsequently applied (while also maintaining the dc stress) without inducing flashover. This led Cherney and Cross to conclude that as the mechanism inducing dc flashover was too slow to respond to a 1/50 μs impulse voltage, then dc and impulse-driven flashover of liquid-immersed solids must occur as a result of different breakdown mechanisms.

The requirements of the power industry have meant that the pre-breakdown and breakdown behaviour of composite gaps consisting of pressboard immersed in insulating oil have frequently been investigated to mimic the conditions within transformers. Krins *et al*. [115], for example, performed experiments in an oil-solid configuration, designed to replicate the dielectric interfaces in the diverter switches of on-load tap changers, with two electrodes positioned perpendicularly at either side of a rod-shaped solid insulator. They compared the breakdown and flashover behaviour of the gap with five different types of solid rod, subjected to both positive and negative-polarity impulses, in a highly-divergent field. A further aim of the study was to determine the effect of the addition of carbon particles to the oil on the insulating properties of the gap.

Several important conclusions were drawn from the experimental work in [115]. Firstly, it was found that the application of positive impulses resulted in markedly lower breakdown and flashover voltages than for negative impulses, as discussed in section 2.2.3. Secondly, it was shown that the addition of carbon particles resulted in a greater reduction of the breakdown/flashover voltages in the negative polarity than in the positive polarity. The fact that carbon particles in mineral oils have a net positive charge [116] contributes to this effect, with carbon particles forming a positive space charge around the negative needle point, again resulting in an effective reduction of the inter-electrode gap length.

In terms of the different solid materials tested in [115], three characteristics were found to influence the flashover voltage: the relative permittivity; the arithmetical mean surface roughness; and the surface profile. The materials chosen had permittivity ranging from 2.3 for polyethylene to 5.6 for laminated paper, with three types of resin with permittivity values of 4.5, 4.8, and 5.3 also being tested. For negative impulses in “technically clean” oil, it was found that the addition of resin and laminated paper rods resulted in a 17-20% reduction in the breakdown strength compared to the oil gap without solid insulation. When the polyethylene solid was added however, the measured breakdown strength was as high as the open (no solid) oil gap. The most important factor in this situation is the permittivity match or

mismatch between the oil (ε_r = 2.2) and the solid. In the case of the high-permittivity solids, the field lines are bent towards the surface of the solid from the needle tip. Streamers then develop in this direction of highest field strength and tend to propagate along the liquid-solid interface rather than directly through the solid because of the high bulk breakdown strength of the solid. In the case of the polyethylene rod, where the permittivity is very similar to that of the oil, the field lines will closely resemble those in the open oil gap and, hence, similar breakdown voltages exist for these two insulating arrangements.

With positive impulses however, the measured breakdown strength was the same for the open oil gap and for the gap with any of the different types of solid rod, in spite of the range of permittivity. Krins *et al*. [115] argue that since charge carriers are generated in the liquid as a result of field ionisation under positive stress, secondary electron emission from the solid surface cannot contribute charge carriers. This means that the addition of the solid effectively reduces the volume of oil – where the charge carriers are initiated – between the electrodes, leading to an increase in the breakdown strength that counteracts the reduction in breakdown strength due to permittivity mismatch.

Polymers have also found application as the insulating layer in coaxial high-voltage cables, and hence studies of the breakdown and flashover properties of the different interfaces found within high-voltage cable assemblies are of particular importance. Katahoire *et al*. [75] investigated the breakdown properties of cross-linked polyethylene (XLPE) immersed in silicone oil, with electrode profiles chosen to replicate the interfaces found within cable terminations. They state that the breakdown voltages associated with flashover of liquid-solid interfaces are usually lower than those of a liquid gap of the same length, but without a solid spacer. The main reason for this is again the higher dielectric permittivity of the solid when compared with the liquid, creating a high-field region at the interface which leads to flashover.

Under uniform-field conditions, both the liquid and the solid should be subjected to equal stress, and bulk breakdown of the liquid should in theory occur rather than interfacial flashover, independent of the presence of the solid. The presence of microscopic protrusions on the solid surface, however, leads to field enhancement at these surface defects, and when the relative permittivity of the solid is greater than that of the liquid, these effects lead to decreased breakdown voltages. Experimental results in [117], [118] have shown that interfacial breakdown voltages can be increased by the minimisation of pits on the surface of the solid, and of voids at the liquid-solid-electrode triple point, although the breakdown voltages were still lower than those of the liquid gap without a spacer. Katahoire *et al*. [75] provided examples of a reduction in breakdown voltage of transformer oil with relative permittivity of 2.2 by 6.5% when a PMMA spacer (ε_r = 3.5) is added, and by as much as 50% when the added material is phenolic cloth (ε_r = 12.2). When the solid has a slightly lower relative permittivity than the liquid, the breakdown voltage is also lower than that of the liquid gap alone; Cherney [118] suggests that this is due to drifting of a pre-existing molecular ion distribution, weakly bound to the surface of the solid, towards the liquid-solid-electrode triple junction upon application of an electric field. This leads to field enhancement and a resultant greater probability that breakdown will occur at the triple-junction via field emission due to surface defects on the electrode.

Measurements utilising the Kerr effect [119], [120] to characterise field distortion in liquids due to the presence of a solid spacer between the electrodes have shown that the magnitude of the electric-field distortion is greatest at the liquid-solid interface, with the effect gradually decreasing with increasing distance from the interface up to 5 mm. Cross and Tobazeon [120] determined that field distortion is partially due to bulk polarisation of the solid, as the magnitude of the distortion and the time required to establish the field-induced optical-fringe pattern varied with the solid material type. An increased current density was detected around the interface in [119], and changing the solid material did not result in corresponding changes in the current density.

Propagation of Streamers

Rzad *et al*. [121] showed that there is a limiting voltage below which streamer propagation does not occur on the wave-tail of an impulse. The same authors show that while streamer propagation occurs well below this voltage so long as the voltage is still rising, the propagation velocity decreases to zero within 1-2 μs of the voltage falling to this limiting voltage after passing the impulse peak [54].

When a PMMA (ε_r ~2.6) spacer was introduced into an oil gap, it was found that streamer velocities were increased compared to the open oil gap, and were comparable to streamer velocities under point-plane geometry in open oil gaps [122]. Results obtained with oil-impregnated pressboard interfaces (ε_r ~4.5) also indicated that even higher streamer velocities were induced [123], with a rapid transition to fast streamer modes occurring with an increase in the applied field. Such an effect was not observed for point-plane gaps in oil alone, where the velocity did increase linearly with applied field, but with a very shallow gradient leading to a limiting velocity of around 2 km/s.

This previous work on liquid-solid interfaces clearly suggests that although the breakdown voltage may be unaffected by the introduction of a solid spacer under certain circumstances, an increased streamer propagation velocity is induced.

Triple Point Effects

Polymers have become increasingly used for outdoor insulation. Hammam *et al*. [124] cite excellent mechanical strength, shock resistance, arc resistance, light weight, compactness, and the ability to be readily formed into complex shapes as advantages of polymers over traditional porcelain insulators. Problems, however, have included erosion, surface tracking, and water absorption, which can lead to either surface flashover or electrical breakdown of the solid material bulk [125]-[129].

Experimental work on the flashover of 15 kV high-density polyethylene (HDPE) insulators for use in an outdoor weather shed arrangement was conducted by

Hammam *et al*. [124]. Three different scenarios were investigated to simulate different outdoor conditions, with flashover voltages measured:

- in a dry environment;
- immediately after immersion of the upper shed and body of the insulator in saline water; and
- immediately after immersion of the complete insulator arrangement in saline water.

For the application of negative lightning impulse voltages, the 50% flashover voltage was found to be ~210 kV in a dry environment, falling to ~160 kV in both wet environments. To explain this behaviour, the authors suggest that homo charges accumulated on the insulator surface directly beneath the triple junction, and in voids, relax the electric field and suppress streamer progress in a dry environment. In wet environments on the other hand, the probability of electron attachment on the saline water-insulator interface is much reduced. The homo-charge accumulated beneath the triple junction decreases accordingly, increasing the electric field intensity in this region and resulting in lower flashover voltage. When the impulse polarity was positive, the 50% flashover voltage was found to be in the narrow range 150-160 kV for all three conditions. The reduction in flashover voltage in a dry environment with positive impulses (~50 kV lower than for negative impulses) can be attributed to the different breakdown mechanisms. Free electrons in the gas are attracted to the anode in the positive polarity, leading to an effective reduction of the inter-electrode gap similar to the situation depicted in Figure 2.11; higher applied voltages are required for charge injection from the cathode in the negative polarity.

2.4.3 Interaction Between Discharge and Dielectric

Interfacial Polarisation

When considering heterogeneous dielectrics subjected to tangential field stress, interfacial polarisation can occur due to "the migration of charge carriers to the interfacial boundaries under the effect of an applied (time varying) electric field" [130]. In the Maxwell-Wagner theory that describes interfacial effects in

heterogeneous dielectric systems, "the physical assumption is that the conduction currents do not violate the local electro-neutrality condition in the volume of the conducting components" [131]. Free electrical charge will accumulate along a liquid-solid interface due to the conductivity of the liquid, σ_l (S/m). In accordance with the charge continuity equations, a boundary condition can be established to describe the rate-of-change of the surface charge density, which is equal to the difference between the conduction current densities associated with the liquid, J_l (A/m^2) and with the solid, J_s (A/m^2), as described by equation (2.16) [132]:

$$J_l - J_s = \sigma_l E_0(t) - \sigma_s E_s(t) = -\frac{\partial \gamma_s(t)}{\partial t} \tag{2.16}$$

where σ_s (S/m) is the conductivity of the solid, $E_0(t)$ (kV/cm) is the external applied electric field, $E_s(t)$ (kV/cm) is the electric field in the solid, and $\gamma_s(t)$ is the non-compensated free surface charge. This surface charge is related to the electric flux density on either side of the liquid-solid interface (equation (2.17)) [132]:

$$\gamma_s(t) = \varepsilon_0 \varepsilon_l E_0(t) - \varepsilon_0 \varepsilon_s E_s(t) \tag{2.17}$$

where ε_0 is the permittivity of free space (ε_0 ~8.85×10^{-12} F/m), ε_l is the relative permittivity of the liquid, and ε_s is the relative permittivity of the solid.

For the present study, the practical significance is that surface charge will be developed in non-uniform fields when the liquid and solid phases have different relative permittivity and Ohmic conductivity, giving rise to a potential coupling of the discharge channel to the solid surface.

Image Forces

The creation of electric double layers, defined as near-surface layers with a high concentration of charge carriers [133], can lead to flashover of dielectric solids immersed in non-polar liquids such as insulating oil. Landau and Lifshitz [134] state

that when charge '*e*' is situated close to the boundary of two different phases, the charge experiences an 'image force' *F* (N) as described in equation (2.18):

$$F = \frac{ee'}{4\pi\varepsilon_1\varepsilon_0(2h)^2} \tag{2.18}$$

where *h* is the distance between the charge and the liquid-solid boundary (m), and *e'* is the image charge (C), defined in equation (2.19):

$$e' = \frac{e(\varepsilon_1 - \varepsilon_2)}{(\varepsilon_1 + \varepsilon_2)} \tag{2.19}$$

where ε_1 is the relative permittivity of the liquid, and ε_2 is the relative permittivity of the material forming the surface interface.

Depicted in Figure 2.13, adapted from [135], are three possible scenarios to describe image-force behaviour:

(1) in the case of a charge in the liquid near the electrode, where the permittivity can be considered infinite ($\varepsilon_2 = \infty$), the image force is negative, and the charge is attracted to the electrode surface;
(2) in the case of a charge in the liquid near a relatively high permittivity solid, the image force is again negative, and the charge is attracted to the solid surface; and
(3) in the case of a charge in the liquid near a bubble filled with a gas of low permittivity ($\varepsilon_2 = 1$), the image force is positive (i.e. the charge and the image charge have the same sign), and the charge is repelled from the bubble surface.

Korobeynikov *et al*. [135] discuss the behaviour of solids with higher permittivity than that of the liquid in which they are immersed. Image forces result in increasing ion concentration at the liquid-solid interface. Ions are trapped near the surface, as proposed in [136] for ions trapped in a potential well at the surface of an electrode, and diffusion aids injection into the liquid bulk. The molecules in non-polar liquids

are in the form of ion pairs, and the energy of dissociation of these ion pairs at the liquid-solid boundary will be less than that for dissociation in the liquid bulk due to the negative image force. Korobeynikov *et al*. used equations proposed in [137], [138] to estimate rates of dissociation and recombination, and calculated a recombination rate near a surface of high permittivity of around one order of magnitude less than in the liquid bulk, and a dissociation rate of around seven orders of magnitude greater than in the liquid bulk. This would lead to a layer of increased conductivity at the boundary, increasing the probability of surface flashover. Finally, it was calculated that an applied electrical field level of 200 kV/cm would result in a strong increase in the dissociation rate if the nominal direction of the electric field was parallel to the solid surface.

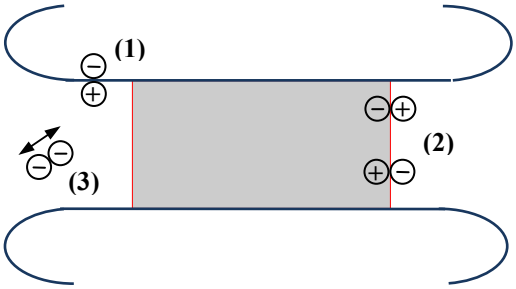

Figure 2.13. Sketch highlighting the effects of image forces (adapted from [135]): (1) the high permittivity of the metal causes charges in the liquid to be attracted to the electrode surface; (2) charges in the liquid can be attracted towards the surface of a relatively high permittivity solid; and (3) in the case of a bubble with permittivity of 1, the image charge is of the same sign, and the charge is repelled from the bubble surface.

2.4.4 Interfacial Breakdown Voltages

For the application of positive-polarity lightning impulses (1.2/50 μs) under a cup-plane electrode geometry in [75], the breakdown voltages were slightly lower with the inclusion of an XLPE spacer in the oil gap than for a gap consisting only of silicone oil, but the difference observed was much lower than that for ac voltages. The impulse breakdown field varied from 540 kV/cm for a 2.5 mm oil gap to 380 kV/cm for a 7.5 mm oil gap with no solid, and from 500 kV/cm for a 2.5 mm XLPE spacer/oil gap to 350 kV/cm for a 7.5 mm XLPE spacer/oil gap. For

comparison, the ac breakdown field for a 2.5 mm oil gap was 215 kV/cm, reducing to 160 kV/cm for a 2.5 mm XLPE spacer/oil gap.

Wang *et al*. [6] have investigated dielectric surface discharges in insulating oil in the ns timescale. The authors applied ~40 ns-wide, 50-200 kV impulses to column-shaped and trapezoidal samples held between plane-plane electrodes, and found that the breakdown voltages associated with the surface discharges were very high compared to those measured previously for dc, ac, and lightning impulse regimes. Both nylon 6 and poly(methyl methacrylate) (PMMA) samples, showed the highest hold-off voltages when the angle between the electrode and the sample surface was 45°. The breakdown field of cylindrical PMMA samples was found to increase from 450 kV/cm to 700 kV/cm when the rate of voltage rise was raised from 11 kV/ns to 22 kV/ns, but was not affected by the thickness of the samples (1-3 mm).

The effect of applying narrow (30-40 ns) pulses, with a rise time of ~10 ns and peak voltages of up to 300 kV, on PMMA spacers (30 x 23 x 5 mm) in insulating oil was investigated by Guangjie *et al*. [7]. They subjected 102 individual samples to a single surface flashover, with flashover occurring on the rising edge, and found that the breakdown voltage varied by up to 190 kV for the same experimental conditions. The measured breakdown voltages varied from 180 kV to 370 kV for a 2 mm inter-electrode gap, corresponding with electrical field levels in the range 900 kV/cm to 1.85 MV/cm.

The purpose of the present work is to compare the interfacial breakdown behaviour of composite liquid-solid insulation with different types of polymer immersed in insulating oil, when subjected to the similar levels of electrical field and the types of voltage wave-shape found in pulsed-power machines. The experimental results and corresponding statistical analysis presented in Chapters 4 to 7 are intended to provide information to system designers regarding the probability of surface flashover occurring, as well as confidence intervals for which a given electrical field can be applied to a composite insulation system without resulting in surface flashover for different applied voltage wave-forms.

Chapter 3

EXPERIMENTAL EQUIPMENT AND METHODS

3.0 INTRODUCTION

This chapter describes details regarding the equipment and procedures used in the experimental programme. The description includes:

- the high-voltage power supply and impulse generator;
- the test cells and electrodes;
- the liquid and solid dielectric samples;
- the gas handling and pneumatic control; and
- the diagnostic equipment utilised throughout the course of the study.

The layout of the components which provides the complete measurement facility is also described.

3.1 HIGH-VOLTAGE IMPULSE GENERATION

The impulse generator utilised throughout the duration of the study was a ten-stage, air-insulated, inverting Marx generator, operated in the single-shot regime. A photograph of the Marx generator is provided in Figure 3.1. The storage capacitors were charged by a 100-kV, 2.5-mA, high-voltage dc supply (Glassman Inc., USA), decoupled from the impulse generator by a 1-MΩ charging resistor, made up of 100 Meggitt (UK) 10 kΩ ceramic-cased wirewound resistors connected in series. The dc supply used incorporates a charging current meter, allowing the user to determine when the load capacitors are fully charged; the supply can be current limited to prevent immediate recharging of the capacitors upon discharge. With reference to the polarity effect discussed in section 2.2.3 for open oil gaps and in section 2.4.2 for

flashover of oil-solid interfaces, positive charging voltages were always utilised to yield negative output impulses, in an attempt to maximise breakdown voltages.

The energy-storage components in the generator were 80-nF, single-sided S-type capacitors from Maxwell Inc. (USA), yielding a nominal erected capacitance of 8 nF. Inter-stage charging resistors of value 60 kΩ were formed from flexible PVC tubing filled with aqueous copper sulphate ($CuSO_4$) solution, with ten spherical bronze-phosphor electrodes equally spaced along the length of the pipe. Similar $CuSO_4$ discharge resistors (2 kΩ) were also connected between alternate stages. Switching was achieved by the depressurisation of a cylindrical, in-line, Perspex spark-column, consisting of ten discrete spark-gap switches, filled with compressed air. The switches were each formed from a pair of spherical bronze-phosphor electrodes of diameter 25 mm, separated by a distance of 10 mm. Each sphere was connected to a cylindrical brass electrode external to the spark column, allowing connection to the other system components as illustrated in the schematic diagram of Figure 3.2.

Although the capacitors are rated at 70 kV in air – and up to 100 kV when immersed in insulating oil or a pressurised gas – the distance between the external spark-column electrodes limited the dc charging voltage that could be applied to the system to <50 kV, yielding a maximum nominal output voltage in the region of 500 kV.

The operation of the generator can be described with reference to Figure 3.2. With all storage capacitors (C1-C10) charged to a potential of $+V$, and following the conventional theory where the lowest spark gap (SG1) breaks first, C1 is now connected to ground via the shorted spark gap, so that the polarity is inverted and the side of SG2 connected to C1 is driven to a potential of $-V$. The other side of SG2 is charged to $+V$, giving a theoretical potential difference of $2V$ across SG2; such a level of overvoltage will cause SG2 to break down almost instantaneously. The potential at either side of SG3 is now $-2V$ and $+V$, giving an overvoltage of $3V$ across SG3. This process continues across all the spark gaps, with the level of overvoltage increasing until a potential of $-10V$ appears across SG10, all of the capacitors are connected in series, and an impulse voltage of magnitude nominally 10

times the charging voltage appears at the output. In the system used in this study, the gaps are forced to self-break by depressurisation of the spark column as discussed in section 3.4. Ultraviolet (UV) light generated upon breakdown of each gap can provide initiatory electrons to other gaps in the column, minimising the statistical time lag associated with the breakdown of each gap. The discharge resistors (R_g0-R_g8) also aid the breakdown sequence by ensuring the existence of capacitive coupling between the stages to assist in maximising the spark gap over-voltages following closure of the first gap [139].

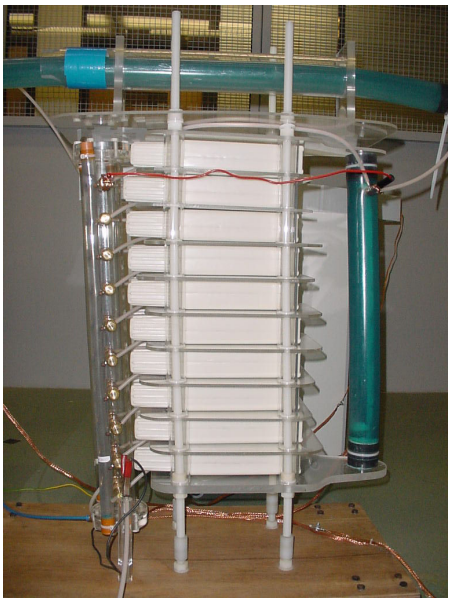

Figure 3.1. Photograph showing the side profile of the ten-stage Marx generator.

As discussed in section 2.1.2, one of the advantages of a Marx generator is the achievable variability in the output voltage wave-shape. The Marx generator described above was used in two forms, with different output voltage wave-forms achieved by varying the wave-shaping components.

In the configuration depicted in Figure 3.2, a 200-Ω $CuSO_4$ wave-tail resistor (R_{wt} in Figure 3.2; R_e in the single-stage equivalent circuits of Figure 2.10) was connected in parallel with the load, controlling the fall-time to half-peak value and providing an

alternative path to earth for the stored energy of the stages should no breakdown occur in the test cell. The output impedance was 600 Ω, in the form of a second $CuSO_4$ (wave-front) resistor (R_{out} in Figure 3.2; R_d in Figure 2.10). This configuration was utilised to provide a 100/600 ns voltage wave-shape for the work detailed in Chapter 5.

In the second form, the wave-tail resistance was increased to 800 Ω, and the wave-front resistance was 1.6 kΩ. A wave-front capacitance of 200 pF was also connected in parallel with the load, and this configuration was utilised to provide a 1/6.5 μs voltage wave-shape for the work described in Chapters 6 & 7. The wave-front capacitance consisted of five × 1 nF NWL (USA) capacitors connected in series; the voltage rating of these capacitors is 70 kV, restricting the maximum output voltage to 350 kV in this configuration.

Example voltage wave-forms for both configurations are shown in section 3.5.2.

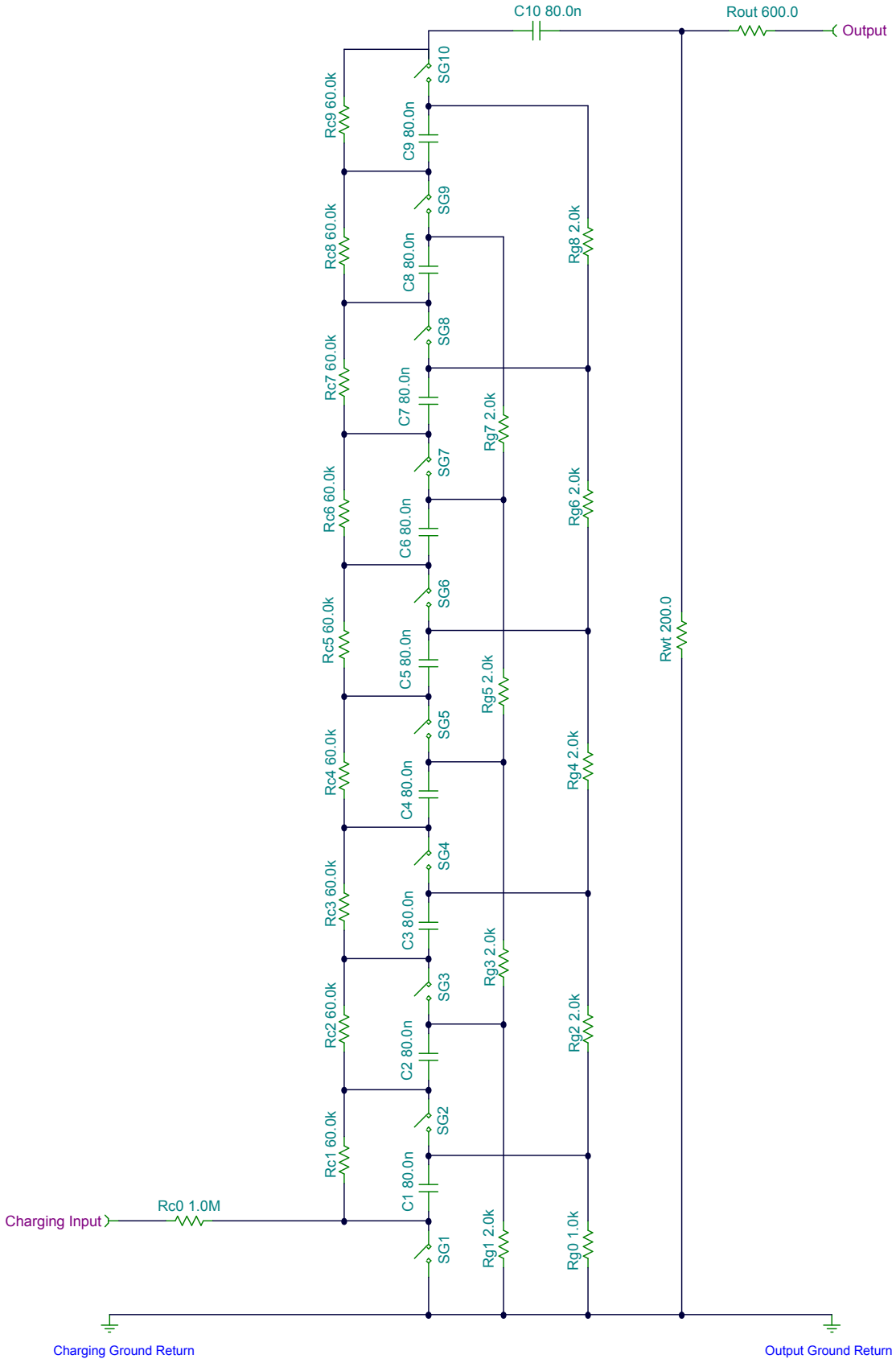

Figure 3.2. Schematic diagram of ten-stage Marx generator as configured for 100 ns rise-time.

3.2 TEST CELLS

The Marx generator was utilised in conjunction with two modular test cells of broadly similar design: one to study surface flashover and other breakdown events in composite liquid-solid gaps; and one to study the breakdown of open oil gaps (that is, gaps without a solid spacer). Each test cell consisted mainly of a pair of aluminium electrodes, as illustrated in Figure 3.3. The electrodes were inter-changeable between test cells.

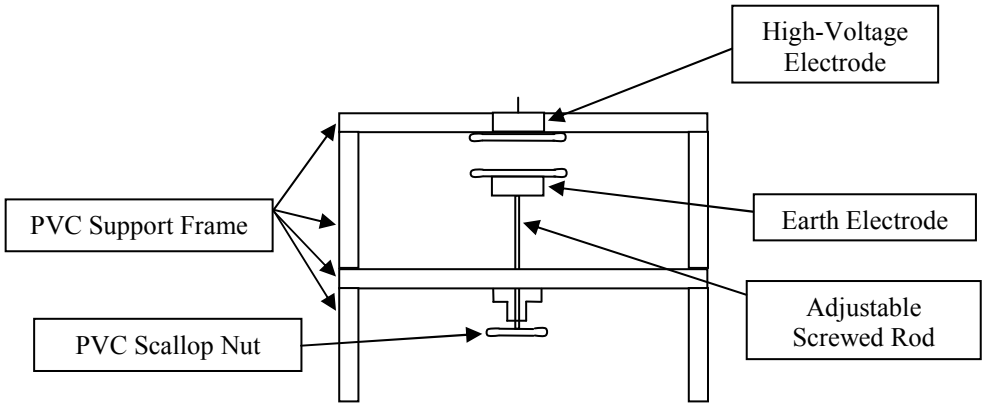

Figure 3.3. Diagram showing basic structure of test cells.

The main body of each test cell was made from machined PVC sections. The electrodes were supported by two 12-mm thick, 200-mm diameter securing plates, the upper of which held the high-voltage electrode in position, and the lower of which held a length of aluminium screwed rod for connection to the earthed electrode. This arrangement can be seen in Figure 3.4. The securing plates were separated by three PVC pillars of length 70 mm and diameter 15 mm. Three similar pillars of length 65 mm were positioned beneath the lower plate to raise this from the base of the oil-filled container, and to allow the earth connection to the external circuit to be made. The inter-electrode gap was readily adjustable by varying the position of the earthed electrode, which consisted of a 50-mm-diameter plane, using a PVC scallop nut. A further three electrodes, also 50 mm in diameter, were used as inter-changeable high-voltage electrodes.

The main body of the second test cell was identical to that described above. Whereas a solid sample was required to fix the inter-electrode gap length in the first test cell, the second design incorporated control over the gap length to allow measurements to be made in open oil gaps. The screwed rod on the adjustable earth electrode was chosen such that each complete 360° turn corresponded to a change in gap length of 1 mm. When using this test cell, the earth electrode was first adjusted until it met flush with the high-voltage electrode; the earth electrode was then turned through the appropriate number of revolutions to set the required gap length. A digital micrometer was then used to confirm the gap spacing.

All of the electrodes used were based on an aluminium plane of diameter 50 mm, and thickness 10 mm. The profiles of the electrodes were rounded to minimise field enhancement effects at the edges. Protruding from the rear of each electrode was a 10-mm thick section, such that the overall thickness of each aluminium piece was 20 mm, machined to a reduced diameter of 30 mm. For connection to the external circuitry, each high-voltage electrode had an M6 threaded hole to accept a short section of screwed rod, and each earth electrode had an M12 threaded hole for connection to the adjustable screwed rod as indicated in Figure 3.3.

For clarity, a photograph of the different types of electrode is provided in Figure 3.5. The first type of electrode, type A, had a 3-mm-long, 1-mm-diameter, tungsten-alloy pin protruding from the main body to provide point-plane electrode geometry. The second type, type B, also provided non-uniform field geometry, with a 25-mm-diameter collar centred on the electrode body. The collar was machined at an angle of 45°, with the sharp edge positioned beside the sample surface. The length of the collar was 3 mm at the point in contact with the sample surface, and the diameter at the tip was again 1 mm. The third type of high-voltage electrode, type C, was simply a 50-mm-diameter plane, providing plane-parallel electrode geometry. This geometry was chosen over Rogowski profile electrodes for ease of machining, and to replicate the conditions found in many practical systems. The relevant electrodes were inserted into the appropriate cell and immersed in ~20 litres of EOS Ltd. (UK) L10B insulating oil for testing.

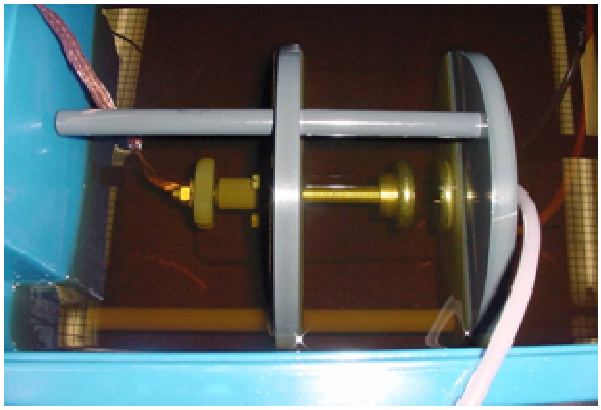

Figure 3.4. Photograph of test cell immersed in insulating oil. The test cell is pictured on the horizontal axis only to show the electrodes, and was positioned vertically for testing.

Figure 3.5. Photograph of different high-voltage electrodes. From left to right: type A, type B and type C.

3.3 COMPOSITE INSULATION SYSTEM

3.3.1 Liquid Dielectric

As mentioned briefly in section 2.2.4, the liquid dielectric used throughout the study was EOS Ltd (UK) L10B mineral oil, reprocessed to the requirements of British Standard Specification BS 148:2009 [91]. The minimum ac breakdown voltage, measured in accordance with BS EN 60156 [140], is quoted by the manufacturer as 30 kV [141]. The BS EN 60156 standard specifies testing the oil in a 2.5-mm gap between spherical electrodes of radius 25 mm [142].

Also quoted by the manufacturer is the "polycyclic aromatics mass," with a maximum of 3% when measured according to BS 2000-346 [143].

3.3.2 Solid Dielectrics

As discussed in section 2.3.3, the solid materials selected for use in this study were:

- polypropylene (PP);
- low-density polyethylene (LDPE);
- ultra-high molecular weight polyethylene (UHMWPE);
- Rexolite (cross-linked polystyrene); and
- Torlon (polyamide-imide).

Contained in Table 3.1 are manufacturer's data on the important electrical properties of the five different materials. As the bulk breakdown strength quoted by manufacturers is measured at power frequency, in accordance with either the ASTM D149 [144] or the IEC 60243 [145] standard, these values were deemed irrelevant for the impulse conditions investigated in this work, and they have not been included in Table 3.1.

Table 3.1. Relative permittivity, dissipation factor (tan δ), and resistivity of solid samples.

Material	Relative Permittivity @ 1 MHz	Dissipation Factor @ 1 MHz	Surface Resistivity (Ω/sq)	Volume Resistivity (Ω.cm)
PP	2.25 [146]	3×10^{-4} [147]	10^{13} [147]	10^{16}-10^{18} [147]
LDPE [147]	2.2	1×10^{-4}	10^{13}	10^{15}-10^{18}
UHMWPE [148]	3.0	1×10^{-3}	$>10^{13}$	$>10^{14}$
Rexolite [149]	2.5	1.2×10^{-3}	$>10^{14}$	$>10^{16}$
Torlon [150]	3.9	3.1×10^{-2}	$>10^{13}$	$>10^{14}$

Three different types of solid sample were machined to match the geometries of the different high-voltage electrodes, as illustrated in the sketch of Figure 3.6. The samples used varied in length, but each type was based on a cylinder of diameter 25 mm. Samples had different features to correspond to the different high-voltage electrodes, in order to initiate breakdown events in close proximity to the surface of the solid dielectric.

Samples were initially manufactured with a 1-mm-diameter, 3-mm-long recess cut into the curved surface at one end (sample type I) to accommodate the pin from high-voltage electrode type A. Samples with a 3-mm-long section at the 'high-voltage end' machined to a reduced diameter of 24 mm, with the rest of the sample remaining at 25 mm in diameter (sample type II), were deployed with high-voltage electrode types A and B. Finally, cylindrical samples with no modifications (sample type III) were tested in conjunction with high-voltage electrode types B and C.

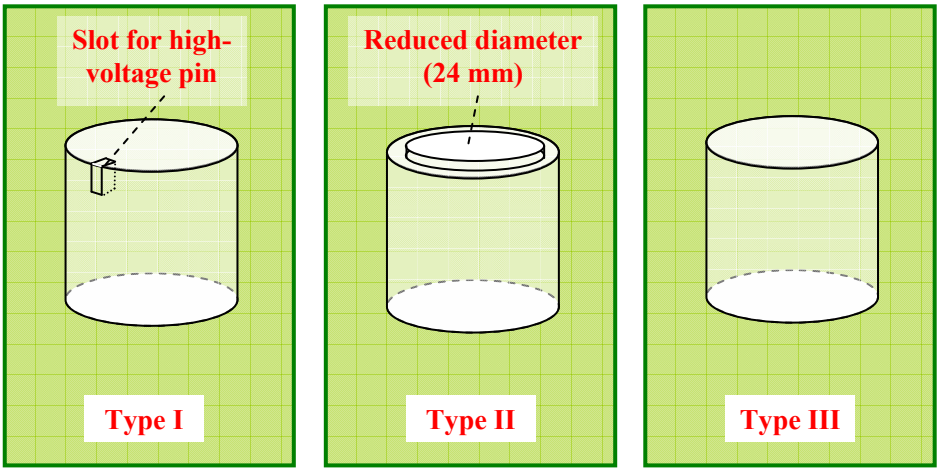

Figure 3.6. Sketch showing outlines of the different types of sample.

Table 3.2. Descriptions of the different types of high-voltage electrode and sample.

High-Voltage Electrodes		Samples	
Type A	A 3-mm-long, 1-mm-diameter, tungsten pin protrudes perpendicular to the aluminium surface, at a radial distance of 12.5 mm from the electrode centre.	*Type I*	A 3-mm-long, 1-mm-diameter recess is cut into the curved surface at one end to accommodate the pin from high-voltage electrode type A.
Type B	A 25-mm-diameter, aluminium collar protrudes perpendicular to the surface at the centre of the plane. The length of the collar is 3 mm at the point in contact with the sample surface.	*Type II*	A 3-mm-long section is machined to a reduced diameter of 24 mm at the end to be in contact with the high-voltage electrode.
Type C	A 50-mm-diameter plane with no modifications.	*Type III*	A 25-mm-diameter cylinder with no modifications.

For ease of reference, the characteristics of each type of high-voltage electrode and sample are summarised in Table 3.2.

Prior to treatment, all solid samples were rinsed in warm tap water with a small amount of detergent to remove any surface grease, and then rinsed in isopropyl alcohol and dried in an oven at 50°C for one hour to remove surface moisture. The required sample was placed between the electrodes and secured in position by tightening the scallop nut on the earthed electrode, before the entire test cell was immersed in the oil tank. Powder-free latex gloves were worn throughout the pre-treatment process to prevent re-contamination of the sample surfaces.

After testing, magnified photographs of damage to the surfaces of the solid samples were taken using a Nikon (Japan) 4500 digital camera in conjunction with a Nikon SMZ800 stereoscopic zoom microscope.

3.3.3 Electrode/Sample Arrangements

In order to best describe the various types of liquid-solid gap used, an illustration of the five different combinations of electrode and sample type is provided in Figure 3.7.

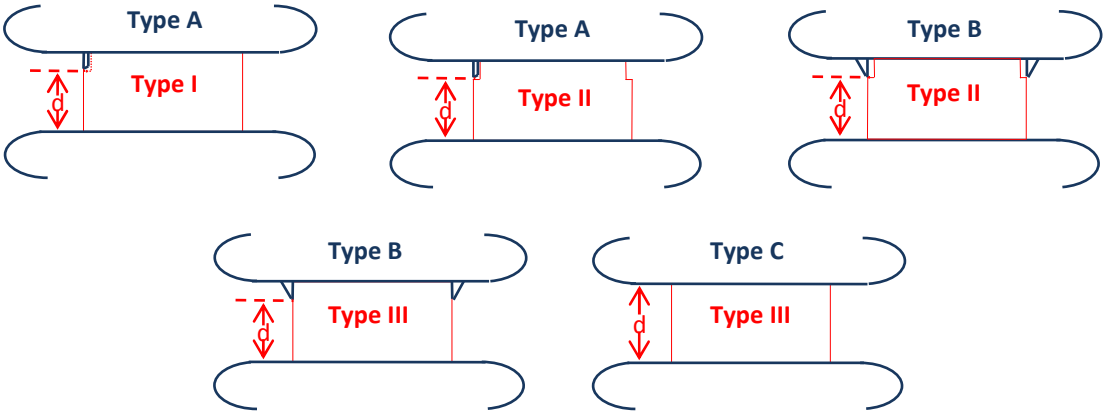

Figure 3.7. Sketch of the different electrode/sample arrangements used throughout the study (AI, AII, BII, BIII, CIII).

Only in the case of parallel-plane electrode geometry did the sample length correspond to the inter-electrode gap length, *d*. Hence, an indication of *d* has been added to each part of Figure 3.7 to indicate the gap between the closest point on the high-voltage electrode – that is, the tip of the pin and the edge of the collar in the non-uniform field geometries – and the earth plane.

3.4 GAS HANDLING

The spark column was filled and evacuated using a pneumatic control system, as illustrated in Figure 3.8. The gas supply was a cylinder from BOC (UK), initially filled with compressed air to 200 bar. A Speciality Gases (UK) L201 two-stage regulator was fitted to the output of the gas cylinder, the first stage indicating the spark column gas pressure, and the second stage indicating the gas cylinder pressure. The regulator provided the safety feature of a 3 bar absolute self-venting pressure.

An Edwards E2M2 2-stage high-vacuum rotary vane pump was utilised to evacuate the spark column. The exhaust port was connected to a central gas control system to ensure the safe removal of waste gas from the vicinity of the user. The pump is specified to provide an ultimate vacuum pressure of 10^{-3} mbar, with maximum pumping speed of 2 m^3/h.

Prior to charging the impulse generator stages, the spark column was pressurised in accordance with the graph in Figure 3.9. Once the capacitors were fully charged, the pressure in the column was reduced by opening the vacuum valve until firing was effected. The vacuum valve was immediately closed upon firing, and the pressure returned to its initial level. The spark-column pressure was monitored throughout the firing process using a Budenberg (UK) premium range pressure gauge, with a range of −30 inHg (0 bar absolute) to +7 bar absolute.

An exhaust manifold was also incorporated into the gas control board to ensure all waste gas was vented to atmosphere via the central gas control network. All

components and valves in the gas handling system were inter-connected using 6 mm flexible nylon tubing.

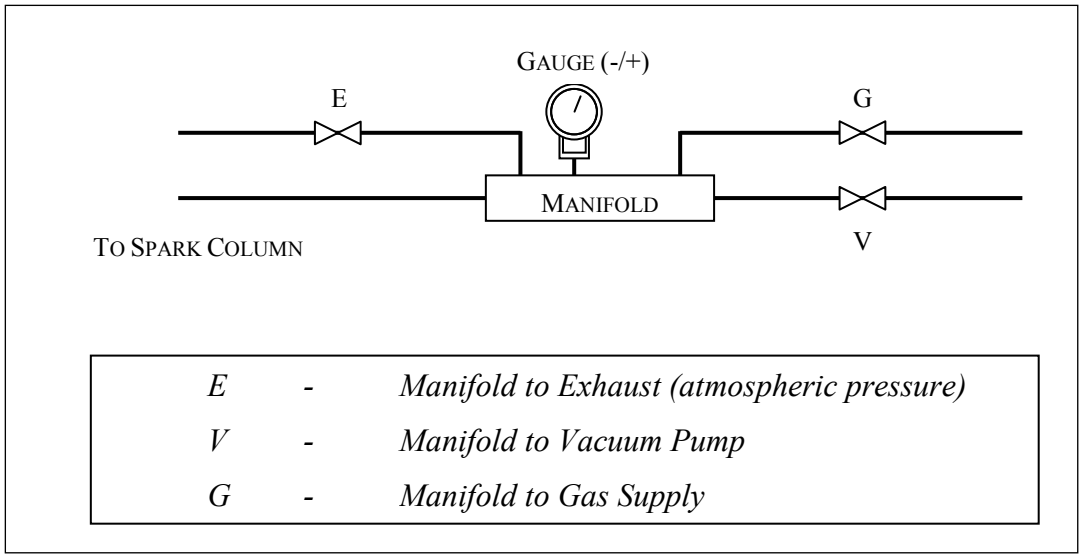

Figure 3.8. Diagram showing layout of gas control board.

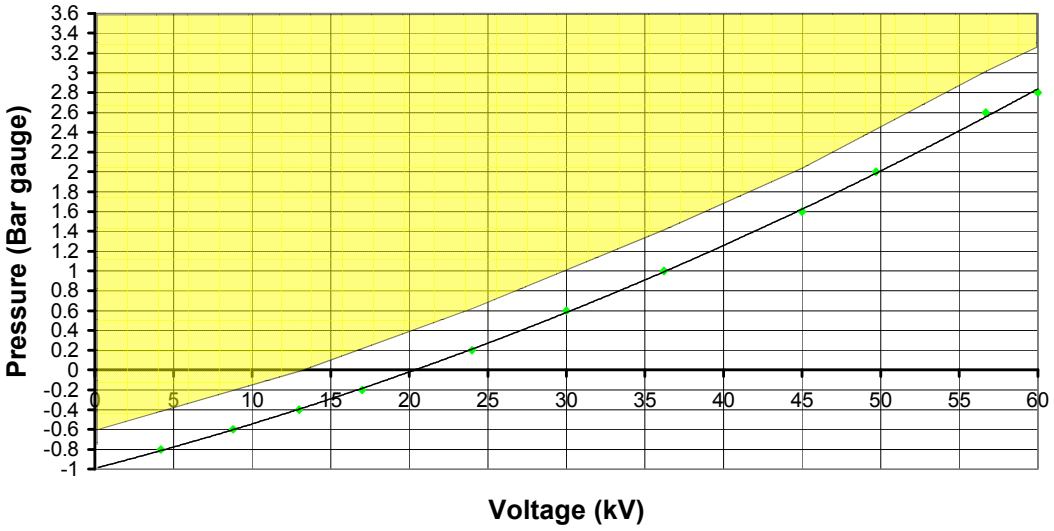

Figure 3.9. Gauge pressure versus self-breakdown voltage* for spark column. The yellow shaded region represents the initial gas pressure before charging the impulse generator stages, bounded by a region at least 0.4 bar above the self-breakdown pressure. *The dc charging voltage was limited to <50 kV.

3.5 DIAGNOSTICS

3.5.1 Diagnostic Equipment

In order to measure impulse voltages of hundreds of kV in magnitude, a two-stage voltage division system was adopted. A Samtech Ltd. (UK) DE(LRP)-02 liquid-resistive voltage divider, as illustrated in Figure 3.10, was connected in parallel with the test cell.

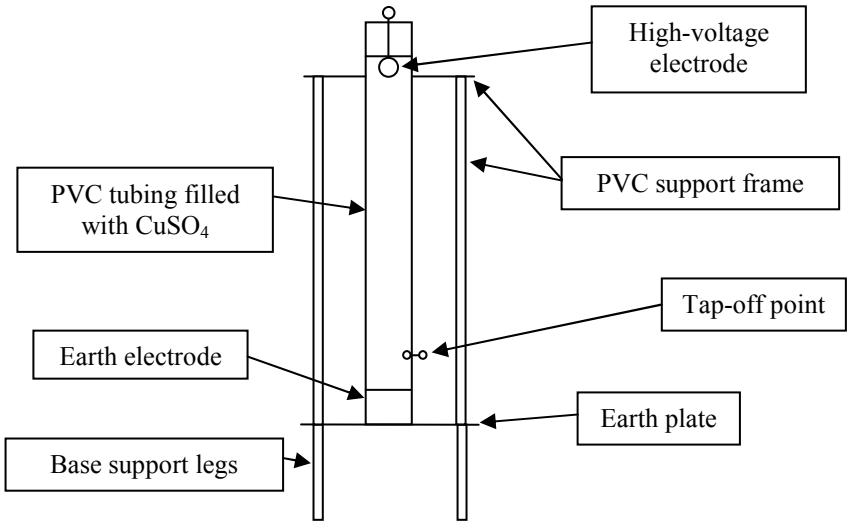

Figure 3.10. Diagram of Samtech DE(LRP)-02 voltage divider.

The response time of a resistive impulse voltage divider depends upon the resistance (R) of the divider and the stray earth and self capacitance (C_e) associated with the high-voltage arm. For such a vertical, cylindrical divider, C_e is in the range 12-20 pF per metre height, and the response time can be calculated using equation (3.1) [15]:

$$T = \frac{1}{6} R \cdot C_e \tag{3.1}$$

The resistance of the divider was dependent upon the output voltage wave-shape, and the impact of this on the theoretical response time is detailed in section 3.5.2.

The divider was configured such that the length between the tap-off point and the earth electrode (70 mm) was one-tenth of the length between the high-voltage electrode and the earth electrode (700 mm), yielding a nominal division ratio of 10:1. The vessel was formed from 50-mm diameter PVC tubing, filled with aqueous $CuSO_4$ solution of appropriate resistivity to yield the required input impedance.

A bronze-phosphor sphere of diameter 25 mm formed the high-voltage electrode; a short length of M6 screwed rod was used to connect this internal sphere to the external circuit via a glass-filled nylon lead-through. A 19-mm diameter bronze-phosphor sphere was used to cover the sharp edges of the threaded connection externally, as shown in Figure 3.10. The earth electrode was formed from a 40-mm long section of 50-mm diameter brass rod, connected to a 250-mm diameter aluminium plate of thickness 3 mm. The tap-off point consisted of an internal bronze-phosphor sphere of diameter 10 mm, fed through the side wall of the vessel by M3 screwed rod, and covered externally by a second 10-mm diameter bronze-phosphor sphere.

The structure was supported by three cylindrical aluminium legs underneath the earth plate, and by a PVC support frame consisting of a 250-mm diameter disc with a central clearance hole for the vessel, and three 650-mm long sections of 20-mm diameter rod between this disc and the earth plate. The aluminium support legs were 130-mm long and 25 mm in diameter.

For voltage measurement, either a North Star (USA) PVM-2 or a Tektronix (USA) P6015A high-voltage probe (both 1,000:1 division ratio) was connected between the tap-off point on the voltage divider and ground, such that the total division ratio was 10,000:1. The North Star probe has a peak impulse voltage measurement capability of 60 kV, meaning that impulse voltages up to 600 kV in magnitude could potentially be measured in conjunction with the liquid-resistive voltage divider, whereas the corresponding voltage levels for the Tektronix probe are 40 kV alone and 400 kV with the liquid-resistive divider. The nominal bandwidth of the North Star probe is 80 MHz, and the bandwidth of the Tektronix probe is 75 MHz.

Voltage wave-forms were viewed and recorded with a Tektronix (USA) TDS3032 digital phosphor oscilloscope with a bandwidth of 300 MHz and a sampling rate of 2.5 GS/s.

3.5.2 Wave-Shaping and Measurement Circuitry

In order to measure the delay times to breakdown and voltages associated with breakdown events occurring on the falling edge of an applied impulse voltage, the experimental arrangement shown in Figure 3.11 was utilised. In this configuration, the resistivity of the $CuSO_4$ solution in the liquid-resistive voltage divider was set to provide an input impedance of 2 kΩ. Using equation (3.1), the theoretical response time is around 5 ns.

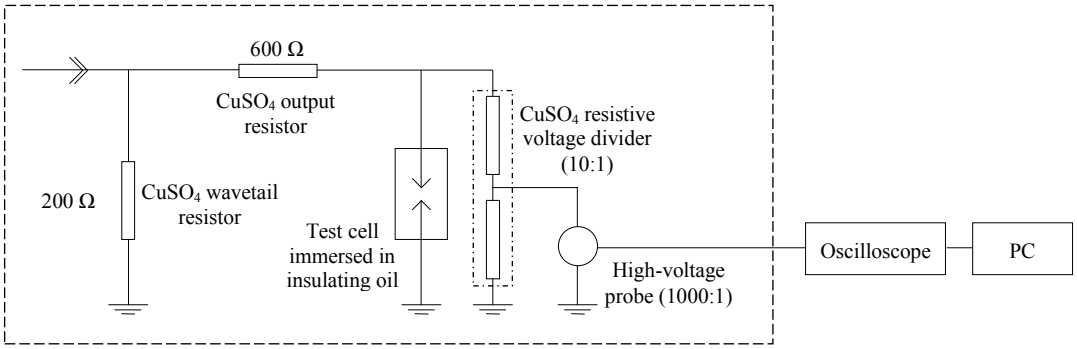

Figure 3.11. Schematic diagram of output/measurement circuitry for the generation of impulses with 100 ns rise-time.

As with the liquid-resistive voltage divider, the vessels for the $CuSO_4$ wave-shaping resistors were simply 50-mm diameter PVC tubing. The electrodes were cylindrical lengths of 50-mm diameter copper rod. The wave-front (output) resistor was 1000-mm long and the wave-tail resistor 600-mm long to ensure that each could withstand the full output voltage.

Typical output voltage wave-forms achieved with the arrangement of Figure 3.11 are shown in Figure 3.12, with the recorded parameters associated with breakdown indicated. These impulses are of the characteristic double-exponential shape

discussed in section 2.1.2. It is clear from Figure 3.12a that the rise-time was ~100 ns, and the fall-time to half-peak value was ~600 ns (these parameters are equivalent to the "front time" and "time to half-value" defined in IEC 60060-1 [151]). Figure 3.12b shows a typical voltage wave-form associated with surface breakdown of a solid dielectric sample; in this case, occurring more than 400 ns after the voltage has passed its peak.

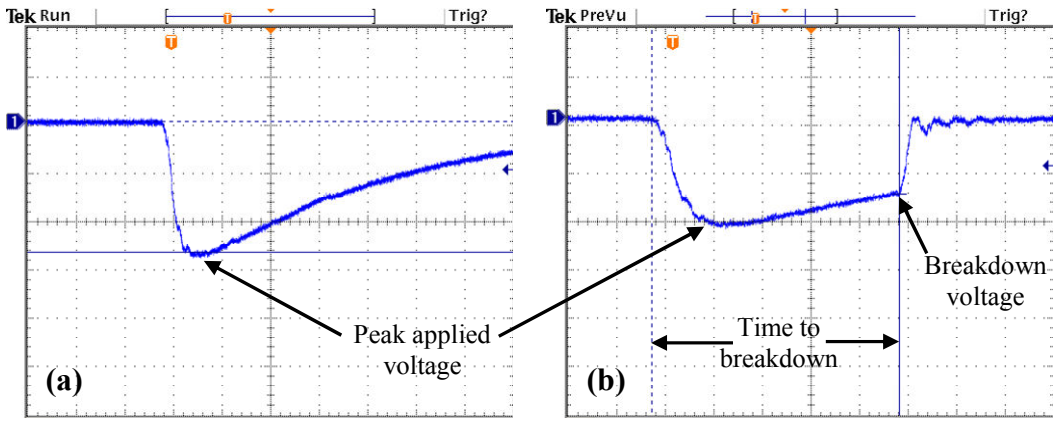

Figure 3.12. Typical voltage waveforms for (a) no breakdown and (b) surface flashover of dielectric sample. Waveform (b) was recorded for breakdown of a type I polypropylene sample, with high-voltage electrode type A; the peak applied voltage is −222 kV, the breakdown voltage is −158 kV, and the time to breakdown is 510 ns. Note that the time-base is 200 ns/division in (a), and 100 ns/division in (b). The vertical axis is on a scale of 100 kV/division in both (a) and (b).

The experimental arrangement illustrated in Figure 3.13 was adopted to measure the voltages and times associated with breakdown events occurring on the rising edge of each applied impulse voltage. In order to modify the voltage wave-form as necessary, the resistivity of the liquid in the wave-tail resistor was increased to raise the resistance to 800 Ω. Rather than removing and changing the liquid in the much longer wave-front resistor, an additional 1 kΩ $CuSO_4$ resistor, of length 450 mm, was added in series.

The increased value of the wave-tail resistor required to provide the desired wave-shape meant that the resistivity of the $CuSO_4$ in the liquid resistive voltage divider

had to be increased to provide an input impedance of 10 kΩ; the theoretical response time is around 25 ns when this value is substituted into equation (3.1).

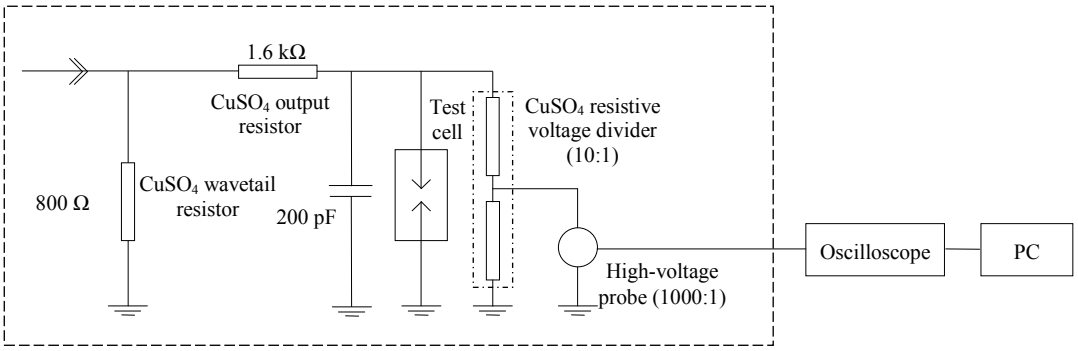

Figure 3.13. Schematic diagram of output/measurement circuitry for the generation of impulses with 1 µs rise-time.

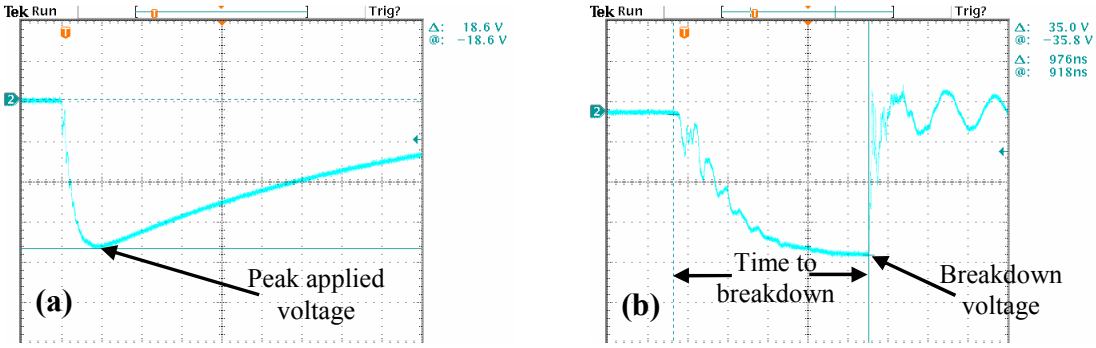

Figure 3.14. Typical voltage waveforms for (a) no breakdown and (b) surface flashover of dielectric sample. Waveform (b) was recorded for breakdown of a type I LDPE sample, with high-voltage electrode type A; the breakdown voltage is −350 kV, and the time to breakdown is 976 ns. Note that the time-base is 1 µs/division in (a), and 200 ns/division in (b). The vertical axis is on a scale of 100 kV/division in both (a) and (b).

Inspection of Figure 3.14a reveals that the total rise-time from zero to peak was ~1 µs, and the fall-time to half-peak value was 6.5 µs for this configuration. When measured in accordance with IEC 60060-1, the "front time" is around 700 ns. It is clear from Figure 3.14b that breakdown events occurred on the rising edge of the impulse; in this case, after 976 ns.

3.6 LABORATORY LAYOUT

The laboratory used for this study was divided into two sections: a high-voltage test area (3.7 m × 4.6 m); and a diagnostic and control area (3.7 m × 2.4 m), separated by an earthed, screened enclosure. The general layout of the laboratory is shown in Figure 3.15.

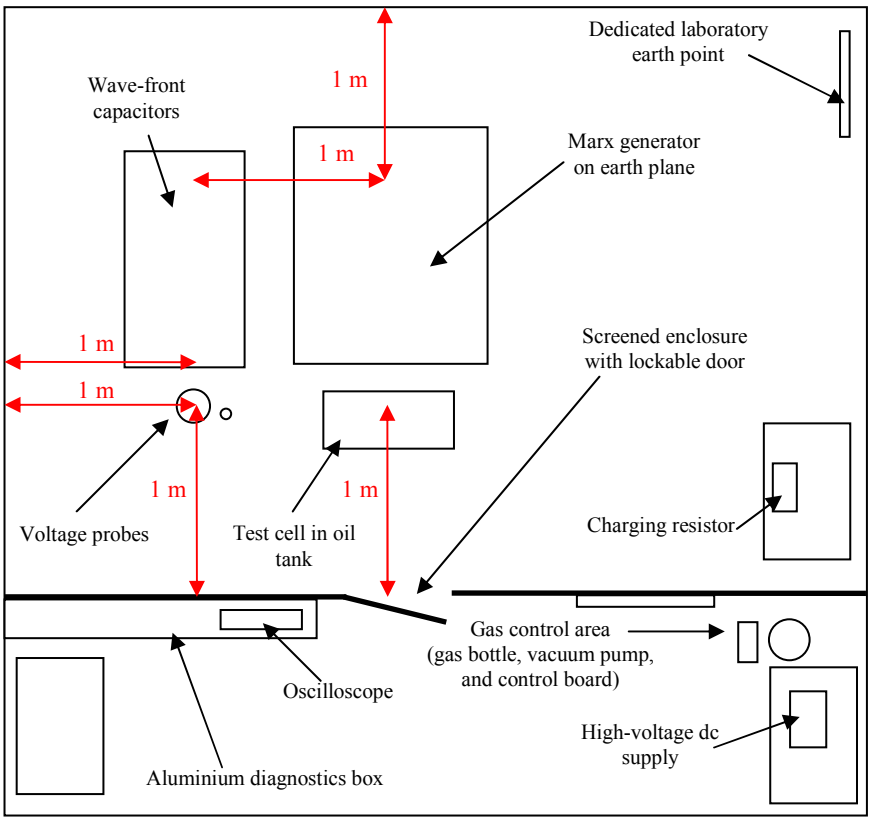

Figure 3.15. A sketch showing the general high-voltage laboratory layout*. The red arrows indicate clearances between high-voltage points and earth. *The sketch is not to scale, and is designed to illustrate the clearances adopted between high-voltage points and parts at earth potential, including the laboratory cage.

In order to safely measure impulse voltages of up to 500 kV in magnitude within the available space, safety clearances between high-voltage points and earth had to be considered. According to Kind and Feser [152], a spacing of 2 m per MV is required

for impulse voltages. In accordance with this, the floor space in the laboratory was utilised such that 1 m clearance existed between all high-voltage points and earth, including the earthed laboratory cage, as indicated in Figure 3.15.

The clearances between the high-voltage output of the Marx generator and the earth plane on the laboratory floor, and between the high-voltage output and the metallic cage ceiling, were both 1.4 m.

All earth connections were referenced to an earth plane underneath the Marx generator on the laboratory floor, which was connected to the dedicated laboratory earth point. The components were laid out such that the shortest distance between all high-voltage points and the earth plane was at least 1 m.

An earthing stick, consisting of an insulating rod with a copper hook connected to earth via a 200-Ω $CuSO_4$ resistor, was positioned beside the door and was used to remove residual charge from all high-voltage points after ceasing operation, and to ground the capacitors. Before the system was handled, hard earth connections were made to short-circuit the spark gaps, and also to connect the Marx-generator output to earth via the wave-tail resistor.

Chapter 4

BREAKDOWN OF OPEN OIL GAPS

4.0 INTRODUCTION

The breakdown characteristics of the three electrode geometries described in Chapter 3, and depicted with different geometries of solid spacer in Figure 3.7, were first examined in oil and in the absence of any solid spacer. The results allowed a baseline reference to be established for breakdown data obtained in the studies of the solid dielectrics in Chapters 5, 6, and 7. The voltages and times associated with breakdown of oil were determined for three different electrode geometries, with gap lengths corresponding to those to be used in the experiments on solid dielectrics.

4.1 EXPERIMENTAL METHOD

Oil gaps were subjected to impulse voltages for the following electrode geometries:

- pin-plane, using high-voltage electrode type A;
- collar-plane, using high-voltage electrode type B; and
- plane-parallel, using high-voltage electrode type C.

As the results were intended to provide reference data for comparison with those results obtained in liquid-solid gaps rather than for a detailed statistical analysis, the number of impulses applied in each test was restricted to five. A period of five minutes was allowed to elapse between impulse applications.

For all geometries, five impulses of rise-time 100 ns were first applied across the electrodes utilising the circuit of Figure 3.11. The peak voltage applied to the gap was fixed at −400 kV for these initial measurements, resulting in breakdown of the

oil on the falling edge of the impulse (over-voltage tests). The breakdown voltage and pre-breakdown delay time were recorded for each breakdown event.

Maintaining the 100-ns rise-time, oil gaps were then subjected to a test in order to determine the peak applied voltages required to initiate breakdown (breakdown initiation tests). The approach taken was designed to replicate the conditions during testing of a new system, where the output voltage would be gradually increased until either the full output voltage was achieved, or an insulation failure occurred. This involved subjecting the oil gap to multiple negative-polarity impulses, the majority of which did not result in breakdown, with the following test sequence. For both non-uniform geometries, where the electrode separation was 10 mm, a peak voltage of −200 kV (average field of 200 kV/cm) was initially applied across the electrodes. For uniform plane-parallel geometry, where the electrode separation was 4 mm, the voltage initially applied was −120 kV (average field 300 kV/cm). No breakdown event was ever found to occur at these levels of applied voltage. For each electrode geometry, the charging voltage was raised in steps of 2 kV (~20 kV increase in output voltage) until a breakdown occurred, upon which the peak applied voltage, the breakdown voltage, and the delay time to breakdown were recorded (see Figure 3.12b). The charging voltage was then reduced to return the peak applied voltage to −200 kV or −120 kV, depending upon the electrode configuration, and the process was repeated until a total of five breakdowns had occurred.

The breakdown initiation test procedure used here is similar to “the step-up test method,” described by Hirose as being suitable for the estimation of the breakdown voltage of non-self-restoring electrical insulation [153]. This method was initially chosen for testing of the liquid-solid insulation systems described in section 5.3, and the same method has been deployed here for consistency. Lightning-impulse withstand voltage test methods presently used in the power industry for self-restoring insulation include “the multiple-level method” and “the up-and-down method” [151]. These test procedures involve evaluation of the voltage where the probability of the occurrence of a disruptive discharge is 10% (U_{10}); the withstand test is considered to be passed if U_{10} is “not less than the specified impulse withstand voltage.”

The voltage rise-time was then increased by an order of magnitude to 1 μs using the circuit shown in Figure 3.13. The longer rise-time allowed for measurements to be made where breakdown occurred on the impulse rising edge or around the peak of the impulse. Only over-voltage tests were carried out, with a peak voltage of −350 kV applied across the gap five times, again, for each electrode geometry. When breakdown initiation measurements were attempted for the longer rise-time, breakdown events generally occurred on the falling edge, with pre-breakdown delay times up to 4 μs, and this type of measurement was not pursued.

The electrodes were removed and polished after completion of each test sequence, in order to remove any surface pits.

4.2 EXPERIMENTAL RESULTS

4.2.1 Over-Volted Gaps

Non-uniform Fields

The breakdown voltages and corresponding average fields, calculated simply by dividing the breakdown voltage by the inter-electrode gap length, for the pin and collar high-voltage electrodes, are listed in Table 4.1. It is clear that for the 100-ns rise-time, the breakdown voltages are higher for the pin (average breakdown voltage 385±11 kV) than for the collar (average breakdown voltage 307±14 kV) electrode. At 1 μs rise-time, the breakdown voltages are very similar for both the pin-plane (average breakdown voltage 335±2 kV) and the collar-plane (average breakdown voltage 336±1 kV) oil gap, and there is only a small variation in the breakdown voltage over the five shots for either type of gap.

The ± values quoted throughout this chapter correspond to the standard deviation, calculated using equation (4.1):

$$\sigma = \sqrt{\frac{\sum x^2 - \frac{\left(\sum x\right)^2}{n}}{(n-1)}} \tag{4.1}$$

where σ is used to represent standard deviation, x represents each value in the dataset, and n is the number of data points in the sample.

Table 4.1. Breakdown voltages and corresponding average fields, calculated by dividing the breakdown voltage by the inter-electrode gap length (d = 8.5 mm), for non-uniform field geometries.

		Breakdown Voltage (kV)	Average Field (kV/cm)
Pin 100 ns	1	378	445
	2	394	464
	3	378	445
	4	374	440
	5	400	471
Collar 100 ns	1	318	374
	2	320	376
	3	300	353
	4	286	336
	5	310	365
Pin 1 µs	1	336	395
	2	336	395
	3	338	398
	4	334	393
	5	332	391
Collar 1 µs	1	336	395
	2	336	395
	3	336	395
	4	336	395
	5	334	393

It is important to note that although the breakdown voltages are lower for the collar electrode at 100 ns rise-time, this corresponds with longer pre-breakdown delay times as breakdown occurs on the falling edge. For clarity, the differences in time to breakdown are illustrated diagrammatically in Figure 4.1.

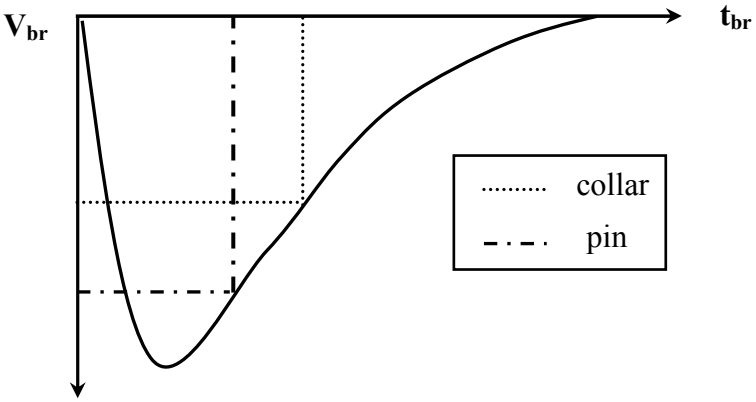

Figure 4.1. Sketch illustrating the differences in time to breakdown for impulses of rise-time 100 ns.

Displayed in Figure 4.2 are time-to-breakdown data for both non-uniform geometries at 100 ns rise-time. It is clear that the times to breakdown are much longer for the collar electrode; in fact, the average pre-breakdown delay time of 499±43 ns over the five shots is over twice that of the average time for the pin electrode (223±15 ns).

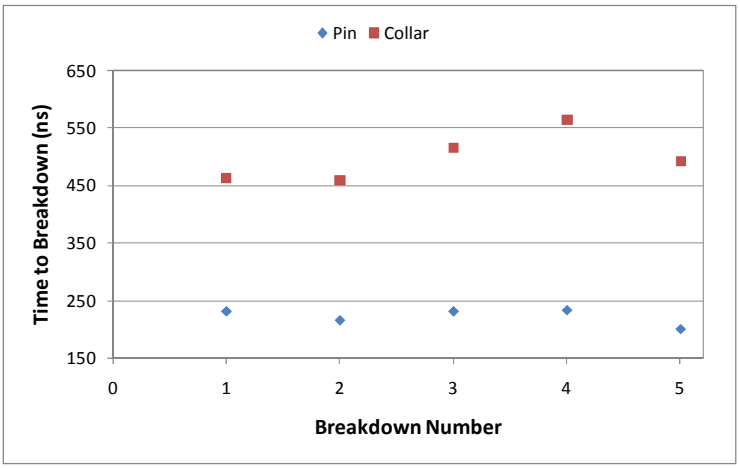

Figure 4.2. Time to breakdown versus breakdown number for non-uniform geometries for rise-time 100 ns.

Although the breakdown voltages for the pin and collar electrodes were equal for rise-time 1 µs, the pre-breakdown delay times were again longer for the collar electrode, as illustrated in Figure 4.3.

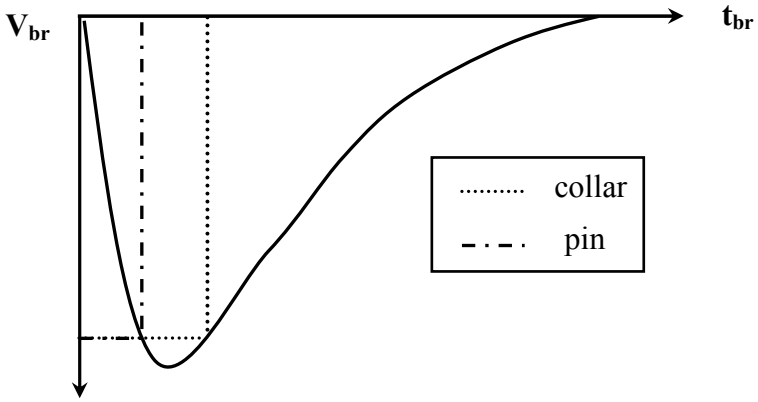

Figure 4.3. Sketch illustrating the differences in time to breakdown for impulses of rise-time 1 μs.

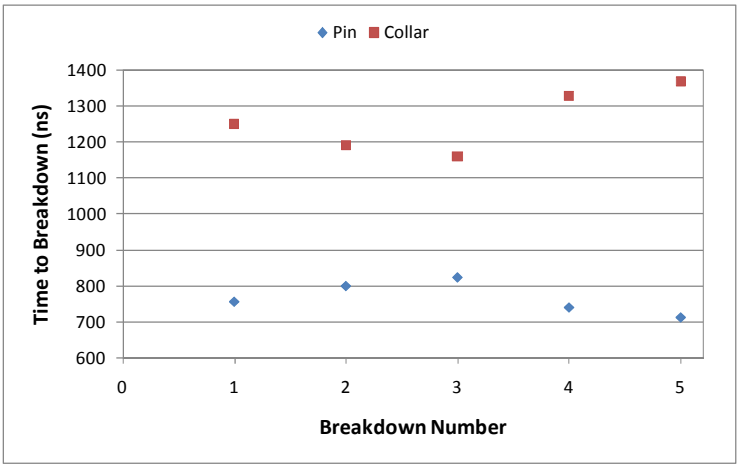

Figure 4.4. Time to breakdown versus breakdown number for non-uniform geometries for rise-time 1 μs.

Figure 4.4 provides a comparison of the breakdown time data for 1 μs rise-time. While breakdown events occurred on the rising edge for the pin-plane geometry, it is clear that times to breakdown longer than 1 μs were obtained for collar-plane geometry. As the corresponding breakdown voltage was always within 5% of the peak voltage, as evidenced by the similar breakdown voltages for both geometries in Table 4.1, the data was accepted in order to provide a comparison with the pin-plane geometry. The high-voltage pin again clearly induces shorter delay times to breakdown. The average breakdown times are 766±45 ns and 1260±89 ns for the pin-plane and the collar-plane oil gaps, respectively. This behaviour is discussed by

way of analysis of the peak electrical field for the pin and collar electrodes in section 4.3.

In Figures 4.5 and 4.6, the time-to-breakdown data are displayed separately for the two non-uniform electrode systems. Figure 4.5 shows how the time to breakdown varies with impulse rise-time for high-voltage electrode type A (pin). The time to breakdown is approximately 500 ns shorter for 100-ns rise-time impulses than for impulses of 1-µs rise-time.

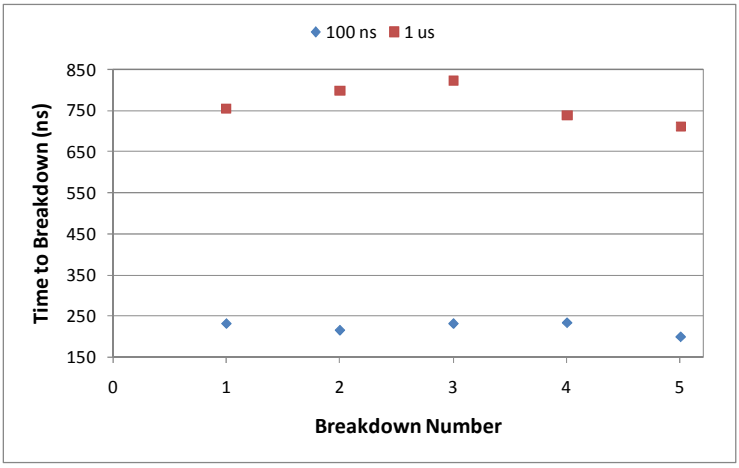

Figure 4.5. Time to breakdown versus breakdown number for the different rise-times under high-voltage electrode type A (pin).

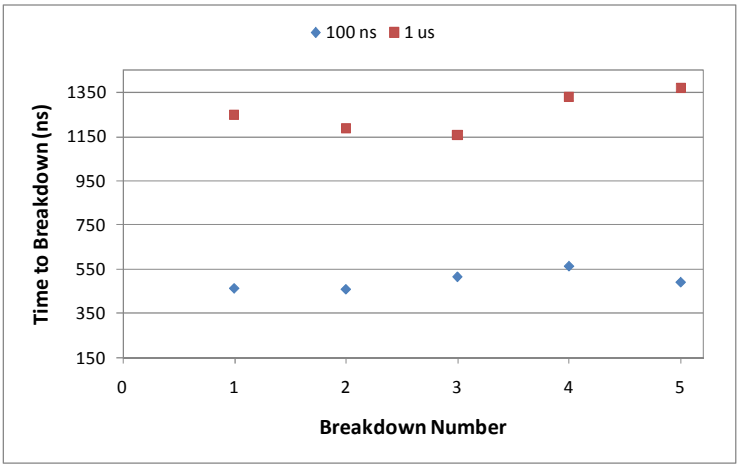

Figure 4.6. Time to breakdown versus breakdown number for the different rise-times under high-voltage electrode type B (collar).

For the type B (collar) high-voltage electrode (Figure 4.6), again the 100-ns rise-times impulses provide a shorter time to breakdown, this time the difference compared to the 1-μs impulses is around 700 ns.

At such short time intervals and high *dV/dt*, a streamer mechanism of breakdown can be assumed to be integral to the breakdown process. While the actual velocity of the streamer that propagates to the point of breakdown cannot be accurately determined without spatial and temporal imaging of the streamer development, an average streamer velocity, estimated by dividing the inter-electrode gap length by the time to breakdown, can provide a minimum implied velocity of streamer propagation and a basis for comparison with the results from other studies.

Table 4.2. Implied average streamer propagation velocities under non-uniform field geometries, calculated by dividing the inter-electrode gap length (d = 8.5 mm) by the time to breakdown.

	AVERAGE PROPAGATION VELOCITY (km/s)				
	1	2	3	4	5
Pin 100 ns	37	39	37	36	43
Collar 100 ns	18	19	17	15	17
Pin 1 μs	11	11	10	12	12
Collar 1 μs	7	7	7	6	6

The implied average streamer velocities are listed in Table 4.2 for the various non-uniform field tests. The data suggest that faster streamer velocities are found under higher *dV/dt*. For example, the propagation velocity for pin-plane geometry with a 1-μs rise-time is 10-12 km/s. At 100 ns rise-time for the same electrode geometry, the average propagation velocity exceeds 40 km/s for the final breakdown.

Uniform Fields

The breakdown voltages recorded for the different rise-times for plane-parallel geometry are listed in Table 4.3 along with the calculated average electrical field. It must be noted that while the inter-electrode gap length was 8 mm for 100-ns rise-

time, it was necessary to reduce the gap length to 4 mm for 1-μs rise-time in order to ensure that breakdown events occurred only on the rising edge of the applied impulse. When an 8-mm gap length was tested under the longer rise-time, breakdown events commonly occurred up to several μs after the impulse peak. The main purpose of the results is to provide reference data for comparison with the breakdown characteristics of the various liquid-solid gaps to be tested in Chapters 5-7 – the gap lengths tested here correspond to the lengths of the solid surfaces subjected to the relevant impulse wave-shape in these chapters.

Table 4.3. Breakdown voltages and corresponding average electric fields, calculated by dividing the breakdown voltage by the inter-electrode gap length, for uniform field geometry.

		Breakdown Voltage (kV)	Average Field (kV/cm)
100 ns (d = 8 mm)	1	350	438
	2	340	425
	3	356	445
	4	336	420
	5	332	415
1 μs (d = 4 mm)	1	284	710
	2	306	765
	3	296	740
	4	290	725
	5	280	700

Table 4.4. Implied average streamer propagation velocities for uniform-field geometry, calculated by dividing the inter-electrode gap length by the time to breakdown.

	AVERAGE PROPAGATION VELOCITY (km/s)				
	1	2	3	4	5
100 ns (d = 8 mm)	21	23	26	21	22
1 μs (d = 4 mm)	10	8	9	9	10

Forster and Wong [154] have previously reported on streamers in hydrocarbons under uniform-field conditions, at electric fields 300-500 kV/cm. The implied

average streamer propagation velocities for both impulse wave-shapes applied in the present study are displayed in Table 4.4.

4.2.2 Breakdown Initiation

As explained in section 4.1, breakdown initiation experiments were confined to impulses having a rise-time of 100 ns.

Non-uniform Fields

The data plotted in Figure 4.7 are the average applied field data for both non-uniform geometries. The average applied field has been calculated simply by dividing the peak applied voltage (refer to Figure 3.12b) inducing breakdown by the inter-electrode gap length, *d*. Higher applied voltages/fields are evidently required to initiate breakdown events using the collar-plane geometry compared to the pin-plane geometry. The difference between the average applied fields for breakdown in the two geometries is around 10%.

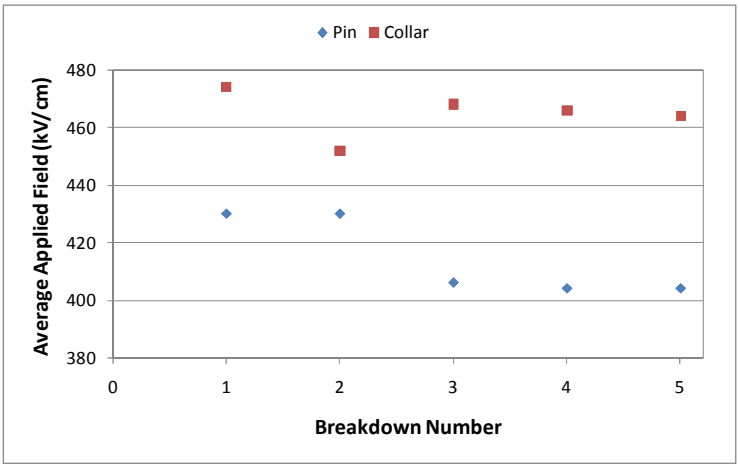

Figure 4.7. Average applied field versus breakdown number for breakdown initiation measurements under non-uniform geometries.

The results in Figure 4.8 show how the average breakdown field varies with breakdown number for the pin and collar electrodes, and Figure 4.9 contains data on the time to breakdown. The data points in both figures are scattered as they represent

breakdown occurring on the falling edge of the impulse after a variable time delay. As in the over-volted gap measurements described in section 4.2.1, the time to breakdown was generally longer for the collar configuration as compared with the pin geometry.

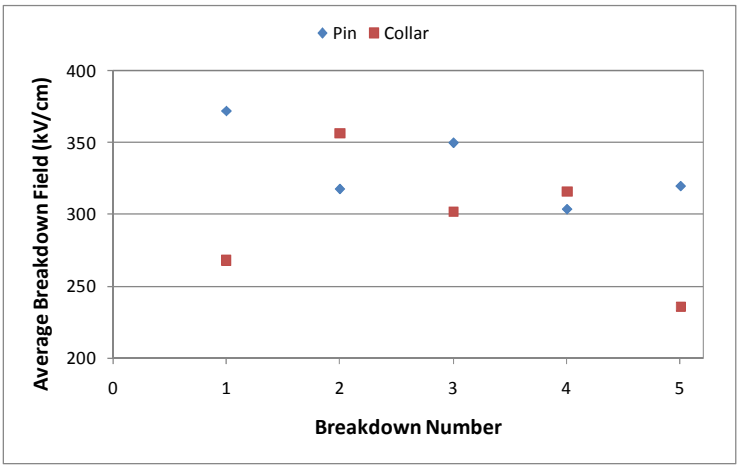

Figure 4.8. Average breakdown field versus breakdown number for breakdown initiation measurements for non-uniform geometries.

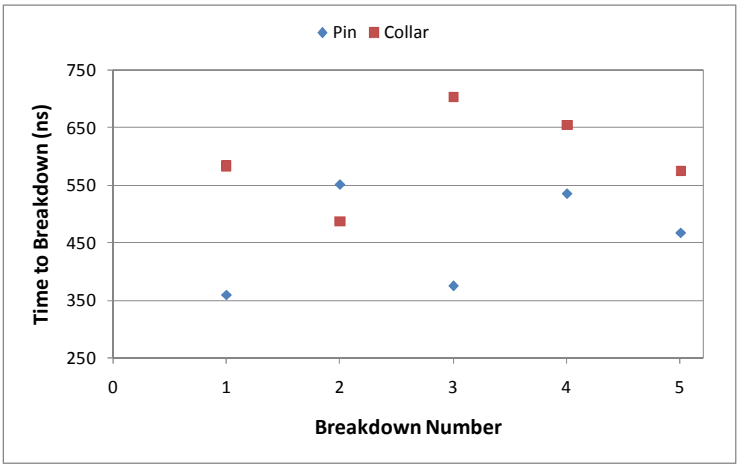

Figure 4.9. Time to breakdown versus breakdown number for breakdown initiation measurements for non-uniform geometries.

The longer times to breakdown for the collar translate to slower streamer propagation, as summarised in Table 4.5.

Table 4.5. Implied average streamer propagation velocities for breakdown initiation measurements under non-uniform field geometries, calculated by dividing the inter-electrode gap length (d = 10 mm) by the time to breakdown.

	AVERAGE PROPAGATION VELOCITY (km/s)				
	1	2	3	4	5
Pin	28	18	27	19	21
Collar	17	21	14	15	17

Comparing the propagation velocities to those for gaps subjected to over-voltages with 100-ns rise-time (Table 4.2), the values are similar for collar-plane geometry. The velocities for pin-plane geometry however, are substantially faster for the over-volted gap measurements compared to the velocities obtained from breakdown initiation measurements.

Uniform Fields

For a 4-mm open oil gap between plane-parallel electrodes, the highest applied field required to initiate breakdown was 765 kV/cm, as measured for the final breakdown event (see Figure 4.10). The applied field for the other breakdown events was in the range 515 kV/cm to 670 kV/cm. The breakdown field varied form 405 kV/cm up to 750 kV/cm. As expected, the applied fields necessary to cause breakdown are higher than those obtained in non-uniform geometries; the shorter gap length in uniform fields should be noted.

The time to breakdown data and the corresponding implied streamer velocities are displayed in Figure 4.11, and Table 4.6, respectively. As might be expected, the higher the applied field required for breakdown initiation, the shorter the delay time until breakdown on the falling edge of the impulse. The calculated streamer velocities are generally slower than those in non-uniform fields, by up to 2.5 times in collar-plane geometry, and by a maximum of 3.5 times in pin-plane geometry.

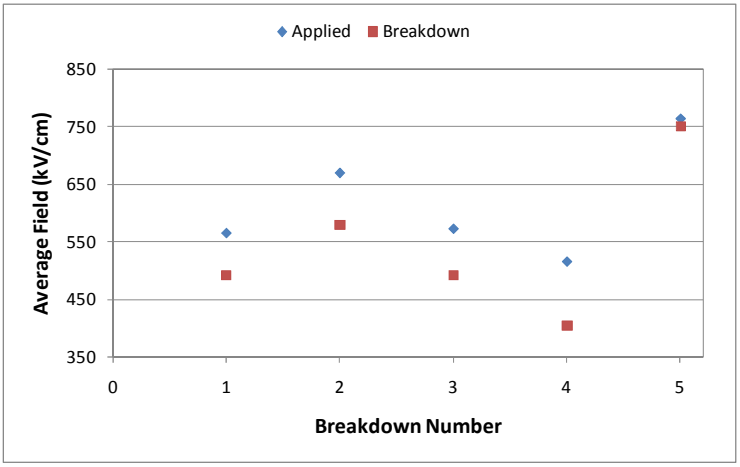

Figure 4.10. Average applied and breakdown fields versus breakdown number for breakdown initiation measurements under uniform-field conditions.

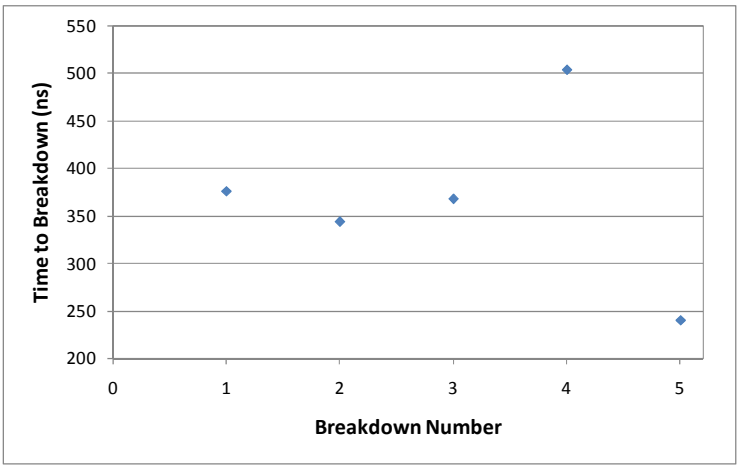

Figure 4.11. Time to breakdown versus breakdown number for breakdown initiation measurements under uniform-field conditions.

Table 4.6. Implied average streamer propagation velocities for breakdown initiation measurements under uniform-field geometry, calculated by dividing the inter-electrode gap length (d = 4 mm) by the time to breakdown.

	AVERAGE PROPAGATION VELOCITY (km/s)				
	1	2	3	4	5
Plane	11	12	11	8	17

4.3 DISCUSSION

The breakdown characteristics of open oil gaps have been studied under three different electrode geometries, and with two applied voltage wave-shapes.

In oil gaps subjected to over-voltages, the time to breakdown under collar-plane geometry was longer than that under pin-plane geometry for rise-times of both 100 ns and 1 μs. As would be expected, the pre-breakdown delay times were longer for the 1-μs rise-time for each of these non-uniform geometries.

Despite the shorter breakdown times for the pin electrode under 1-μs rise-time, the breakdown voltages in Table 4.1 are very similar to those for the collar electrode. This is facilitated by a period of approximately 400 ns around the impulse peak where the rate of voltage change is low.

The times to breakdown are generally much longer for collar-plane geometry than pin-plane geometry, suggesting that the field enhancement provided by the pin is playing a greater role compared with that for the collar. The greater surface area of the collar may result in higher leakage current through ionic conduction, leading to energy losses and longer times to breakdown. However, as the voltage wave-forms displayed no notable difference, it is unlikely that these effects played a significant role.

Only the average electric fields have been presented here, by calculating the ratio of the breakdown voltage and the inter-electrode gap length. The field enhancement under the point-plane geometry can be estimated using equation (4.2) [155] to calculate the peak field at the tip of the point:

$$E_{pk} = \frac{2V}{r_p \cdot \ln\left(\frac{4d}{r_p}\right)} \tag{4.2}$$

where V is the voltage across the electrodes, r_p is the radius of the pin, and d is the inter-electrode gap length. For a pin radius of 0.5 mm, inter-electrode gaps of 8.5-10 mm, and applied voltage magnitude up to 400 kV, the peak fields generated here are of the order of 4 MV/cm.

In order to estimate the peak field with collar-plane electrodes, this geometry was modelled using the electrostatic field solver QuickField (Tera Analysis Ltd.). The solver is based on finite element analysis, and produces a rotationally symmetric solution [156]. The field distribution for an applied voltage of 400 kV and an inter-electrode gap length of 8.5 mm is shown in Figure 4.12. The estimated peak field is around 1 MV/cm.

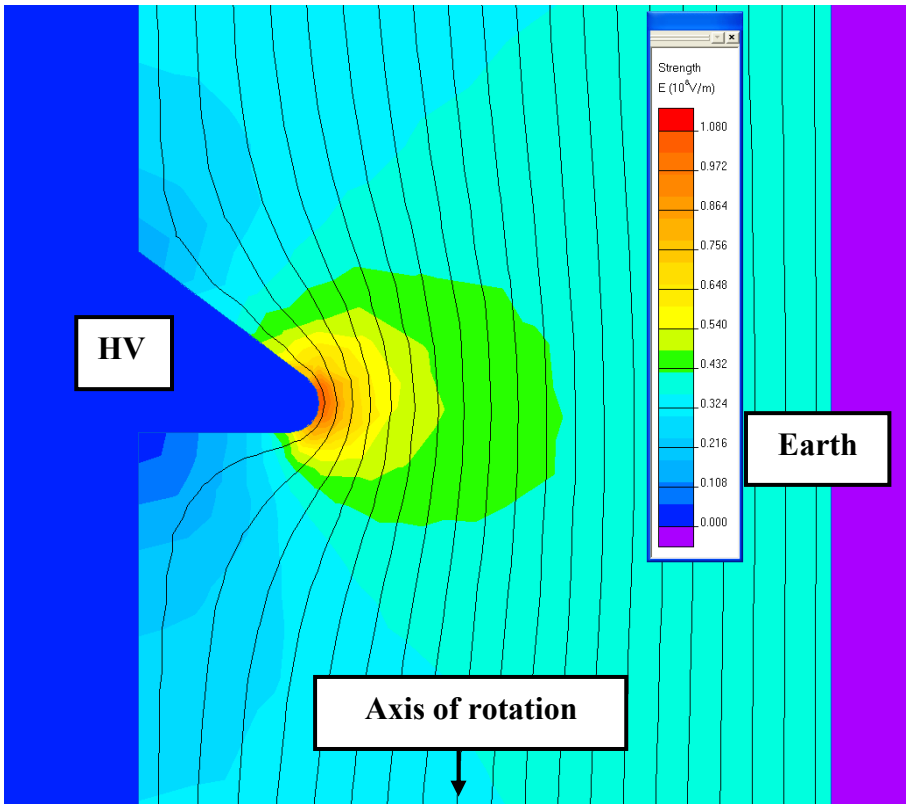

Figure 4.12. Electric field plot for collar-plane electrode geometry in mineral oil, with inter-electrode gap d = 8.5 mm. The axis of rotation lies horizontally along the bottom of the geometry, as indicated. The estimated peak field is of the order of 1 MV/cm.

As discussed in section 2.2.2, the formation of gas cavities in liquids is assumed to be central to the breakdown process. This theory is supported by the dependence of liquid breakdown voltage on hydrostatic pressure. Jones and Kunhardt [157], for example, found that the time to breakdown increased with increasing pressure, but was not affected by the conductivity of the liquid, upon application of 100-ns duration impulse voltages to a uniform-field electrode geometry in water. Hence, it is considered that low-density vapour phases within the liquid bulk are central to the liquid breakdown process. Qian *et al*. [158] hypothesise that stable low-density regions, or micro-bubbles, are pre-existing in the liquid, and hence that no localised heating or vaporisation process is required for their generation. Lewis [159] suggests that the production of a low-density region at the electrode-liquid interface is central to the breakdown initiation process, and that such a low-density region can be generated on the surface of an electrode due to the reduction of interfacial tension caused by the electric field associated with the electric double layer (Lippmann effect). In either case, initiatory electrons are assumed to be generated as a result of field emission within micro-bubbles upon application of a high electric field.

The time-to-breakdown data has been used to calculate minimum implied average streamer velocity. The velocity of sound in mineral oil has previously been measured as 1.5 km/s [160], so streamers generated under the conditions investigated here propagate with supersonic velocity in all cases. The maximum velocity recorded was over 40 km/s under pin-plane geometry with rise-time 100 ns. Propagation velocities for collar-plane geometry were similar for both over-volted gap and breakdown initiation measurements, but under pin-plane geometry the velocities were up to 24 km/s faster when the gap was subjected to over-voltage rather than breakdown initiation tests. For all geometries, the ratio of propagation velocity is around 2.5-3:1 for 100-ns rise-time impulses (dV/dt up to 4 MV/μs) compared to 1 μs rise-time impulses (dV/dt up to 350 kV/μs), a direct effect of the shorter times to breakdown discussed above.

Under plane-parallel electrodes, which were used to provide uniform field distribution, the highest average field required to cause breakdown was 765 kV/cm.

This field was recorded twice for breakdown of a 4-mm oil gap: first in over-voltage tests with a 1-μs rise-time, and also in breakdown initiation measurements with rise-time 100 ns. For an 8-mm oil gap subjected to over-voltages with 100-ns rise-time, the highest breakdown field was 518 kV/cm, with breakdown occurring on the falling edge. This suggests that breakdown of longer gaps can occur at lower fields, as discussed previously in section 2.4.4 in relation to the results reported in [75].

As already commented, the measurements presented in this chapter are intended to be used as a reference point, in order to allow judgements to be made on the influence of the various spacer materials when introduced into the gap under different conditions in Chapters 5-7.

Chapter 5

SURFACE BREAKDOWN EVENTS ON THE WAVE-FORM FALLING EDGE

5.0 INTRODUCTION

This chapter deals with the application of fast-rising impulses to the five different solid dielectrics described in Chapter 3, and the occurrence of breakdown on the falling edge of the voltage impulse. The rise-time of the applied impulses was 100 ns and the fall-time to half peak value was 600 ns, as shown in Figure 3.12a.

The majority of the voltage wave-forms took the form of that shown in Figure 3.12b where, despite initially holding off the peak applied voltage of −400 kV, breakdown occurred on the falling edge of the impulse after a time delay that varied from shot to shot. Some breakdowns occurred on the impulse rising edge. The breakdown voltage and time to breakdown, as indicated in Figure 3.12b, were recorded for each discharge. The time between impulse applications was five minutes.

The first test cell described in section 3.2 was utilised along with the different types of electrode shown in Figure 3.5 to provide three different electrode geometries:

- pin-plane (A);
- collar-plane (B); and
- plane-parallel (C).

Samples of all five solid dielectrics were examined, utilising the different sample types (I with recess for pin; II with shoulder; III with no modification) shown in Figure 3.6 to form the five different electrode/sample geometries illustrated in Figure 3.7 (AI, AII, BII, BIII, CIII).

Two types of measurement were performed, as follows:

First, the voltage applied to the sample was set such that the inter-electrode gap was over-volted, and breakdown occurred on the falling edge for every applied impulse. This procedure was carried out for both non-uniform and uniform fields, with breakdown voltage and the time to breakdown being measured simultaneously for each electrode/dielectric material combination.

Second, the average applied electric field required to initiate surface breakdown of the dielectric was measured, by first applying lower voltages that did not result in breakdown, and then increasing the applied voltage until a breakdown event occurred. Again, this procedure was carried out for both non-uniform and uniform fields.

Both the applied voltage data and the breakdown voltage data from breakdown initiation measurements were subjected to statistical analysis using the Weibull distribution, where breakdown is assumed to be caused by a weak point in the system [161]. The Weibull distribution has been reported as appropriate for modelling voltages associated with breakdown of insulation systems [162], and can be utilised to estimate the voltage, and hence the electric field, associated with low probability of breakdown for a particular engineering design.

The results presented in this chapter will provide designers of pulsed-power system with comparative data regarding:

- which material will hold-off breakdown for longer for the same level of peak applied voltage
- how modifications to sample geometry can affect the breakdown voltage
- the level of peak applied field necessary to initiate surface breakdown events, and how this varies between the five different materials

5.1 OVER-VOLTED GAPS AND NON-UNIFORM FIELDS

Type I (recess) and type II (shoulder) samples of each material were tested with high-voltage electrode type A (pin). Type II (shoulder) and type III (no modifications) samples of each material were tested with high-voltage electrode type B (collar). All samples were 11.5 mm in length, such that the inter-electrode gap length, *d*, was 8.5 mm. Refer to Figure 3.7 in section 3.3.3 for a sketch of the various electrode/sample geometries.

For each test sequence, the sample was subjected to 35 negative-polarity impulses. Application of this number of impulses allowed discrimination between the different materials, in terms of the effect of surface damage caused by previous discharges on subsequent breakdown events. The peak applied voltage for each shot was −400 kV, resulting in a breakdown event for every applied impulse. Both the high-voltage electrode and the earth electrode were removed and polished between test sequences.

Despite the surface damage caused by each discharge, it was found that the breakdown voltage and/or the time to breakdown did not always fall with increasing breakdown number, and hence the mean breakdown voltage and mean time to breakdown over the 35 shots were considered to be of value. The mean breakdown voltage and mean time to breakdown is provided in Table 5.1 and Table 5.2, respectively, along with the standard deviation (± values), again calculated using equation (4.1) (see section 4.2.1) throughout this chapter.

Table 5.1. Average breakdown voltages and standard deviation (± values) for non-uniform field measurements.

Electrode Geometry	Type A (Pin)	Type A (Pin)	Type B (Collar)	Type B (Collar)
Sample Geometry	Type I (Recess)	Type II (Shoulder)	Type II (Shoulder)	Type III (No mods.)
PP	287±31 kV	298±27 kV	311±27 kV	277±43 kV
LDPE	327±23 kV	304±14 kV	305±34 kV	306±17 kV
UHMWPE	258±24 kV	298±25 kV	311±27 kV	283±20 kV
Rexolite	263±60 kV	253±57 kV	308±32 kV	250±38 kV
Torlon	290±38 kV	308±46 kV	245±40 kV	219±66 kV

Table 5.2. Average times to breakdown and standard deviation (± values) for non-uniform field measurements.

Electrode Geometry	Type A (Pin)	Type A (Pin)	Type B (Collar)	Type B (Collar)
Sample Geometry	Type I (Recess)	Type II (Shoulder)	Type II (Shoulder)	Type III (No mods.)
PP	107±86 ns	112±57 ns	105±36 ns	88±29 ns
LDPE	154±35 ns	175±29 ns	105±42 ns	112±37 ns
UHMWPE	303±80 ns	165±94 ns	115±72 ns	184±60 ns
Rexolite	96±56 ns	144±165 ns	89±20 ns	113±91 ns
Torlon	74±17 ns	79±42 ns	66±10 ns	74±30 ns

In order to further illustrate the differences in behaviour observed between solid material type under the various electrode geometries, the mean breakdown voltage and mean time to breakdown data over shots 1-17 and shots 18-35 were also analysed separately, and this information is presented in Table 5.3 and Table 5.4, respectively.

Analysing the data in Table 5.3, the average breakdown voltage and standard deviation for PP, LDPE, and UHMWPE samples is similar over shots 1-17 and shots 18-35 for both sample types. The average breakdown voltage for both types of Rexolite sample however, is ~20% lower over shots 18-35 than over shots 1-17. The opposite effect was observed for Torlon, where the breakdown voltage increased by ~10% for both sample types over shots 18-35 compared to shots 1-17. The behaviour found under collar-plane geometry was different. The average breakdown voltage over shots 18-35 was slightly lower than that over shots 1-17 for type II samples of PP, Rexolite, and Torlon. The opposite effect was found for UHMWPE, where the average breakdown voltage was ~8% higher over shots 18-35 compared to shots 1-17. The average breakdown voltage was very similar for the type II LDPE sample over both data sets, although the standard deviation was found to decrease over shots 18-35. For type III samples, reduced average breakdown voltage over shots 18-35 was found for all materials. The maximum reduction in average breakdown voltage was over 20% for Torlon. The effect of these changes in breakdown voltage on the time to breakdown can be taken from Table 5.4.

Table 5.3. Average breakdown voltages and standard deviation (± values) over shots 1-17 and shots 18-35 for non-uniform field measurements.

Electrode Geometry		Type A (Pin)	Type A (Pin)	Type B (Collar)	Type B (Collar)
Sample Geometry		Type I (Recess)	Type II (Shoulder)	Type II (Shoulder)	Type III (No mods.)
PP	Shots 1-17	286±33 kV	293±30 kV	315±24 kV	301±29 kV
	Shots 18-35	288±30 kV	302±25 kV	308±31 kV	254±44 kV
LDPE	Shots 1-17	322±27 kV	306±13 kV	304±41 kV	313±13 kV
	Shots 18-35	331±20 kV	303±14 kV	306±28 kV	299±19 kV
UHMWPE	Shots 1-17	262±25 kV	292±29 kV	299±32 kV	292±22 kV
	Shots 18-35	254±25 kV	304±20 kV	322±18 kV	275±15 kV
Rexolite	Shots 1-17	291±31 kV	281±45 kV	314±25 kV	276±33 kV
	Shots 18-35	236±70 kV	227±58 kV	302±37 kV	225±26 kV
Torlon	Shots 1-17	277±48 kV	296±45 kV	258±46 kV	246±77 kV
	Shots 18-35	303±22 kV	320±46 kV	233±33 kV	193±44 kV

Table 5.4. Average times to breakdown and standard deviation (± values) over shots 1-17 and shots 18-35 for non-uniform field measurements.

Electrode Geometry		Type A (Pin)	Type A (Pin)	Type B (Collar)	Type B (Collar)
Sample Geometry		Type I (Recess)	Type II (Shoulder)	Type II (Shoulder)	Type III (No mods.)
PP	Shots 1-17	137±118 ns	130±76 ns	113±47 ns	107±30 ns
	Shots 18-35	79±16 ns	96±25 ns	98±21 ns	70±11 ns
LDPE	Shots 1-17	165±38 ns	171±29 ns	111±59 ns	124±49 ns
	Shots 18-35	144±32 ns	179±29 ns	99±14 ns	101±20 ns
UHMWPE	Shots 1-17	290±89 ns	226±86 ns	140±99 ns	150±50 ns
	Shots 18-35	314±74 ns	108±63 ns	92±8 ns	215±55 ns
Rexolite	Shots 1-17	131±61 ns	240±200 ns	99±23 ns	170±107 ns
	Shots 18-35	63±23 ns	53±14 ns	79±11 ns	60±7 ns
Torlon	Shots 1-17	68±16 ns	94±57 ns	68±11 ns	85±40 ns
	Shots 18-35	79±16 ns	65±15 ns	64±9 ns	64±9 ns

5.1.1 Breakdown Voltage

As well as comparing the average breakdown voltage for the different materials, it was interesting to analyse the variation in breakdown voltage on a shot-to-shot basis. In order to facilitate discussion while avoiding repetition, the behaviour for one configuration (type A electrode with type I sample geometry) illustrating typical sample behaviour has been included below; the corresponding graphs for the other

three non-uniform configurations (AII, BII, BIII) are displayed in *Appendix A* for reference. The graphs for all four configurations have a similar form.

Figure 5.1 shows how the magnitude of the breakdown voltage varied with an increasing number of breakdown events for high-voltage electrode type A (pin) and sample type I (recess). The effect of surface damage from previous discharges on the breakdown voltage can be clearly seen for Rexolite, the breakdown voltage falling steadily over the final few shots as breakdown began to occur on the rising edge of the impulse. Low-density polyethylene, on the other hand, with the highest mean breakdown voltage (327±23 kV), recorded some of the highest breakdown voltages in the last five shots. In terms of predictability, LDPE also exhibited the smallest difference (100 kV) between the maximum and minimum breakdown voltages, along with UHMWPE. Ultra-high molecular weight polyethylene exhibited the lowest mean breakdown voltage (258±24 kV), while Rexolite displayed the largest difference (187 kV) between the maximum and minimum breakdown voltages. Torlon also showed a wide spread (166 kV) of breakdown voltages.

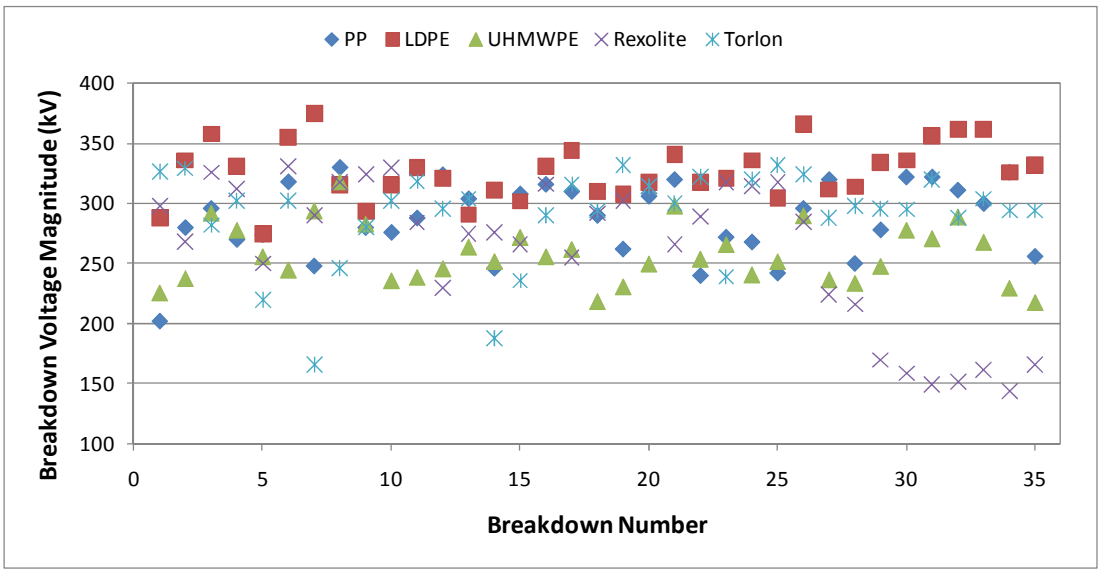

Figure 5.1. Breakdown voltage magnitude versus breakdown number for high-voltage electrode type A (pin) and sample type I (recess).

Post-test visual inspection revealed clear evidence of surface discharge damage on all of the samples. This damage was restricted to one location around the circumference of the sample, dictated by the position of the pin, for samples tested with high-voltage electrode type A. Despite being initiated from the same point however, the discharges did not all follow an identical path from the tip of the high-voltage pin to the earth plane. Damage was found in at least two different locations around the circumference of each of the samples tested with high-voltage electrode type B (collar), indicating that subsequent surface discharges did not necessarily follow the path established by the previous discharge. It is anticipated that each different path followed by the discharge would result in a different time to breakdown, and hence a different breakdown voltage, contributing to the variations in breakdown voltage observed in Figure 5.1.

For PP, LDPE, and UHMWPE, electrical-discharge damage took the form of surface traces, where it appears that the discharges cause ablation and modification of the top layer of the sample surface, most likely through melting, and subsequent evaporation of material from the discharge channel. The visible surface damage was more severe on the PP samples when compared with the LDPE and UHMWPE samples. Pinhole puncture marks were visible at both ends of several of the samples, indicating that some of the electrical breakdowns had occurred through the bulk of the material. Such damage was apparent in three of the four PP samples, and the only material that did not appear to suffer bulk breakdown damage in at least one of the four tests was LDPE. The influence of bulk breakdowns on the results is discussed in relation to Volt-time (V-t) plots in section 5.1.3. The Rexolite and Torlon samples were found to be more severely damaged, with relatively large portions of material removed from the surface discharge locations.

Comparing the average values in Table 5.1 for the type II (shoulder) and type III (no modifications) samples, treated using high-voltage electrode type B (collar), shows that the mean breakdown voltage was increased by: 23% for Rexolite, 12% for both PP and Torlon, and 10% for UHMWPE, through the introduction of the shoulder in the type II samples. The only material that did not show an increase was LDPE,

where the mean breakdown voltage was similar for the type II and type III samples. The average time to breakdown, however, was generally shorter for the type II (shoulder) samples than the type III (no modifications) samples, as discussed below.

5.1.2 Time to Breakdown

Figure 5.2 shows the time to breakdown versus breakdown number for high-voltage electrode type A (pin) and sample type I (recess). Although UHMWPE had the lowest average breakdown voltage under this geometry, it is clear from Figure 5.2 that the times to breakdown for this material were significantly longer than those for the other four materials. The times to breakdown for LDPE and Torlon are fairly consistent from shot to shot in comparison with the other materials. A clear fall in time to breakdown can be seen for PP following the first breakdown. The short times to breakdown for Rexolite are evident towards the end of the test.

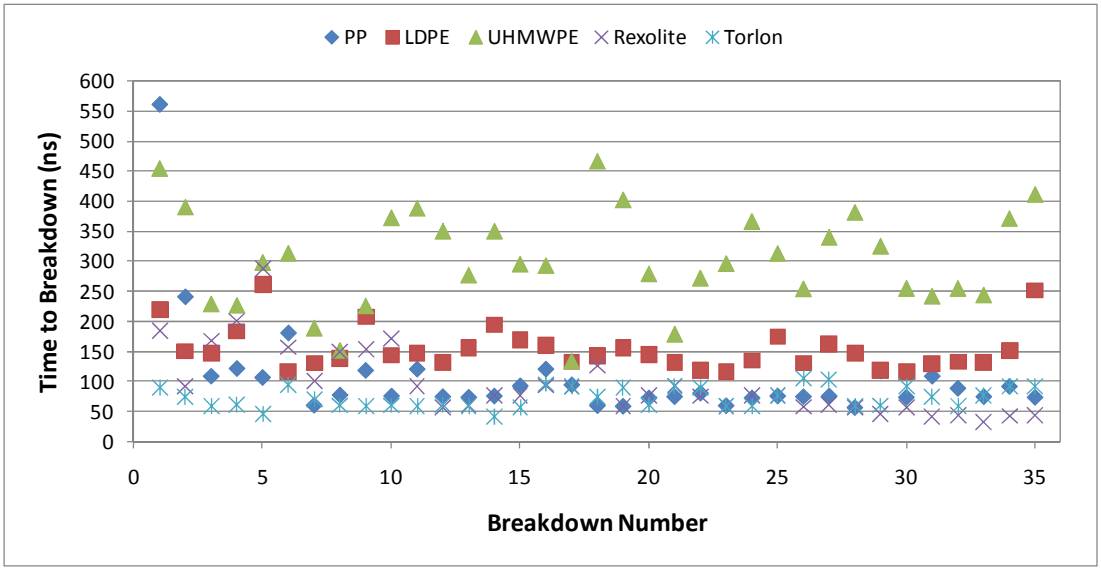

Figure 5.2. Time to breakdown versus breakdown number for high-voltage electrode type A (pin) and sample type I (recess).

The graphs showing time to breakdown versus breakdown number for the other electrode/sample configurations (AII, BII, BIII) have a similar form to that for the AI configuration, and are displayed in *Appendix B*.

Overall, UHMWPE had the longest mean time to breakdown under three of the four non-uniform geometries cases, indicating that this material could hold off breakdown for longer than the other materials for the same level of peak applied voltage. The material with the shortest mean time to breakdown for all four geometries was Torlon.

With high-voltage electrode type A (pin), the type II (shoulder) samples had a longer mean time to breakdown than the type I (recess) samples for all materials except UHMWPE. For high-voltage electrode type B (collar), the type III (no modifications) samples yielded a longer mean time to breakdown than the type II (shoulder) samples for all materials except PP.

5.1.3 Volt-time Plots

In addition to individual analysis of the average breakdown voltages and times to breakdown, it was also considered useful, from an overall insulation assessment perspective, to show the information obtained as V-t plots.

Throughout this work, the term "Volt-time (V-t) plot" is used to mean a plot of the breakdown voltages against the corresponding times to breakdown for a particular set of conditions, rather than the "Voltage/time curves" defined in IEC 60060-1 [151].

Figure 5.3 shows the V-t plot for type I (recess) samples tested with high-voltage electrode type A (pin). It is clear that the time to breakdown was less than 100 ns for the majority of breakdowns of the PP, Rexolite, and Torlon samples, corresponding with breakdown occurring on the rising edge of the applied impulses; evidence of both bulk breakdown damage and significant surface damage was apparent on each of these samples (refer to Figure 5.17 in section 5.5). The outlying PP data point at 562 ns corresponds with the first breakdown for this material. Significant clustering of the LDPE data points indicates that the point of breakdown would be more predictable for this material than for the other four materials, with 74% of the data points located in the range between 116-163 ns and 308-375 kV. It is also clear that

the time to breakdown for UHMWPE was generally much longer than for the other materials, with 31 of the 35 breakdowns occurring after a time of greater than 200 ns.

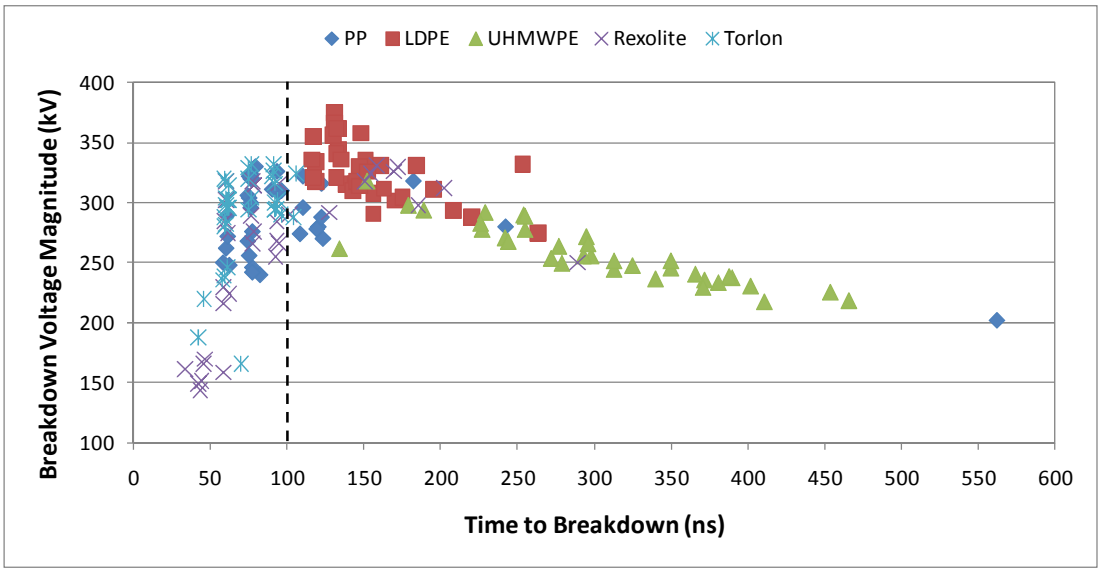

Figure 5.3. Volt-time plot for surface flashover along type I (recess) samples with high-voltage electrode type A (pin). The dashed line at 100 ns separates the rising edge of the pulse (<100 ns) from the falling edge of the pulse (>100 ns).

Volt-time plots for the other electrode/sample configurations (AII, BII, BIII) are presented for completeness in *Appendix C*. These curves have the same general form as those in Figure 5.3 for configuration AI, but some differences are worth noting. For configuration AII (165±94 ns), the average time to breakdown for UHMWPE is much shorter than for AI (303±80 ns), and this may be due to greater bulk breakdown damage occurring for AII. For configuration BII, the data points for all the materials are more clustered than for the electrode A configurations, indicating that breakdown is more predictable for the geometry of BII. For configuration BIII, clustering is most significant for LDPE, as was found using configuration AI. This suggests that breakdown may generally be more predictable for LDPE than for the other sample materials, this being somewhat independent of geometry.

5.2 OVER-VOLTED GAPS AND UNIFORM FIELDS

Type III (no modifications) samples of each material were tested with a plane-parallel electrode configuration (high-voltage electrode type C). The samples were 8 mm long, and as before the electrodes were removed and polished after testing of each sample. While the initial intention was to subject each sample to 35 impulses, as in section 5.1, the collection of data related to surface breakdown events was restricted by the occurrence of bulk breakdown at an early stage in the test sequence. Each sample was therefore initially subjected to five shots with a peak applied voltage of −400 kV. The breakdown voltages over the five shots, and up to 14 shots for Rexolite, are shown in Figure 5.4. With this electrode configuration, and based on the data for the first five shots only for each material, Rexolite showed the highest mean breakdown voltage of 266±69 kV, with a variation of 150 kV between the maximum and minimum recorded voltages. Ultra-high molecular weight polyethylene had the second highest mean breakdown voltage of 248±36 kV, and the least variation between the maximum and minimum voltages of 94 kV.

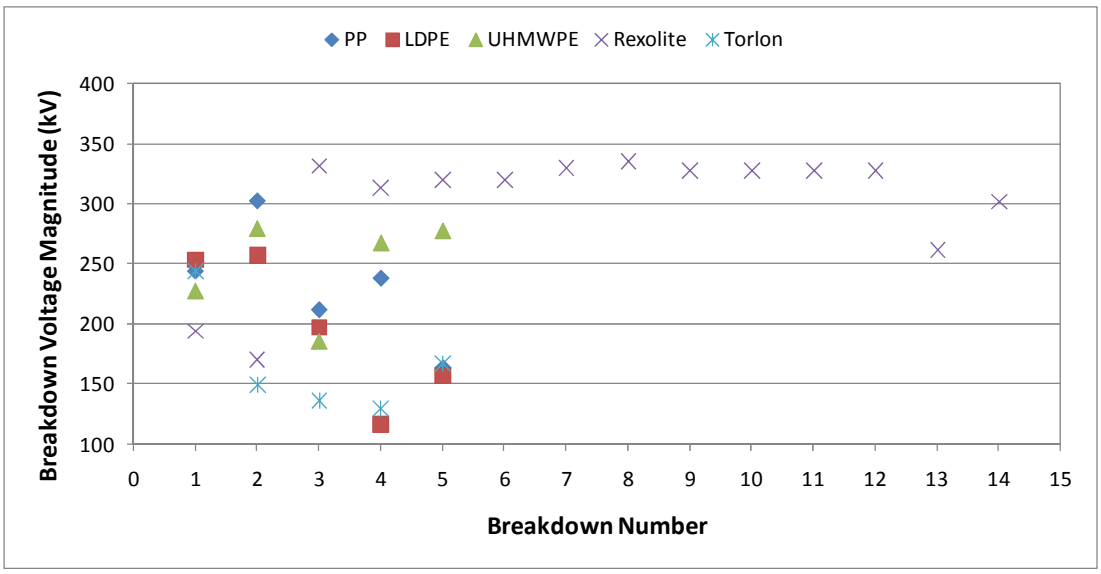

Figure 5.4. Breakdown voltage magnitude versus breakdown number for high-voltage electrode type C (plane) and sample type III (no modifications).

As aforementioned, bulk breakdowns were more readily observed in this plane-parallel geometry than with the point-plane geometries, where the pin or collar on the high-voltage electrode tended to guide the initial discharges along the surface of the sample. This discharge behaviour has previously been observed with plane-parallel electrodes immersed in insulating oil [6]. Bulk breakdown events were characterised by much shorter delay times to breakdown compared to those for surface flashover. The pattern generally observed was for the time to breakdown to be in the range 300-500 ns for one or two shots, and thereafter dropping to below 80 ns for the remaining shots, corresponding with breakdown occurring on the impulse rising edge. Post-test visual inspection of the samples revealed both surface flashover and bulk breakdown damage to all five material samples.

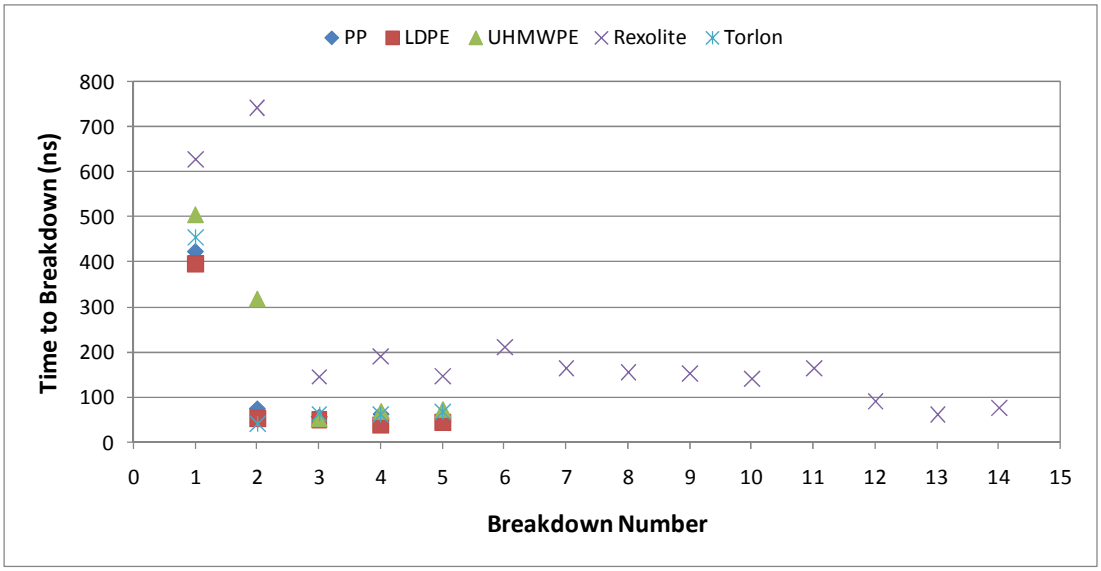

Figure 5.5. Time to breakdown versus breakdown number for high-voltage electrode type C (plane) and sample type III (no modifications).

The exception to this behaviour was Rexolite, as the time-to-breakdown data illustrates in Figure 5.5. The first two shots with the Rexolite sample resulted in breakdown after delay times of 628 ns and 742 ns respectively, followed by three breakdown events with a delay time in the relatively narrow range 150-200 ns. This test was, therefore, extended, and six more breakdowns with a delay time of 150-

200 ns were observed, before the delay time fell to less than 80 ns for three consecutive shots (14 shots in total), and the test was terminated. The breakdown voltage remained relatively constant over shots three to nine, varying by only 22 kV over the range 314 kV to 336 kV.

A V-t plot for all five materials is shown in Figure 5.6. For PP, LDPE, UHMWPE, and Torlon, the data points in the range 300-500 ns correspond to the first 1-2 shots, with all subsequent breakdowns occurring on the rising edge. The clustering of the Rexolite data points at around 320 kV and 150 ns can be clearly seen in Figure 5.6, reflecting the consistent behaviour found only for Rexolite and not for the other materials in uniform-field gaps subjected to over-voltages.

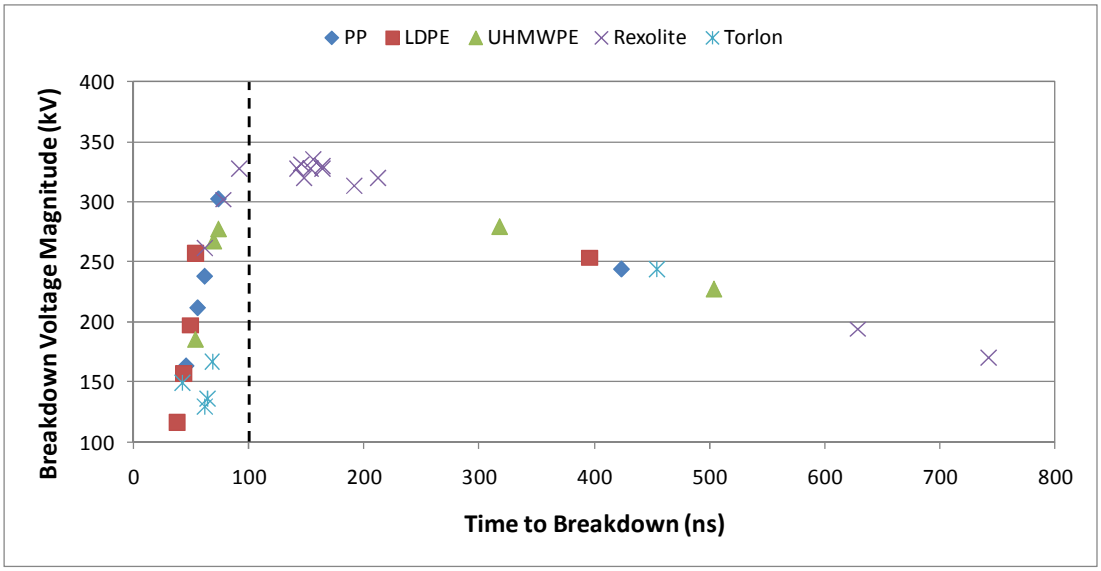

Figure 5.6. Volt-time plot for surface flashover along type III (no modifications) samples with high-voltage electrode type C (plane). The dashed line at 100 ns separates the rising edge of the pulse (<100 ns) from the falling edge of the pulse (>100 ns).

5.3 BREAKDOWN INITIATION

After analyzing the behaviour of the different materials in over-volted gaps, tests were performed to find the average applied electrical fields (defined here as the peak applied voltage divided by the inter-electrode gap length) necessary to initiate surface breakdown, by first applying lower-voltage impulses that did not result in breakdown (see Figure 3.12a), and then incrementally increasing the applied voltage until a breakdown event occurred. The voltage wave-shape was again 100/600 ns, as in sections 5.1 and 5.2.

As previously discussed in section 4.1, the breakdown initiation test procedure used here for estimation of the voltages/fields necessary to initiate surface breakdown in the various liquid-solid gaps is similar to "the step-up test method" described by Hirose [153].

Samples of each material were placed between the electrodes and subjected to negative-polarity impulses, with the following test sequence:

For both non-uniform geometries, where the electrode separation was 10 mm, a peak voltage of −140 kV (average applied field of 140 kV/cm) was initially applied across the electrodes, and for plane-parallel electrodes, where the electrode separation was 4 mm, the voltage initially applied was −80 kV (average applied field of 200 kV/cm). No breakdown event was ever found to occur at these levels of applied voltage. The charging voltage was raised in steps of 2 kV (~20 kV increase in output voltage) until a breakdown occurred, at which point the peak applied voltage, the breakdown voltage, and the delay time to breakdown were recorded (see Figure 3.12b). The charging voltage was then reduced to return the peak applied voltage to −140 kV or −80 kV, depending upon the electrode configuration.

The above process was then repeated until a total of five breakdowns had occurred. As the voltages/fields of interest in this type of measurement were those required to initiate these first few breakdown events, three samples of each material were treated

to aid determination of the variation for each data point, rather than increasing the number of impulses applied to each sample as in sections 5.1 and 5.2. The electrodes were removed and polished between test sequences.

Unlike the measurements reported in sections 5.1 and 5.2, all of the voltage waveforms upon breakdown took the form of that shown in Figure 3.12b, and no breakdown events occurred on the impulse rising edge.

The results of these measurements are summarized in Tables 5.5-5.6, which contain data for the peak applied voltage (Table 5.5), and for the breakdown voltage and corresponding time to breakdown (Table 5.6), for all five breakdown events for each of the materials and electrode/sample combinations. Three samples of each material were treated for every data point, and the data contained in Tables 5.5-5.6, as well as the data points shown in Figures 5.7-5.9, represent the mean values from the three samples. The peak applied voltage data in Table 5.5 and the breakdown voltage data in Table 5.6 have been represented as average electrical fields (applied field or breakdown field as appropriate) in Figures 5.7-5.9, calculated by dividing the recorded voltages by the inter-electrode gap length. Unlike the tests reported in sections 5.1 and 5.2, post-test inspection revealed only surface damage, and no bulk breakdown damage to any of the samples.

Table 5.5. Mean value of peak applied voltage (V_{ap}(av.)) for breakdown initiation measurements (all data is for the treatment of 3 samples for each material and electrode/sample combination; ± values represent standard deviation).

		High-Voltage Electrode Type A/ Sample Type I	High-Voltage Electrode Type B/ Sample Type III	High-Voltage Electrode Type C/ Sample Type III
		V_{ap} (av.) (kV)	V_{ap} (av.) (kV)	V_{ap} (av.) (kV)
PP	1	325±83	391±27	255±23
	2	293±107	345±48	238±27
	3	287±69	328±60	271±67
	4	285±41	324±73	247±52
	5	303±25	316±53	237±12
LDPE	1	325±34	337±25	252±58
	2	284±27	281±18	255±104
	3	253±34	275±18	182±12
	4	266±21	262±14	211±53
	5	265±57	275±28	190±9
UHMWPE	1	305±32	353±27	193±26
	2	250±5	277±43	131±24
	3	257±45	267±35	154±35
	4	265±88	261±26	135±7
	5	282±39	279±40	150±29
Rexolite	1	284±26	346±24	201±28
	2	257±18	266±12	173±1
	3	281±20	244±7	178±10
	4	294±2	250±36	177±7
	5	299±10	241±44	154±18
Torlon	1	178±13	242±13	180±15
	2	157±32	185±42	127±23
	3	184±20	185±37	115±25
	4	205±1	176±47	115±12
	5	218±26	177±31	115±13

Table 5.6. Mean breakdown voltages (V_{br}(av.)) and mean times to breakdown (t_{br}(av.)) for breakdown initiation measurements (all data is for the treatment of 3 samples for each material and electrode/sample combination; ± values represent standard deviation).

		High-Voltage Electrode Type A/ Sample Type I		High-Voltage Electrode Type B/ Sample Type III		High-Voltage Electrode Type C/ Sample Type III	
		V_{br} (av.) (kV)	t_{br} (av.) (ns)	V_{br} (av.) (kV)	t_{br} (av.) (ns)	V_{br} (av.) (kV)	t_{br} (av.) (ns)
PP	1	257±27	392±91	377±21	235±74	211±34	388±74
	2	258±138	355±174	312±23	229±228	190±57	419±233
	3	232±60	417±35	254±58	445±315	251±85	289±87
	4	214±30	480±45	292±37	318±109	214±52	360±98
	5	229±12	471±57	279±68	347±105	189±36	417±217
LDPE	1	165±60	832±223	308±51	269±153	177±55	548±313
	2	202±45	533±286	247±53	361±149	218±73	289±174
	3	215±32	343±181	204±23	493±130	162±29	316±194
	4	187±37	521±194	247±33	252±150	185±54	297±187
	5	198±2	464±205	266±25	248±60	187±8	193±70
UHMWPE	1	239±78	463±212	223±25	619±161	129±40	611±162
	2	243±8	174±99	246±24	319±150	108±11	341±251
	3	211±5	351±198	215±14	411±155	140±40	311±157
	4	203±33	403±196	233±7	325±86	107±15	445±170
	5	203±59	509±237	277±43	224±25	107±23	547±38
Rexolite	1	254±28	333±62	314±41	284±169	178±33	323±85
	2	187±49	516±177	261±19	196±70	154±7	335±51
	3	209±46	509±133	235±17	231±83	148±9	397±95
	4	226±22	460±96	240±45	232±83	152±16	384±80
	5	183±19	616±91	239±46	177±54	123±19	433±125
Torlon	1	163±12	300±29	222±26	299±121	154±11	395±62
	2	145±21	301±94	185±42	223±51	123±26	245±101
	3	174±14	277±20	175±29	273±47	94±9	464±149
	4	175±3	397±24	154±67	440±298	104±20	367±162
	5	163±27	559±184	163±48	312±230	88±7	557±67

5.3.1 Non-uniform Fields

The applied field results for collar-plane geometry (configuration BIII) are shown in Figure 5.7, which shows how the average applied field required to initiate breakdown varied over five breakdowns for type III (no modifications) samples. The average applied fields required to initiate the first breakdown for each material were higher than with high-voltage electrode type A, suggesting that the field enhancement provided by the pin is greater than that for the collar. The applied field required to initiate breakdown generally decreased with an increasing number of breakdowns. Higher average applied fields were clearly required to cause flashover of the PP surface compared with the other materials. The applied fields for breakdown of Torlon surfaces are lowest, and are 1.5-2 times lower than those for PP.

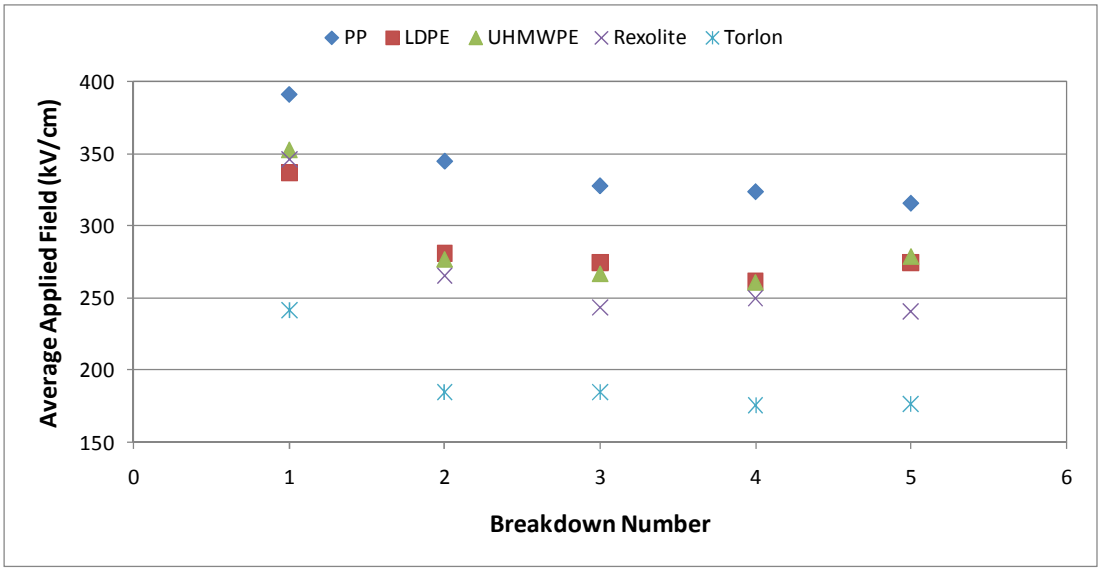

Figure 5.7. Average applied fields to cause surface flashover across type III (no modifications) dielectric samples with high-voltage electrode type B (collar). Each data point represents the mean value from 3 samples.

Figure 5.8 shows that PP had the highest average breakdown field of all of the materials for all five breakdown events. Torlon had the lowest average breakdown field for all five breakdown events. Rexolite had the most predictable time to breakdown, settling at ~200 ns after the first breakdown (Figure 5.9). Ultra-high

molecular weight polyethylene had a long mean delay time for the first breakdown, at over 600 ns compared to 200-300 ns for the other materials.

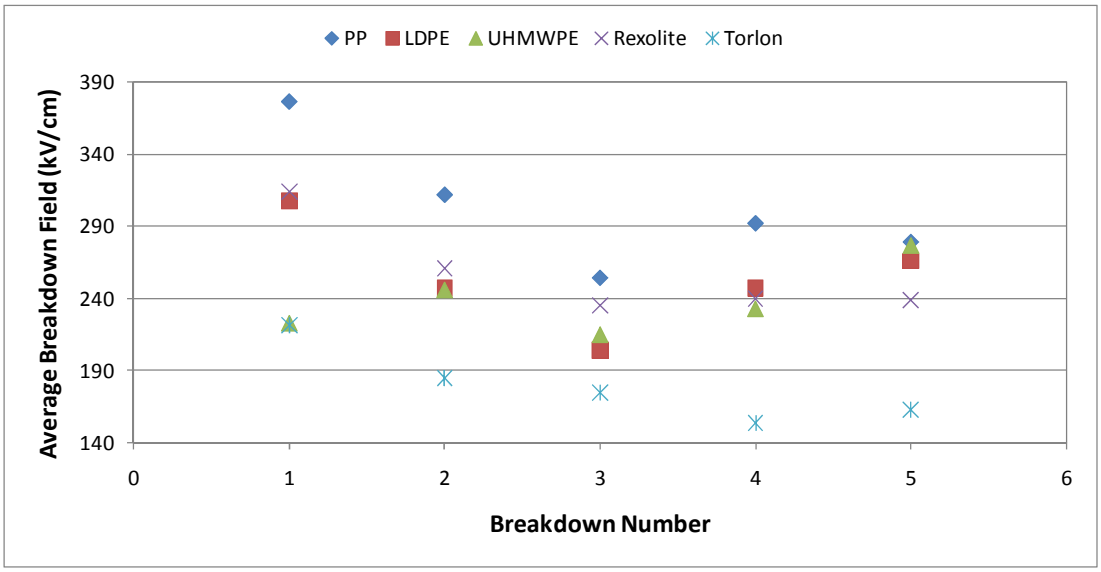

Figure 5.8. Average breakdown fields for surface flashover across type III (no modifications) dielectric samples with high-voltage electrode type B (collar). Each data point represents the mean value from 3 samples.

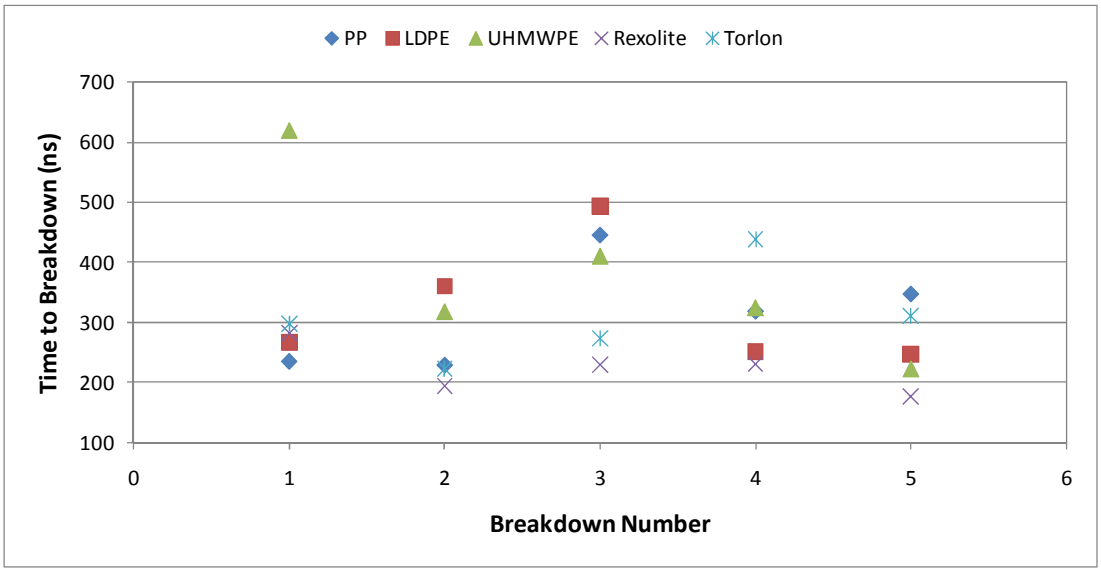

Figure 5.9. Times to breakdown for surface flashover across type III (no modifications) dielectric samples with high-voltage electrode type B (collar). Each data point represents the mean value from 3 samples.

The corresponding graphs of the peak applied electric field, the breakdown electric field, and time to breakdown for pin-plane geometry (configuration AI) are presented in *Appendix D* for completeness. The average applied fields required to initiate the first breakdown for each material were lower than with high-voltage electrode type B, indicative of the fact that the field enhancement provided by the pin is greater than that for the collar. The average breakdown fields were generally lower for configuration AI, whereas the times to breakdown were generally longer.

5.3.2 Uniform Fields

Type III (no modifications) samples of each material were tested with plane-parallel electrodes (high-voltage electrode type C) to provide uniform-field testing conditions. The sample length, and hence, the inter-electrode gap length, was set at 4 mm. The variation in the average applied electric field required to initiate five breakdowns is shown in Figure 5.10.

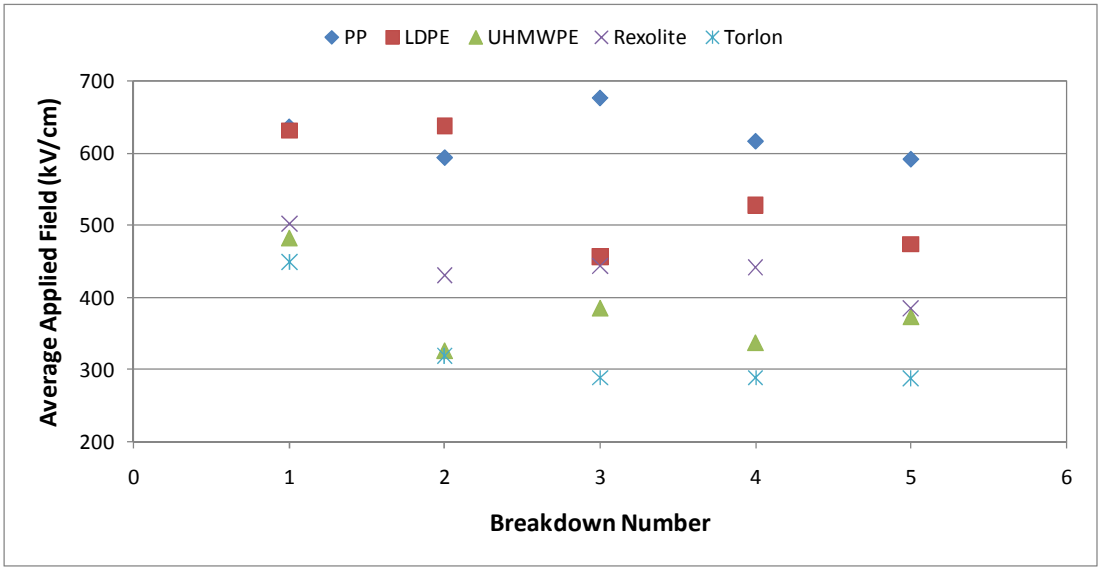

Figure 5.10. Average applied fields to cause surface flashover across type III (no modifications) dielectric samples with high-voltage electrode type C (plane). Each data point represents the mean value from 3 samples.

The average applied fields (V_{ap}/d) required to initiate surface breakdown were 1.5-2 times higher for all materials than those for the non-uniform configurations, and the differences between materials were more pronounced. As with both non-uniform geometries, the average applied fields required to cause surface breakdown were generally higher for PP than for the other materials.

The breakdown electric fields (V_{br}/d) for the uniform geometry (Figure 5.11) were also, in general, higher for all materials than for the non-uniform configurations. Again, the differences between the materials were more pronounced, with PP having the highest average breakdown electric fields (190-250 kV/cm), and UHMWPE (135-175 kV/cm) and Torlon (90-155 kV/cm) the lowest breakdown electric fields.

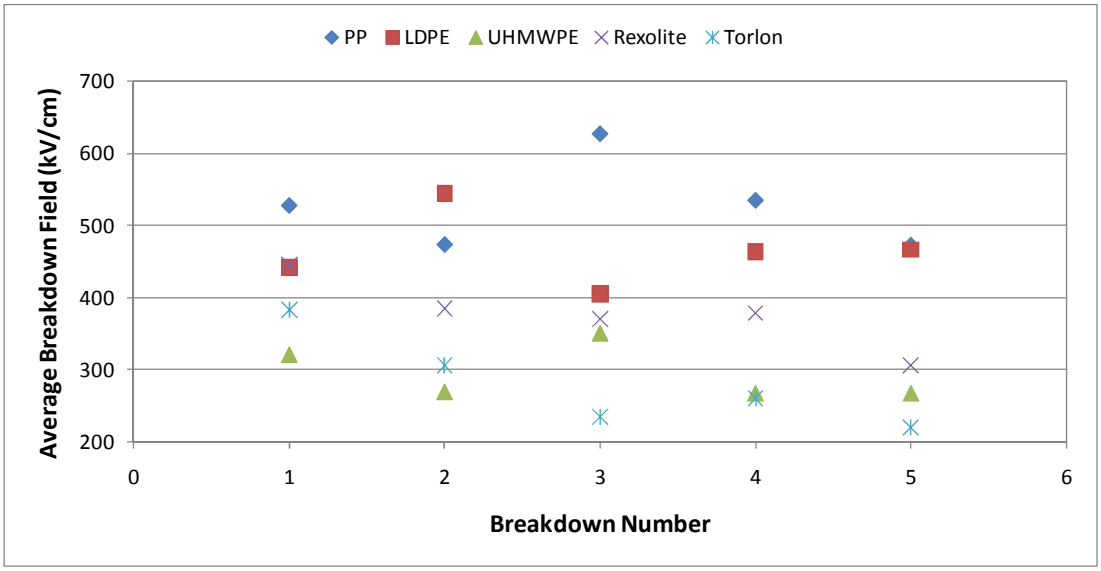

Figure 5.11. Average breakdown fields for surface flashover across type III (no modifications) dielectric samples with high-voltage electrode type C (plane). Each data point represents the mean value from 3 samples.

The range of the times to breakdown (Figure 5.12) for the uniform geometry was similar to those for the non-uniform geometries. For all of the geometries considered, the times to breakdown for each material had a substantial spread. It is interesting to note, however, that Rexolite demonstrated a significantly smaller

spread of times for both the uniform geometry of configuration CIII and the non-uniform geometry of configuration BIII (Figure 5.9). Furthermore, the times to breakdown for Rexolite were shorter for the BIII geometry (180-285 ns) than for either of the CIII (325-435 ns) or AI (335-615 ns) geometries.

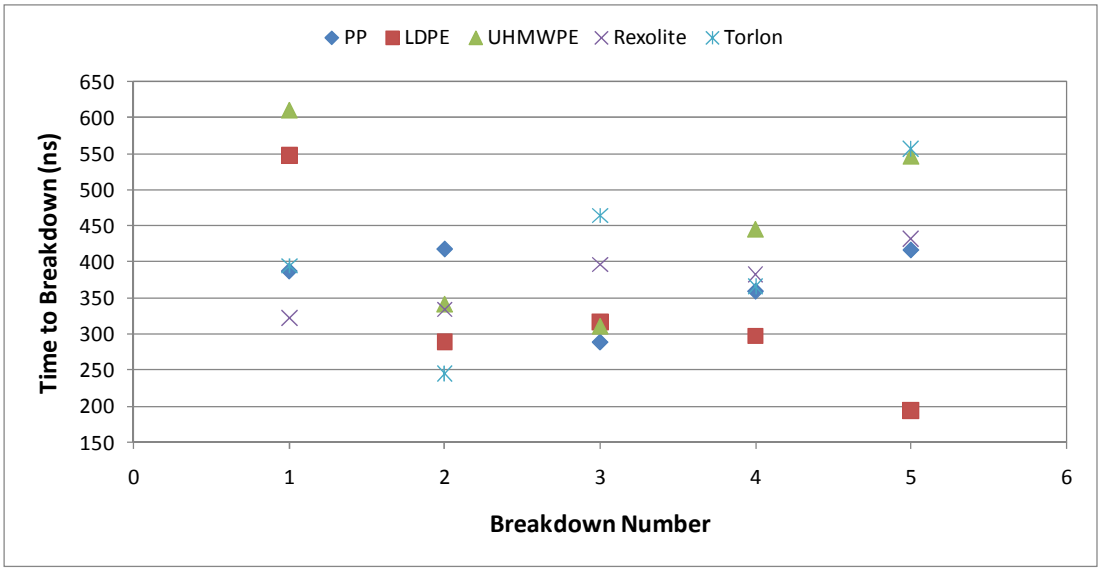

Figure 5.12. Times to breakdown for surface flashover across type III (no modifications) dielectric samples with high-voltage electrode type C (plane). Each data point represents the mean value from 3 samples.

5.4 WEIBULL STATISTICAL ANALYSIS

The experimental data recorded in section 5.3 was subjected to a Weibull statistical analysis, in order to compare the probability of breakdown of the various tested materials at different voltages. Both the applied voltage data and the breakdown voltage data were analysed in order to facilitate comparison of the behaviour of each of these voltage parameters. The data were mostly found to be best described by a three-parameter Weibull distribution, where the cumulative probability of failure, $F(V)$, is defined by equation (5.1) [161]:

$$F(V) = 1 - \exp\left[-\left(\frac{V - \gamma}{\alpha} \right)^{\beta} \right] \tag{5.1}$$

For this study, V is either the peak applied voltage or the breakdown voltage as appropriate. As normal, α is the scale parameter, β is the shape parameter, and γ is the location parameter. The probability of failure at a voltage of α (kV) is 0.632, equivalent to the mean of the Normal distribution [163]. The shape parameter β provides a measure of how sensitive the insulation system is to an increase in voltage, while γ (kV) provides an estimate of the voltage below which the probability of breakdown is zero.

In order to form probability plots to compare the behaviour of the different liquid-solid gaps, the cumulative distribution function is converted into a linear form before plotting. When equation (5.1) is rearranged into the form of a straight line ($y = mx+c$), we find equation (5.2):

$$\ln\left[\ln\left(\frac{1}{1 - F(V)} \right) \right] = \beta \ln(V - \gamma) - \beta \ln(\alpha) \tag{5.2}$$

where y is equivalent to the left-hand side of the equation, m is equivalent to β, x corresponds to $\ln(V-\gamma)$, and c is equivalent to $-\beta\ln(\alpha)$.

In certain cases, the data were best described by a two-parameter Weibull distribution – in such instances the value of the location parameter γ is listed as zero in the relevant table in the following analysis. For clarity, *F(V)* is redefined for a two-parameter distribution in equation (5.3):

$$F(V) = 1 - \exp\left[-\left(\frac{V}{\alpha} \right)^{\beta} \right] \tag{5.3}$$

Equation (5.4) is obtained following rearrangement of equation (5.3) into the form of a straight line:

$$\ln\left[\ln\left(\frac{1}{1-F(V)}\right)\right] = \beta\ln(V) - \beta\ln(\alpha) \tag{5.4}$$

where all parameters are the same as those defined in equation (5.2), only this time x corresponds to $\ln(V)$ rather than $\ln(V-\gamma)$.

In order to produce the Weibull plots discussed in sections 5.4.1 to 5.4.3, the following procedure was followed:

- the (peak applied or breakdown) voltage data was sorted in ascending numerical order;
- each voltage was assigned a rank from 1 (lowest voltage) to 15 (highest voltage);
- Bernard's approximation of the median ranks, as defined in equation (5.5), was used in order to estimate the unreliability, $F(V)$;
- equation (5.4) was then used to find the y-axis values for the plot;
- the values for the x-axis were found using $\ln(V)$;
- linear regression analysis was then used in order to determine the values of β, determined directly from the gradient of the straight line, and α $\left[\alpha = \exp-\left(\frac{c}{\beta}\right)\right]$;
- if the data points did not fall onto a straight line, then the location parameter γ was made to be non-zero, and the value was changed until the line of best fit was determined – in such cases, equation (5.2) was used to find the values for the y-axis, and the x-axis values were found using $\ln(V-\gamma)$.

$$\text{median ranks} = \frac{(i-0.3)}{(n+0.4)} \tag{5.5}$$

where i represents the rank order (for example, i = 1 for the lowest breakdown voltage), and n represents the number of values in the dataset (here, n = 15).

All of the above analysis was performed using Microsoft Excel, with the Analysis ToolPak add-in loaded, as described in [164].

5.4.1 Peak Applied Voltage Data

The calculated values of α, β, and γ for each of the materials and electrode types are listed in Table 5.7 for the peak applied voltage data.

Table 5.7. Weibull distribution parameters for peak applied voltage data.

		MATERIAL				
		PP	LDPE	UHMWPE	Rexolite	Torlon
Pin-Plane (AI)	Scale α (kV)	123	151	292	293	79
	Shape β	1.68	4.37	6.64	14.5	2.88
	Location γ (kV)	190	135	0	0	120
Collar-Plane (BIII)	Scale α (kV)	115	52	69	79	210
	Shape β	1.56	1.35	1.17	1.52	4.73
	Location γ (kV)	240	240	225	200	0
Plane-Parallel (CIII)	Scale α (kV)	66	81	206	64	51
	Shape β	1.75	1.27	4.98	2.68	1.33
	Location γ (kV)	192	160	0	165	85

The shape parameter β describes the gradient of the straight lines fitted to the data in the probability plots in Figure 5.13. All values of β in Table 5.7 are greater than 1, meaning that the probability of breakdown increases with increasing voltage, as would be expected. The higher the value of β, the more sensitive the sample is to an increase in voltage – that is, the probability of breakdown increases more sharply with increasing voltage. The extreme case here is Rexolite for pin-plane geometry (AI), where β is 14.5, shown by the steep gradient in Figure 5.13.

By analysing the β values in Table 5.7, it is clear that the probability of breakdown is less sensitive to increasing applied voltage for the type B (collar) electrode than for

the type A (pin) electrode. Again, this effect would be expected due to the degree of field enhancement generated by the type A (pin) electrode.

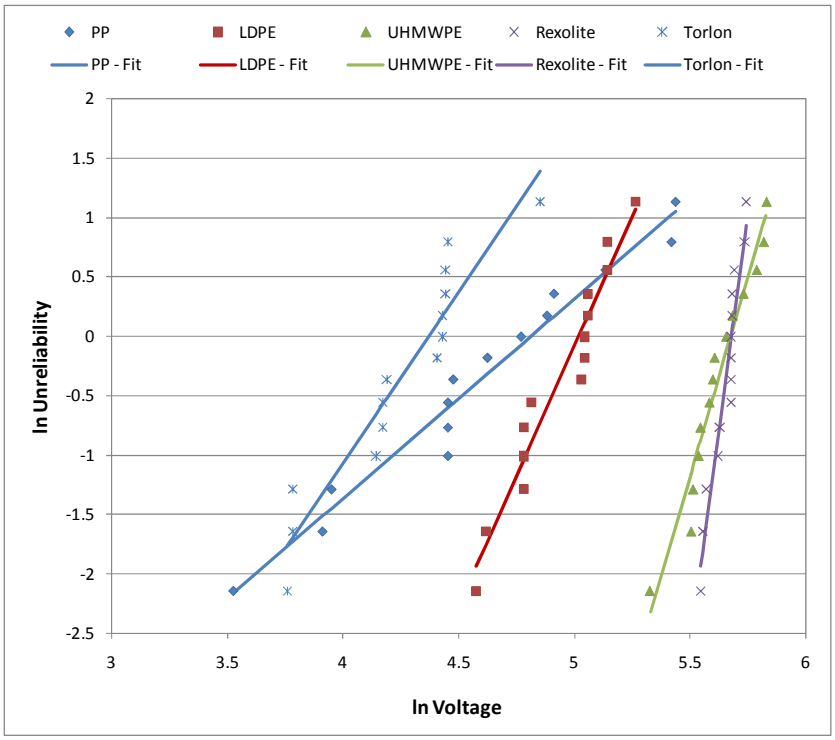

Figure 5.13. Weibull plots and curve fits of peak applied voltage data for type I (recess) samples tested with high-voltage electrode type A (pin).

The Weibull plots of the peak applied voltage data for the collar-plane (BIII) and plane-parallel (CIII) electrodes are included in *Appendix E* for completeness. Comparing Figure 5.13 with the collar-plane plots, it is clear that the probability of breakdown is generally less sensitive to increasing applied voltage for the type B (collar) electrode than for the type A (pin) electrode, evidenced by the shallower gradients of the collar-plane plots.

The plane-parallel plots for PP, LDPE, Rexolite, and Torlon suggest a similar behaviour for these materials. The behaviour for UHMWPE is best described by a two-parameter Weibull distribution, and hence there is a clear distinction between the UHMWPE plane-parallel plot and those for the other materials.

5.4.2 Breakdown Voltage Data

The calculated values of α, β, and γ for each of the materials and electrode types are listed in Table 5.8 for the breakdown voltage data.

Table 5.8. Weibull distribution parameters for breakdown voltage data.

		MATERIAL				
		PP	LDPE	UHMWPE	Rexolite	Torlon
Pin-Plane (AI)	Scale α (kV)	94	209	238	228	172
	Shape β	1.54	5.11	5.11	5.29	9.79
	Location γ (kV)	155	0	0	0	0
Collar-Plane (BIII)	Scale α (kV)	327	162	49	94	200
	Shape β	5.31	3.00	1.38	1.90	4.15
	Location γ (kV)	0	110	195	175	0
Plane-Parallel (CIII)	Scale α (kV)	110	217	57	126	41
	Shape β	1.95	4.54	1.57	3.80	1.15
	Location γ (kV)	115	0	98	75	75

Figure 5.14 shows Weibull plots of breakdown voltage data for type I samples tested with high-voltage electrode type A (pin). The data for LDPE, UHMWPE, and Rexolite were all best described by a two-parameter Weibull distribution, and the curves are almost identical; Torlon data were also best described by a two-parameter distribution, although the gradient of the line is twice that of the three aforementioned materials.

For collar-plane geometry (BIII), there is a clear distinction in the behaviour of each of the materials. The location parameter γ decreases from 195 kV for UHMWPE to zero for PP and Torlon. The shape parameter β increases from 1.38 for UHMWPE to 5.31 for PP.

Under plane-parallel configuration (CIII), the probability of breakdown for Torlon is the least sensitive to increasing voltage (β = 1.15). Polypropylene has the highest γ value of 115 kV.

The Weibull plots of the breakdown voltage data for high-voltage electrodes type B (collar) and type C (plane), both with the unmodified sample surface (type III), are displayed in *Appendix F* for completeness.

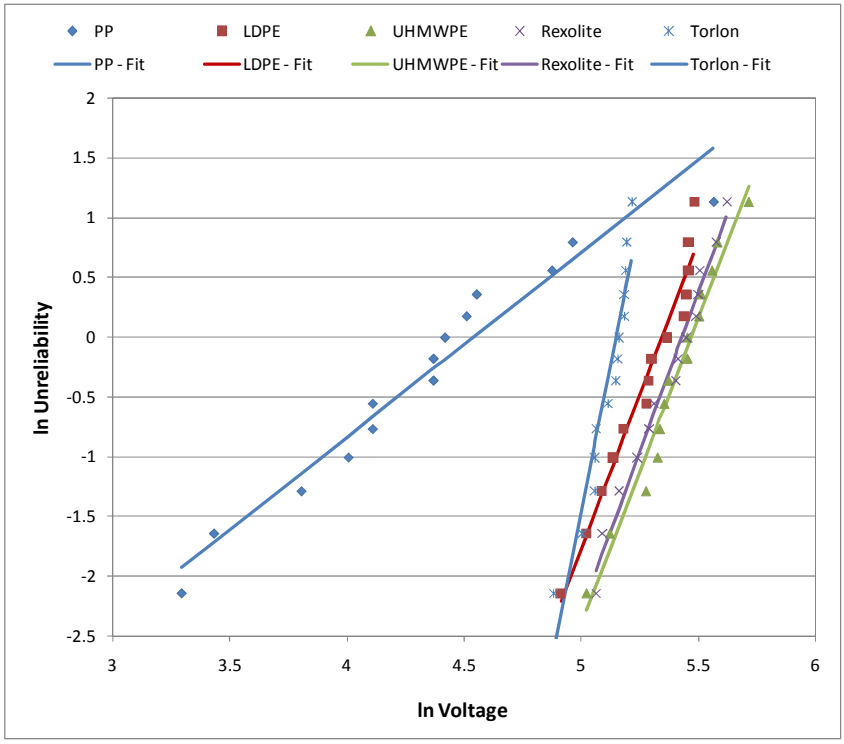

Figure 5.14. Weibull plots and curve fits of breakdown voltage data for type I (recess) samples tested with high-voltage electrode type A (pin).

5.4.3 Material Comparison

Figure 5.15 shows the Weibull plots for PP for the same applied voltage data presented in Table 5.7, and for the three configurations described above (AI, BIII, and CIII). Polypropylene has been selected as an example material for discussion, and Figure 5.15 illustrates the fact that the gradient of the curves is very similar for all three electrode configurations for this material.

The breakdown voltage plots for PP are displayed in Figure 5.16. The steeper gradient for the collar electrode (BIII) is indicative of the fact that these data were best described by a two-parameter distribution, while the date for geometries AI and CIII were best described by a three-parameter distribution.

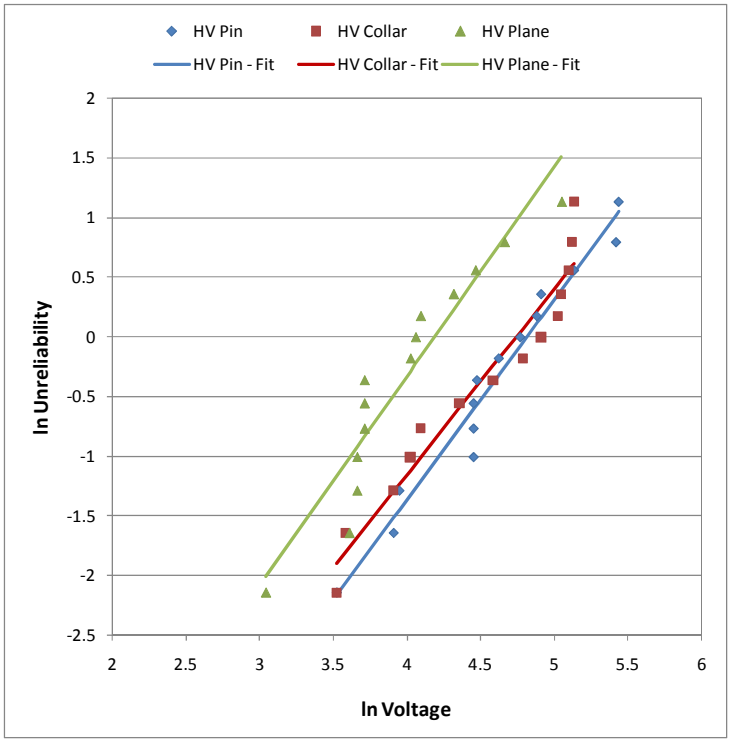

Figure 5.15. Weibull plots and curve fits of applied voltage data for PP samples.

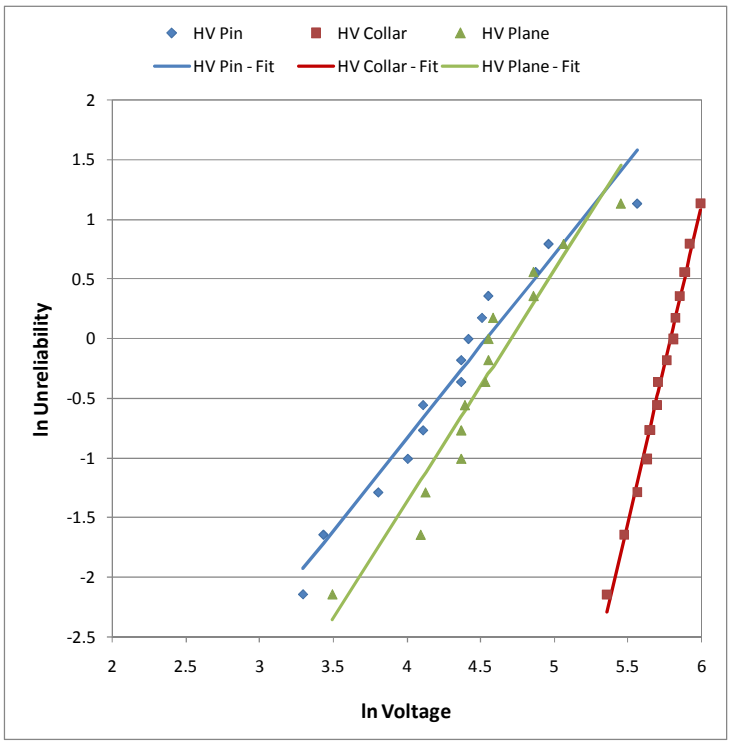

Figure 5.16. Weibull plots and curve fits of breakdown voltage data for PP samples.

Similar behaviour is found for all of the studied materials, as illustrated by the Weibull plots for LDPE, UHMWPE, Rexolite, and Torlon displayed in *Appendix G* for both the applied voltage data and the breakdown voltage data.

5.5 DISCUSSION AND CONCLUSIONS

Impulse voltage breakdown data have been obtained for five dielectric materials considered for use as oil-immersed insulators in high-voltage, pulsed-power machines.

For over-volted pin-plane and collar-plane gaps, low-density polyethylene showed a relatively small variation in breakdown voltage and time to breakdown, and of the five dielectrics studied, this was the only material not to suffer any bulk (solid) breakdown damage under non-uniform geometries, despite being repeatedly subjected to over-voltages. This suggests that the bulk breakdown strength of LDPE is higher than that of the other materials for the stressing regimes investigated here.

Different sample geometries have been tested, and the results have shown that the average breakdown voltage can be raised by up to 23% (as compared with an unmodified cylindrical sample) by introducing a 'shoulder' of reduced diameter at the end of the solid sample in contact with the high-voltage electrode. Due to the fact that breakdown generally occurred on the falling edge of the voltage impulse however, this increase in breakdown voltage corresponds with shorter pre-breakdown delay times. It is possible that the addition of the shoulder acts to influence both the electric-field distribution at the interface between the insulation system and the high-voltage electrode, and the statistical delay time associated with initiatory electron production. The effect on breakdown voltage and time to breakdown with breakdown occurring only on the rising edge of the voltage impulse is investigated and discussed in Chapter 6.

The times to breakdown can be compared with those obtained in open oil gaps in section 4.2.1 for the same applied wave-shape (100/600 ns). For pin-plane geometry, the baseline pre-breakdown delay time in oil was found to be ~225 ns. The implied average streamer propagation velocity, calculated by dividing the inter-electrode gap length by the time to breakdown, is 38 km/s. Comparing this with the data in Table 5.2, it is clear that the introduction of a solid spacer between the electrodes generally causes a reduction in this delay time. The type I UHMWPE sample presents an anomaly however, and the average delay time was around 300 ns in this case. In collar-plane geometry in oil, the baseline pre-breakdown delay time was more than double that for pin-plane geometry, at ~500 ns, corresponding with an average streamer propagation velocity of 17 km/s. In this case, the effect of including a solid spacer between the electrodes is much more pronounced, with a decrease in the pre-breakdown delay time by a factor of five in most cases. Ultra-high molecular weight polyethylene again reflected the longest average time to breakdown of 184 ns (geometry BIII), and the long pre-breakdown delay times with UHMWPE samples are discussed further in the subsequent chapters.

In uniform-field measurements in section 4.2.1, the average propagation velocity for an 8-mm open oil gap was found to be of the order of 20 km/s.

The average streamer propagation velocities for over-volted liquid-solid gaps are indicated in Table 5.9 for the various non-uniform field geometries (section 5.1), and in Table 5.10 for plane-parallel electrodes (section 5.2).

The upper and lower velocities quoted in Table 5.9 and Table 5.10 refer to the calculated velocities for the shortest and the longest time to breakdown for each sample, respectively. The streamer modes in the final column of Tables 5.9 and 5.10 have been identified as classified in [165], where the following average streamer propagation velocities are reported as typical in dielectric liquids:

- 1st mode 0.1 km/s
- 2nd mode 1-5 km/s
- 3rd mode 10-20 km/s
- 4th mode 100 km/s

Under this classification then, streamer velocity increases by an order of magnitude with each propagation mode.

Table 5.9. Average streamer velocities and corresponding propagation modes for over-volted gaps and non-uniform fields (± values indicate standard deviation).

		Average Velocity (km/s)	**Upper Velocity (km/s)**	**Lower Velocity (km/s)**	**Streamer Mode [165]**
Pin/Recess (AI)	PP	98±30	147	15	$4^{th}/3^{rd}$
	LDPE	58±11	73	32	$4^{th}/3^{rd}$
	UHMWPE	31±10	63	18	$4^{th}/3^{rd}$
	Rexolite	115±54	258	29	$4^{th}/3^{rd}$
	Torlon	122±29	202	80	4^{th}
Pin/Shoulder (AII)	PP	88±29	149	30	$4^{th}/3^{rd}$
	LDPE	50±7	63	32	$4^{th}/3^{rd}$
	UHMWPE	69±39	139	18	$4^{th}/3^{rd}$
	Rexolite	118±68	266	13	$4^{th}/3^{rd}$
	Torlon	126±40	213	38	$4^{th}/3^{rd}$
Collar/Shoulder (BII)	PP	88±22	144	37	$4^{th}/3^{rd}$
	LDPE	91±28	157	36	$4^{th}/3^{rd}$
	UHMWPE	84±19	113	18	$4^{th}/3^{rd}$
	Rexolite	100±19	144	52	$4^{th}/3^{rd}$
	Torlon	133±21	207	94	4^{th}
Collar/No mods. (BIII)	PP	105±28	147	46	$4^{th}/3^{rd}$
	LDPE	82±19	121	33	$4^{th}/3^{rd}$
	UHMWPE	52±18	94	24	$4^{th}/3^{rd}$
	Rexolite	106±48	224	18	$4^{th}/3^{rd}$
	Torlon	126±31	189	44	$4^{th}/3^{rd}$

Comparing the data in Tables 5.9 and 5.10 with that obtained in open oil gaps, it is clear that the introduction of a solid spacer into the gap can promote conditions for the initiation and propagation of streamers in the faster 4^{th} mode, where the average propagation velocity is of the order of 100 km/s. In fact, the upper velocity

calculated for type I and type II Rexolite samples in pin-plane geometry exceeds 250 km/s (Table 5.9). The lower velocities in the range 10-20 km/s in Table 5.10 all correspond to the first or second breakdown event, and the upper velocities correspond to the later discharges, where bulk breakdown behaviour was dominant. Space charge injected by the electrodes during the initial discharges may be important in the appearance of 4^{th} mode streamers in uniform fields, where the resulting local field enhancement has more of an influence in determining the streamer path than in the non-uniform geometries where a high field is generated on the pin or collar.

Table 5.10. Average streamer velocities and corresponding propagation modes for over-volted gaps and uniform fields (± values indicate standard deviation).

		Average Velocity (km/s)	**Upper Velocity (km/s)**	**Lower Velocity (km/s)**	**Streamer Mode [165]**
Plane/No mods. (CIII)	PP	115±59	174	19	$4^{th}/3^{rd}$
	LDPE	144±73	211	20	$4^{th}/3^{rd}$
	UHMWPE	82±59	148	16	$4^{th}/3^{rd}$
	Rexolite	35±22	55	11	3^{rd}
	Torlon	116±62	190	18	$4^{th}/3^{rd}$

Measurements of the average applied electric fields required to initiate surface flashover reveal that the applied-field threshold necessary to cause flashover is lowered following the first flashover event. With particular reference to Figure 5.7, the electric field required to initiate the first flashover event was higher than that for subsequent flashovers, and the gradient of the curves became shallower with increasing flashover number. This suggests that the surface conditioning caused by the first flashover is more damaging to the sample integrity than cumulative damage from subsequent discharges. From a design perspective, the measurements associated with the later flashover events, when the applied field begins to level out, should be consulted in preference to the measurements associated with the first flashover. Polypropylene has shown the highest levels of average applied field necessary to initiate flashover in all electrode configurations tested, at ~640 kV/cm in

uniform fields, and ~325 kV/cm in non-uniform fields. The reduction in the applied fields necessary to cause flashover in point-plane gaps when compared with plane-parallel gaps may be useful for predicting the effect of pollution on the electrode/insulator surface [65], [66], for example, that due to debris present in the bulk of the oil from previous discharges.

The calculated average streamer propagation velocities for breakdown initiation measurements are presented in Table 5.11. When comparing these data with the corresponding geometries in Tables 5.9 and 5.10, it is apparent that the average velocity is generally lower than that for over-volted gaps, as would be expected. Importantly for uniform-field measurements (geometry CIII), no 4th mode streamers were observed, and this can be correlated with the observation that only surface breakdown behaviour, and no bulk breakdown behaviour, was observed in these measurements.

Table 5.11. Average streamer velocities and corresponding propagation modes breakdown initiation measurements (± values indicate standard deviation).

		Average Velocity (km/s)	**Upper Velocity (km/s)**	**Lower Velocity (km/s)**	**Streamer Mode [165]**
Pin/No mods. (AI)	PP	26±10	60	19	3rd
	LDPE	25±17	74	10	3rd
	UHMWPE	38±26	88	14	3rd
	Rexolite	22±7	37	14	3rd
	Torlon	30±8	43	14	3rd
Collar/No mods. (BIII)	PP	43±27	106	13	4th/3rd
	LDPE	40±24	98	16	4th/3rd
	UHMWPE	31±12	49	13	3rd
	Rexolite	53±23	109	24	4th/3rd
	Torlon	40±19	89	13	3rd
Plane/No mods. (CIII)	PP	12±4	20	6	3rd/2nd
	LDPE	18±11	45	4	3rd/2nd
	UHMWPE	13±14	63	5	3rd/2nd
	Rexolite	11±3	17	7	3rd/2nd
	Torlon	12±6	30	6	3rd/2nd

When comparing the uniform-field results in Figure 5.10, the materials can be ranked in terms of decreasing peak applied field inducing breakdown as follows:

1. PP
2. LDPE
3. Rexolite
4. UHMWPE
5. Torlon

corresponding with increasing relative permittivity, and increasing permittivity mismatch with the surrounding mineral oil. This finding is in agreement with those of Taylor [166] and Krins *et al*. [115], both of which studies found that higher flashover voltages were yielded by matching the permittivity of the parallel solid surface to that of the oil in which it was immersed.

Examining the applied field levels required to initiate breakdown of the PP and LDPE surfaces (geometry CIII) in Figure 5.10, an approximate range of 450-680 kV/cm is found. These levels are very similar to those found in open oil gaps in section 4.2.2, where the range of applied fields that resulted in uniform-field breakdown of the oil was 515-765 kV/cm.

In both non-uniform geometries, the applied field required to initiate breakdown was always lower with a spacer between the electrodes. The minimum applied field inducing breakdown in an open oil gap was ~405 kV/cm (pin-plane electrodes), and the maximum field was ~390 kV/cm for a type III PP surface (collar-plane electrodes). In all cases, higher fields were required to initiate breakdown in collar-plane geometry.

Post-test inspection revealed clear visible surface-discharge damage on all of the samples. This damage was restricted to one location around the circumference of the sample, dictated by the position of the pin, for samples tested with high-voltage electrode type A. Despite being initiated from the same point however, the

discharges did not all follow an identical path from the tip of the high-voltage pin to the earth plane. Damage was found in at least two different locations around the circumference of each of the samples tested with high-voltage electrode type B (collar), indicating that subsequent surface discharges did not all follow the path established by the first discharge. It is anticipated that each different path followed by the discharge would result in a different time to breakdown, and hence a different breakdown voltage, contributing to the variations in breakdown voltage and time observed in sections 5.1 and 5.2.

For PP, LDPE, and UHMWPE, damage took the form of surface traces (see Figure 5.17a – Figure 5.17c), where it appears that the discharges cause penetration of the top layer of the sample surface, most likely through melting, and ablate material around the discharge channel. The visible surface damage was more severe on the PP samples (Figure 5.17c) when compared with the LDPE and UHMWPE samples. Pinhole puncture marks were visible at both ends of several of the samples, indicating that some bulk sample breakdowns had also taken place (see Figure 5.17f). Such damage was apparent on three of the four PP samples, and the only material that did not suffer bulk breakdown damage in at least one of the tests was LDPE.

The Rexolite (Figure 5.17d) and Torlon (Figure 5.17e) samples were found to be the most severely damaged, with large parts of material removed from the surface-discharge locations. This resulted in all four Rexolite samples being fractured into two main sections through the bulk of the material. The occurrence of bulk breakdown events is likely to have shortened some of the average times to breakdown recorded in Tables 5.2 and 5.4, compared to what would be expected if only surface flashover had occurred (as for the LDPE samples). The data presented in Table 5.4 provide an indication of how the time to breakdown was affected as the various tests progressed. The type III Rexolite sample tested with high-voltage electrode type B, for example, shows a reduction in time to breakdown of over 75% for shots 18-35 compared to the average time to breakdown for shots 1-17. The

major mechanical damage to the Rexolite and Torlon samples suggests that these materials are not appropriate choices for insulation under the conditions studied.

Post-test visual observation of the samples, and analysis of the pre-breakdown time delays, revealed that surface flashover was the only breakdown mode for the initiation measurements reported in section 5.3, and the primary breakdown mode for the over-voltage non-uniform field measurements reported in section 5.1. Although one or two surface flashover events were observed initially, repeated measurements in over-volted plane-parallel gaps (section 5.2) were restricted by the occurrence of bulk solid breakdown events, characterised by a sharp drop in the time to breakdown from several hundred nanoseconds to below 80 ns.

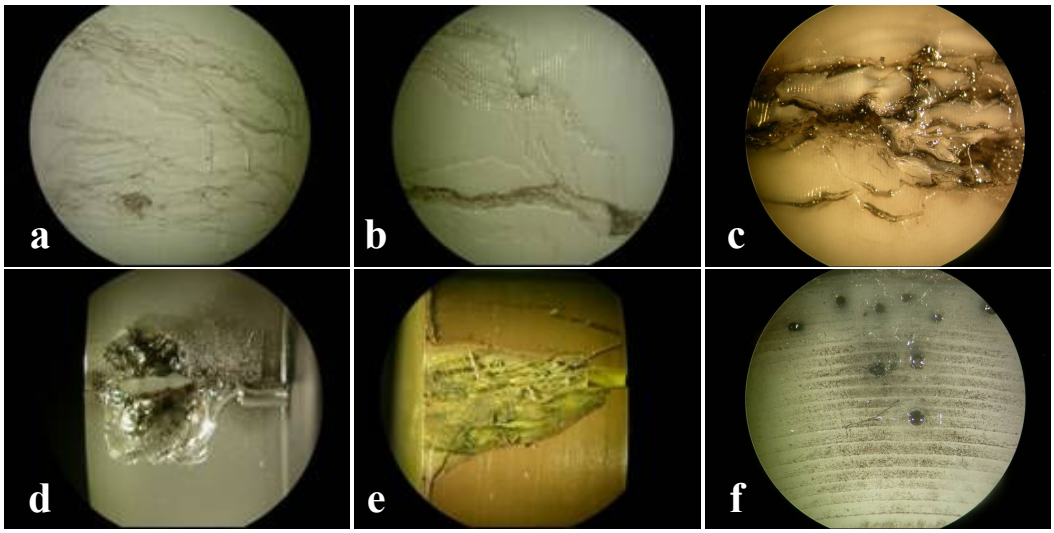

Figure 5.17. Photographs of type I sample surfaces following treatment with high-voltage electrode type A (pin) in section 5.1. a – LDPE; b – UHMWPE; c – PP; d – Rexolite; e – Torlon; f – PP surface in contact with the earthed electrode. a-c: magnification ×20 to show surface tracking; d-e: magnification ×10 to show surface damage; f: magnification ×40 to show pinhole puncture marks.

Data on the time to breakdown are important in determining the shape of impulse that can be applied to a given length of insulator without inducing a breakdown event, and the longer times to breakdown shown by UHMWPE in both types of

measurement suggest that this material could potentially hold off breakdown for longer than the other materials for the same level of applied voltage.

Rzad *et al*. [121] report the existence of a defined minimum voltage on the tail of an impulse, below which streamers cannot propagate to the point of breakdown. In general, the maximum pre-breakdown time delays recorded here are shorter than 600 ns; that is, breakdown occurs before the impulse voltage has fallen to half of the peak voltage.

In the over-volted gap measurements reported in section 5.1, the pre-breakdown delay times are generally less than 200 ns. At such short time intervals and high *dV/dt* (4 kV/ns), a streamer breakdown mechanism can be assumed. The minimum delay times recorded were of the order of 30-40 ns, translating to average streamer propagation velocities in excess of 250 km/s. Streamer velocities up to 300 km/s in mineral oil have previously been measured by Lesaint and Massala [167], who found that such fast streamers could be observed through the inclusion of a solid pressboard surface parallel to the electric field, in a similar arrangement to the non-uniform field geometries utilised in the present study. Lesaint and Massala achieved these measurements in a 10-cm point-plane gap, with a steel point of radius 100 μm forming the high-voltage electrode. It should be noted that the fastest breakdown times in the present study were recorded towards the end of the over-voltage test series (section 5.1) for Rexolite and Torlon samples, and would have occurred after the solid material had suffered considerable damage (Figure 5.17d and Figure 5.17e).

Cumulative failure probability distributions were produced for both the applied voltage data and the breakdown voltage data obtained in breakdown initiation measurements. Some data were best described by two-parameter Weibull distributions, suggesting that the breakdown strength will steadily decrease with increasing shot number. For those data with a positive-value location parameter γ, this suggests that there is a minimum voltage/field value below which breakdown will not occur independent of shot number [163]. The minimum field value is highest for PP for all applied field plots, and for two of three breakdown plots, BIII

being the exception. The Weibull plots for high-voltage electrode type B (collar) were generally of shallower gradient than for high-voltage electrode type A (pin), suggesting that the probability of breakdown was more sensitive to increases in applied voltage for the pin geometry compared with the collar geometry. Comparing data for the pin-plane and collar-plane geometries in Table 5.5, higher applied voltages were clearly required to initiate the first flashover with high-voltage electrode type B (collar), suggesting that the field enhancement provided by the pin was greater than that provided by the collar.

When designing a high-voltage system, the length of the insulator should be chosen using information on the known maximum operating voltage of the system and its temporal behaviour, so that the maximum electric-field stress does not exceed a value significantly lower than the mean average applied field threshold for breakdown. This could lead to a reduction in downtime for multi-megavolt systems. The values of γ obtained for the applied voltages (Table 5.7) using Weibull statistical analysis in section 5.4 provide an estimate of the applied voltage below which breakdown will not occur for a given solid dielectric material, and PP shows the highest values of γ for all tested configurations.

Chapter 6

SURFACE BREAKDOWN EVENTS ON THE WAVE-FORM RISING EDGE

6.0 INTRODUCTION

After studying the performance of the five materials when subjected to fast-rising impulses in Chapter 5, experiments were performed in order to compare their performance with breakdown occurring only on the rising edge. This involved the application of impulses of longer rise-time (1 μs), achieved by deploying the second experimental arrangement described in section 3.5.2, in order to remove the variable delay time to breakdown discussed in Chapter 5. The experimental results obtained and detailed statistical analyses from this investigation are presented in this chapter.

6.1 EXPERIMENTAL METHOD

The circuit shown schematically in Figure 3.13 was employed to produce impulses of rise-time ~1 μs and a fall-time to half peak value of 6.5 μs. The peak impulse voltage was −350 kV for all shots. As described in Chapter 5, the high-voltage output of the Marx generator was connected to the oil-immersed test cell, and breakdown events were studied with solid samples held between a pair of electrodes. The five different electrode/sample topologies depicted in Figure 3.7 were again utilised to provide non-uniform and uniform field distributions. The input impedance of the liquid-resistive voltage divider was 10 kΩ for all measurements presented in this chapter, as discussed in section 3.5.2.

Five test series were conducted, each of which involved subjecting a solid sample of each material to a number of impulse voltages and recording the breakdown voltages

and corresponding times to breakdown in each case. The electrodes were removed and polished between every sample tested in the sequence.

Sample lengths were chosen such that breakdown events would occur on the rising edge of every applied impulse. For non-uniform field measurements, the samples were 11.5 mm long, giving an inter-electrode gap of 8.5 mm, and thus corresponding with the inter-electrode gap lengths used in section 5.1. For uniform-field measurements (plane-parallel electrodes), the sample/inter-electrode gap length was 4 mm, this being the maximum length at which breakdown events could be guaranteed to occur only on the rising edge. All samples were pre-treated and handled according to the protocol described in section 3.3.2. The time between impulse applications was again five minutes.

6.2 NON-UNIFORM FIELDS

Type I (recess) and type II (shoulder) samples of each material were tested with high-voltage electrode type A (pin); and type II (shoulder) and type III (no modifications) samples were tested with high-voltage electrode type B (collar). For each test series, the sample was subjected to 35 impulse voltage applications, thus corresponding with the procedure in section 5.1.

As in Chapter 5, the electrode/sample combinations have been labelled as follows for ease of reference:

- AI for pin/recess
- AII for pin/shoulder
- BII for collar/shoulder
- BIII for collar/no modifications

6.2.1 Breakdown Voltage

Average values have been calculated for the breakdown voltage for the different experimental geometries and materials, and these are shown in Table 6.1. The standard deviation has again been calculated using equation (4.1) (see section 4.2.1) throughout this chapter. These data confirm that the breakdown voltages were generally higher with the type A (pin) high-voltage electrode when compared to those observed using the type B (collar) electrode.

Table 6.1. Average breakdown voltages and standard deviation (± values) for non-uniform field measurements.

Electrode Geometry	Type A (Pin)	Type A (Pin)	Type B (Collar)	Type B (Collar)
Sample Geometry	Type I (Recess)	Type II (Shoulder)	Type II (Shoulder)	Type III (No mods.)
PP	338±18 kV	337±7 kV	314±12 kV	310±20 kV
LDPE	346±8 kV	341±14 kV	340±18 kV	301±21 kV
UHMWPE	338±11 kV	356±9 kV	326±23 kV	305±12 kV
Rexolite	239±66 kV	283±19 kV	245±50 kV	195±65 kV
Torlon	222±30 kV	220±30 kV	227±27 kV	225±36 kV

As in Chapter 5, the mean breakdown voltage data over shots 1-17 and shots 18-35 were also analysed separately, and this information is presented in Table 6.2. Analysis of this data reveals that the average breakdown voltage was fairly consistent over the two data sets for samples of PP, LDPE, UHMWPE, and Torlon, for all experimental geometries. A decrease in average breakdown voltage over shots 18-35 compared to that for shots 1-17 was normally observed for Rexolite samples. The maximum value of this decrease was ~35% for geometries AI and BIII.

The average breakdown voltage under the pin-plane geometry was found to be very similar between the two types of tested sample for all five materials. Comparing the average data for breakdown events measured under collar-plane geometry, however, it is clear that the breakdown voltages for the type III (no modifications) samples are lower than those observed for the type II (shoulder) samples. This suggests that the

addition of the shoulder in the type II samples acts to increase the breakdown voltage compared to the unmodified cylindrical samples. Importantly, as breakdown occurs on the rising edge, this means that the time to breakdown is increased by the addition of the shoulder. This is in contrast to the results reported in Chapter 5, where the addition of the shoulder resulted in a reduction in the delay time to breakdown, with breakdown occurring on the falling edge of the impulse.

It should be noted that the calculated values for the standard deviation of the breakdown voltage are relatively large, particularly for the Rexolite samples (for example, 195±65 kV for geometry BIII). The average values of the breakdown voltage indicate a broadly similar breakdown performance for the PP, LDPE and UHMWPE samples for all experimental geometries. The Rexolite and Torlon samples perform relatively poorly, with significantly lower values of average breakdown voltage.

Table 6.2. Average breakdown voltages and standard deviation (± values) over shots 1-17 and shots 18-35 for non-uniform field measurements.

Electrode Geometry		Type A (Pin)	Type A (Pin)	Type B (Collar)	Type B (Collar)
Sample Geometry		Type I (Recess)	Type II (Shoulder)	Type II (Shoulder)	Type III (No mods.)
PP	Shots 1-17	333±24 kV	338±8 kV	317± 12kV	312± 23kV
	Shots 18-35	343±6 kV	336±7 kV	311±11 kV	309±18 kV
LDPE	Shots 1-17	346± 9kV	333±17 kV	351±6 kV	312± 18kV
	Shots 18-35	345±7 kV	348±5 kV	331±20 kV	290±18 kV
UHMWPE	Shots 1-17	336± 14kV	346± 11kV	334± 15kV	307± 11kV
	Shots 18-35	339±7 kV	345±6 kV	318±27 kV	303±13 kV
Rexolite	Shots 1-17	295± 44kV	278±21 kV	265± 60kV	241± 58kV
	Shots 18-35	186±29 kV	288±17 kV	226±27 kV	152±35 kV
Torlon	Shots 1-17	227± 30kV	215± 39kV	230± 36kV	227± 42kV
	Shots 18-35	217±31 kV	225±17 kV	224±13 kV	223±30 kV

As in Chapter 5, it was also interesting to analyse the variation in breakdown voltage on a shot-to-shot basis. Again the behaviour for one configuration (type A electrode with type I sample geometry) illustrating typical sample behaviour has been included

below to facilitate discussion. The corresponding graphs for the other three non-uniform configurations (AII, BII, BIII) are included in *Appendix H* for reference. The graphs for all four configurations have a similar form. For configuration AII (Figure H.1), it is expected that the lower breakdown voltages, at around 180 kV, correspond with bulk solid breakdown events, as will be discussed in section 6.5.

The results of Figure 6.1 show how the magnitude of the breakdown voltage was found to vary over the course of the test for configuration AI. Low-density polyethylene showed a relatively flat curve in this configuration, with breakdown voltages consistently in the range 330-350 kV, corresponding with breakdown occurring around the peak of the impulse. Polypropylene and UHMWPE exhibited some initial variation in breakdown voltage, but settled at around the same level as LDPE towards the end of the test. Rexolite and Torlon both exhibited a significant drop in breakdown voltage after a few discharges, ending up at around half the voltage of the other materials. A wide variation in breakdown voltage was apparent after breakdown number 10 with Rexolite and Torlon samples, suggesting the occurrence of competing breakdown processes.

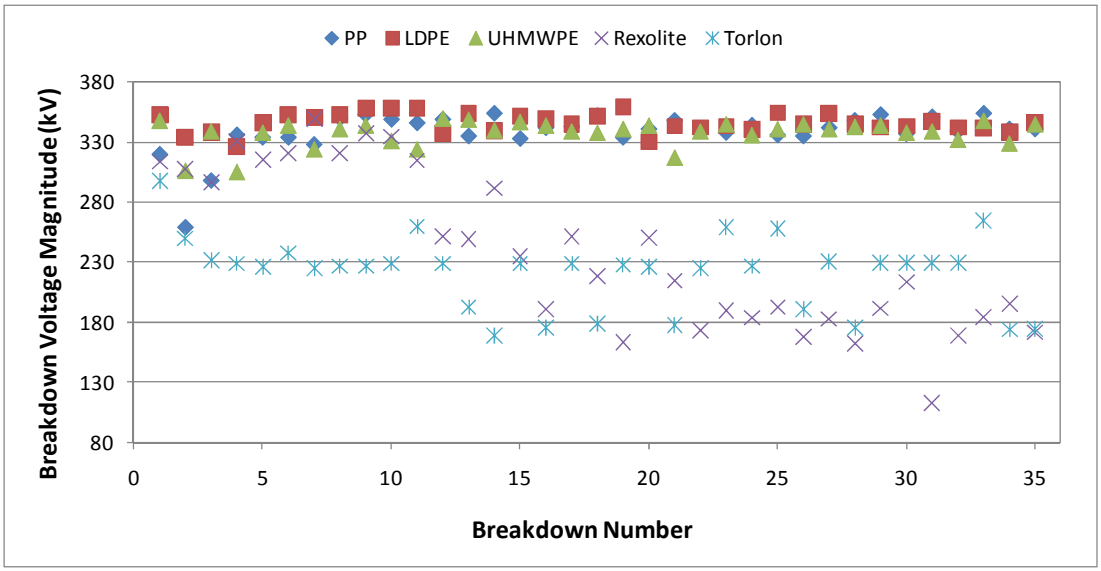

Figure 6.1. Breakdown voltage magnitude versus breakdown number for high-voltage electrode type A (pin) and sample type I (recess).

6.2.2 Time to Breakdown

In addition to the breakdown voltage data, the associated time-to-breakdown data can be used to calculate an indicative average streamer propagation velocity, which can in turn be used to reveal information about the mode of breakdown and how this varies with an increasing number of applied impulses. The shape of the impulse, with a relatively long period of time spent around peak voltage (refer to Figure 3.14), also means that the time to breakdown can vary for the same breakdown voltage.

Despite the consistent breakdown voltages for PP, LDPE, and UHMWPE samples tested with high-voltage electrode type A (pin), there is considerable variation in the time-to-breakdown data in Figure 6.2 (configuration AI). This may be associated with variation in the statistical delay time associated with initiatory electron production. Alternatively, the variation in time to breakdown may be as a result of variation in the formative time lag due to the propagation of streamers in different modes. The variation in time to breakdown does not translate to the breakdown voltage curves as the breakdown events all occur around the relatively flat impulse peak for these materials.

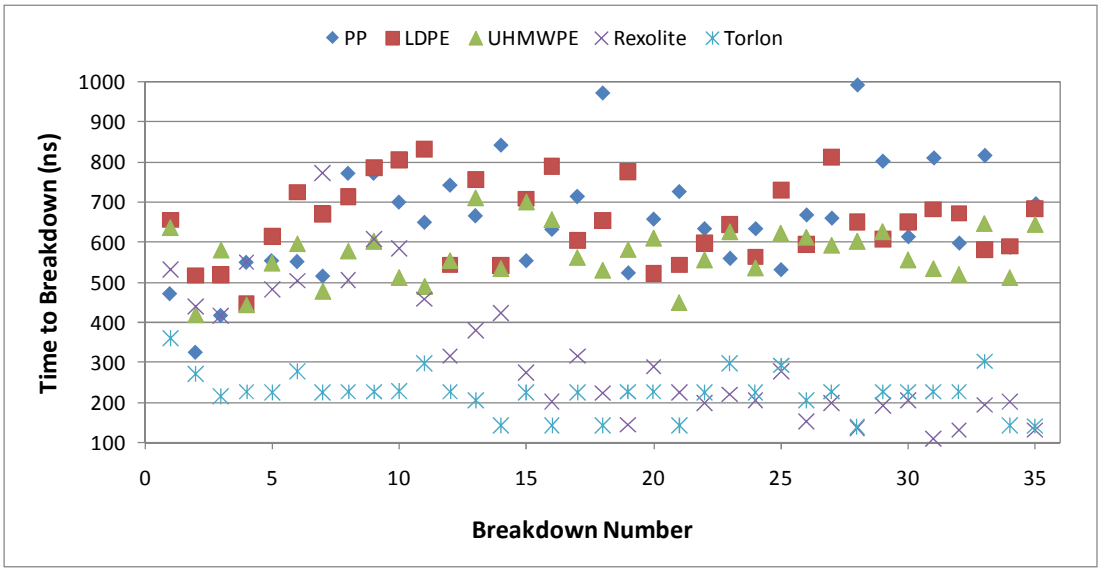

Figure 6.2. Time to breakdown versus breakdown number for high-voltage electrode type A (pin) and sample type I (recess).

The graphs presented in *Appendix I* showing time to breakdown versus breakdown number for the other electrode/sample configurations (AII, BII, BIII) have a similar form to that for the AI configuration.

Average time-to-breakdown values and their standard deviation have been calculated, and these data are presented in Table 6.3. Excepting the AI geometry, the time to breakdown is more consistent for PP than LDPE; the standard deviation varies from 12-16% of the average time to breakdown for PP, compared to 23-33% for LDPE. The time to breakdown for Rexolite and Torlon samples was consistently lower than that for the other three materials, at less than 400 ns for most breakdown events. The standard deviation exceeds 50% of the average time to breakdown for the type I Rexolite sample under pin-plane geometry.

Table 6.3. Average times to breakdown and standard deviation (± values) for non-uniform field measurements.

Electrode Geometry	Type A (Pin)	Type A (Pin)	Type B (Collar)	Type B (Collar)
Sample Geometry	Type I (Recess)	Type II (Shoulder)	Type II (Shoulder)	Type III (No mods.)
PP	655±141 ns	541±65 ns	453±63 ns	448±71 ns
LDPE	651±97 ns	677±155 ns	716±195 ns	415±138 ns
UHMWPE	570±68 ns	659±99 ns	542±138 ns	412±35 ns
Rexolite	320±169 ns	360±52 ns	306±152 ns	220±142 ns
Torlon	224±52 ns	225±55 ns	247±58 ns	247±70 ns

The average time to breakdown data has also been analysed separately over shots 1-17 and over shots 18-35, and this information is presented in Table 6.4. Some variation in the average time to breakdown was found for the LDPE samples: for geometry AII, the average time to breakdown based on shots 18-35 was almost 30% longer than that based on shots 1-17; for geometries BII and BIII however, the average time to breakdown based on shots 18-35 was 20-30% shorter than that based on shots 1-17. The average time to breakdown for Rexolite samples was also generally shorter based on the data for shots 18-35 compared to shots 1-17.

Table 6.4. Average times to breakdown and standard deviation (± values) over shots 1-17 and shots 18-35 for non-uniform field measurements.

Electrode Geometry		Type A (Pin)	Type A (Pin)	Type B (Collar)	Type B (Collar)
Sample Geometry		Type I (Recess)	Type II (Shoulder)	Type II (Shoulder)	Type III (No mods.)
PP	Shots 1-17	614± 138ns	550± 79ns	481± 66ns	459±89 ns
	Shots 18-35	694± 137ns	533± 50ns	427±47 ns	438±47 ns
LDPE	Shots 1-17	661± 117ns	589±147 ns	854±139 ns	464±184 ns
	Shots 18-35	642± 77ns	760±114 ns	586±145 ns	368±34 ns
UHMWPE	Shots 1-17	565± 82ns	672±112 ns	576±150 ns	422±39 ns
	Shots 18-35	575± 54ns	646±87 ns	509±122 ns	403±29 ns
Rexolite	Shots 1-17	457± 138ns	353±58 ns	375±192 ns	301±161 ns
	Shots 18-35	191± 49ns	367±46 ns	241±49 ns	144±55 ns
Torlon	Shots 1-17	233± 51ns	225±74 ns	258±79 ns	255±82 ns
	Shots 18-35	215± 53ns	226±30 ns	238±25 ns	239±57 ns

6.2.3 Volt-time Plots

In selecting one of the five materials for use as an oil-immersed insulator, it is important to consider the relative variation in breakdown voltage as well as its magnitude. In order to illustrate the trade-off between high breakdown voltages and predictability of time to breakdown, and also to provide data in a convenient form for comparison with existing data in the literature, the results have been plotted in the form of Volt-time (V-t) plots.

For example, it is clear from Figure 6.3 that although the data points for type I LDPE and UHMWPE are clustered at around peak voltage, the range of breakdown times is wide, at around 300 ns for UHMWPE and 400 ns for LDPE.

Volt-time plots for the remaining configurations (AII, BII, BIII) are included for reference in *Appendix J*. The plots are broadly similar to that in Figure 6.3, although for configuration AII, the UHMWPE data points are spread over a wider range of 500 ns, and the LDPE data points over a 600-ns range. There exists significant clustering of the Rexolite data points at around 280 kV and 350 ns for configuration AII, but any advantage offered by a predictable point of breakdown is offset by the poor physical condition of the sample at the end of the test. As well as the impact on

the insulation integrity, this could additionally lead to mechanical instability if undiscovered in large-scale industrial machines which are fully immersed in insulating oil.

For configuration BII, there exists a cluster of PP data points at around 300 kV and 450 ns, indicating a relatively predictable point of breakdown. It is interesting to note that although the breakdown voltage for both polyethylene materials was generally higher than that for PP, the time to breakdown was considerably more stable for PP. As discussed in relation to V-t plots in section 5.1.3, this again poses the question of whether a material with a more predictable time to breakdown is a more appropriate choice than a material with a higher average breakdown voltage – this will be discussed further in section 6.5, following the Weibull statistical analysis of the non-uniform field data presented in section 6.4.

The reduced breakdown times for configuration BIII are obvious on inspection of Figure J.3, with all but three breakdown events occurring within 600 ns; the breakdown times greater than 600 ns correspond with the first breakdown event for PP, LDPE, and Rexolite samples.

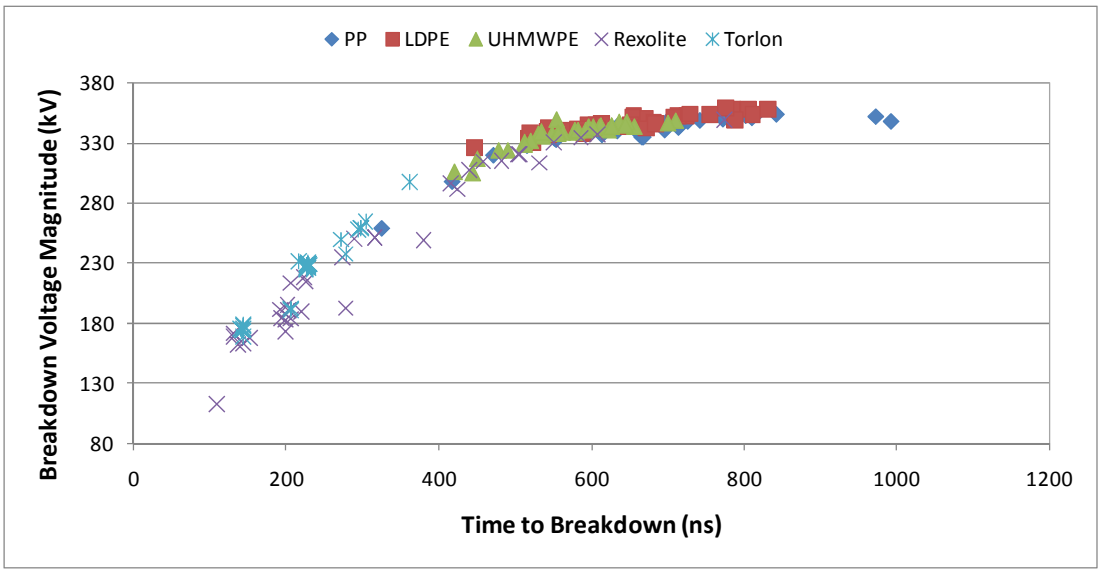

Figure 6.3. Volt-time plot for surface flashover along type I (recess) samples with high-voltage electrode type A (pin).

6.3 UNIFORM FIELDS

Type III (no modifications) samples of each material were tested with high-voltage electrode type C (plane) to provide uniform-field conditions, and the results are displayed in Figure 6.4. The flashover behaviour in general was difficult to determine in this regime due to the occurrence of bulk solid breakdown events at an early stage in the tests. As in section 5.2, the number of impulse applications was thus limited accordingly, this time to 10. The breakdown voltage for LDPE steadily reduced from breakdown number five onwards as bulk solid breakdown behaviour began to dominate, characterised by shorter times to breakdown and corresponding lower breakdown voltages. The breakdown voltage for the other materials varied significantly over the first five breakdown events, and thereafter appeared to level out over breakdown numbers 6-10.

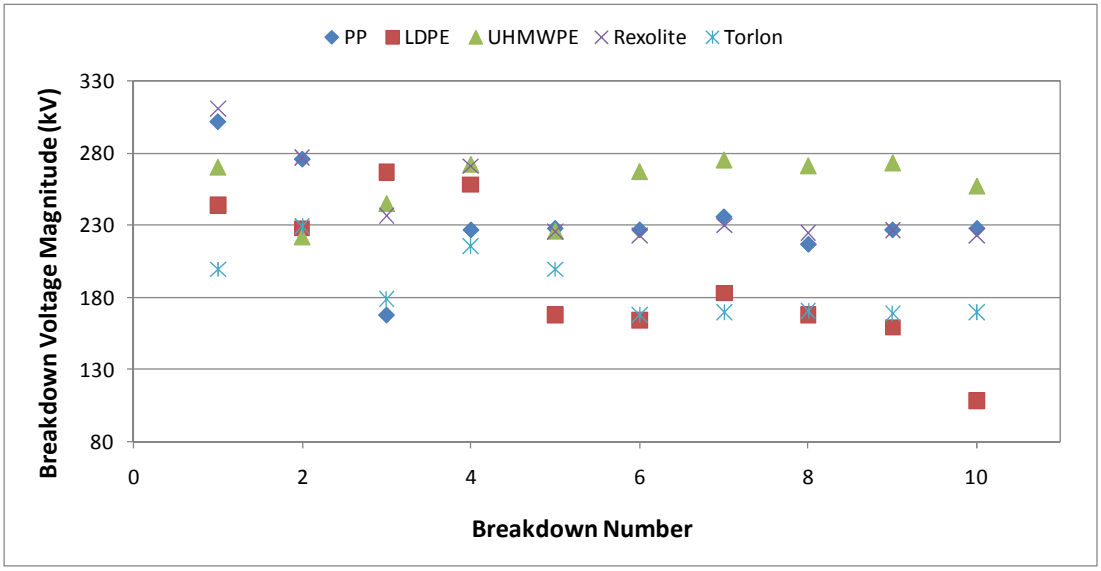

Figure 6.4. Breakdown voltage magnitude versus breakdown number for high-voltage electrode type C (plane) and sample type III (no modifications).

Ultra-high molecular weight polyethylene clearly had the highest breakdown voltages based on the data for breakdown numbers 6-10, and the average breakdown field over all ten breakdown events was 645±50 kV/cm for this material, the highest

of the five tested materials. This is around 1.5-times higher than the highest average breakdown field for UHMWPE in non-uniform field tests.

Figure 6.5 shows time to breakdown versus breakdown number data for all five materials. The shorter times to breakdown when compared with those under non-uniform field geometries can be attributed to the shorter inter-electrode gap length of 4 mm. The time to breakdown appears to be more consistent after breakdown number 5 for all materials, suggesting a consistent breakdown mechanism for the later discharges.

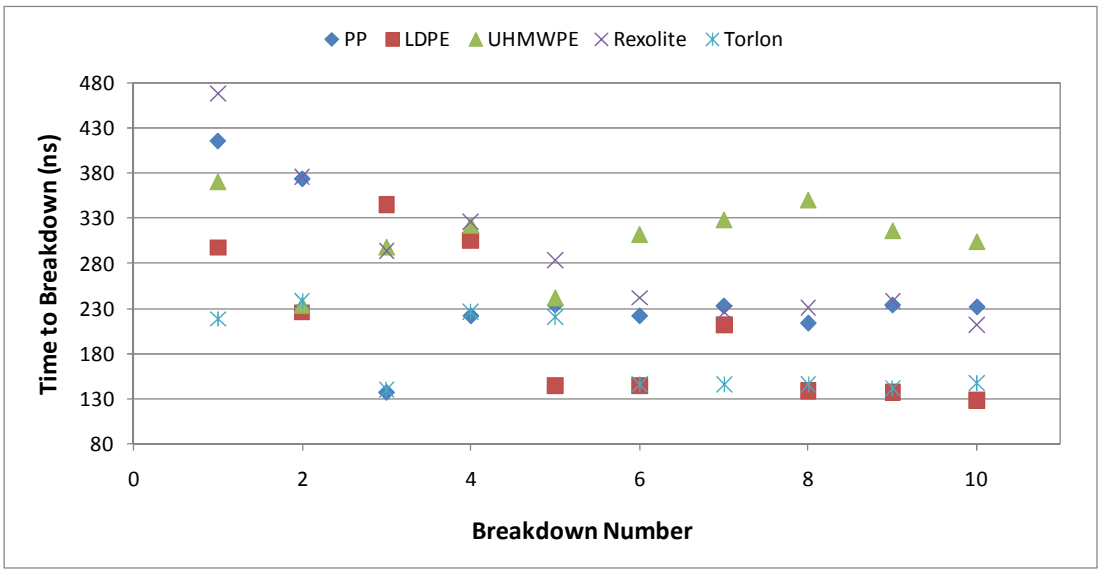

Figure 6.5. Time to breakdown versus breakdown number for high-voltage electrode type C (plane) and sample type III (no modifications).

The data are represented as V-t plots in Figure 6.6, which appears to show several discrete clusters of data points, possibly corresponding with different modes of breakdown, which will be explored further in section 6.5.

The average breakdown voltage and time to breakdown data are presented in Table 6.5. The average breakdown voltage and average time to breakdown over shots 1-5 and over shots 6-10 have also been calculated separately, and this

information is presented in Table 6.6. It is noteworthy that the standard deviation values for both the breakdown voltage and time to breakdown decrease significantly over shots 6-10 compared to shots 1-5. The values of average breakdown voltage and average time to breakdown were both observed to be higher for shots 6-10 than for shots 1-5 for UHMWPE.

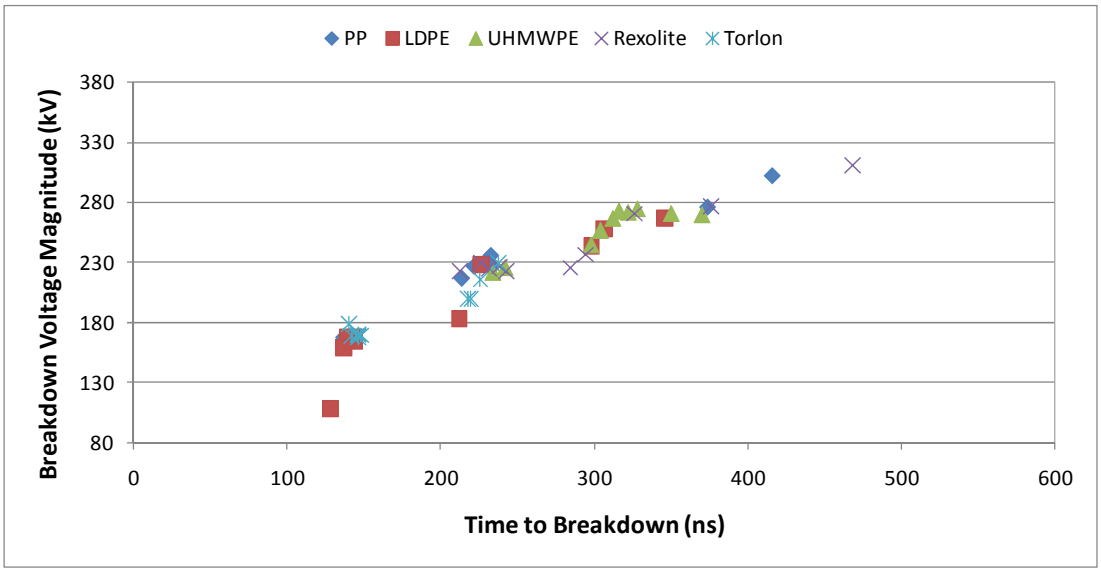

Figure 6.6. Volt-time plot for surface flashover along type III (no modifications) samples with high-voltage electrode type C (plane).

Table 6.5. Average breakdown voltages, times to breakdown, and standard deviation (± values) for uniform-field measurements.

Material	Breakdown Voltage	Time to Breakdown
PP	234±35 kV	252±82 ns
LDPE	195±52 kV	208±83 ns
UHMWPE	258±20 kV	308±42 ns
Rexolite	245±31 kV	290±81 ns
Torlon	187±23 kV	177±42 ns

Bulk breakdown damage was observed on all samples, and as there was a change in the breakdown mechanism, with bulk breakdowns occurring after a relatively low

number of shots under these conditions, no attempt has, therefore, been made to produce Weibull plots of these data.

Table 6.6. Average breakdown voltages, times to breakdown, and standard deviation (± values) over shots 1-5 and shots 6-10 for uniform-field measurements.

Material	Shots	Breakdown Voltage	Time to Breakdown
PP	1-5	240±52 kV	277±115 ns
	6-10	227±7 kV	227±9 ns
LDPE	1-5	233±39 kV	264±80 ns
	6-10	156±29 kV	152±34 ns
UHMWPE	1-5	247±24 kV	293±57 ns
	6-10	269±7 kV	322±18 ns
Rexolite	1-5	264±34 kV	350±75 ns
	6-10	226±3 kV	230±12 ns
Torlon	1-5	205±19 kV	208±39 ns
	6-10	170±1 kV	146±2 ns

6.4 WEIBULL STATISTICAL ANALYSIS

6.4.1 Breakdown Voltage Data

The breakdown voltage data presented in section 6.2 were subjected to a Weibull statistical analysis, following the procedure described in section 5.4. A two-parameter distribution, described by equation (5.3) (section 5.4), was found to best describe most of the data. Values of the scale parameter α and the shape parameter β for the four non-uniform field geometries are listed in Table 6.7.

Figure 6.7 shows Weibull plots of the breakdown voltage data for type I (recess) samples tested with high-voltage electrode type A (pin). It can be seen that the plots for PP, LDPE and UHMWPE all follow a reasonably linear behaviour. The plots for Rexolite and Torlon deviate markedly from the behaviour expected from flashovers following a process modelled by the Weibull distribution.

Table 6.7. Weibull distribution parameters for breakdown voltage data.

		MATERIAL				
		PP	LDPE	UHMWPE	Rexolite	Torlon
Pin/ Recess (AI)	Scale α (kV)	346	349	343	264	236
	Shape β	29.7	50.2	35.2	3.87	7.50
Pin/ Shoulder (AII)	Scale α (kV)	340	348	349	292	234
	Shape β	51.3	26.7	67.2	15.3	7.18
Collar/ Shoulder (BII)	Scale α (kV)	320	349	337	264	240
	Shape β	28.4	20.3	15.8	5.36	8.46
Collar/ No mods. (BIII)	Scale α (kV)	320	311	311	217	241
	Shape β	16.8	15.2	33.1	3.30	6.66

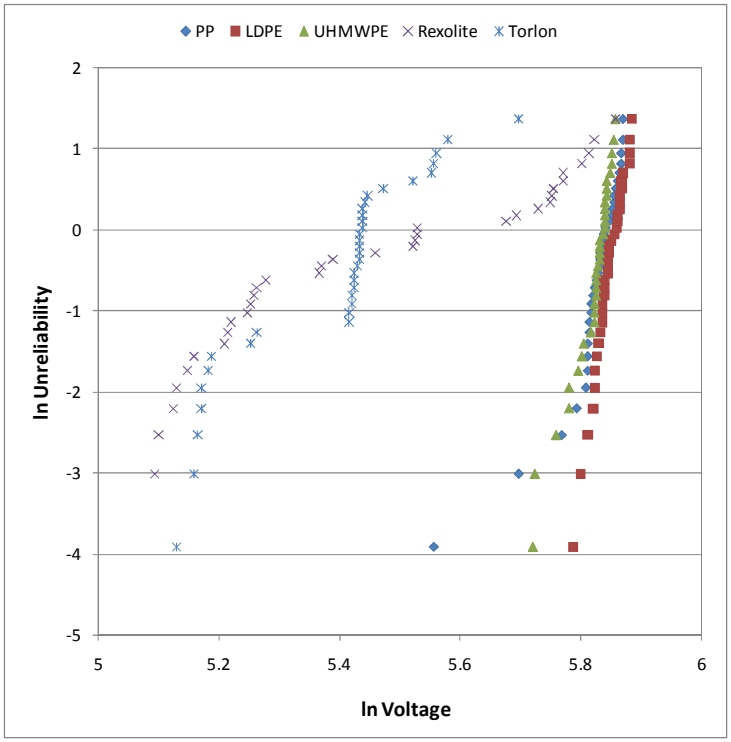

Figure 6.7. Weibull plots of breakdown voltage data for type I (recess) samples tested with high-voltage electrode type A (pin).

The breakdown voltage data for UHMWPE have been isolated from Figure 6.7 for further analysis, and the Weibull plot is shown in Figure 6.8, where there appear to be two distinct regions characterising the breakdown behaviour. The change in

gradient observed for breakdowns that occur at lower voltages cannot be explained in terms of a three-parameter Weibull distribution, where it would be expected that the points would follow a curve. In addition, the value of the location parameter γ would have to be negative to bring the points onto a single line, which is physically unrealistic under these conditions, since a negative γ would suggest that breakdown could occur before the application of a voltage to the insulation system. The plot therefore suggests that there are two different processes occurring during the sequence of breakdown events.

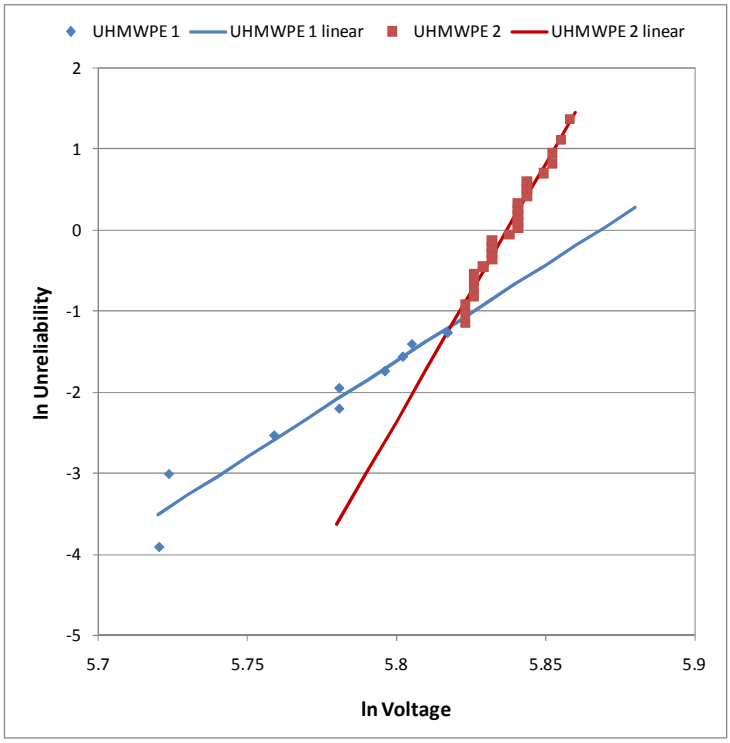

Figure 6.8. Weibull plot for type I (recess) UHMWPE sample tested with high-voltage electrode type A (pin). Two distinct linear regions are shown, suggesting two different breakdown mechanisms.

To determine if the observed change in breakdown behaviour was a result of cumulative damage or due to ageing of the solid UHMWPE surface, the plot of breakdown rank versus breakdown number shown in Figure 6.9 was examined. Breakdown rank, in this context, refers to the order of the 35 breakdown voltages when organised from highest (rank 35) to lowest (rank 1). From Figure 6.9 it can be

seen that there is no correlation between shot number and the corresponding rank of the breakdown voltage. Furthermore, there was no evidence of bulk breakdown events having occurred in the PP, LDPE, or UHMWPE samples.

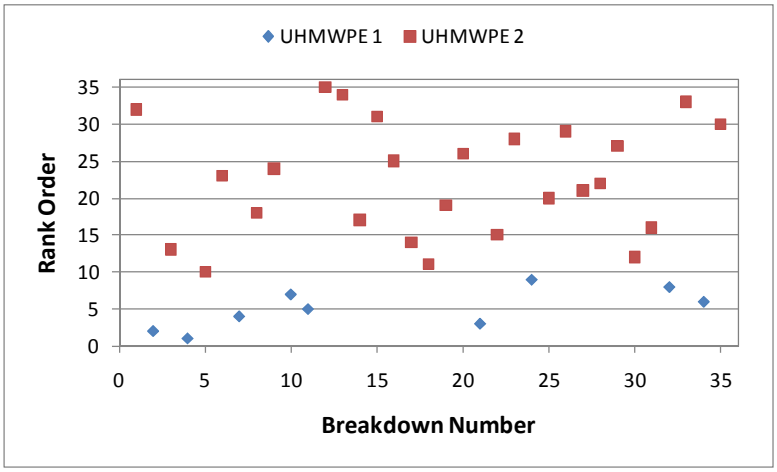

Figure 6.9. Plot of breakdown voltage rank versus breakdown number for type I (recess) UHMWPE sample tested with high-voltage electrode type A (pin). Blue diamonds and red squares correspond to the two different behaviours identified using the same symbols in Figure 6.8.

The behaviour of the Weibull plot for Rexolite (Figure 6.10), again isolated from Figure 6.7, shows a more complicated structure, with two broadly straight line regions and a shoulder. The corresponding plot of breakdown voltage rank versus shot number (Figure 6.11) shows two regions, an initial region for low breakdown numbers – *Rexolite 2* in Figures 6.10 & 6.11 – where the breakdown voltage is constant or perhaps rising slightly, followed by a region where the breakdown voltage is decreasing as the sample material is repeatedly broken down – *Rexolite 1* on Figures 6.10 & 6.11. The behaviour for Rexolite suggests that some ageing process is occurring in the system as the sample is repeatedly broken down. A similar behaviour is observed for Torlon, although there is a greater drop in breakdown voltage observed between the two straight-line regions.

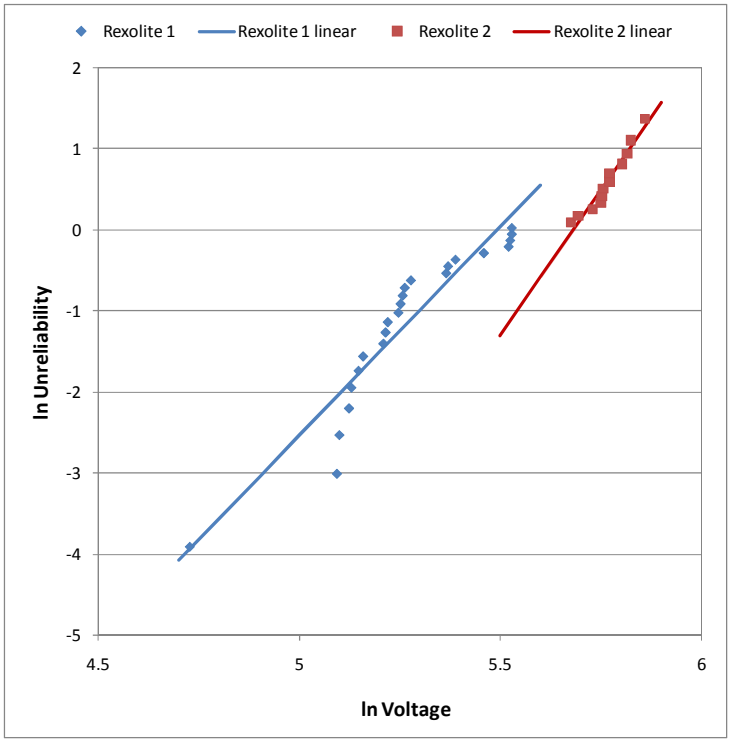

Figure 6.10. Weibull plot for type I (recess) Rexolite sample tested with high-voltage electrode type A (pin). Two distinct linear regions are shown, suggesting two different breakdown mechanisms.

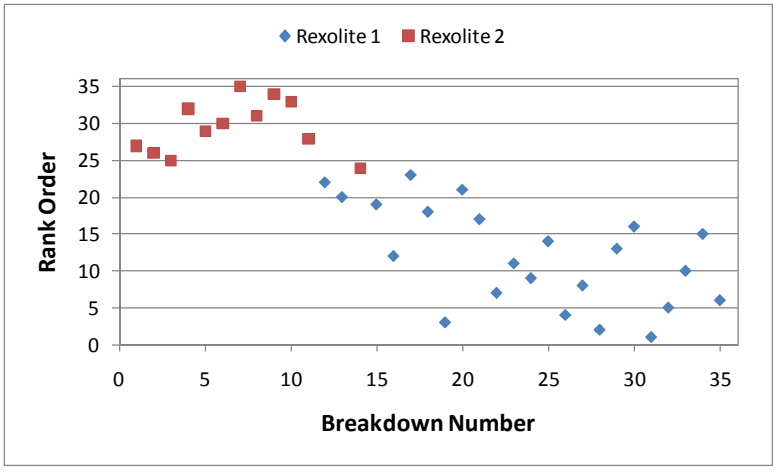

Figure 6.11. Plot of breakdown voltage rank versus shot number for type I (recess) Rexolite sample tested with high-voltage electrode type A (pin). Blue diamonds and red squares correspond to the two different behaviours identified using the same symbols in Figure 6.10.

A much clearer separation in the breakdown behaviour associated with the PP, LDPE and UHMWPE data is apparent in Figure 6.12, Weibull plots of the data for

configuration BII. In terms of the form of the traces, the curves are broadly similar when compared with the data associated with high-voltage electrode type A (pin). This suggests that the properties of the solid material have a greater influence on the initiation of streamers than the electrode geometry, for the materials and geometries investigated here.

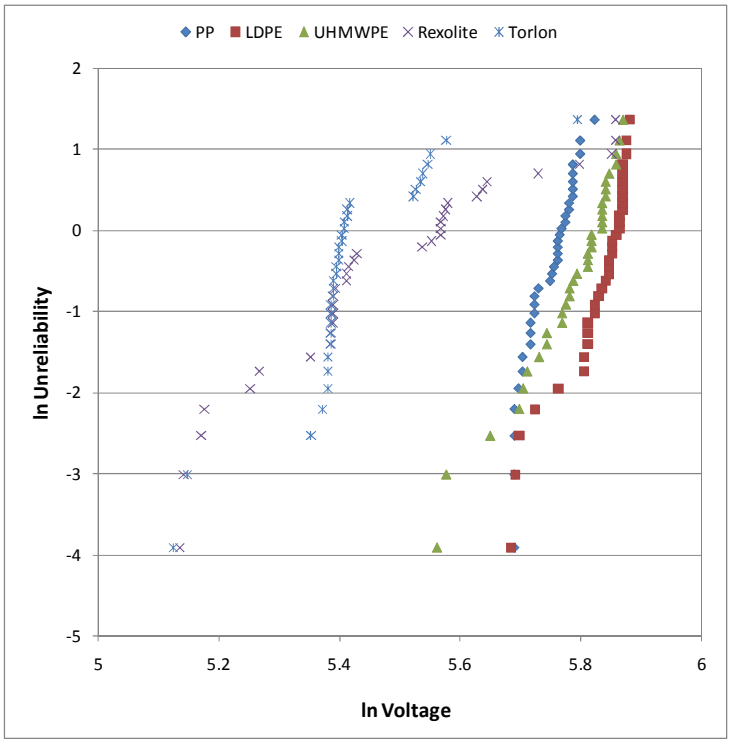

Figure 6.12. Weibull plots of breakdown voltage data for type II (shoulder) samples tested with high-voltage electrode type B (collar).

Torlon displays an interesting behaviour in Figure 6.12, and the plot for this material has been isolated and re-plotted in Figure 6.13. Whereas two linear regions were identified for UHMWPE and Rexolite samples in Figures 6.8 and 6.10 respectively, there appears to be a third region in the Torlon plot, as labelled in Figure 6.13. The point labelled *Torlon 4* is assumed to be a solitary outlier.

Figure 6.14 shows a plot of the breakdown rank versus breakdown number for the Torlon sample, but no obvious trend identifying an ageing process is apparent.

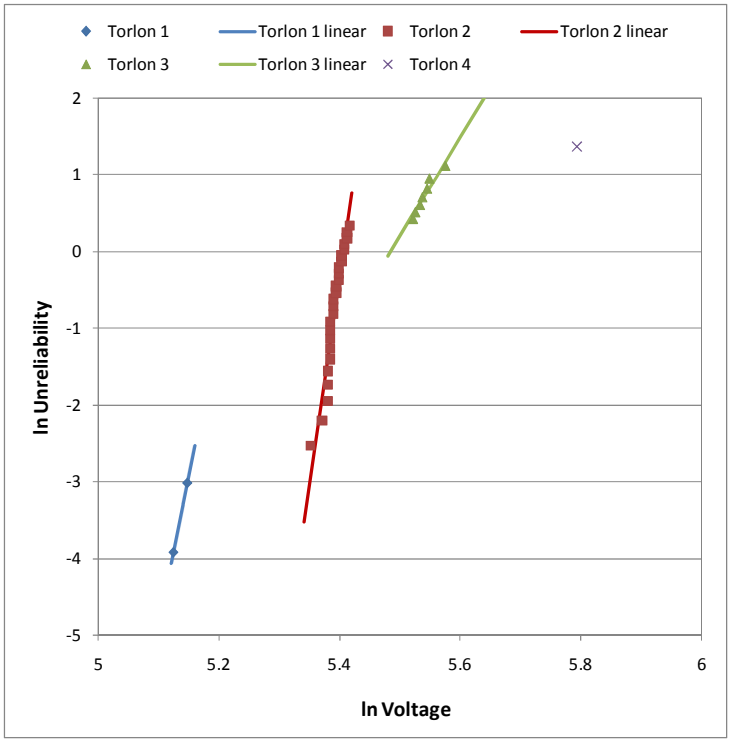

Figure 6.13. Weibull plot for type II (shoulder) Torlon sample tested with high-voltage electrode type B (collar). Three distinct linear regions are shown, suggesting at least three different breakdown mechanisms.

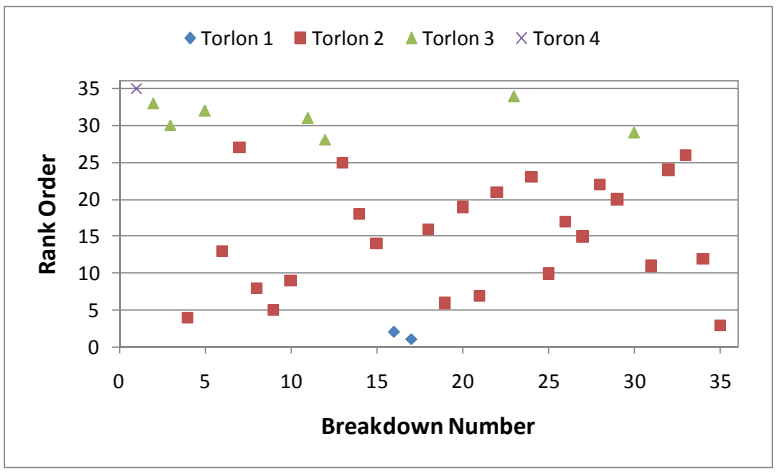

Figure 6.14. Plot of breakdown voltage rank versus shot number for type II (shoulder) Torlon sample tested with high-voltage electrode type B (collar). The different symbols correspond to the different behaviours identified using the same symbols in Figure 6.13.

The Weibull plots of the data for configurations AII and BIII are included in *Appendix K*. For configuration AII, the plots are broadly similar to those shown in Figure 6.7 for configuration AI. The data for PP fall closer to a straight line for configuration AII than for configuration AI. In the AI, AII, and BII geometries, the lower ranked breakdowns for LDPE and UHMWPE file on a line with a lower gradient than that for the higher ranked breakdowns, but the opposite effect is observed in configuration BIII. The behaviour for Rexolite and Torlon in configuration BIII shows similarities to the other three geometries in the form of the Weibull plots, but a more significant shift in the breakdown voltage is observed as the breakdown rank decreases.

6.4.2 Material Comparison

The experimental data have also been plotted as sorted by electrode geometry for each individual material. Figure 6.15 shows the Weibull plots for UHMWPE for the various electrode/sample geometries used. It can be seen that the breakdown voltages for the highest ranked breakdowns for the AI, AII, and BII configurations are similar in value. It appears that the breakdown voltages associated with the type A (pin) electrode are slightly higher than those for the type B (collar) electrode.

The Weibull plots for the other four materials are contained in *Appendix L*. The behaviour for PP and LDPE is broadly linear for all experimental conditions. In some cases a three-parameter Weibull distribution would bring the data points onto a single straight line, but as the curves are concave down this would require a negative value of the location parameter, an unrealistic notion for the reasons discussed previously. A large number of the LDPE data points for both pin geometries (AI and AII) and the collar/shoulder geometry (BII) appear on the same straight line, particularly for higher ranked breakdown events.

For Rexolite samples, there is a larger spread in the plots compared to those observed with UHMWPE. For the higher ranked breakdowns, it is not possible to separate the behaviour of the different geometries consistently. For the lower ranked breakdowns, the plots are more distinct. Unlike the results for UHMWPE, the

sample type is more significant, with the data for the type II (shoulder) samples being associated with higher breakdown voltages. Again, the combination of a type III (no modifications) sample and type B (collar) electrode leads to the lowest breakdown voltages in this regime.

The three different regimes identified for the type II Torlon sample in Figure 6.13 appear to be common to all four geometries. Likely reasons for the different behaviours will be discussed further in section 6.5, although this is thought to be related in part to a surface breakdown mechanism versus a bulk breakdown mechanism.

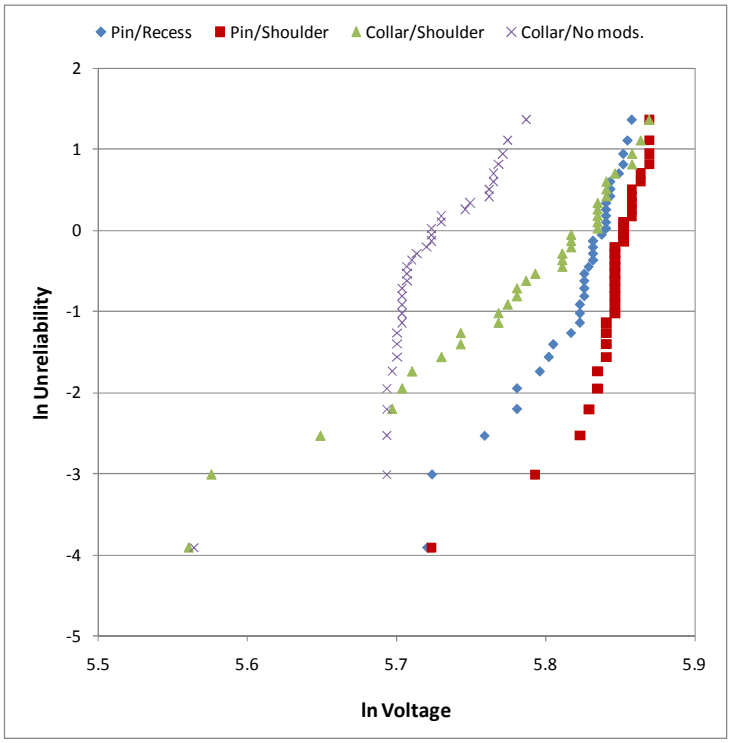

Figure 6.15. Weibull plots of UHMWPE breakdown voltages for the different experimental geometries.

Overall, the breakdown voltage for the combination of a type III (no modifications) sample with a type B (collar) electrode is distinctly lower than those for the other electrode/sample combinations. A much clearer separation in the breakdown

behaviour at lower ranked breakdowns is apparent, with higher values of breakdown voltage generally being observed for the pin geometries. The change of gradient between the higher and lower ranked breakdowns for the BIII geometry is distinct.

6.5 DISCUSSION AND CONCLUSIONS

The high-voltage impulse breakdown behaviour of five different types of dielectric solid immersed in mineral oil have been investigated in non-uniform and uniform fields under impulse voltages with a rise-time of 1 μs. The experimental conditions were designed in order that the breakdown events occurred on the rising edge of the voltage impulse.

The breakdown voltage was found to be increased by a maximum of 23% for the Rexolite material via the introduction of a shoulder on the sample geometry in Chapter 5. As discussed in section 5.5, this meant a reduction in the time to breakdown, and the overall influence of the introduction of a shoulder on the solid samples was difficult to determine with breakdown occurring on the falling edge. With breakdown occurring on the rising edge, it was found here that the average breakdown voltage was increased by up to 26% for the type II (shoulder) Rexolite sample compared to the type III (no modifications) Rexolite sample, tested with high-voltage electrode type B. The corresponding increase in the time to breakdown was almost 40% for the type II Rexolite sample. An increase in time to breakdown of over 70% was found for the type II (shoulder) LDPE sample compared to the type III (no modifications) LDPE sample. This data suggests that the introduction of a shoulder into the sample geometry can act to increase the delay time to breakdown by influencing the conditions for streamer initiation at the interface of the insulation system and the high-voltage electrode.

Post-test inspection of the samples treated under non-uniform field geometries revealed different aspects of behaviour: damage to PP, LDPE, and UHMWPE samples consisted of shallow surface traces; while significant amounts of material

was found to be removed from all Rexolite and Torlon samples, due to the propagation of discharges through the bulk of the solid as well as over the liquid-solid interface. This behaviour is reflected by the wide variation in breakdown voltage for both Rexolite and Torlon, as streamers propagate with varying time delay either over the liquid-solid interface, or directly through the bulk of the solid dielectric.

Analysing the data points presented for Torlon in Figure H.1 (*Appendix H*) for example, there appears to be two distinct breakdown voltage levels: one at 230 kV, which is expected to correspond with interfacial liquid-solid breakdown events; and one at 170 kV, which is expected to correspond to bulk solid breakdown events. Division of the inter-electrode gap length by the corresponding pre-breakdown delay times to produce average streamer propagation velocities yields two distinct regimes: a propagation velocity of ~60 km/s for the shorter delay times (170 kV voltage level); and a range of 30-40 km/s for the longer delay times (230 kV voltage level).

Furthermore, similar analysis of the pre-breakdown delay times associated with the three linear regimes for Torlon, identified via Weibull plots in Figure 6.13 and Figure L.4 (*Appendix L*), yields the following propagation velocities:

- 27-29 km/s for the highest ranked breakdowns (*Torlon 3* in Figure 6.13)
- 35-38 km/s for the mid-range breakdowns (*Torlon 2* in Figure 6.13)
- 56 km/s for the lowest ranked breakdowns (*Torlon 1* in Figure 6.13)

Badent *et al*. [168] studied negative streamers in insulating oil and, according to their classification, the first two subsets listed above can be described as secondary streamers (average velocity up to 40 km/s), and the third subset can be described as tertiary streamers (velocity exceeding 47 km/s). Massala and Lesaint [169] define fast streamers in mineral oil as having a velocity higher than 50 km/s. Duy *et al*. [170] classify streamers simply as *slow* for average velocity 1.5-3 km/s, and *fast* for average velocity 20-200 km/s, although this classification is in relation to the propagation of positive streamers.

In order to put these estimated velocities for Torlon into context for discussion, the calculated average streamer velocities for all experimental geometries and materials, averaged over 35 breakdown events, are presented in Table 6.8. As in section 5.5, the upper/lower velocities and the corresponding propagation modes [165] are also provided. Compared to the results in Table 5.9 (section 5.5) where 4th mode streamers were frequently observed, the results in Table 6.8 are mainly indicative of 3rd mode streamer propagation. The average streamer velocities for PP, LDPE, and UHMWPE are in the range 13-21 km/s. Although there is no notable difference between the values for PP under the two different collar geometries, it is clear that the addition of a shoulder has a positive effect on the polyethylene materials, by reducing the propagation velocity compared with the unmodified samples. This effect manifests itself in longer times to breakdown for LDPE and UHMWPE as compared to those found for PP. Using the collar/shoulder (BII) geometry as an example, however, the breakdown time and, hence, the propagation velocity was more predictable for PP, suggesting a more consistent breakdown mechanism. The stability of the breakdown mechanism, and hence the stability of the time to breakdown and breakdown voltage, should be taken into account in any judgment of dielectric performance for a particular applied wave-shape.

Evident from the results presented in Table 6.8 are the faster propagation velocities associated with the Rexolite and Torlon samples compared to the other three materials tested under all geometries. The high value of standard deviation for the combination of collar electrode and unmodified Rexolite sample (geometry BIII) results from variation in the average propagation velocity from 11 km/s for the first breakdown, up to ~200 km/s towards the end of the test.

As all Rexolite and Torlon samples tested were found to have suffered bulk breakdown damage, resulting in significant sample material degradation, it appears clear that the propagation of discharges via paths other than the original liquid-solid interface is central to the appearance of faster streamers, resulting in consistently shorter times to breakdown for these materials. The high permittivity of Torlon (ε_r = 3.9) may contribute to this effect through bending of the electric field lines towards

the solid [115], leading to a higher probability of streamers penetrating the bulk of the solid rather than propagating to the earth plane over the liquid-solid interface.

Table 6.8. Average streamer velocities and corresponding propagation modes for non-uniform fields (± values indicate standard deviation).

		Average Velocity (km/s)	**Upper Velocity (km/s)**	**Lower Velocity (km/s)**	**Streamer Mode [165]**
Pin/Recess (AI)	PP	14±3	26	9	3rd
	LDPE	13±2	19	10	3rd
	UHMWPE	15±2	20	12	3rd
	Rexolite	35±17	78	11	3rd
	Torlon	40±11	61	23	3rd
Pin/Shoulder (AII)	PP	16±2	19	11	3rd
	LDPE	13±4	23	9	3rd
	UHMWPE	13±2	20	9	3rd
	Rexolite	24±3	29	15	3rd
	Torlon	40±10	60	20	3rd
Collar/Shoulder (BII)	PP	19±2	23	13	3rd
	LDPE	13±4	23	8	3rd
	UHMWPE	17±4	28	9	3rd
	Rexolite	33±13	60	11	3rd
	Torlon	36±7	57	17	3rd
Collar/No mods. (BIII)	PP	19±3	27	12	3rd
	LDPE	22±4	28	7	3rd
	UHMWPE	21±2	26	17	3rd
	Rexolite	57±44	202	11	4th/3rd
	Torlon	38±12	61	19	3rd

Such an explanation cannot readily be applied to Rexolite (ε_r = 2.5), however, where the relative permittivity is much closer to that of the oil. The ageing process identified for Rexolite in Figure 6.11 can potentially explain the increased propagation velocities for this material. Given the condition of the samples post-test, it is speculated that the action of the discharge induces some form of chemical interaction between the oil and the solid, leading to cumulative damage and reduced breakdown voltages due to the breakage of molecular bonds in the solid volume.

A further explanation may be that Rexolite and Torlon are more sensitive to space charge deposition in the material volume from previous discharges. Local field enhancements could then potentially lead to the formation of faster streamers that propagate in the bulk of these solid materials, resulting in shorter times to breakdown. In order to confirm this effect, however, more accurate measurements of the volume resistivity than those presented in Table 3.1 (section 3.3.2) are required to distinguish between the relaxation times for the different materials.

Analysing the breakdown behaviour in uniform fields, the V-t plots in Figure 6.6 appear to reveal three different V-t regimes, with average propagation velocities of 10-14 km/s, ~18 km/s, and ~27 km/s. Although space charge injected from the electrodes into both the liquid and solid dielectric will result in some local field enhancements in the 'uniform-field' geometries employed here, particularly at the liquid-solid-electrode triple points, the influence of the effects is considered to be minimal, with the combination of plane-parallel electrode configuration and non-modified cylindrical solid sample providing a reasonable approximation of uniform-field conditions. It is possible that whereas the high-field region at the pin or collar generally determines the streamer path in non-uniform geometries, the effect of space charge injected by the electrodes during previous discharges is more important in determining the discharge path under uniform-field conditions. Again, local field enhancements due to accumulated space charges could result in the propagation of streamers in faster modes in the solid bulk. An in-depth investigation of the effects of space charge in both the liquid and solid dielectric using an electrostatic field solver would provide interesting future work.

The tendency for bulk breakdown events to occur in cylindrical solids between plane-parallel electrodes in insulating oil has been observed before [6]. In this study, Wang *et al*. reported that a field of 700 kV/cm was required to cause flashover of a 3-mm long cylindrical PMMA surface. Ultra-high molecular weight polyethylene reflected the highest breakdown field of 650 kV/cm in a 4-mm gap in the present study – this is despite the rate of voltage rise being around two orders of magnitude lower in the present study (0.35 kV/ns compared to 22 kV/ns). The results indicate

that the average breakdown field for a given material in non-uniform fields can be 1.5-2 times lower than that found in uniform fields, and this reduction in breakdown strength could be useful for predicting the effect of protrusions on the surface of electrodes [65], [66], or of conducting material present on or around the surface of the solid dielectric as a result of previous breakdown events.

The average streamer propagation velocities calculated for uniform-field conditions are displayed in Table 6.9. As in non-uniform fields, streamers mainly propagate in the 3rd mode; the velocity range is 9 km/s to 31 km/s. Compared to the behaviour for rise-time 100 ns in Table 5.10 (section 5.5), the average propagation velocities and standard deviations are much lower. It must be noted that the sample/inter-electrode gap length was 8 mm for the results in Table 5.10, and 4 mm for the results in Table 6.9.

Table 6.9. Average streamer velocities and corresponding propagation modes for uniform fields (± values indicate standard deviation).

		Average Velocity (km/s)	**Upper Velocity (km/s)**	**Lower Velocity (km/s)**	**Streamer Mode [165]**
Plane/No mods. (CIII)	PP	17±5	29	10	3rd
	LDPE	22±8	31	12	3rd
	UHMWPE	13±2	17	11	3rd
	Rexolite	15±3	19	9	3rd
	Torlon	24±5	29	17	3rd

A Weibull analysis of the breakdown voltage data was performed for the results obtained under non-uniform fields. The behaviour of the Weibull plots in general does not follow a simple straight line behaviour associated with a two-parameter Weibull distribution, or the curved behaviour that would be expected for a three-parameter Weibull distribution; the plots instead show several straight line sections. Analysing the Weibull parameters in Table 6.7, the values of the shape parameter β are up to 13 times lower for Rexolite and Torlon samples compared to the other materials, indicative of a lesser sensitivity to an increase in voltage. The values of

the scale parameter α (kV) – a measure of the breakdown voltage with a corresponding probability of failure of 63.2% [163] – however, are around 1.5 times higher for PP, LDPE and UHMWPE samples compared to Rexolite and Torlon samples.

The trends for Torlon appear to support the above theory on different breakdown mechanisms, where the higher ranked voltages correspond with surface breakdown events, and the lower ranked voltages correspond with bulk solid breakdown events. It is proposed that the different behaviours occur as a result of the propagation of streamers in different modes.

For PP, LDPE, and UHMWPE, however, the change in gradient in the Weibull plots could not be attributed to a surface breakdown versus a bulk breakdown mechanism, as no bulk breakdowns were observed in these sample materials. It was further observed that the lower ranked voltages did not occur towards the end of the experimental sequence, and in fact, no particular pattern was revealed. There is the possibility that for these three materials, two competing processes are occurring on the surface of the samples: an ageing process where the surface is damaged, leading to a reduction in the breakdown strength and a possible change in the breakdown mechanism; and a conditioning process whereby the previously damaged surface is modified by a subsequent discharge. Some darker surface channels on the samples suggest propagation of at least two discharges over the same path – this may account for surface discharges with the same time to breakdown and breakdown voltage. Many lighter channels also exist, where only one discharge appears to have propagated, and each different path will likely result in a different point of breakdown on the applied voltage wave-form. As discussed in section 2.0, breakdown events can occur more readily at sites of previous breakdown activity upon re-application of an impulse voltage to the system [10]. While the period of five minutes between impulse applications was intended to permit dielectric relaxation, it is possible that gas bubbles or discharge by-products may have remained in the inter-electrode gap. The location of such impurities could be critical in determining the path between the electrodes followed by subsequent discharges.

Comparing the results of rising-edge breakdown measurements with those obtained when breakdown was allowed to occur on the falling edge of the impulse in Chapter 5, some similarities in the effects of the electrode/sample geometry can be observed. The times to breakdown reported for both forms of impulse application are generally longer for the type A (pin) electrode geometry as compared with the type B (collar) geometry. As was observed in Chapter 5, the breakdown voltages using the type B (collar) electrode here appear to be higher for the type II (shoulder) samples as compared with the type III (no modifications) samples.

Referring to the results obtained in open oil gaps in Chapter 4, it is clear that the introduction of a solid sample between the electrodes causes a reduction in the delay time to breakdown. The times to breakdown of the oil, established in section 4.2.1, were found to be around ~750 ns and ~1250 ns for the pin-plane and collar-plane geometries, respectively. The closest values to these baseline levels were ~680 ns for the type II LDPE sample in pin-plane geometry, and ~715 ns for the type II LDPE sample in collar-plane geometry. It should be noted that the calculated standard deviation was always much lower for the open oil gap, suggesting a more consistent breakdown mechanism. Taking the lower extreme case as an example, the average times to breakdown for Torlon were ~225 ns for the pin and ~250 ns for the collar. The corresponding reductions in breakdown time are 3.3 times and 5 times, respectively, when compared to the baseline times stated above.

Overall, PP, LDPE, and UHMWPE all exhibited desirable properties for use as oil-immersed insulators, with high breakdown voltages/fields in non-uniform field measurements. Rexolite and Torlon appear to be poorer choices to select as oil-immersed insulators for the conditions investigated, with the effects of bulk solid discharges as well as surface flashover events combining to remove large parts of material from the discharge sites. This effect as a result of repeated discharges could lead to a mechanical instability, and if undiscovered in large-scale industrial machines which are fully immersed in oil, could lead to major system failure.

Chapter 7

EFFECT OF APPLIED FIELD AND RATE OF VOLTAGE RISE

7.0 INTRODUCTION

While the results presented in Chapter 5 and Chapter 6 provide sufficient data for surface discharges initiated in divergent fields, characterisation of the behaviour of the different solid dielectric materials in uniform fields has, thus far, been limited by the occurrence of bulk breakdown events relatively early in the various test sequences. Contained within this chapter are the results of experiments designed to compare the performance of the five materials under uniform-field conditions, whilst being subjected to varying rates of voltage rise and levels of peak electrical field. This meant the application of lower voltages than in Chapters 5 and 6, and through this method, it was possible to conduct a more detailed investigation of surface breakdown behaviour in uniform fields.

With reference to image forces and electric double layers, discussed in section 2.4.3, Korobeynikov *et al*. [135] calculate that a 200 kV/cm field will cause a strong increase of ion dissociation in non-polar liquids such as mineral oil when the direction of the field is parallel to the solid surface. Image forces can lead to the attraction of ions from the liquid towards the surface of the electrodes, and also towards the surface of a solid spacer in the case when the spacer material has a higher permittivity than the liquid. This 200 kV/cm electric field level is chosen as the minimum applied field for the experiments detailed herein. Differences in the minimum applied field required to initiate breakdown events, the breakdown voltages, times to breakdown, and corresponding average streamer propagation velocities and modes of propagation are described and discussed.

7.1 EXPERIMENTAL METHOD

As used in Chapter 6, the circuit of Figure 3.13 was deployed to produce impulses with a rise-time of ~1 μs and a fall-time to half peak value of 6.5 μs. As in Chapters 4-6, all applied impulses were of negative polarity. The input impedance of the liquid-resistive voltage divider was 10 kΩ for all measurements presented in this chapter, as discussed in section 3.5.2.

Six test series were conducted, five of which involved subjecting a solid sample of each material to a number of impulse voltages and recording the breakdown voltages and corresponding times to breakdown. The final test series was performed to characterise the behaviour of an open oil gap, that is, an inter-electrode gap of the same length as in the other tests, only without the inclusion of a solid spacer between the electrodes. This provided baseline reference data for direct comparison with the data associated with the various liquid-solid gaps. With a view to subsequent statistical analysis of the results, each liquid-solid gap and the open oil gap were subjected to 20 impulse voltages. The electrodes were removed and polished between every test performed in the sequence.

Tests were conducted with varying rates of voltage rise and levels of peak electrical field. It was desired to produce peak field levels of up to 1 MV/cm – with a peak voltage capability of 350 kV under uniform field, the sample length was hence chosen to be 3.5 mm. All solid samples were pre-treated and handled according to the protocol described in section 3.3.2.

7.2 EXPERIMENTAL RESULTS

A series of tests was conducted at four different levels of peak applied voltage, as listed along with the corresponding average rate of voltage rise and peak applied field level in Table 7.1.

Table 7.1. Peak applied voltage, average rate of voltage rise (*dV/dt*), and peak electric field level for uniform-field measurements.

Voltage (kV)	*dV/dt* (kV/µs)	Electric Field (kV/cm)
70	70	200
140	140	400
245	245	700
350	350	1000

The sample length and inter-electrode gap spacing, *d*, were fixed at 3.5 mm for all tests. In each test, the liquid-solid insulation system was subjected to 20 impulse voltages at the required field level, and the breakdown voltages and times to breakdown were recorded each time that a breakdown event occurred.

7.2.1 Breakdown Voltage

At the lowest applied field level 200 kV/cm (*dV/dt* 70 kV/µs), no breakdown event was found to occur, either on the rising or the falling edge of the impulse, for any of the five solid spacers. The open oil gap also withstood all 20 applied impulse voltages.

When the applied field was increased to 400 kV/cm (i.e. the rate of voltage rise was increased to 140 kV/µs), the open oil gap again withstood all 20 applied impulses. The materials with ε_r close to that of the oil (ε_r = 2.2) – PP, LDPE, and Rexolite – also withstood each applied impulse.

Torlon (ε_r = 3.9), the material with highest ε_r, was subjected to electrical breakdown upon application of each voltage impulse to the insulation system. Between these two extremes of behaviour, the UHMWPE (ε_r = 3.0) sample, with ε_r lower than Torlon but higher than the other three materials, was broken down upon application of 11 of 20 shots, a probability of 0.55.

The breakdown voltages for the Torlon and UHMWPE samples are shown in Figure 7.1. These results suggest that the breakdown initiation field for the gaps with higher ε_r solids lies between 200 kV/cm and 400 kV/cm. The time to breakdown

was up to 4 µs for these measurements, corresponding with slower streamer propagation modes (see section 7.2.3) as breakdown occurred on the falling edge of the impulse. Breakdown events occurred in the latter shots in the test sequence for UHMWPE, and this will be discussed in section 7.4.

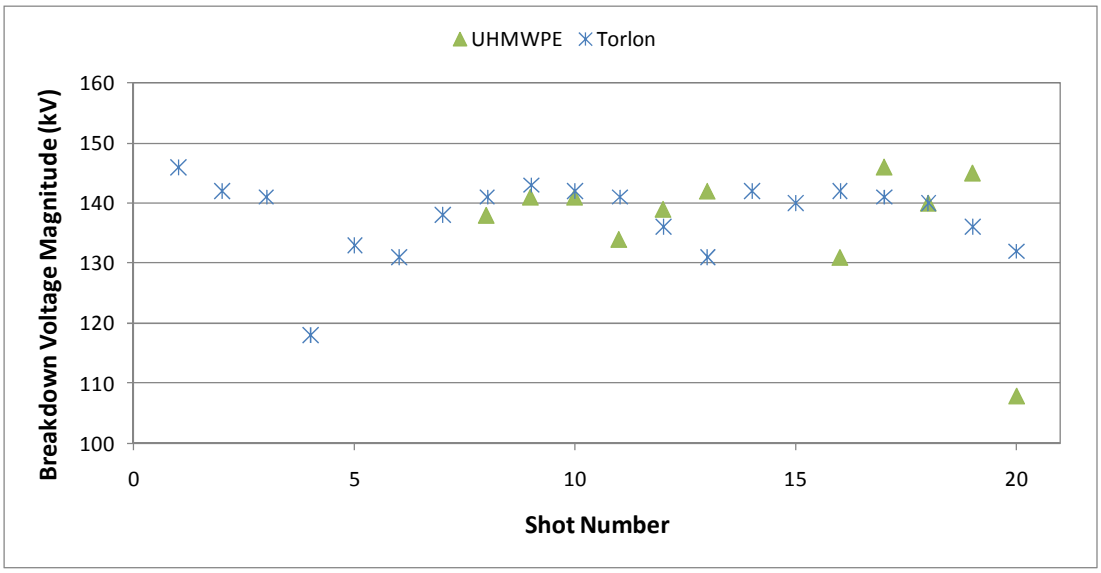

Figure 7.1. Breakdown voltage magnitude versus breakdown number for 400 kV/cm applied field (*dV/dt* 140 kV/µs).

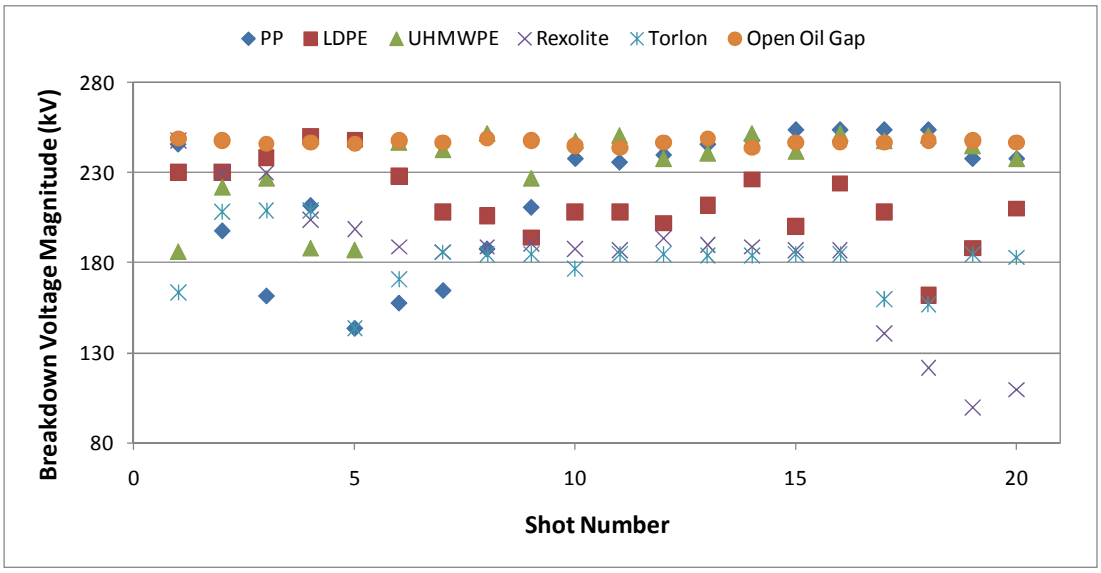

Figure 7.2. Breakdown voltage magnitude versus breakdown number for 700 kV/cm applied field (*dV/dt* 245 kV/µs).

The curves in Figure 7.2 show the breakdown behaviour when the applied field was increased to 700 kV/cm (*dV/dt* 245 kV/μs), which resulted in breakdown of the open oil gap and all liquid-solid gaps for all 20 applied impulses. Breakdown was always found to occur around the peak of the voltage impulse in the open oil gap, and it is clear that the breakdown voltage was found to be more stable than that for any of the liquid-solid gaps: the spread of breakdown voltage is an order of magnitude less than when an insulator is present (see Table 7.2). This suggests a consistent breakdown mechanism for the open oil gap. The breakdown voltage for LDPE decreased with an increasing number of breakdown events, whereas the breakdown voltage for both PP and UHMWPE initially increased and thereafter stabilised at around the peak impulse magnitude for shots 10-20, where the breakdown voltage is similar in value to that of the open oil gap. Torlon showed the least variation in breakdown voltage under this configuration, but at lower voltages than PP, LDPE, and UHMWPE. The breakdown voltage for Rexolite was found to initially decrease, remain relatively constant over shots 6-16, and thereafter rapidly decrease over the remaining shots. The decrease in breakdown voltage could correspond with a reduction in the formative time lag, and may, therefore, be indicative of the propagation of faster streamers in the final few shots.

When the impulse voltage was increased such that the peak applied field was 1 MV/cm and the rate of voltage rise was 350 kV/μs, the breakdown voltage for the open oil gap varied more than at 700 kV/cm and 245 kV/μs, suggesting competing breakdown mechanisms at the higher level of applied field. The variation of breakdown voltage with an increasing number of applied voltage impulses for the open oil gap and for all five liquid-solid gaps is shown in Figure 7.3. In this regime the spread in breakdown voltage for the open oil gap was comparable to that in all of the liquid-solid gaps (see Table 7.2). Polypropylene, LDPE, and UHMWPE reflected a fairly consistent breakdown voltage level, in the range 250-300 kV, from shot 10 onwards. Rexolite reflected a predictable breakdown voltage of 210 kV, with very little variation after shot 4. The response for Torlon was also found to be fairly flat, but again at lower voltages than that found for the other materials (~160 kV).

The results listed in Table 7.2 are the average breakdown voltages and standard deviation (± values) for each of the six types of gap tested. As in Chapters 4-6, the values of standard deviation recorded within this chapter have been calculated using equation (4.1) (see section 4.2.1). At both 700 kV/cm and 1 MV/cm, the open oil gap has the highest average breakdown voltage. The standard deviation is one order of magnitude lower for the open oil gap compared to any of the liquid-solid gaps at 700 kV/cm. Of the five solid materials, Torlon consistently showed the lowest level of standard deviation, suggesting a more consistent breakdown mechanism for this material.

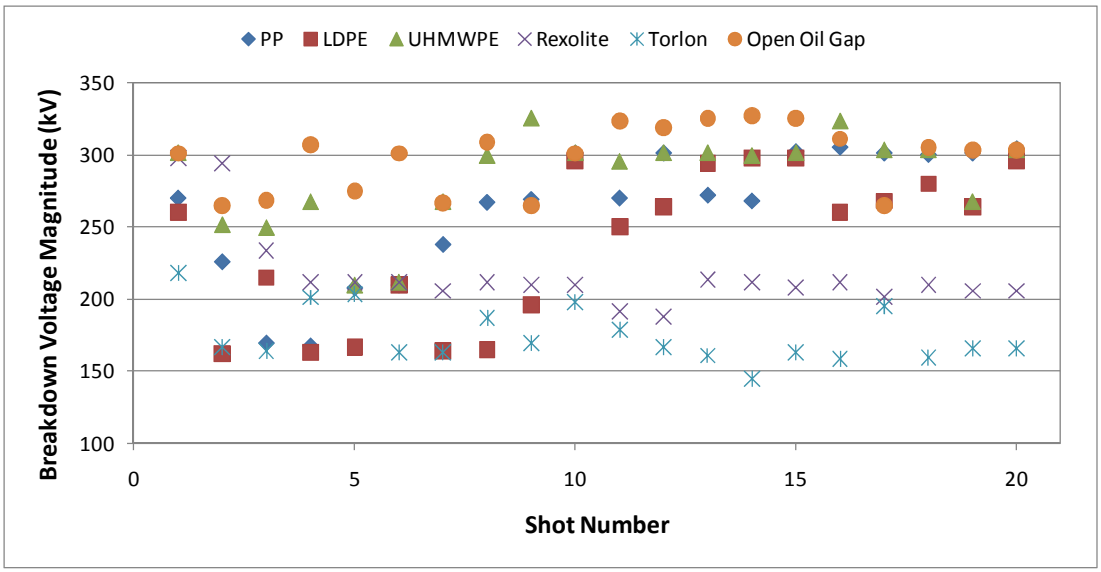

Figure 7.3. Breakdown voltage magnitude versus breakdown number for 1 MV/cm applied field (*dV/dt* 350 kV/µs).

Table 7.2. Average breakdown voltages at applied fields 400 kV/cm, 700 kV/cm, and 1 MV/cm.

	Average Breakdown Voltage (kV)		
	400 kV/cm	**700 kV/cm**	**1 MV/cm**
PP	no breakdown	219±37	263±45
LDPE	no breakdown	214±21	239±53
UHMWPE	137±11	234±22	285±33
Rexolite	no breakdown	183±38	218±28
Torlon	138±6	182±17	175±19
Open Oil Gap	no breakdown	247±1.5	298±22

7.2.2 Time to Breakdown

The time-to-breakdown data can potentially be used to reveal information about the modes of streamer propagation involved in the breakdown of the different gaps.

The results presented in Figure 7.4 show the time to breakdown versus shot number data for a 400 kV/cm applied field (*dV/dt* 140 kV/µs). The time to breakdown for Torlon was generally recorded to be in the range 500-800 ns. Breakdown did not occur with each applied impulse for UHMWPE, and there was a large spread in the delay time when breakdown did occur. Of 11 breakdown events, six occurred after the impulse had passed its peak. Although breakdown was observed in the later shots for UHMWPE, each applied impulse following the first breakdown event did not induce breakdown, and the sequence was: no breakdown for shots 1-7; breakdown for shots 8-13; no breakdown for shots 14-15; and breakdown following shots 16-20.

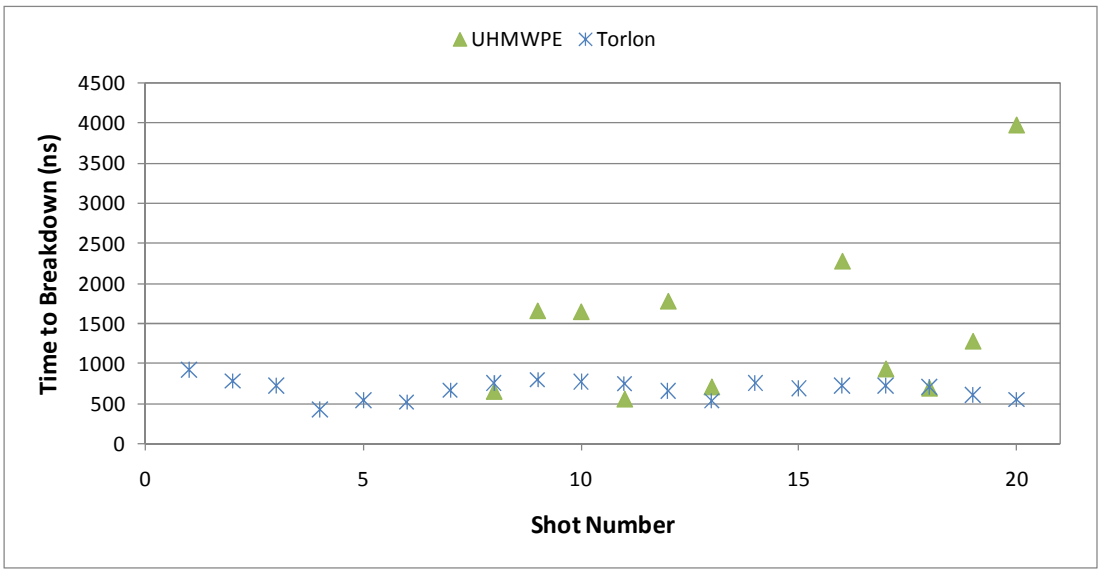

Figure 7.4. Time to breakdown versus breakdown number for 400 kV/cm applied field (*dV/dt* 140 kV/µs).

The times to breakdown for rate of voltage rise 245 kV/µs are displayed in Figure 7.5. The delay times for UHMWPE and Torlon are shorter than those for the

140 kV/µs rate of voltage rise. Although the breakdown voltage for the open oil gap was very stable, considerable spread existed in the time to breakdown, made possible by the relatively long duration at peak voltage; the voltage level is at least 95% of the peak voltage for a period of ~1 µs. As in Chapters 5 and 6, long pre-breakdown delay times were exhibited by UHMWPE when compared to the other solid materials. Interestingly, the time to breakdown for PP was found to increase gradually with each shot from 204 ns at shot 5 to 1140 ns at shot 17.

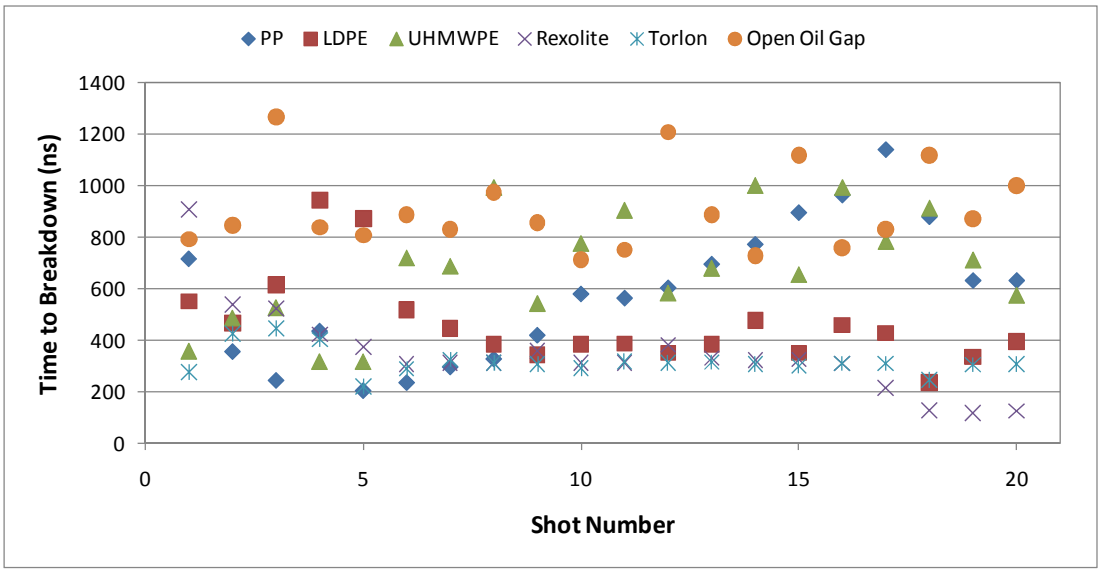

Figure 7.5. Time to breakdown versus breakdown number for 700 kV/cm applied field (*dV/dt* 245 kV/µs).

The times to breakdown at 350 kV/µs, shown in Figure 7.6, were again shorter than those found with slower rates of voltage rise. The open oil gap showed the longest delay times to breakdown. As shown in Figure 7.6, the PP sample again appears to go through a voltage recovery phase, with the breakdown time rising from 128 ns at shot 3 to 420 ns at shot 10. The breakdown times recorded for LDPE are longer for shots 10-20 than for the initial shots. Longer times to breakdown are again reflected in the results found for UHMWPE.

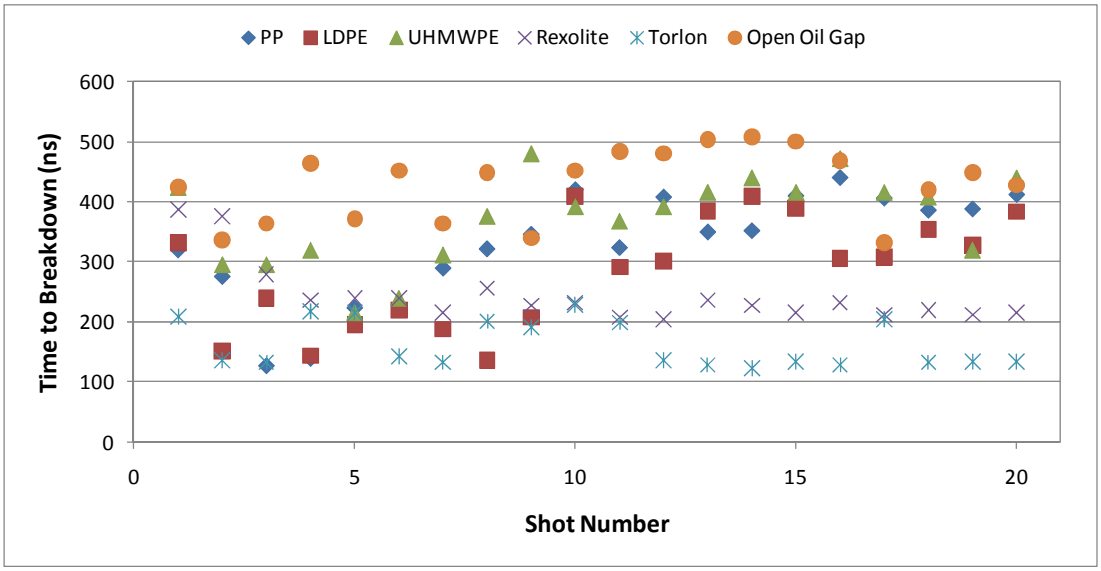

Figure 7.6. Time to breakdown versus breakdown number for 1 MV/cm applied field (*dV/dt* 350 kV/µs).

The average times to breakdown and the standard deviation (± values) for peak applied fields of 400 kV/cm, 700 kV/cm, and 1 MV/cm are listed in Table 7.3. The average delay time is seen to be reduced by the introduction of a solid spacer into the oil gap. At both 245 kV/µs and 350 kV/µs, the rank of the average delay time from longest to shortest was:

1. Open oil gap
2. UHMWPE
3. PP
4. LDPE
5. Rexolite
6. Torlon

The possible reasons for this consistent ranking will be discussed in section 7.4.

In order to compare the times to breakdown by applied field rather than by material, the data is presented separately for each type of gap in Figures 7.7-7.12. It is clear

from all six figures that the time to breakdown is more consistent at the higher applied fields and faster rates of voltage rise, as would be expected.

Table 7.3. Average times to breakdown at applied fields 400 kV/cm, 700 kV/cm, and 1 MV/cm.

Material	ε_r	Average Time to Breakdown (ns)		
		400 kV/cm	700 kV/cm	1 MV/cm
PP	2.25	no breakdown	580±266	329±91
LDPE	2.2	no breakdown	467±173	284±92
UHMWPE	3.0	1472±1005	677±216	372±74
Rexolite	2.5	no breakdown	349±172	244±51
Torlon	3.9	675±119	318±54	164±39
Open Oil Gap	2.2	no breakdown	905±161	429±58

The periods of increasing time to breakdown with shot number for PP at both 700 kV/cm (245 kV/µs) and 1 MV/cm (350 kV/µs) are evident in Figure 7.7. At 1 MV/cm, the time to breakdown clearly steadily increased from shot 4 to shot 10. A similar trend of increasing breakdown time is evident between shot 4 and shot 10 at 700 kV/cm, and the time to breakdown continues to gradually increase to a maximum of longer than 1 µs for shot 17.

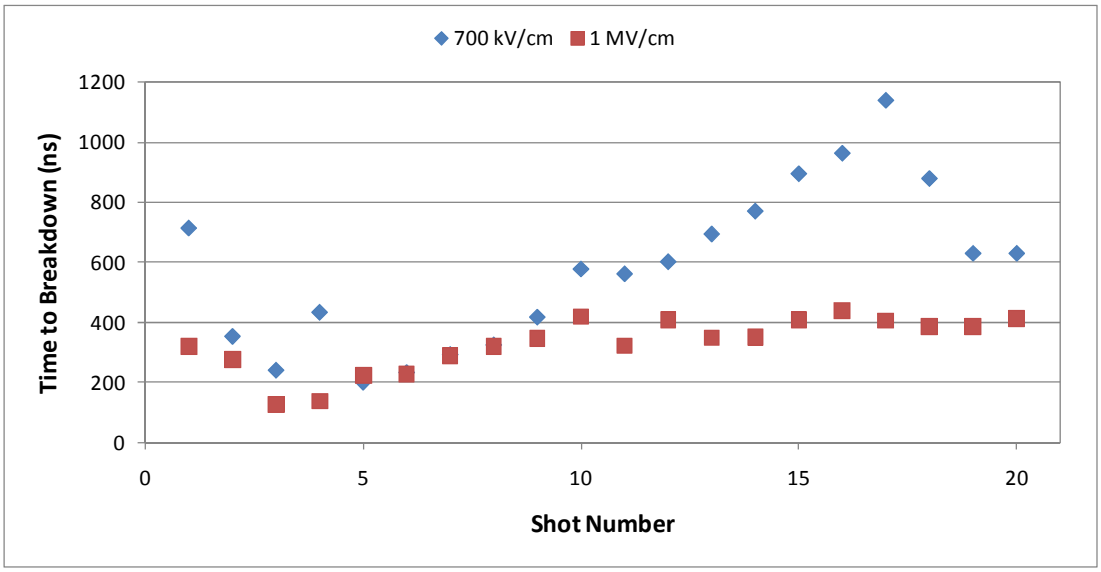

Figure 7.7. Time to breakdown versus breakdown number for PP for applied fields 700 kV/cm (*dV/dt* 245 kV/µs) and 1 MV/cm (*dV/dt* 350 kV/µs).

For shots 1-9 with an LDPE sample, there is a clear difference in the time to breakdown for the two levels of applied field, but the times are more similar for shots 10-20, as shown in Figure 7.8.

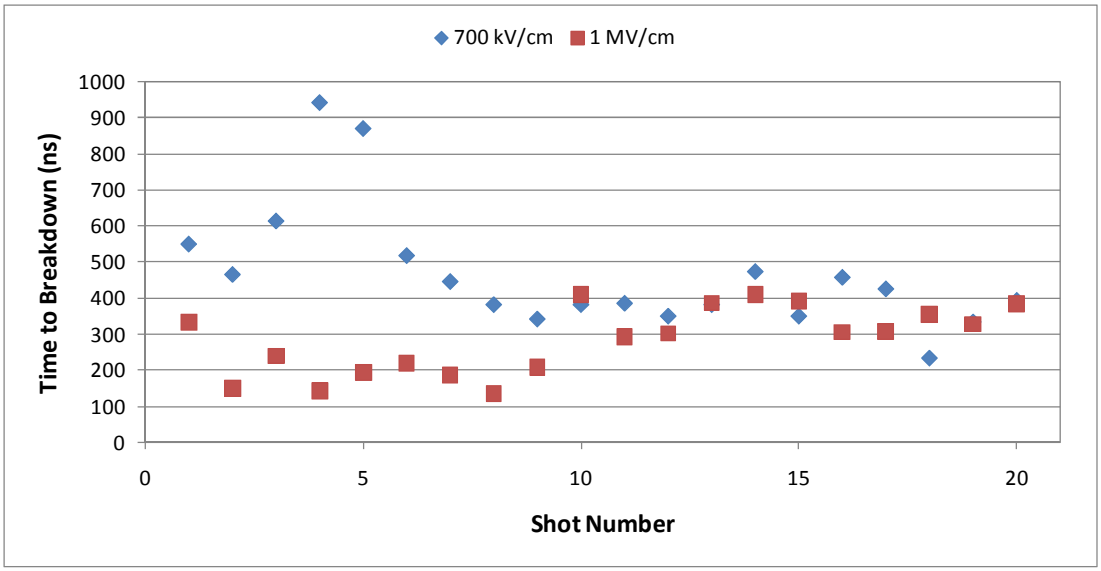

Figure 7.8. Time to breakdown versus breakdown number for LDPE for applied fields 700 kV/cm (*dV/dt* 245 kV/µs) and 1 MV/cm (*dV/dt* 350 kV/µs).

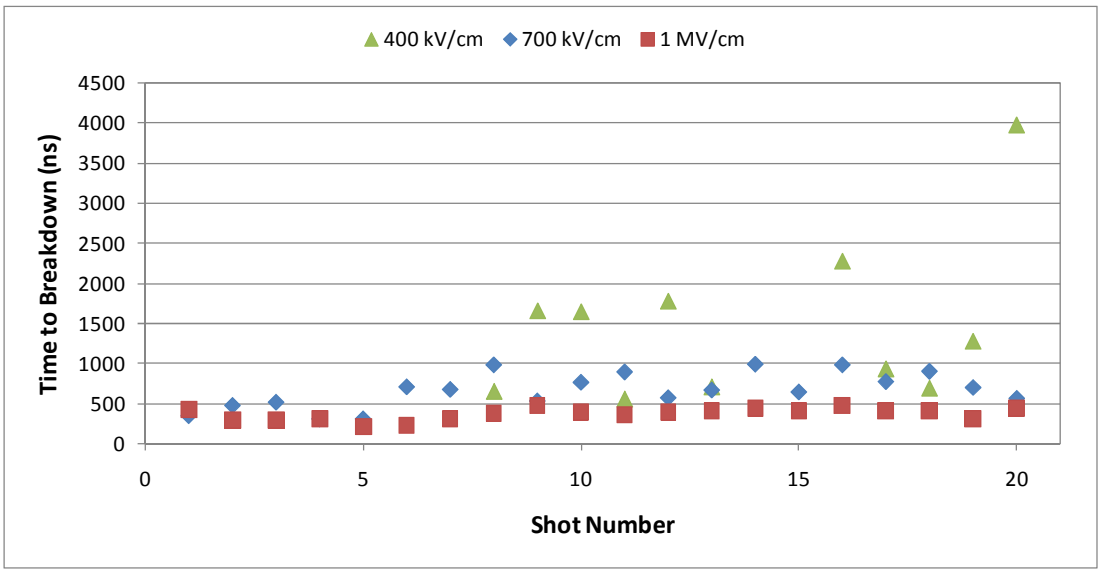

Figure 7.9. Time to breakdown versus breakdown number for UHMWPE for applied fields 400 kV/cm (*dV/dt* 140 kV/µs), 700 kV/cm (*dV/dt* 245 kV/µs) and 1 MV/cm (*dV/dt* 350 kV/µs).

The times to breakdown at 400 kV/cm (140 kV/µs) for UHMWPE, which were up to as long as 4 µs, are displayed in Figure 7.9. The reduction in the spread in delay time with increasing rate-of-rise of voltage is clearly seen in this figure.

As was observed in the results presented in Chapter 6, an ageing effect also appears to have occurred for the Rexolite sample tested at 700 kV/cm (Figure 7.10) – the time to breakdown was found to decrease from shot 1 to 6, was found to be relatively consistent over shots 6 to 16, and thereafter fell further up to shot 20. At 1 MV/cm, the time to breakdown fell from shot 1 to shot 4, and then displayed a fairly flat response for the remainder of the test sequence.

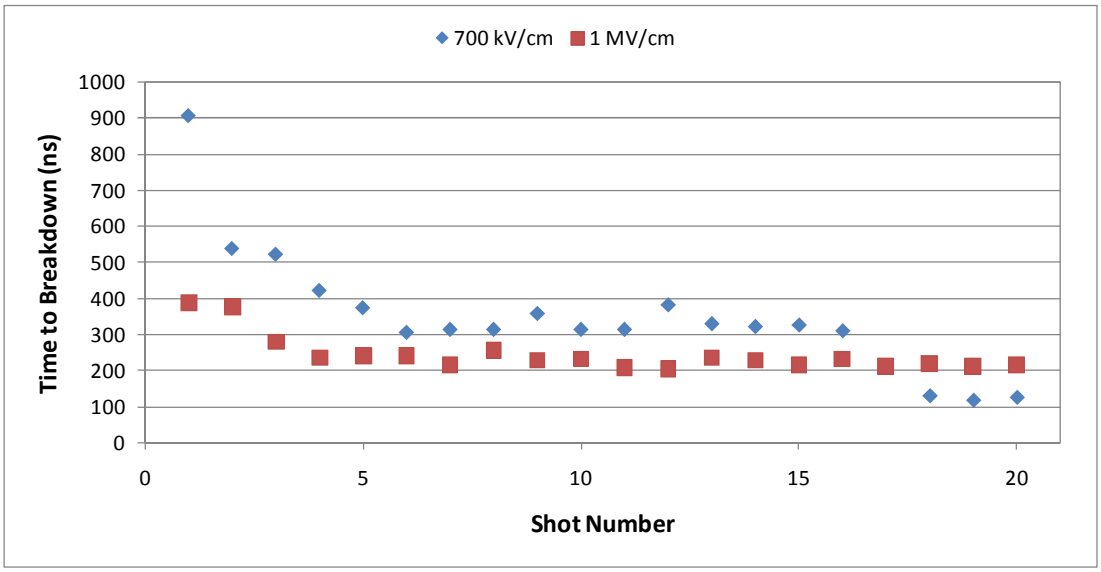

Figure 7.10. Time to breakdown versus breakdown number for Rexolite for applied fields 700 kV/cm (*dV/dt* 245 kV/µs) and 1 MV/cm (*dV/dt* 350 kV/µs).

At 400 kV/cm (140 kV/µs), the time-to-breakdown results for Torlon appear to go through several increasing and decreasing phases, as illustrated by Figure 7.11. There is clearly much less variation in the delay time at 700 kV/cm (245 kV/µs) and 1 MV/cm (350 kV/µs).

For the open oil gap, the consistent time to breakdown at 1 MV/cm, when breakdown generally occurs before the impulse peak, is clear (Figure 7.12). At 700 kV/cm, the variation in the breakdown time due to the long time at peak voltage is apparent.

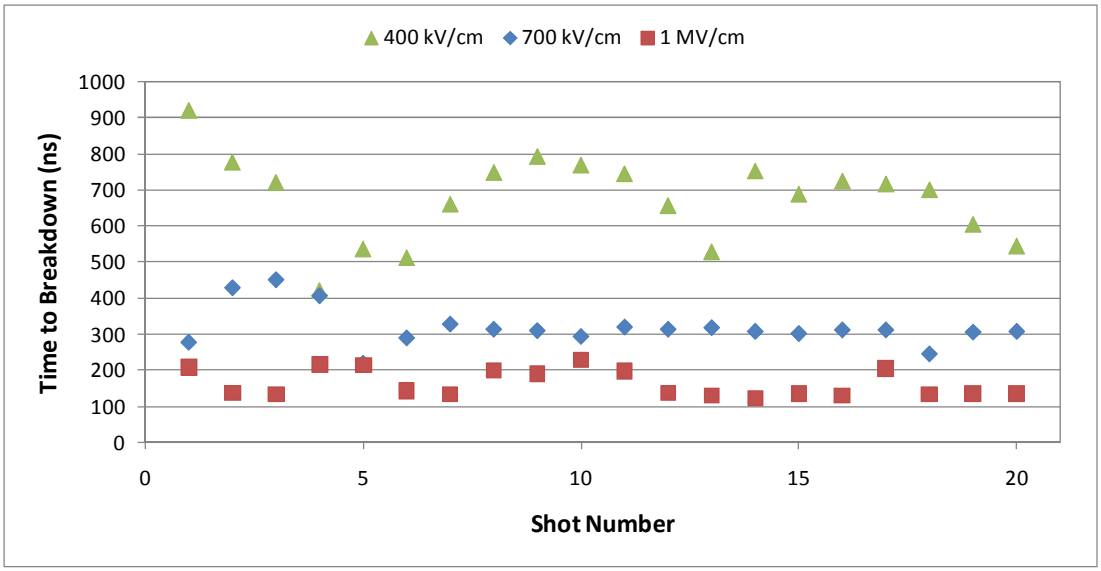

Figure 7.11. Time to breakdown versus breakdown number for Torlon for applied fields 400 kV/cm (*dV/dt* 140 kV/µs), 700 kV/cm (*dV/dt* 245 kV/µs) and 1 MV/cm (*dV/dt* 350 kV/µs).

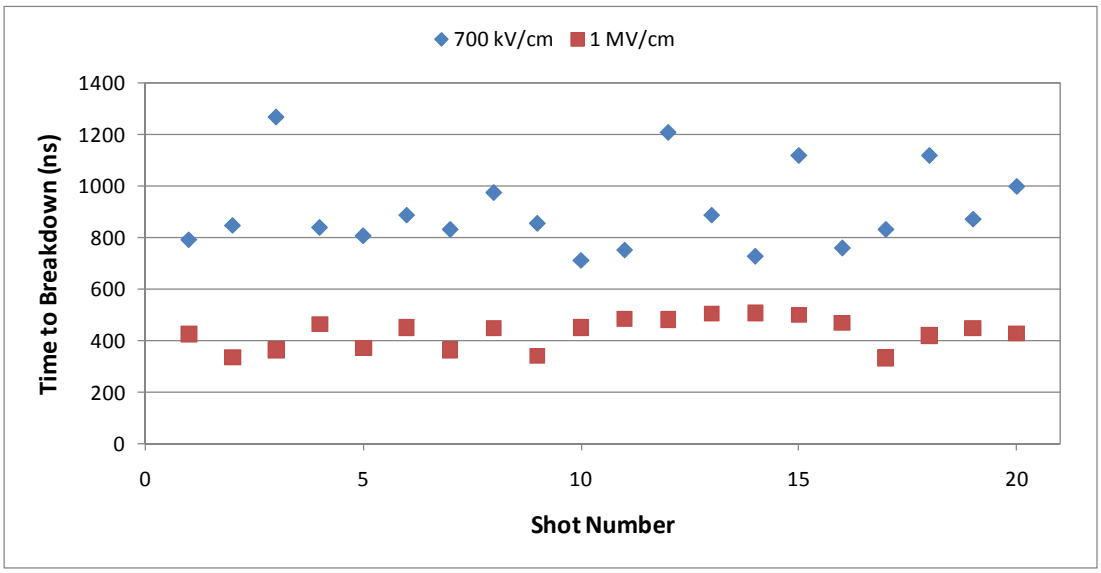

Figure 7.12. Time to breakdown versus breakdown number for open oil gap for applied fields 700 kV/cm (*dV/dt* 245 kV/µs) and 1 MV/cm (*dV/dt* 350 kV/µs).

7.2.3 Volt-time Plots

The breakdown voltage and time data are combined in V-t plots for the different levels of applied field in Figures 7.13-7.15.

At 400 kV/cm (140 kV/µs), the majority of data points are within the time range 500-900 ns, and within the voltage range 130-145 kV (Figure 7.13). The time range suggests that under these conditions, the average streamer propagation velocity is in the range 4-7 km/s for the most common breakdown mechanism. The longer breakdown times for the UHMWPE sample are consistent with slower streamer modes, summarised in the following discussion, with average propagation velocity in the range 1-3 km/s.

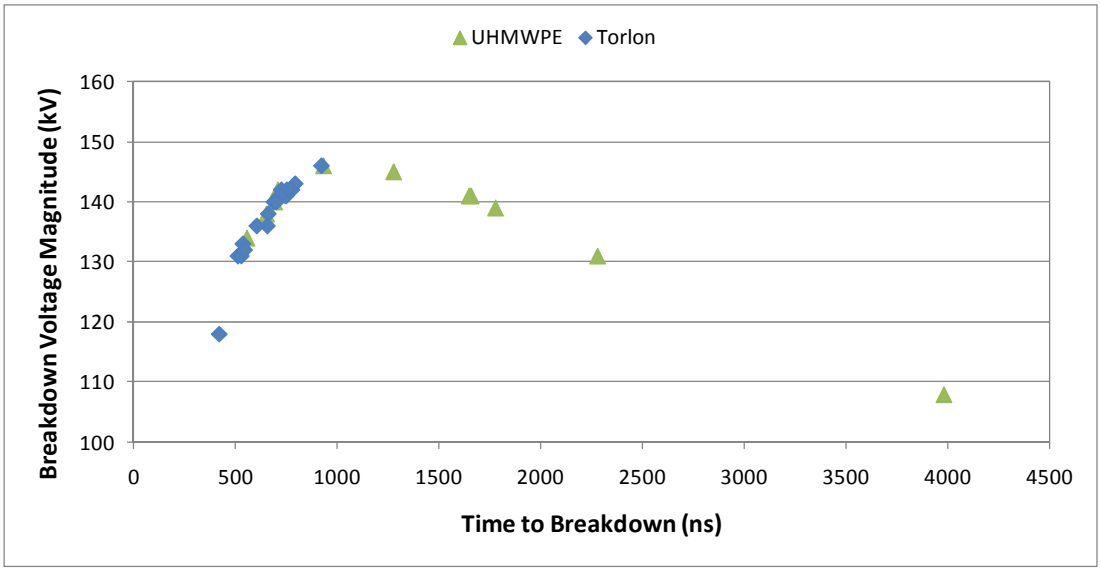

Figure 7.13. Volt-time plot for applied field 400 kV/cm (*dV/dt* 140 kV/µs).

The results in Figure 7.14 show the relative position of the point of breakdown for the five different materials and the open oil gap at 700 kV/cm (245 kV/µs). It is obvious from Figure 7.14 that breakdown of the open oil gap generally follows after a longer delay time than any of the liquid-solid gaps. Although the breakdown voltage was fairly constant for the open oil gap, the wide spread in pre-breakdown delay time is clear, with a 600 ns range between the shortest and longest delay times.

With the exception of Rexolite, the data points with longer delay time to breakdown for the liquid-solid gaps do not correspond to the first few breakdown events.

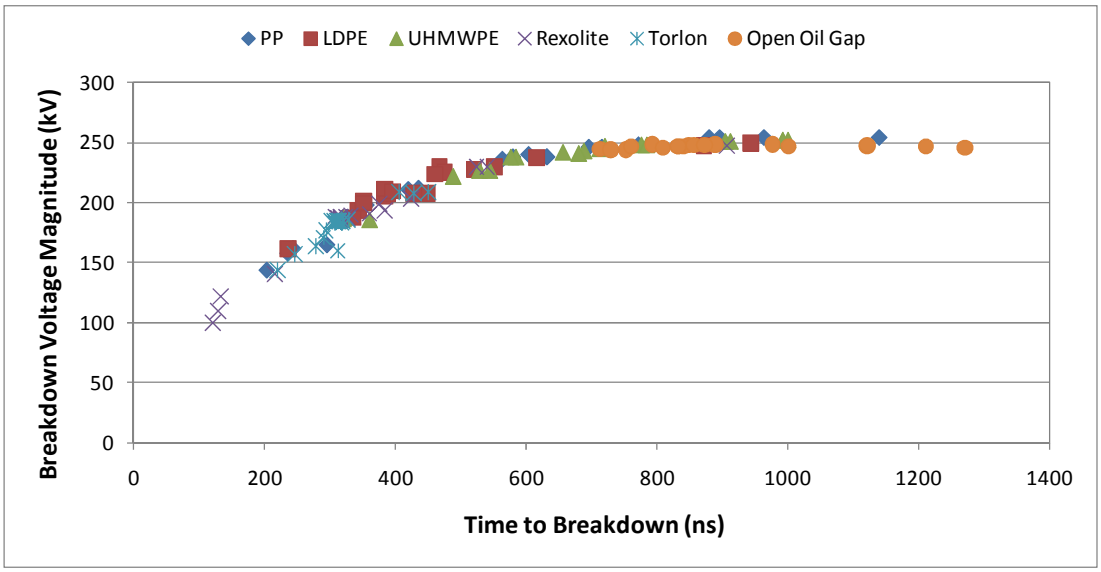

Figure 7.14. Volt-time plot for applied field 700 kV/cm (*dV/dt* 245 kV/µs).

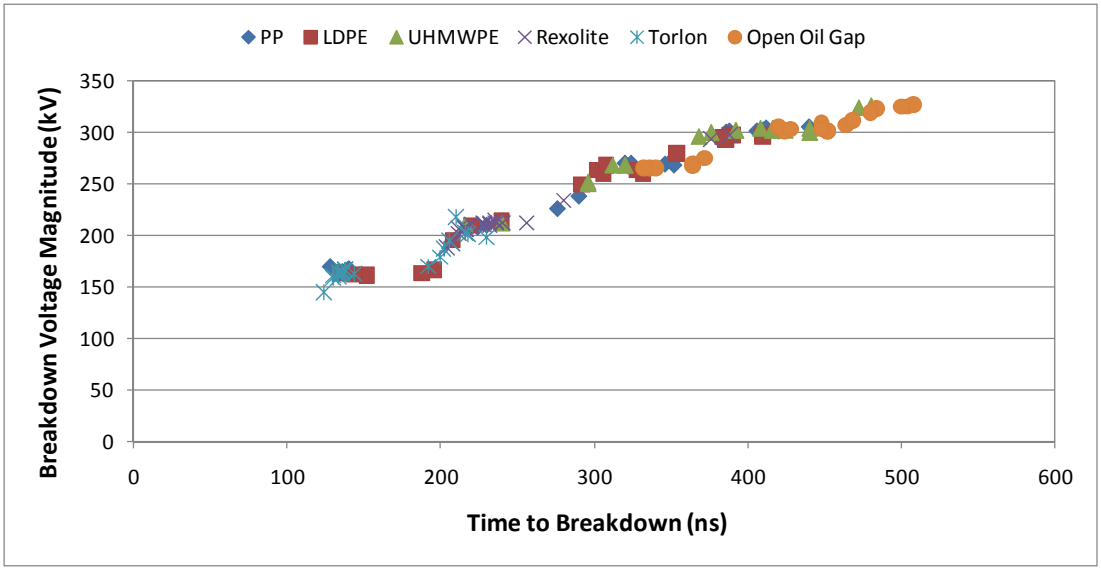

Figure 7.15. Volt-time plot for applied field 1 MV/cm (*dV/dt* 350 kV/µs).

By increasing the rate of voltage rise to 350 kV/µs (peak applied field 1 MV/cm), it was possible to induce all breakdown events on the section of the rising edge where

the voltage was still rising linearly, as illustrated by Figure 7.15. Although peak voltage was not attained until 1 µs, the longest time to breakdown was 508 ns for the open oil gap. Again, the data points for the open oil gap are those of highest breakdown voltage. Of the five liquid-solid gaps, an UHMWPE sample holds off breakdown for the longest times. As in Figure 7.14, the point of breakdown for the Torlon sample is predictable, but at much shorter delay times than the other materials.

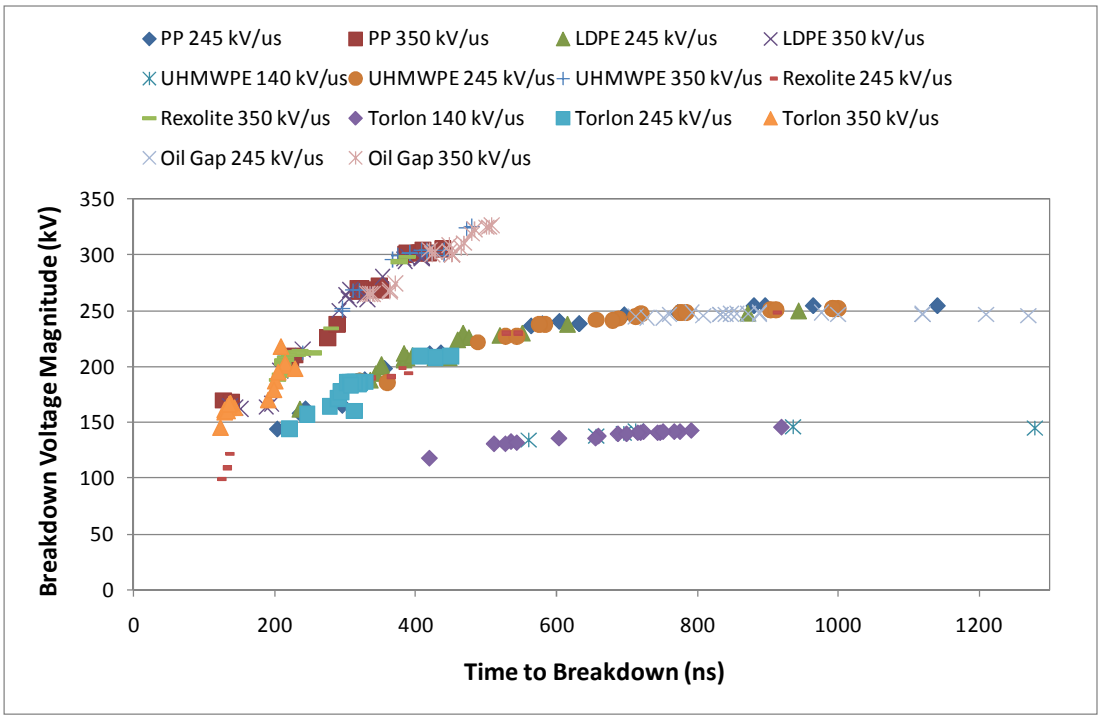

Figure 7.16. Volt-time plot for all samples and open oil gap for applied fields 400 kV/cm (*dV/dt* 140 kV/µs), 700 kV/cm (*dV/dt* 245 kV/µs) and 1 MV/cm (*dV/dt* 350 kV/µs).

The results shown in Figure 7.16 are V-t plots for all combinations of gap and peak field level/rate of voltage rise. Data where breakdown events occurred after 1.3 µs (for five breakdown events with an UHMWPE/oil gap at 140 kV/µs) have been omitted from this figure. It is clear that the gradient of the curves increases with increasing rate of voltage rise, and the average streamer propagation velocities are

indicated in Table 7.4 (140 kV/μs), Table 7.5 (245 kV/μs), and Table 7.6 (350 kV/μs).

The upper and lower velocities quoted in Tables 7.4-7.6 again refer to the calculated velocities for the shortest and the longest time to breakdown for each sample, respectively. It is clear that the average propagation velocities are higher at 350 kV/μs than at 245 kV/μs. For UHMWPE and Torlon samples, the average velocity is higher at 245 kV/μs than at 140 kV/μs. The velocities in Table 7.6 are comparable to those obtained under similar conditions in section 6.5 (Table 6.9), where streamers propagate in the 3rd mode, with an approximate velocity range of 8 km/s to 30 km/s.

As first discussed in section 5.5, the streamer modes in the final column of Tables 7.4-7.6 have been identified as classified in [165]. The classification has been repeated here for ease of reference:

- 1st mode 0.1 km/s
- 2nd mode 1-5 km/s
- 3rd mode 10-20 km/s
- 4th mode 100 km/s

At 140 kV/μs (Table 7.4), average velocities were in the range 1-8 km/s, indicating mainly 2nd mode streamer propagation.

With an increase in rate of voltage rise to 245 kV/μs (Table 7.5), both 2nd and 3rd mode streamer velocities were recorded for all liquid-solid gaps. In the open oil gap however, only 2nd mode streamers propagated, with maximum velocity approaching 5 km/s. The minimum apparent streamer velocity for Torlon is at least double that for the other materials, and the data are indicative of mainly 3rd mode streamer propagation. The high upper velocity for Rexolite in Table 7.5 corresponds with shot number 19 in Figures 7.2 and 7.5, where the breakdown voltage had fallen significantly due to considerable surface damage. If the shortest time to breakdown

was taken at shot 16 before the breakdown voltage collapsed, then the upper velocity would decrease to 11 km/s.

Table 7.4. Calculated streamer velocities and corresponding propagation modes for applied field 400 kV/cm (140 kV/μs).

	Average Velocity (km/s)	**Upper Velocity (km/s)**	**Lower Velocity (km/s)**	**Streamer Mode [165]**
UHMWPE	3±2	6	1	2^{nd}
Torlon	5±1	8	4	2^{nd}

Table 7.5. Calculated streamer velocities and corresponding propagation modes for applied field 700 kV/cm (245 kV/μs).

	Average Velocity (km/s)	**Upper Velocity (km/s)**	**Lower Velocity (km/s)**	**Streamer Mode [165]**
PP	8±4	17	3	$3^{rd}/2^{nd}$
LDPE	8±2	15	4	$3^{rd}/2^{nd}$
UHMWPE	6±2	11	4	$3^{rd}/2^{nd}$
Rexolite	13±7	29	4	$3^{rd}/2^{nd}$
Torlon	11±2	16	8	3^{rd}
Open Oil Gap	4±1	5	3	2^{nd}

Table 7.6. Calculated streamer velocities and corresponding propagation modes for applied field 1 MV/cm (350 kV/μs).

	Average Velocity (km/s)	**Upper Velocity (km/s)**	**Lower Velocity (km/s)**	**Streamer Mode [165]**
PP	12±5	27	8	3^{rd}
LDPE	14±6	26	9	3^{rd}
UHMWPE	10±2	16	7	3^{rd}
Rexolite	15±2	17	9	3^{rd}
Torlon	22±5	28	15	3^{rd}
Open Oil Gap	8±1	11	7	3^{rd}

A further increase in the rate of voltage rise to 350 kV/μs resulted in the propagation of 3^{rd} mode streamers in the main, with velocities approaching 30 km/s recorded

(Table 7.6). The open oil gap showed the slowest propagation velocities. Of the five solid dielectrics, UHMWPE again yielded the slowest propagation velocities, and Torlon the fastest.

In the case where Rexolite and Torlon surfaces were subjected to further discharges, damage occurred to the extent that significant material was removed, and 4th mode streamers were also observed with average propagation velocity ~125 km/s.

7.3 WEIBULL STATISTICAL ANALYSIS

A Weibull statistical analysis was conducted on the data recorded at 245 kV/μs and 350 kV/μs. Both the breakdown voltage and the time to breakdown data was analysed – it was found that a Weibull distribution best described the time to breakdown data, and hence this analysis is presented here.

The procedure described in section 5.4 was followed to produce the probability plots, only this time using data on the time to breakdown, *t*, rather than voltage data.

The cumulative probability of failure, *F(t)*, is defined here for both a three-parameter distribution (equation (7.1)), and a two-parameter distribution (equation (7.2)). The characteristic parameters have been redefined as α_t, β_t, and γ_t, with the subscript notation denoting the analysis of time data rather than voltage data (as was analysed in Chapter 5 and Chapter 6). The probability of failure at a time of α_t (ns) is 0.632, the shape parameter β_t provides a measure of how sensitive the insulation system is to an increase in stressing time, and γ_t (ns) provides an estimate of the stressing time below which the probability of breakdown is zero.

$$F(t) = 1 - \exp\left[-\left(\frac{t - \gamma_t}{\alpha_t} \right)^{\beta_t} \right] \tag{7.1}$$

$$F(t) = 1 - \exp\left[-\left(\frac{t}{\alpha_t} \right)^{\beta_t} \right] \tag{7.2}$$

Listed in Table 7.7 are the values of the location parameter, and the extracted scale and shape parameters for the 245 kV/μs rate of voltage rise, and listed in Table 7.8 are these parameters for the 350 kV/μs rate of voltage rise. Only PP and UHMWPE were best described by a 2-parameter Weibull distribution, shown by the zero value location parameter, for both rates of voltage rise.

The high value of γ_t required to bring the data points for the open oil gap at 245 kV/μs onto a straight line suggests that breakdown would not occur before 700 ns. The other non-zero γ_t values are 230 ns for LDPE and 210 ns for Torlon.

Table 7.7. Weibull distribution parameters for time to breakdown data for *dV/dt* 245 kV/μs.

	GAP					
	PP	LDPE	UHMWPE	Rexolite	Torlon	Open Oil Gap
Scale α_t (ns)	657	268	757	399	126	227
Shape β_t	2.11	1.70	3.03	2.07	2.15	1.23
Location γ_t (ns)	0	230	0	0	210	700

Table 7.8. Weibull distribution parameters for time to breakdown data for *dV/dt* 350 kV/μs.

	GAP					
	PP	LDPE	UHMWPE	Rexolite	Torlon	Open Oil Gap
Scale α_t (ns)	370	319	404	44	48	455
Shape β_t	3.28	2.92	5.24	1.11	0.97	7.32
Location γ_t (ns)	0	0	0	200	120	0

At 350 kV/μs (Table 7.8) only Rexolite and Torlon samples required non-zero γ_t values to bring the data points onto a straight line.

Displayed in Figure 7.17 are the 245 kV/μs Weibull plots. The data points for PP, UHMWPE, and the open oil gap show a linear behaviour. Similar to the statistical

analysis in Chapter 6, the Rexolite and Torlon samples show different straight line regions separated by shoulders, suggesting changing breakdown mechanisms.

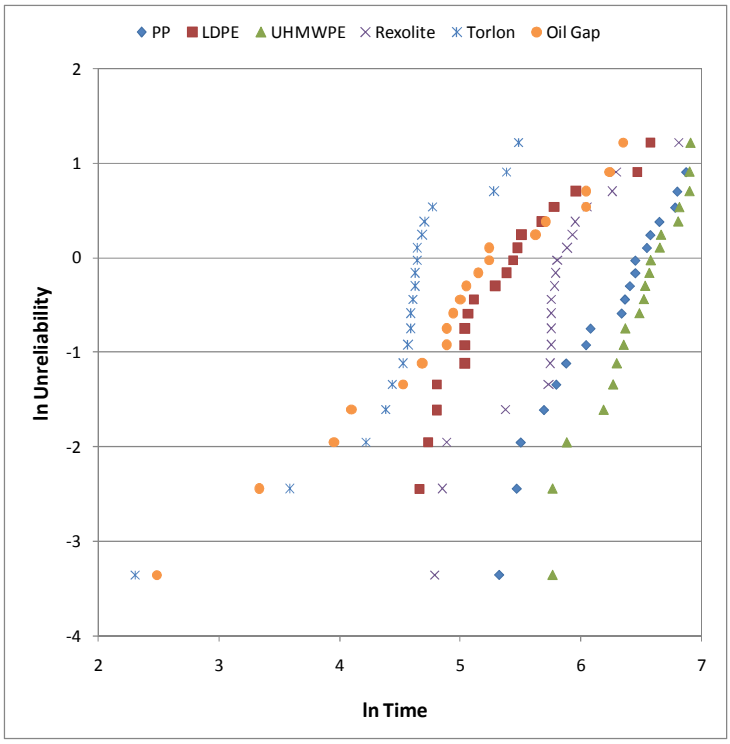

Figure 7.17. Weibull plots of time to breakdown data for peak applied field 700 kV/cm (*dV/dt* 245 kV/µs).

In Figure 7.18, the order of the plots follows the rank order identified in section 7.2.2, with the open oil gap showing the longest times to breakdown, followed by gaps bridged by UHMWPE, PP, and LDPE samples, respectively. The four curves are more separated for the lower ranked breakdown times when compared with the higher ranked times – there is a clear separation between these four curves and those for gaps bridged with Rexolite and Torlon samples.

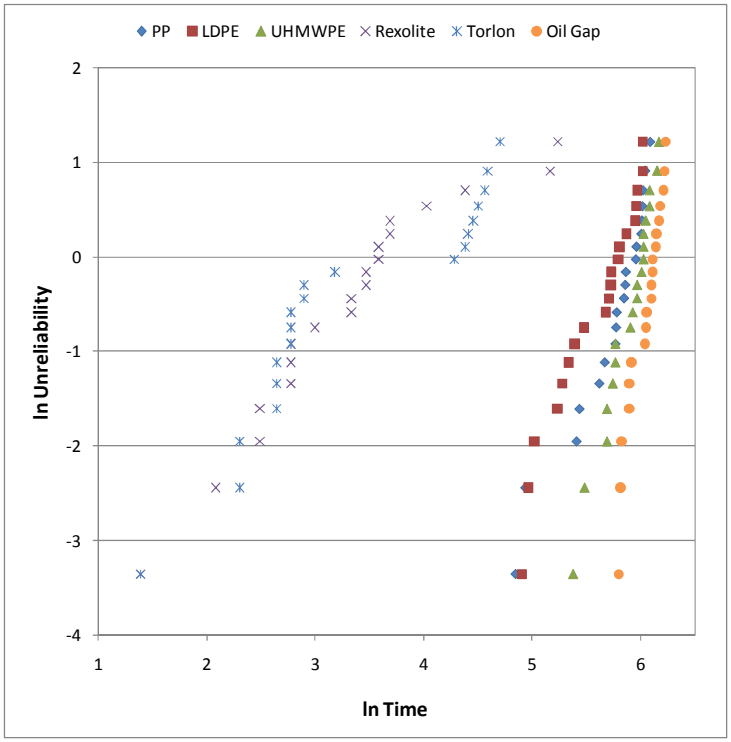

Figure 7.18. Weibull plots of time to breakdown data for peak applied field 1 MV/cm (*dV/dt* 350 kV/µs).

7.4 DISCUSSION AND CONCLUSIONS

The impulse breakdown characteristics of liquid-solid gaps between plane-parallel electrodes have been investigated when subjected to four different levels of peak electrical field/rate of voltage rise. It was found that a peak field of 200 kV/cm (70 kV/µs) could be applied to all tested gaps 20 times without resulting in breakdown. For the open oil gap, and for a gap bridged with solid materials of ε_r close to that of the surrounding oil (ε_r = 2.2), namely PP (ε_r = 2.25), LDPE (ε_r = 2.2), and Rexolite (ε_r = 2.5), an electrical field of 400 kV/cm (140 kV/µs) could also be applied 20 times without inducing breakdown events. Bridging of the inter-electrode gap with higher ε_r solids, namely UHMWPE (ε_r = 3.0) and Torlon (ε_r = 3.9), resulted in breakdown events at 400 kV/cm.

At higher field levels (and rates of voltage rise) of 700 kV/cm (245 kV/µs) and 1 MV/cm (350 kV/µs), all 20 applied voltage impulses resulted in a breakdown event

for all five materials, and also for the open oil gap. Ultra-high molecular weight polyethylene showed the longest times to breakdown, and hence highest breakdown voltages, after the open oil gap under these conditions.

For the field levels tested, the probability of breakdown over 20 applied impulses was usually either 0 or 1, that is, breakdown did not occur following any of the impulse applications, or breakdown did occur following each of the 20 impulse applications. The only test where this was not the case was with an UHMWPE sample at 400 kV/cm, where the probability of breakdown was 0.55. In this test, breakdown did not always follow in subsequent shots following the occurrence of the first breakdown event, and the sequence was: no breakdown for shots 1-7; breakdown for shots 8-13; no breakdown for shots 14-15; and breakdown following shots 16-20. This reveals that even though the samples surface is damaged by each breakdown event, the re-application of the same electric field does not always result in breakdown in subsequent shots.

At such short time intervals and high *dV/dt*, a streamer mechanism of breakdown can be assumed. As stated in section 4.2.1, Forster and Wong [154] have previously reported on streamers in hydrocarbons under uniform-field conditions, at electric fields 300-500 kV/cm.

By modeling streamers as spheres or cylinders, Massala and Lesaint [171] calculated the electric fields associated with streamers in large gaps in mineral oil, and identified a threshold field ~400 kV/cm that defines streamer propagation mode: streamers propagate in the slow 2nd mode if the streamer field is below 400 kV/cm, and in fast 3rd or 4th modes if the field is above this threshold value.

In terms of the breakdown mechanism, the image charge theory described in [135] appears to be corroborated by the results, insofar as gaps with solids of higher permittivity are broken down at lower voltages than those with solids of permittivity closer to that of the oil – this result was also found by the authors of [115] under non-uniform field geometry. Similar concepts are explored for ac voltages in [10], where

the authors propose two different breakdown mechanisms for an oil-pressboard interface: the first is the electric double layer at the liquid-solid interface, where space charge can drift due to the applied electric field and cause tracking; and the second is the oil boundary layer, associated with high-energy flashover.

Devins and Rzad [54] found that streamer velocities in oil gaps with a PMMA spacer were very similar to those in open oil gaps with point-plane geometries. The average streamer velocities calculated for liquid-solid gaps in the present paper are comparable to those presented in [165] for point-plane gaps in mineral oil. A transition from slow streamers of velocity 3.6 km/s to fast streamers of velocity 17 km/s was observed in [54] under point-plane geometry in oil, with the transition occurring for impulses of rise-time 1.2 μs, but not found for impulses of rise-time 4 μs. In the present study, the upper average streamer velocity increased from 5 km/s at *dV/dt* 245 kV/μs to over 10 km/s at 350 kV/μs. Wang *et al*. applied shorter impulses, of duration ~40 ns, to cylindrical samples of PMMA in uniform fields in insulating oil, and found that the breakdown field associated with surface discharges increased from 450 kV/cm to 700 kV/cm when the rate of voltage rise was raised from 11 kV/ns to 22 kV/ns [6].

While the calculated average streamer velocities presented in Tables 7.4-7.6 can provide useful estimates for comparison with different levels of peak applied field, it is important to note that the statistical delay time associated with the appearance of an initiatory electron may be reduced as the rate of voltage rise is also increased. The assumption in calculating streamer velocity using information only on the time to breakdown and the inter-electrode gap length is that the statistical time lag will be short at such high electric field and rate of voltage rise, and therefore, the major contributor to the time to breakdown will be the formative time lag associated with streamer development and propagation. As previously discussed in Chapter 4, spatial and temporal imaging of the streamer development would be required in order to directly investigate streamer velocity.

Katahoire *et al*. [75] found that the breakdown strength of a silicone oil/XLPE interface was reduced compared to that of an open silicone oil gap when subjected to positive-polarity lightning impulses (1.2/50 μs). The measured surface breakdown strength decreased from 500 kV/cm for a 2.5 mm gap to 350 kV/cm for a 7.5 mm gap, compared with respective values of 540 kV/cm and 380 kV/cm for the open oil gap. Open oil gaps were also found to yield the highest breakdown voltages in the present work. At 245 kV/μs, the average breakdown voltage of the open oil gap was 247±1.5 kV, reducing to a maximum of 234±22 kV for an UHMWPE sample, and to a minimum of 182±17 kV for Torlon. The average breakdown voltage of the open oil gap at 350 kV/μs was 298±22 kV, falling to 285±33 kV for UHMWPE, and to 175±19 kV for Torlon, again the maximum and minimum values.

Ultra-high molecular weight polyethylene appears to be desirable for use as an oil-immersed insulator due to its ability to hold-off breakdown for longer than the other materials when subjected to over-voltages. The high ε_r, however, means that breakdown events can be initiated at lower levels of applied electrical field than for materials with ε_r more closely matched to that of the oil.

In terms of the ranking in section 7.2.2, this can potentially be explained in terms of permittivity, apart from UHMWPE (see Table 7.3). Torlon has highest ε_r and the shortest times to breakdown. Rexolite shows the second shortest times to breakdown, and has ε_r higher than that of the oil. Polypropylene and LDPE have very similar ε_r, which is also closely matched to that of the oil, and reflect longer times to breakdown than Rexolite and Torlon. Ultra-high molecular weight polyethylene, however, has higher ε_r than Rexolite, but yields longer pre-breakdown delay times, suggesting that another property of UHMWPE influences streamer initiation conditions to an extent that flashover is inhibited for longer. The values of surface and volume resistivity, listed in Table 3.1 (section 3.3.2), are similar for all five materials. A potential explanation for the longer pre-breakdown delay times consistently measured for UHMWPE could be the high-molecular-weight additive [111].

Chapter 8

CONCLUSIONS AND FUTURE WORK

8.0 CONCLUSIONS

The interface between different dielectric media can often prove to be the weakest link in a composite high-voltage or pulsed-power insulation system, and this study has focused on experimental determination of the breakdown behaviour and characteristics associated with discharges along polymer surfaces immersed in mineral oil. In order to evaluate such systems, two applied voltage wave-shapes were applied to three different electrode geometries, with inter-electrode gap lengths of up to 10 mm, and their impact investigated.

Open oil gaps were initially characterised in order to provide reference data for comparison with the behaviour of the various liquid-solid gaps tested throughout the rest of the study. For non-uniform geometries subjected to over-voltages, the pre-breakdown delay times were found to be, in general, 2.5-3 times longer for impulses rising to peak value in 1 μs than the delay times arising for those impulses of rise-time 100 ns. This tends to suggest that streamers were initiated and propagated with higher velocity using faster-rising impulses. With pin-plane geometry for example, the average propagation velocity inferred from the time-to-breakdown data was 10-12 km/s for rise-time 1 μs, and this was found to increase to over 40 km/s for impulse voltages rising in 100 ns.

For breakdown investigations undertaken with plane-parallel electrodes, the highest average electric field associated with breakdown of a 4-mm oil gap was over 750 kV/cm. This level of breakdown field was recorded in over-voltage tests using a 1-μs rise-time impulse. The highest breakdown field for a 100-ns rise-time impulse was ~450 kV/cm (8-mm oil gap), although this field corresponds with a breakdown event which took place after the peak level on the impulse falling edge. It is

anticipated that this field would be much higher had breakdown only occurred on the 100-ns rising edge, and an experimental arrangement to achieve this is discussed in section 8.1.

In addition to over-voltage tests, breakdown initiation measurements were performed in order to determine the minimum applied fields required to induce breakdown of the various gaps investigated. This involved the application of multiple impulses, the majority of which did not result in electrical breakdown. For the collar-plane geometry, the implied streamer velocities were found to be similar for over-volted gap tests and in the breakdown initiation measurements. For pin-plane geometry however, the streamer velocities in over-volted gaps were found to be up to 24 km/s faster than velocities found for breakdown-initiation measurements.

For composite gaps, cylindrical solid samples of different geometry were treated using both voltage wave-forms. The solid polymers tested were:

- polypropylene (PP);
- low-density polyethylene (LDPE);
- ultra-high molecular weight polyethylene (UHMWPE);
- Rexolite; and
- Torlon

For over-volted gaps with voltages rising to peak magnitude 400 kV in 100 ns (dV/dt = 4 kV/ns), LDPE showed a relatively narrow variation in breakdown voltage/time, and this was the only material not to suffer any bulk (solid) breakdown damage in non-uniform fields despite being repeatedly subjected to over-voltages and breakdown.

A range of different sample geometries were tested, and the results have shown that the average breakdown voltage can be raised by up to 23% by introducing a 'shoulder' of reduced diameter at the end of the solid sample in contact with the high-voltage electrode. This is thought to be due to the reduction in applied field at

the interface, which has an influence on the generation of initiatory electrons. In future work, an impulse generator of higher voltage output would allow for longer samples to be treated using plane-parallel electrode geometry, allowing for confirmation of this effect for uniform-field conditions.

Measurements of the average applied fields required to initiate surface discharge events have revealed that the applied field threshold necessary to cause breakdown was lowered following the first breakdown event. The discharge field was then found to remain fairly constant for subsequent discharges, suggesting that the surface impact or conditioning caused by the first surface breakdown is more damaging and significant to the sample integrity than the cumulative damage arising from subsequent discharges. From a design and practical perspective, the measurements associated with the later breakdown events, when the applied field begins to level out, should be consulted in preference to the measurements associated with the first breakdown. The results of this type of measurement for different voltage wave-shapes relevant to pulsed-power machines could provide an opportunity to incorporate a conservative surface flashover level in the design stage.

Polypropylene has shown to have the highest levels of average applied field necessary to initiate surface breakdown events in all electrode configurations tested, namely ~640 kV/cm in uniform fields, and ~325 kV/cm in non-uniform fields.

Data recorded which measure the time to breakdown are important in determining the profile and duration of an impulsive voltage that can be applied to a given length of insulator without inducing a breakdown event, and the longer times to breakdown shown by UHMWPE in all measurements suggest that this material could hold off breakdown for longer than the other materials for the same level of applied voltage.

When the rise-time was 1 μs, PP, LDPE, and UHMWPE all exhibited desirable properties for use as oil-immersed insulators, with high breakdown voltages/fields in non-uniform field measurements. It was found that the average breakdown voltage was increased by up to 26% for samples with a shoulder compared to the

corresponding unmodified samples. An increase in time to breakdown of over 70% was found for the LDPE sample with a shoulder compared to the unmodified LDPE sample. This data suggests that the introduction of a shoulder into the sample geometry can act to increase the delay time to breakdown by influencing the conditions for streamer initiation at the interface of the insulation system and the high-voltage electrode.

The short pre-breakdown delay times for Rexolite and Torlon samples suggested that there were faster streamer propagation modes present for these materials. An ageing process was identified as taking place for Rexolite through a Weibull statistical analysis, as detailed in Chapter 6, and this can potentially explain the increased propagation velocities observed for this material. In one test the increase was particularly significant, where the implied propagation velocity increased from 11 km/s to 200 km/s. As all Rexolite and Torlon samples were found to have suffered bulk breakdown damage, resulting in significant physical sample degradation, it appears clear that the propagation of discharges via paths other than the original liquid-solid interface is central to the appearance of faster streamers, resulting in consistently shorter times to breakdown for these materials. The high permittivity value of Torlon ($\varepsilon_r = 3.9$) may contribute to this effect, through bending of the electric field lines towards the solid material, leading to a higher probability of streamers penetrating the bulk of the solid material rather than propagating to the earth plane over the surface of the dielectric through the liquid-solid interface.

Comparing the rising-edge breakdown results with those obtained when breakdown was allowed to occur on the falling edge of the impulse in Chapter 5, some similarities in the influence of the electrode/sample geometry were observed. The times to breakdown reported in both series of experiments were generally longer for the pin-plane geometry as compared with those recorded for the collar-plane geometry. Furthermore, the breakdown voltages recorded using the collar electrode geometry were higher, by up to 23%, for the type II (shoulder) samples as compared with those found for the type III (no modifications) samples.

The effect of the rate of voltage rise was studied under plane-parallel electrode geometry conditions, where higher breakdown voltages and longer pre-breakdown delay times were always recorded for an open oil gap. The introduction of a solid spacer into the oil gap, therefore, serves to reduce the delay time to breakdown, and hence, the breakdown voltage. It is anticipated that the presence of the solid surface enables the propagation of streamers in faster modes. This can be explained by considering the electric-double layer theory proposed by Korobeynikov *et al*. [135]. In this theory, negative image forces result in increasing ion concentration at the liquid-solid interface when the solid has higher relative permittivity than the surrounding liquid. The increased conductivity at the interface results in a higher probability of surface flashover, manifested in shorter pre-breakdown delay times.

When ranked by decreasing time to breakdown, the gaps consistently followed this order when subjected to impulse voltages of different levels of peak electric field and rate of voltage rise:

1. Open oil gap
2. UHMWPE
3. PP
4. LDPE
5. Rexolite
6. Torlon

While the open oil gap and gaps bridged with solid materials of permittivity close to that of the surrounding oil were able to withstand 20 impulses of peak electrical field 400 kV/cm (dV/dt = 140 kV/μs), bridging of the gap with higher permittivity solids resulted in the occurrence of breakdown events. It can, therefore, be concluded that the matching of the permittivity of the chosen solid spacer to that of the surrounding oil is an important consideration in order to maximise the voltage required to cause breakdown of the gap – that is, to ensure that the breakdown voltage is close to that exhibited by the open oil gap.

Despite the longer times to breakdown shown by the UHMWPE dielectric for all of the experiments, its high permittivity (ε_r = 3.0) can mean that this material is a poor choice for use as mineral-oil immersed insulation. This is because surface breakdown events can be initiated at lower levels of electric field than for materials with permittivity closer to that of the surrounding mineral oil. It appears that another aspect associated with UHMWPE is the influence on streamer-initiation conditions, to the extent that flashover can be inhibited for longer. This behaviour suggests that UHMWPE would be suitable for use as solid supports in liquids of higher permittivity, such as vegetable and seed oils which have a permittivity of around 3.0 [172], and in ester fluids which have a permittivity of around 3.2 [165]. A study of the breakdown and pre-breakdown characteristics of such composite insulation systems would provide an interesting theme for future work, and may enable discernment as to whether or not the longer times are truly associated with reduced streamer propagation velocities, whether there is indeed an influence on the temporal behaviour of initiatory electron production, or a combination of both of these effects.

If the UHMWPE material is removed from the above ranking due to concerns over the issue of permittivity mismatch, then it is clear that the materials of permittivity closely matched to that of the oil – namely PP and LDPE – give the most stable performance, in terms of longer times to breakdown, higher breakdown voltages, and higher levels of applied electric field required to initiate breakdown events.

In breakdown initiation measurements for a 100/600 ns wave-shape, detailed in Chapter 5, the following rank order of the applied field necessary to cause breakdown was observed:

1. PP
2. LDPE
3. Rexolite
4. UHMWPE
5. Torlon

This ranking now closely follows with the rank of increasing permittivity. Although it was difficult to differentiate between the applied field required to initiate the first surface breakdown event for PP (ε_r = 2.25) and LDPE (ε_r = 2.2), the applied field for LDPE dropped slightly with increasing breakdown number, while the applied field remained relatively constant for PP. As a consequence of this behaviour, therefore, PP has been ranked highest in the above list.

A useful guide for the determination of conservative safety margins is the finding that a 200 kV/cm (dV/dt = 70 kV/μs) pulse could be applied 20 successive times to a 3.5-mm open oil gap, and to gaps bridged by 3.5-mm long cylindrical samples of all materials, without resulting in electrical breakdown for the 1/6.5 μs wave-shape.

Overall, it can be concluded that Rexolite and Torlon are poor choices to act as oil-immersed insulators for the conditions investigated. Gaps bridged by these materials are able to facilitate the propagation of streamers in faster modes, reducing the pre-breakdown delay times and, hence, resulting in a corresponding reduction in the breakdown voltages. The combined effects of bulk solid discharges as well as surface breakdown events act to remove large portions of the material from the discharge sites, and as well as the impact on the insulation integrity, this could additionally lead to mechanical instability if undiscovered in large-scale industrial machines which are fully immersed in insulating oil.

While UHMWPE yielded longer times to breakdown in all measurements, its high permittivity means that this material is not ideally suited for use in mineral oils with permittivity around 2.2.

Polypropylene and LDPE, the materials with permittivity that are closely matched to that of the mineral oil, yield the highest levels of applied field necessary to initiate surface breakdown events, and these materials are recommended as the most appropriate choice, of the materials investigated, for use as mechanical supports in mineral-oil immersed high-voltage systems, operating with similar voltage wave-shapes and levels of applied field to those reported here.

Overall, with regard to industrial-scale pulsed-power machines, the broad study aim of providing comparative data on the behaviour of solid dielectrics immersed in insulating oil has been achieved. The data on electric field levels required to initiate breakdown and the time to breakdown can be utilised in conjunction with the corresponding Weibull statistical analyses, to facilitate a more robust design of insulators and material choice to be used in pulsed-power applications.

8.1 FUTURE WORK

As stated throughout the experimental results sections of this thesis, information on streamer propagation velocity has been limited to estimates given by the ratio of the inter-electrode gap length and the time to breakdown. The deployment of a fast optical detection system, incorporating a "fast, intensified charge coupled device (CCD) camera" [173] would provide interesting future work, with the aim of building a detailed picture of streamer development at liquid-solid interfaces.

Negative-polarity impulse voltages were utilised throughout the present study, and a repeat of the measurements with positive impulses would allow for the polarity effects discussed in Chapter 2 to be confirmed for the regimes investigated here. This would allow closer understanding of the influence of polarity and, where appropriate, may influence the polarity of choice for particular applications.

In order to study breakdown events occurring only on the 100-ns rising edge, the applied impulse should be chopped at peak voltage, thereby removing the possibility for streamers propagating in slower modes to cause breakdown on the falling edge. Future work should include the design of a suitable crowbar switch capable of reliably chopping voltages of magnitude up to 500 kV after 100 ns with low jitter. Such a crowbar system would most likely comprise a point-plane electrode system immersed in distilled water [174]. For higher voltages in the multi-megavolt regime, a pair of spherical electrodes immersed in mineral oil could be utilised as a crowbar [175]. The applied field necessary to cause breakdown on the 100-ns rising edge

could then be compared with the fields reported in breakdown initiation measurements in Chapter 5 herein. Higher peak voltages, and hence a higher-voltage crowbar system, may then become necessary to induce surface breakdown events, however, particularly for sample lengths around 8-10 mm.

It was not possible to perform breakdown initiation measurements with breakdown only occurring on the rising edge for the 1/6.5 μs wave-shape in the present study, due to the tendency for breakdown events to occur with pre-breakdown delay times of up to 4 μs as the voltage was increased in increments of ~20 kV. Again, a crowbar switch capable of diverting the energy associated with the wave-tail of the impulse away from the load would allow for these measurements to be made.

Some evidence was found to suggest that the introduction of a shoulder on the dielectric solid can increase the breakdown voltage compared to unmodified cylindrical samples. This result was found in non-uniform fields, and further study should include both confirmation of this result, and a detailed investigation of the effect of a shoulder and other sample modifications on the uniform-field breakdown characteristics. Such a study should focus on whether the influence is directly associated with initiatory electron production, or electric-field suppression at the most critical interface.

Further work is also required to expand upon the breadth of knowledge base, particularly regarding modifications to electrode/sample geometry and pre-treatment procedures that will facilitate the minimisation of future pulsed-power systems. Modelling of a variety of geometries using an electrostatic field solver would provide an initial basis for the practical investigation of modified geometries. The influence of space charge in both the liquid and solid dielectric should be incorporated into this type of study to enable analysis of the local field enhancements likely to occur in practical systems due to charge injection from the electrodes.

Advances in both liquid and solid dielectrics with the inclusion of nano-particles are also likely to offer improvements in the breakdown strength of various liquid-solid

insulation systems [176], [177]. Detailed experimental and statistical analyses of the breakdown voltages for different composite insulation systems with nano-particle inclusions should be conducted, for different applied voltage wave-forms applicable to pulsed-power systems. For example, a comparative study of the breakdown characteristics of low-density polyethylene samples with silicone dioxide nano-particle inclusions, and of conventional low-density polyethylene samples, when immersed in a dielectric liquid, would allow for definitive conclusions to be drawn as to the tangible benefits offered by the introduction of such insulation systems into pulsed-power machines. The desired outcome, of course, would be the eventual production of more compact machines, or at the very least, a significant increase in their reliability.

In conclusion, the experimental results, interpretation, and discussion presented here can provide a baseline for the establishment of more robust selection criteria, which can hopefully contribute to the eventual development of reliable design rules and test procedures similar to those used in the power industry.

REFERENCES

[1] Y. Kamata, A. Miki, and S. Furukawa, "A singular flashover path observed on the surface of synthetic-resin-bonded paper cylinders immersed in transformer oil under switching impulse voltage conditions," *IEEE Trans. Electr. Insul.*, vol. 26 (2), pp. 300-310, 1991.

[2] Y. Mizuno, T. Kimura, and K. Naito, "Surface flashover along polymeric rods partially immersed in LN_2," *IEEE Trans. Dielectr. Electr. Insul.*, vol. 5 (6), pp. 809-813, 1998.

[3] H. Hama, H. Yamamoto, S. Sakuma, K. Takatsuka, and T. Yamauchi, "Surface flashover characteristic of disc-type spacer system initiated by wedge shaped gas gap and its improvement," *IEEE Trans. Power Del.*, vol. 8 (3), pp. 1070-1079, 1993.

[4] X. Jiang, J. Hu, Z. Zhang, and J. Yuan, "Switching impulse flashover performance of different types of insulators at high altitude sites of above 2800 m," *IEEE Trans. Dielectr. Electr. Insul.*, vol. 15 (5), pp. 1340-1345, 2008.

[5] M. Jayaraju, P.S. Chandramohanan Nair, and B.R. Prabhakar, "Oscillatory switching impulse flashover characteristics of insulator strings under normal weather conditions," *Electr. Power Comp. Syst.*, vol. 31 (2), pp. 171-188, 2003.

[6] J. Wang, Y.X. Zhou, P. Yan, W.L. Huang, G.J. Li, S.C. Zhang, and G.S. Sun, "Study on dielectric surface discharge in transformer oil under high voltage nanosecond pulse," *J. Electrostatics*, vol. 63 (6-10), pp. 665-671, 2005.

[7] L. Guangjie, W. Jue, Y. Ping, Z. Shichang, and S. Yaohong, "Experimental study on statistical characteristics of surface flashover under nanosecond pulse in transformer oil," *Proc. 2006 IEEE International Power Modulator Conference*, pp. 97-99, 2006.

[8] H. Borsi, K. Dumke, and E. Gockenbach, "Relation between faults and generated gases in transformer liquids," *Proc. 13th IEEE International Conference on Conduction and Breakdown in Dielectric Liquids*, pp. 487-490, 1999.

[9] J.H. Tortai, "Insulating properties of some liquids after an electrical arc," *IEEE Trans. Dielectr. Electr. Insul.*, vol. 9 (1), pp. 3-9, 2002.

[10] P.M. Mitchinson, P.L. Lewin, and B.D. Strawbridge, "Tracking and surface discharge at the oil-pressboard interface," *IEEE Electr. Insul. Mag.*, vol. 26 (2), pp. 35-41, 2010.

[11] T. Takuma, T. Kouno, and H. Matsuda, "Field behaviour near singular points in composite dielectric arrangements," *IEEE Trans. Electr. Insul.*, vol. EI-13 (6), pp. 426-435, 1978.

[12] T. Takuma, T. Kawamoto, and H. Fujinami, "Effect of conduction on field behaviour near singular points in composite medium arrangements," *IEEE Trans. Electr. Insul.*, vol. EI-17 (3), pp. 269-275, 1982.

[13] T. Takuma, "Field behaviour at a triple junction in composite dielectric arrangements," *IEEE Trans. Electr. Insul.*, vol. 26 (3), pp. 500-509, 1991.

[14] T. Kawamoto, T. Takuma, H. Goshima, H. Shinkai, and H. Fujinami, "Triple-junction effect and its electric field relaxation in three dielectrics," *Electrical Engineering in Japan*, vol. 167 (1), pp. 1-8, 2009.

[15] D. Kind, and K. Feser, "Fundamental principles of high-voltage test techniques," in *High Voltage Test Techniques*, 2nd ed. London: Newnes, 2001, ch. 1, pp. 1-109.

[16] K.H. Schoenbach, M. Kristiansen, and G. Schaefer, "A review of opening switch technology for inductive energy storage," *Proc. IEEE*, vol. 72 (8), pp. 1019-1040, 1984.

[17] A.H. Bushnell, "Interfacing pulsed power systems to switching power supplies," *Proc. 2002 IEEE International Power Modulator Conference*, pp. 290-292, 2002.

[18] J. Mankowski, and M. Kristiansen, "A review of short pulse generator technology," *IEEE Trans. Plasma Sci.*, vol. 28 (1), pp. 102-108, 2000.

[19] J.R. MacDonald, M.A. Schneider, J.B. Ennis, F.W. MacDougall, and X.H. Yang, "High energy density capacitors," *Proc. 2009 IEEE Electrical Insulation Conference*, pp. 306-309, 2009.

[20] R.D. Edwards, and M.A. Sinclair, "High density relativistic E-beam focusing," *Proc. IEE Colloquium Pulsed Power '97*, pp. 24/1-2, 1997.

[21] M.A. Sinclair, and T.F. Bryant, "E Minor upgrade," *Proc. Pulsed Power Plasma Science 2001*, vol. 2, pp. 1499-1501, 2001.

[22] M. Sinclair, "Current radiographic pulsed power machines at AWE," *Proc. 15th IEEE International Pulsed Power Conference*, pp. 124-127, 2005.

[23] D. Short, M. Sinclair, D. Rose, and J. Maenchen, "LSP simulations of the paraxial diode and comparisons with experimental data," *Proc. 14th IEEE International Pulsed Power Conference*, vol. 2, pp. 744-747, 2003.

[24] I. Crotch, J. Threadgold, M. Sinclair, and A. Pearce, "Self magnetic pinch diode experiments at AWE," *Proc. 14th IEEE International Pulsed Power Conference*, vol. 1, pp. 507-509, 2003.

[25] R.C. Fletcher, "Production and measurement of ultra-high speed impulses," *Rev. Sci. Instruments*, vol. 20 (12), pp. 861-869, 1949.

[26] A.D. Blumlein, *UK patent* No. 589127, 1941.

[27] I.C. Somerville, S.J. MacGregor, and O. Farish, "An efficient stacked-Blumlein HV pulse generator," *Meas. Sci. Technol.*, vol. 1 (9), pp. 865-868, 1990.

[28] W.J. Sarjeant, and R.E. Dollinger, "Introduction to high-power electronics," *High-power electronics*, 1st ed., W.J. Sarjeant, R.E. Dollinger, B.J. Peterson, Ed. TAB BOOKS Inc., 1989, ch. 1, pp. 1-27.

[29] D.L. Pulfrey, "A generator of high voltage pulses with subnanosecond risetime and adjustable duration," *J. Phys. E: Sci. Instrum.*, series 2, vol. 2, pp. 503-505, 1969.

[30] J.R. Beveridge, K. Wall, S.J. MacGregor, J.G. Anderson, N.J. Rowan and O. Farish, "Pulsed electric field inactivation of spoilage microorganisms in alcoholic beverages," *Proc. IEEE*, vol. 92 (7), pp. 1138-1143, 2004.

[31] R.A. Fitch, and V.T.S. Howell, "Novel principle of transient high-voltage generation," *Instn. Elec. Engrs. – Proc.*, vol. 111 (4), pp. 849-855, 1964.

[32] W.L. Willis, "Pulse-voltage circuits," in *High-power electronics*, 1st ed., W.J. Sarjeant, R.E. Dollinger, B.J. Peterson, Ed. TAB BOOKS Inc., 1989, ch. 3, pp. 87-116.

[33] G.J. Rohwein, "High-voltage air core pulse transformers," *High-power electronics*, 1st ed., W.J. Sarjeant, R.E. Dollinger, B.J. Peterson, Ed. TAB BOOKS Inc., 1989, ch. 9, pp. 276-296.

[34] P.N. Graneau, J.O. Rossi, M.P. Brown, and P.W. Smith, "A high-voltage transmission-line pulse transformer with very low droop," *Rev. Sci. Instrum.*, vol. 67 (7), pp. 2630-2635, 1996.

[35] J. Millman, and H. Taub, *Pulse, digital, and switching waveforms*, New York: McGraw Hill, ch. 3, 1985.

[36] O. Maulat, M. Roche, F. Le Coeur, O. Lesaint, Y. Arnal, and J. Pelletier, "New line of high voltage high current pulse generators for plasma-based ion implantation," *J. Vac. Sci. Technol. B*, vol. 17 (2), pp. 879-882, 1999.

[37] G.J. Rohwein, "A three megavolt transformer for PFL pulse charging," *IEEE Trans. Nucl. Sci.*, vol. NS-26 (3), pp. 4211-4213, 1979.

[38] D. Wang, J. Qiu, and K. Liu, "All-solid-state repetitive pulsed-power generator using IGBT and magnetic compression switches," *IEEE Trans. Plasma Sci.*, vol. 38 (10), pp. 2633-2638, 2010.

[39] Y.S. Mok, H.W. Lee, and Y.J. Hyun, "Flue gas treatment using pulsed corona discharge generated by magnetic pulse compression modulator," *J. Electrostatics*, vol. 53 (3), pp. 195-208, 2001.

[40] A.A. Neuber, and J.C. Dickens, "Magnetic flux compression generators," *Proc. IEEE*, vol. 92 (7), pp. 1205-1215, 2004.

[41] R.E. Reinovsky, W.L. Atchison, J.H. Goforth, I.R. Lindemuth, E.A. Lopez, and S.P. Marsh, "Caballero: A high current flux compressor system for 100 MJ solid liner experiments," *IEEE Trans. Plasma Sci.*, vol. 26 (5), pp. 1454-1462, 1998.

[42] E. Marx, *Deutsches Reichpatent* No. 455 933, 1923.

[43] F. Heilbronner, "Firing of multistage impulse generators," *Elektrotech Z Ausg A*, vol. 92 (6), pp. 372-376, 1971.

[44] R.A. Cooper, J.B. Ennis, W.J. Gratza, R. Miller, S.K. Lam, and P.S. Sincerny, "100 kV capacitor development for fast Marx generators," *Proc. 14th IEEE International Pulsed Power Conference*, vol. 1, pp. 530-533, 2003.

[45] V.Y. Ushakov, "Impulse breakdown of liquids," in *Power Systems*, Berlin Heidelberg: Springer-Verlag, 2007, pp. XI-XXVI.

[46] E. Schamiloglu, K.H. Schoenbach, and R. Vidmar, "Basic research on pulsed power for narrowband high power microwave sources," *Proc. SPIE Int. Soc. Opt. Eng.*, vol. 4720, pp. 1-9, 2002.

[47] V.M. Atrazhev, V.S. Vorob'ev, I.V. Timoshkin, M.J. Given, and S.J. MacGregor, "Mechanisms of impulse breakdown in liquid: The role of Joule heating and formation of gas cavities," *IEEE Trans. Plasma Sci.*, vol. 38 (10), pp. 2644-2651, 2010.

[48] J. Qian, R.P. Joshi, K.H. Schoenbach, M. Laroussi, E. Schamiloglu, and C.G. Christodoulou, "Percolative model of electric breakdown in liquid dielectrics," *IEEE Trans. Plasma Sci.*, vol. 30 (5), pp. 1931-1938, 2002.

[49] B. Singh, W.G. Chadband, C.W. Smith, and J.H. Calderwood, "Prebreakdown processes in electrically stressed insulating liquids," *J. Phys. D: Appl. Phys.*, vol. 5 (8), pp. 1457-1466, 1972.

[50] T.J. Gallagher, *Simple liquid dielectrics*, Clarendon Press, Oxford, 1975.

[51] A.H. Sharbaugh, J.C. Devins, and S.J. Rzad, "Progress in the field of electrical breakdown in dielectric liquids," *IEEE Trans. Electr. Insul.*, vol. 13 (4), pp. 249-276, 1978.

[52] E.O. Forster, "Research in the dynamics of electrical breakdown in liquid dielectrics," *IEEE Trans. Electr. Insul.*, vol. 15 (3), pp. 182-185, 1980.

[53] J.C. Devins, S.J. Rzad, and R.J. Schwabe, "Breakdown and prebreakdown phenomena in liquids," *J. Appl. Phys.*, vol. 52 (7), pp. 4531-4545, 1981.

[54] J.C. Devins, and S.J. Rzad, "Streamer propagation in liquids and over liquid solid interfaces," *IEEE Trans. Electr. Insul.*, vol. EI-17 (6), pp. 512-516, 1982.

[55] R.E. Hebner, E.F. Kelley, G.J. FitzPatrick, and E.O. Forster, "The effect of pressure on streamer inception and propagation in liquid hydrocarbons," *Proc. 9th International Conference on Conduction and Breakdown in Dielectric Liquids*, pp. 26a-26e, 1987.

[56] A. Beroual, "Electronic processes and streamer propagation phenomena in liquid dielectrics," *Arch. Electr. Eng.*, vol. 44 (4), pp. 579-592, 1995.

[57] A. Beroual, M. Zahn, A. Badent, K. Kist, A.J. Schwabe, H. Yamashita, K. Yamazawa, M. Danikas, W.G. Chadband, and Y. Torshin, "Propagation and structure of streamers in liquid dielectrics," *IEEE Electr. Insul. Mag.*, vol. 14 (2), pp. 6-17, 1998.

[58] O. Lesaint, ""Streamers" in liquids: relation with practical high voltage insulation and testing of liquids," *Proc. 2008 IEEE International Conference on Dielectric Liquids*, pp 1-6, 2008.

[59] R.E. Hebner, "Measurements of electrical breakdown in liquids," in *The Liquid State and its Electrical Properties*, E.E. Kunhardt, Ed., L.G. Christophoreau, Ed., L.H. Luessen, Ed. New York: Plenum Press, 1988, pp. 519-537.

[60] M. Haidra, and A. Denat, "Electron multiplication in liquid cyclohexane and propane," *IEEE Trans. Electr. Insul.*, vol. 26 (4), pp. 592-597, 1991.

[61] A. Denat, J.P. Gosse, and B. Gosse, "Electrical conduction of purified cyclohexane in divergent electric field," *IEEE Trans. Electr. Insul.*, vol. 23 (4), pp. 545-554, 1988.

[62] P. Gournay, and O. Lesaint, "A study of the inception of positive streamers in cyclohexane and pentane," *J. Phys. D: Appl. Phys.*, vol. 26 (11), pp. 1966-1974, 1993.

[63] L. Dumitrescu, O. Lesaint, N. Bonifaci, A. Denat, and P. Notingher, "Study of streamer inception in cyclohexane with a sensitive charge measurement technique under impulse voltage," *J. Electrostatics*, vol. 53 (2), pp. 135-146, 2001.

[64] M. Butcher, A.A. Neuber, M.D. Cevallos, J.C. Dickens, and H. Krompholz, "Conduction and breakdown mechanisms in transformer oil," *IEEE Trans. Plasma Sci.*, vol. 34 (2), pp. 467-475, 2006.

[65] T.V. Top, and O. Lesaint, "Streamer initiation in mineral oil part II: Influence of a metallic protrusion on a flat electrode," *IEEE Trans. Dielectr. Electr. Insul.*, vol. 9 (1), pp. 92-96, 2002.

[66] T.V. Top, G. Massala, and O. Lesaint, “Streamer propagation in mineral oil in semi-uniform geometry,” *IEEE Trans. Dielectr. Electr. Insul.*, vol. 9 (1), pp. 76-83, 2002.

[67] A. Beroual, and R. Tobazeon, “Prebreakdown phenomena in liquid dielectrics,” *IEEE Trans. Electr. Insul.*, vol. EI-21 (4), pp. 613-627, 1986.

[68] A. Beroual, and R. Tobazeon, “Effects of hydrostatic pressure on the prebreakdown phenomena in liquid dielectrics,” C.R. Acad. Sci. II, vol. 303 (12), pp. 1081-1084, 1986.

[69] A. Beroual, “Electronic and gaseous processes in the prebreakdown phenomena of dielectric liquids,” *J. Appl. Phys.*, vol. 73 (9), pp. 4528-4533, 1993.

[70] I. Timoshkin, S. MacGregor, M. Given, V. Atrazhev, and V. Vorob’ev, “Critical parameters of gas cavities in dielectric liquids stressed with high electric fields,” *Acta Phys. Pol. A*, vol. 115 (6), pp. 1022-1024, 2009.

[71] P.J. Leask, “Pulse breakdown strengths of liquid, gel and solid insulating materials using closely spaced spherical electrodes,” *Acta Phys. Pol. A*, vol. 115 (6), pp. 998-1000, 2009.

[72] N.G. Trinh, C. Vincent, and J. Régis, “Statistical degradation of large-volume oil insulation,” *IEEE Trans. Power App. Syst.*, vol. PAS-101 (10), pp. 3712-3721, 1982.

[73] O. Lesaint, and T.V. Top, “Streamer initiation in mineral oil part I: Electrode surface effect under impulse voltage,” *IEEE Trans. Dielectr. Electr. Insul.*, vol. 9 (1), pp. 84-91, 2002.

[74] W.R. Wilson, “A fundamental factor controlling the unit dielectric strength of oil,” *Trans. AIEE, Part III: Power App. Syst.*, vol. 72 (2), pp. 68-74, 1953.

[75] A.M.S. Katahoire, M.R. Raghuveer, and E. Kuffel, “Power frequency and impulse voltage breakdown along silicone oil/XLPE interface,” *IEEE Trans. Electr. Insul.*, vol. EI-15 (2), pp. 97-104, 1980.

[76] J.M. Lehr, F.J. Agee, R. Copeland, and W.D. Prather, “Measurement of the electric breakdown strength of transformer oil in the sub-nanosecond regime,” *IEEE Trans. Dielectr. Electr. Insul.*, vol. 5 (6), pp. 857-861, 1998.

[77] K.A. Zheltov, S.A. Korobkov, A.N. Petrenko, and V.F. Shalimanov, “Picosecond high-current electron accelerator,” *Instrum. Exp. Tech.*, vol. 33 (1), pp. 17-21, 1990.

[78] J.C. Martin, “Liquid breakdown,” in *J.C. Martin on Pulsed Power*, vol. 3, T.H. Martin, Ed., A.H. Guenther, Ed., and M. Kristiansen, Ed. New York and London: Plenum Press, 1996, ch. 7, pp. 177-179.

[79] W. Jue, Y. Ping, Z. Shichang, and S. Yaohong, “Transformer oil breakdown under nanosecond pulse,” *Proc. 2006 IEEE International Power Modulator Conference*, pp. 100-103, 2006.

[80] J. Mankowski, J. Dickens, and M. Kristiansen, “High voltage subnanosecond breakdown,” *IEEE Trans. Plasma Sci.*, vol. 26 (3), pp. 874-881, 1998.

[81] ASTM International, ASTM Standard D3300, “Standard test method for dielectric breakdown voltage of insulating oils of petroleum origin under impulse conditions,” 2000 (2006).

[82] Shell Lubricants Product Data Sheet, Lubricants Report: Diala AX Oil, http://www-static.shell.com/static/can-en/downloads/shell_for_businesses/oils_lubricants/3-17.pdf, accessed 4th May 2011.

[83] ESSO Imperial Oil Product Data Sheet: VOLTESSO, http://www.imperialoil.ca/Canada-English/Files/Products_Lubes/IOCAENWPOESVoltesso.pdf, accessed 4th May 2011.

[84] ABB Data Sheet: BIOTEMP Biodegradable Dielectric Insulating Fluid, http://library.abb.com/global/scot/scot252.nsf/veritydisplay/c1256b3c00492da685256c85006d74dc/$File/1LUS471050-LTE_BIO.PDF, accessed 4th May 2011.

[85] I.V. Timoshkin, M.J. Given, M.P. Wilson, and S.J. MacGregor, "Review of dielectric behaviour of insulating liquids," *Proc. 44th International Universities Power Engineering Conference*, 2009.

[86] T.O. Rouse, "Mineral insulating oil in transformers," *IEEE Electr. Insul. Mag.*, vol. 14 (3), pp. 6-16, 1998.

[87] D. Dohnal, and R. Frotscher, "Investigation and guidelines for the application of natural and synthetic ester liquids to tap-changers for power transformers," *Proc. 17th Conference of the Electric Power Supply Industry*, 2008.

[88] R. Bartnikas, "Electrical insulating liquids," *Engineering Dielectrics*, vol. 3, Philadelphia, pp. 284-301, 1994.

[89] C. Mazzetti, M. Pompili, and E.O. Forster, "Study of the time to breakdown in transformer oil under impulse conditions," *IEEE Trans. Electr. Insul.*, vol. 25 (6), pp. 1111-1116, 1990.

[90] L. Lundgaard, D. Linhjell, B. Gunnar, S. Svein, "Propagation of positive and negative streamers in oil with and without pressboard interfaces," *IEEE Trans. Dielectr. Electr. Insul.*, vol. 5 (3), pp. 388-395, 1998.

[91] British Standards Institution, British Standard BS 148:2009, "Reclaimed mineral insulating oil for transformers and switchgear," 2009.

[92] E. Kuffel, W.S. Zaengl, and J. Kuffel, "Breakdown in solid and liquid dielectrics," *High Voltage Engineering: Fundamentals*, 2nd ed., Newnes, 2000, ch. 6, pp. 367-394.

[93] D.L. Pulfrey, "The electrical breakdown of solid dielectrics in non-uniform fields," *J. Phys. D: Appl. Phys.*, vol. 5, pp. 647-655, 1972.

[94] W. Schottky, "Cold and hot electron discharges," *Z. Phys.*, vol. 14 (2), pp. 63-106, 1923.

[95] R.H. Fowler, and L. Nordheim, "Electron emission in intense electric fields," *Proc. R. Soc. Lond. A*, vol. 119, pp. 173-181, 1928.

[96] R. Cooper, C.H. Rowson, and D.B. Watson, "Intrinsic electric strength of polythene," *Nature*, vol. 197, pp. 663-664, 1963.

[97] J. Artbauer, and J. Griac, "Intrinsic electric strength of polythene in the high-temperature region," *Instn. Elec. Engrs. – Proc.*, vol. 112 (4), pp. 818 & 828-830, 1965.

[98] R.A. Fava, "Intrinsic electric strength and electromechanical breakdown in polythene," *Instn. Elec. Engrs. – Proc.*, vol. 112 (4), pp. 819-823 & 828-830, 1965.

[99] O.S. Gefle, S.M. Lebedev, and Y.P. Pokholkov, "Influence of morphology, irradiation and prestressing on the breakdown of LDPE," *2004 International Conference on Solid Dielectrics*," 2004.

[100] A. Bradwell, R. Cooper, and B. Varlow, "Conduction in polythene with strong electric fields and the effect of prestressing on the electric strength," *Instn. Elec. Engrs. – Proc.*, vol. 118 (1), pp. 247-254, 1971.

[101] Y. Suzuoki, Y. Matsukawa, S. Han, A. Fujii, J. Kim, T. Mizutani, M. Ieda, and N. Yoshifuji, "Study of space-charge effects on dielectric breakdown of polymers by direct probing," *IEEE Trans. Electr. Insul.*, vol. 27 (4), pp. 758-762, 1992.

[102] M. Ieda, T. Mizutani, Y. Suzuoki, and Y. Yokota, "Study of space charge effects in polyethylene by thermal-pulse current techniques," *IEEE Trans. Electr. Insul.*, vol. 25 (3), pp. 509-514, 1990.

[103] Y. Suzuoki, T. Furuta, H. Yamada, S.O. Han, T. Mizutani, M. Ieda, and N. Yoshifuji, "Study of space charge in polyethylene by direct probing: Effects of oxidation," *IEEE Trans. Electr. Insul.*, vol. 26 (6), pp. 1073-1079, 1991.

[104] I. Kitani, and K. Arii, "Impulse breakdown of polymer dielectrics in the ns range in divergent fields," *IEEE Trans. Electr. Insul.*, vol. EI-16 (2), pp. 134-139, 1981.

[105] J.H. Mason, "Breakdown of solid dielectrics in divergent field," *Instn. Elec. Engrs. – Proc.*, vol. 102 (C), pp. 254-263, 1955.

[106] J.C. Devins, S.J. Rzad, and R.J. Schwabe, "Prebreakdown phenomena in liquids: electronic processes," *J. Phys. D: Appl. Phys.*, vol. 9 (L87), 1976.

[107] I. Kitani, and K. Arii, "Impulse breakdown of prestressed polyethylene films in the ns range," *IEEE Trans. Electr. Insul.*, vol. EI-17 (3), pp. 228-233, 1982.

[108] D. Malec, R. Essolbi, M. Farkh, Hoang-The-Giam, B. Ai, N. Zebouchi, and M. Bendaoud, "Modelling of the dielectric breakdown phenomenon in polymer with the new parameter pressure," *J. Phys. D: Appl. Phys.*, vol. 27, pp. 360-364, 1994.

[109] Y. Maeda, and K. Yahagi, "Directional effect of impulse breakdown strength in polyethylene," *Japan. J. Appl. Phys.*, vol. 16 (1), pp. 179-180, 1977.

[110] N. Hozumi, M. Ishida, T. Okamoto, and H. Fukagawa, "The influence of morphology on electrical tree initiation in polyethylene under ac and impulse voltages," *IEEE Trans. Electr. Insul.*, vol. 25 (4), pp. 707-714, 1990.

[111] M. Kawahigashi, Y. Miyashita, and H. Kato, "Influence of morphology on electrical breakdown strength for polypropylene," *Proc. 3rd International Conference on Properties and Applications of Dielectric Materials*, pp. 1156-1160, 1991.

[112] D. Duffield, "Material at microwaves," *New Electron.*, vol. 7 (13), pp. 25, 1974.

[113] M.E. Savage, R. Starbird, G. Ziska, and R. Sharpe, "Automatic test system for lifetime testing of 100 kilovolt Scyllac-style energy storage capacitors," *Proc. 14th IEEE International Pulsed Power Conference*, vol. 2, pp. 1225-1228, 2003.

[114] E.A. Cherney, and J.D. Cross, "Electrical breakdown at solid-liquid interfaces," *IEEE Trans. Electr. Insul.*, vol. EI-12 (3), pp. 214-218, 1977.

[115] M. Krins, H. Borsi, and E. Gockenbach, "Impact of carbon particles on the impulse flashover behaviour of different solid/liquid interfaces in a non-uniform field," *Proc. 1998 International Symposium on Electrical Insulating Materials*, pp. 363-368, 1998.

[116] C. Vincent, N.G. Trinh, R. Olivier, and J. Aubin, "Behavior of an oil-paper interface in presence of carbon particle contamination," *Proc. 1994 IEEE International Symposium on Electrical Insulation*, pp. 534-537, 1994.

[117] K. Wechsler, and M. Riccitiello, "Electric breakdown of a parallel solid and liquid dielectric system," *Trans. AIEE III, Power Appar. Syst.*, vol. 80, pp. 365-369, 1961.

[118] E.A. Cherney, "High voltage flashover along a solid-liquid interface," *Proc. 39th Annual Conference on Electrical Insulation and Dielectric Phenomena*, pp. 187-190 (1970 Annual Report), 1970.

[119] E.A. Cherney and J.D. Cross, "Space charge effects in chlorobiphenyls at solid/liquid interfaces," *Proc. 1972 Annual Conference on Electrical Insulation and Dielectric Phenomena*, pp. 84-90, 1973.

[120] J.D. Cross, and R. Tobazeon, "Electric field distortions produced by solid dielectric spacers separating uniform field electrodes in nitrobenzene," *IEEE Trans. Electr. Insul.*, vol. EI-8 (1), pp. 25-29, 1973.

[121] S.J. Rzad, J.C. Devins, and R.J. Schwabe, "Transient behavior in transformer oils: Prebreakdown and breakdown phenomena," *IEEE Trans. Electr. Insul.*, vol. EI-14 (6), pp. 289-296, 1979.

[122] S.J. Rzad, J.C. Devins, and R.J. Schwabe, "Prebreakdown events and breakdown involving solid-liquid interfaces," *1980 Annual Report: Conference on Electrical Insulation and Dielectric Phenomena*, pp. 411-417, 1980.

[123] S.J. Rzad, J.C. Devins, and R.J. Schwabe, "The influence of a dc bias on streamers produced by step voltages in transformer oil and over solid-liquid interfaces," *IEEE Trans. Electr. Insul.*, vol. EI-18 (1), pp. 1-10, 1983.

[124] M.S.A.A. Hammam, S. Ochiai, and C. Burns, "Effect on 50% flashover voltage due to accumulated charges on the surface of polymer insulators," *Proc. 3rd International Conference on Properties and Applications of Dielectric Materials*, pp. 981-984, 1991.

[125] D.J. Parr, and R.M. Scarisbrick, "Performance of synthetic insulating materials under polluted conditions," *Proc. Inst. Electr. Eng.*, vol. 112 (8), pp. 1625-1632, 1965.

[126] A.W. Stannett, P.J. Lambeth, D.J. Parr, R.M. Scarisbrick, A. Wilson, and R.C. Kingston, "Resin-bonded glass-fibre outdoor h.v. insulators," *Proc. Inst. Elec. Eng.*, vol. 116 (2), pp. 261-272, 1969.

[127] T. Tanaka, K. Naito, and J. Kitagawa, "A basic study on outdoor insulators of organic materials," *IEEE Trans. Electr. Insul.*, vol. EI-13 (3), pp. 184-193, 1978.

[128] E.A. Cherney, and D.J. Storkus, "Non-ceramic insulators for contaminated environments," *IEEE PAS-100*, pp. 131-142, 1981.

[129] H.M. Schneider, J.F. Hall, G. Karady, and J. Renowden, "Nonceramic insulators for transmission lines," *IEEE Trans. Power Del.*, vol. 4 (4), pp. 2214-2221, 1989.

[130] M.R. Wertheimer, L. Paquin, H.P. Schreiber, and S.A. Boggs, "Dielectric permittivity, conductivity, and breakdown characteristics of polymer-mica composites," *IEEE Trans. Electr. Insul.*, vol. EI-12 (2), pp. 137-141, 1977.

[131] A. Bonincontro, C. Cametti, and A. Di Biasio, "Effect of volume ion polarisations on Maxwell-Wagner dielectric dispersions," *J. Phys. D: Appl. Phys.*, vol. 13 (8), pp. 1529-1535, 1980.

[132] I.V. Timoshkin, S.J. MacGregor, R.A. Fouracre, B.H. Crichton, and J.G. Anderson, "Transient electrical field across cellular membranes: pulsed electric field treatment of microbial cells," *J. Phys. D: Appl. Phys.*, vol. 39 (3), pp. 596-603, 2006.

[133] S.R. Morrison, *The Chemical Physics of Surfaces*, New York and London: Plenum Press, 1977.

[134] L.D. Landau, and E.M. Lifshitz, *Electrodynamics of Continuous Media*, 2nd ed., Oxford: Pergamon, 1984.

[135] S.M. Korobeynikov, A.V. Melekhov, G.G. Furin, V.P. Charalambakos, and D.P. Agoris, "Mechanism of surface charge creation due to image forces," *J. Phys. D: Appl. Phys.*, vol. 35 (11), pp. 1193-1196, 2002.

[136] A. Denat, B. Gosse, and J.P. Gosse, "Ion injections in hydrocarbons," *J. Electrostatics*, vol. 7, pp. 205-225, 1979.

[137] A.I. Zakin, *Magnitnaya Hydrodynamika*, Riga: Latvija Acad. Nauka, pp. 63-70, 1991.

[138] A.I. Zakin, F.F. Nijazi, A.E. Kukzo, and S.A. Lunev, *Trans. Kursk State Technical University (Kursk)*, vol. 7, pp. 58-85, 2001.

[139] J.C. Martin, "High voltage design considerations," in *J.C. Martin on Pulsed Power*, vol. 3, T.H. Martin, Ed., A.H. Guenther, Ed., and M. Kristiansen, Ed. New York and London: Plenum Press, 1996, ch. 12, pp. 489-501.

[140] British Standards Institution, British Standard BS EN 60156, "Insulating liquids – Determination of the breakdown voltage at power frequency – Test method," 1996.

[141] Electrical Oil Services Limited Data Sheet, Reclaimed Insulating Oil BS 148:2009, http://www.eosl.co.uk/datasheets/pdf/prod_spec_l10b_reclaimed_insulating_oil.pdf, accessed 4th May 2011.

[142] M. Nagel, and T. Leibfried, "Investigation on the high frequency, high voltage insulation properties of mineral transformer-oil," *2006 Annual Report: Conference on Electrical Insulation and Dielectric Phenomena*, pp. 226-228, 2006.

[143] British Standards Institution, British Standard BS 2000-346:1996, "Methods of test for petroleum and its products – Determination of polycyclic aromatics in unused lubricating base oils and asphaltene free petroleum fractions – Dimethyl sulphoxide extraction refractive index method," 1996.

[144] ASTM International, ASTM Standard D149, "Standard test method for dielectric breakdown voltage and dielectric strength of solid electrical insulating materials at commercial power frequencies," 2009.

[145] International Electrotechnical Commission, International Standard IEC 60243-1, "Electrical strength of insulating materials – Test methods – Part 1: Test at power frequencies," Second edition, 1998-01.

[146] The Plastic Shop Technical Data Sheet, PP, http://www.theplasticshop.co.uk/plastic_technical_data_sheets/fluted_polypropylene_technical_data_sheet.pdf, accessed 4th May 2011.

[147] Goodfellow Data Sheet, Polymer – Electrical Properties, https://www.goodfellow.com/PDF/TAB301E.pdf, accessed 4th May 2011.

[148] Quadrant Engineering Plastic Products – Product Data Sheet, Ultra-High Molecular Weight Polyethylene, http://www.alperton.com/alperton/Files/PDS_CESTILENE_HD1000_EN.pdf, accessed 4th May 2011.

[149] Ensinger Ltd. – Product Data Sheet, REXOLITE® 1422, http://www.ensinger.ltd.uk/1809.file.dld, accessed 4th May 2011.

[150] Quadrant Engineering Plastic Products – Product Data Sheet, Torlon 4203 PAI, http://www.theplasticshop.co.uk/plastic_technical_data_sheets/torlon_4203_technical_data_sheet.pdf, accessed 4th May 2011.

[151] International Electrotechnical Commission, International Standard IEC 60060-1, "High-voltage test techniques – Part 1: General definitions and test requirements," Edition 3.0, 2010-09.

[152] D. Kind, and K. Feser, "Layout and operation of high-voltage test setups," in *High Voltage Test Techniques*, 2nd ed. London: Newnes, 2001, ch. 2, pp. 110-147.

[153] H. Hirose, "More accurate breakdown voltage estimation for the new step-up test method," *IEEE Trans. Dielectr. Electr. Insul.*, vol. 10 (3), pp. 475-482, 2003.

[154] E. O. Forster, and P. Wong, "High speed laser Schlieren studies of electrical breakdown in liquid hydrocarbons," *IEEE Trans. Electr. Insul.*, vol. EI-12 (6), pp. 435-442, 1977.

[155] R. Coelho, and J. Debeau, "Properties of the tip-plane configuration," *J. Phys. D: Appl. Phys.*, vol. 4 (9), pp. 1266-1280, 1971.

[156] Tera Analysis Ltd., QuickField™ Finite Element Analysis System User's Guide, available online at http://www.quickfield.com/demo/manual.pdf, accessed 4th May 2011.

[157] H.M. Jones, and E.E. Kunhardt, "The influence of pressure and conductivity on the pulsed breakdown of water," *IEEE Trans. Dielectr. Electr. Insul.*, vol. 1 (6), pp. 1016-1025, 1994.

[158] J. Qian, R.P. Joshi, J. Kolb, K.H. Schoenbach, J. Dickens, A. Neuber, M. Butcher, M. Cevallos, H. Krompholz, E. Schamiloglu, and J. Gaudet, "Microbubble-based model analysis of liquid breakdown initiation by a submicrosecond pulse," *J. Appl. Phys.*, vol. 97 (11), pp. 113304-1 – 113304-10, 2005.

[159] T.J. Lewis, "Breakdown initiating mechanisms at electrode interfaces in liquids," *IEEE Trans. Dielectr. Electr. Insul.*, vol. 10 (6), pp. 948-955, 2003.

[160] R. Ohyama, A. Watson, and J.S. Chang, "Electrical current conduction and electrohydrodynamically induced fluid flow in an AW type EHD pump," *J. Electrostatics*, vol. 53 (2), pp. 147-158, 2001.

[161] W. Weibull, "Statistical distribution function of wide applicability," *Am. Soc. Mech. Engrs. – Trans. (J. Applied Mechanics)*, vol. 18 (3), pp. 293-297, 1951.

[162] M.M. Morcos, and S.E. Cherukupalli, "Review of statistical testing of solid insulating materials," *Proc. 3rd International Conference on Conduction and Breakdown in Solid Dielectrics*, pp. 574-581, 1989.

[163] International Electrotechnical Commission, International Standard IEC 62539(E):2007 (IEEE Std 930-2004), "Guide for the statistical analysis of electrical insulation breakdown data," First edition, 2007-07.

[164] W.W. Dorner, "Using Microsoft Excel for Weibull analysis," *Quality Digest*, 1999, http://www.qualitydigest.com/jan99/html/body_weibull.html, accessed 4th May 2011.

[165] R. Liu, C. Törnkvist, V. Chandramouli, O. Girlanda, and L.A.A. Pettersson, "Ester fluids as alternative for mineral oil: The difference in streamer velocity and LI breakdown voltage," *2009 Annual Report: Conference on Electrical Insulation and Dielectric Phenomena*, pp. 543-548, 2009.

[166] R.J. Taylor, "Effect of permittivity matching on the flashover of solid/liquid interfaces," *Proc. IEE*, vol. 124 (10), pp. 899-904, 1977.

[167] O. Lesaint, and G. Massala, "Transition to fast streamers in mineral oil in the presence of insulating solids," *Proc. 1996 IEEE International Symposium on Electrical Insulation*, vol. 2, pp. 737-740, 1996.

[168] R. Badent, K. Kist, and A.J. Schwab, "Streamer initiation and propagation in insulating oil in weakly non-uniform fields under impulse conditions," *Proc. 1996 IEEE International Symposium on Electrical Insulation*, vol. 2, pp. 720-723, 1996.

[169] G. Massala, and O. Lesaint, "A comparison of negative and positive streamers in mineral oil at large gaps," *J. Phys. D: Appl. Phys.*, vol. 34 (10), pp. 1525-1532, 2001.

[170] C.T. Duy, O. Lesaint, A. Denat, and N. Bonifaci, "Streamer propagation and breakdown in natural ester at high voltage," *IEEE Trans. Dielectr. Electr. Insul.*, vol. 16 (6), pp. 1582-1594, 2009.

[171] G. Massala, and O. Lesaint, "Positive streamer propagation in large oil gaps: Electrical properties of streamers," *IEEE Trans. Dielectr. Electr. Insul.*, vol. 5 (3), pp. 371-381, 1998.

[172] E. A. Al-Ammar, "Evaluation of seed oils based on statistical breakdown data for their application as insulating fluids in distribution transformers," *European Journal of Scientific Research*, vol. 40 (1), pp. 15-26, 2010.

[173] J. Krile, A. Neuber, J. Dickens, and H. Krompholz, "Imaging of dielectric surface flashover in atmospheric conditions," *IEEE Trans. Plasma Sci.*, vol. 33 (2), pp. 270-271, 2005.

[174] S.M. Turnbull, S.J. MacGregor, F.A. Tuema, and A.J. McPhee, "A self-activating high-voltage, high-energy crowbar," *J. Phys. D: Appl. Phys.*, vol. 33 (11), pp. 1410-1416, 2000.

[175] S.G. Clough, "Viable options for improved switch performance on EROS," *Proc. 2008 IEEE International Power Modulators and High Voltage Conference*, pp. 461-464, 2008.

[176] R.C. Smith, C. Liang, M. Landry, J.K. Nelson, and L.S. Schadler, "The mechanisms leading to the useful properties of polymer nanodielectrics," *IEEE Trans. Dielectr. Electr. Insul.*, vol. 15 (1), pp. 187-196, 2008.

[177] J.G. Hwang, M. Zahn, F.M. O'Sullivan, L.A.A. Pettersson, O. Hjortstam, and R. Liu, "Effects of nanoparticle charging on streamer development in transformer oil-based nanofluids," *J. Appl. Phys.*, vol. 107 (1), pp. 014310-014310-17, 2010.

ACKNOWLEDGEMENTS

The author would firstly like to formally thank his supervisors Prof Scott MacGregor and Dr Martin Given for their continuous technical input, guidance, support and encouragement throughout the course of this study.

Many thanks are due to Dr Igor Timoshkin for the invaluable technical input provided throughout the study. Thanks also to Dr Tony Fouracre for his help in the initial stages of the project.

Funding from AWE Aldermaston is gratefully acknowledged. In particular, thank you to Mark Sinclair and Dr Ken Thomas of AWE Aldermaston for their input on multi-megavolt pulsed-power systems, and for the provision of solid dielectric samples throughout the course of the study.

Thank you to Prof Gerry Woolsey for his guidance and assistance in producing this thesis.

Thanks to Joe McKechnie, Frank May, Andy Carlin, Sean Doak, and David Griffin of the High-Voltage Mechanical Workshop for their assistance in producing the test cells, and particularly for machining and maintaining many electrodes and solid dielectric samples throughout.

Thanks also to Maureen Cooper for her administrative assistance over the course of the study, particularly in organising conference trips and examination of this thesis.

The author would finally like to thank his family, friends and, in particular, his wife Michelle, for encouragement, support, and understanding throughout the duration of the study.

Appendix A (reference section 5.1.1)

OVER-VOLTED GAPS AND NON-UNIFORM FIELDS

Breakdown Voltage

Presented herein are the graphs of breakdown voltage magnitude versus breakdown number referenced in section 5.1.1:

- Figure A.1. configuration AII
- Figure A.2. configuration BII
- Figure A.3. configuration BIII

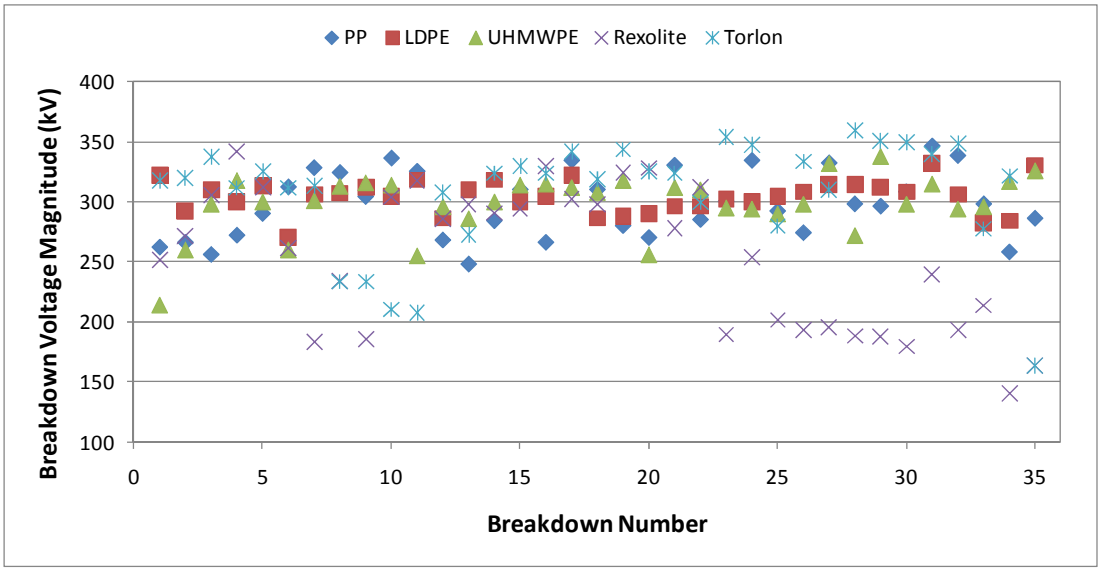

Figure A.1. Breakdown voltage magnitude versus breakdown number for high-voltage electrode type A (pin) and sample type II (shoulder).

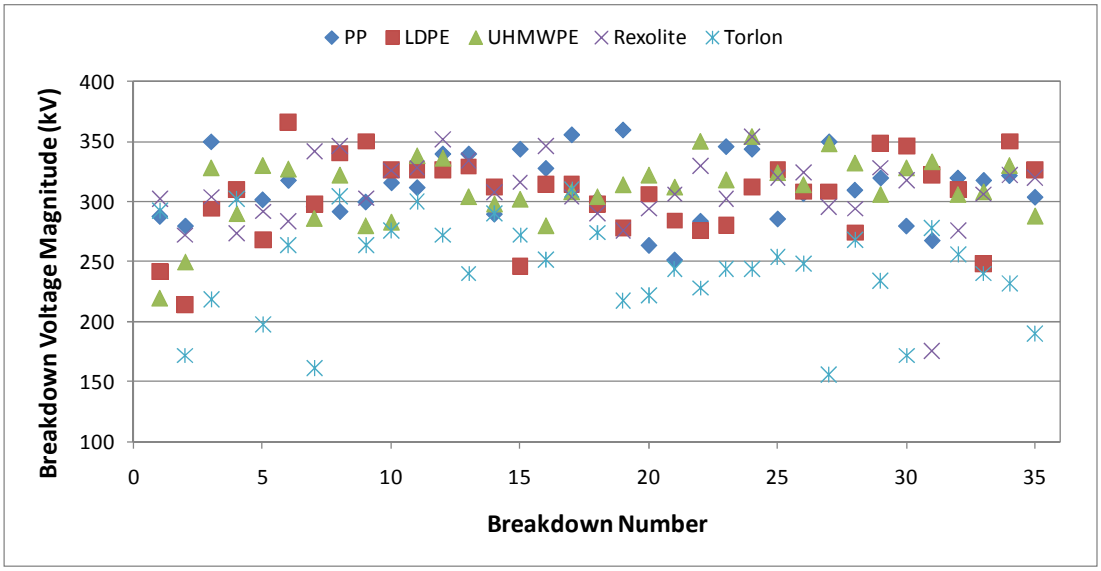

Figure A.2. Breakdown voltage magnitude versus breakdown number for high-voltage electrode type B (collar) and sample type II (shoulder).

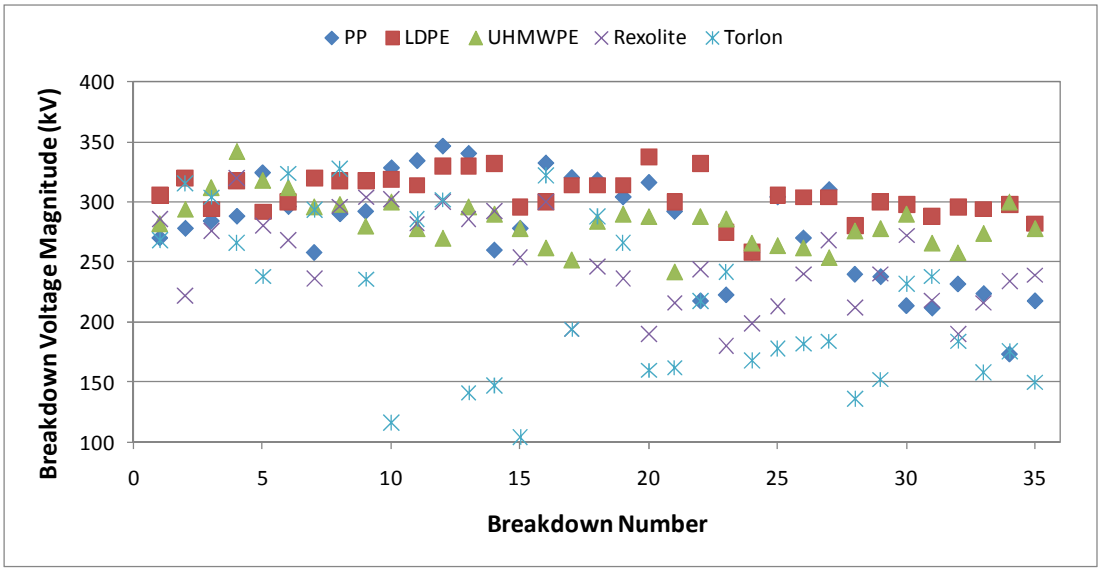

Figure A.3. Breakdown voltage magnitude versus breakdown number for high-voltage electrode type B (collar) and sample type III (no modifications).

Appendix B (reference section 5.1.2)

OVER-VOLTED GAPS AND NON-UNIFORM FIELDS

Time to Breakdown

Presented herein are the graphs of time to breakdown versus breakdown number referenced in section 5.1.2:

- Figure B.1. configuration AII
- Figure B.2. configuration BII
- Figure B.3. configuration BIII

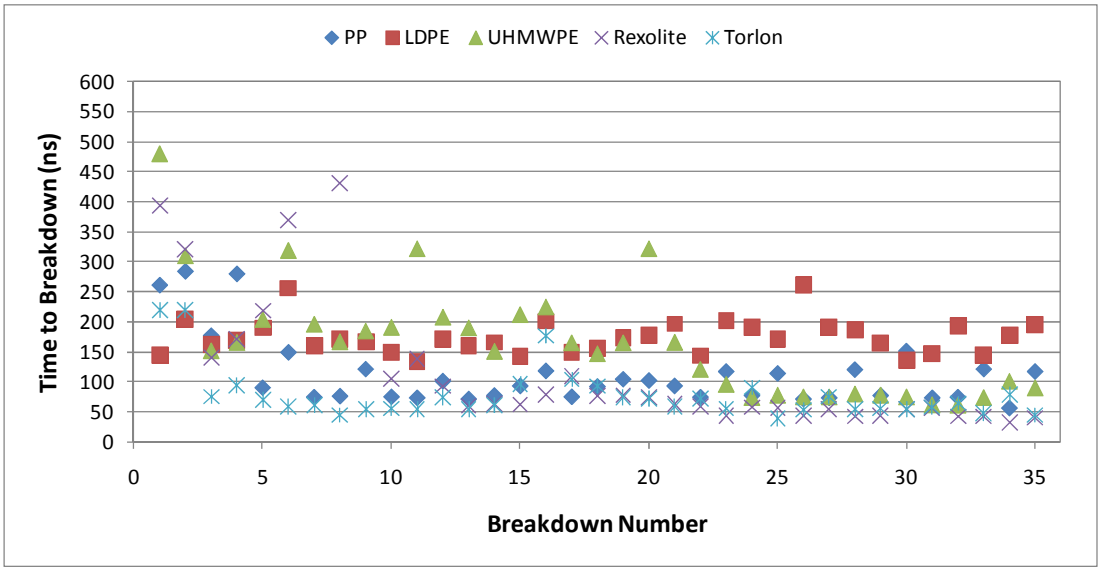

Figure B.1. Time to breakdown versus breakdown number for high-voltage electrode type A (pin) and sample type II (shoulder).

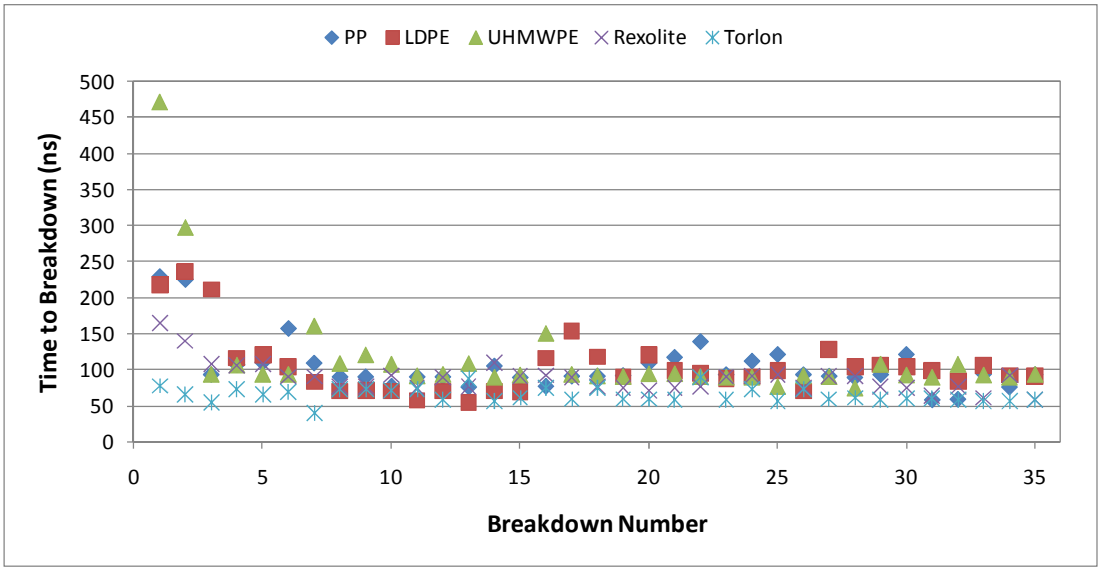

Figure B.2. Time to breakdown versus breakdown number for high-voltage electrode type B (collar) and sample type II (shoulder).

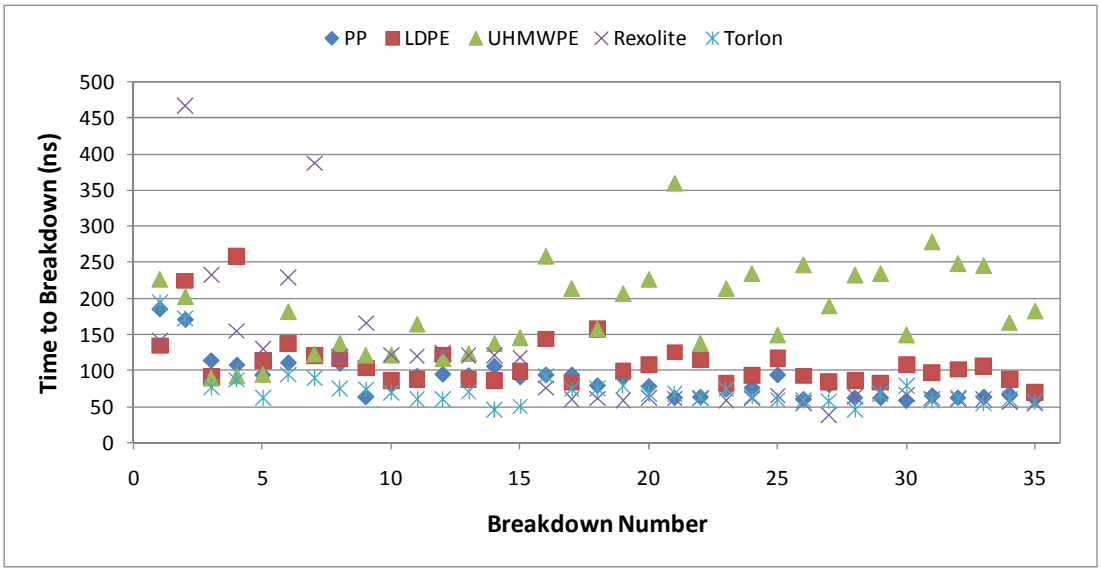

Figure B.3. Time to breakdown versus breakdown number for high-voltage electrode type B (collar) and sample type III (no modifications).

Appendix C (reference section 5.1.3)

OVER-VOLTED GAPS AND NON-UNIFORM FIELDS

Volt-time Plots

Presented herein are the Volt-time (V-t) plots referenced in section 5.1.3:

- Figure C.1. configuration AII
- Figure C.2. configuration BII
- Figure C.3. configuration BIII

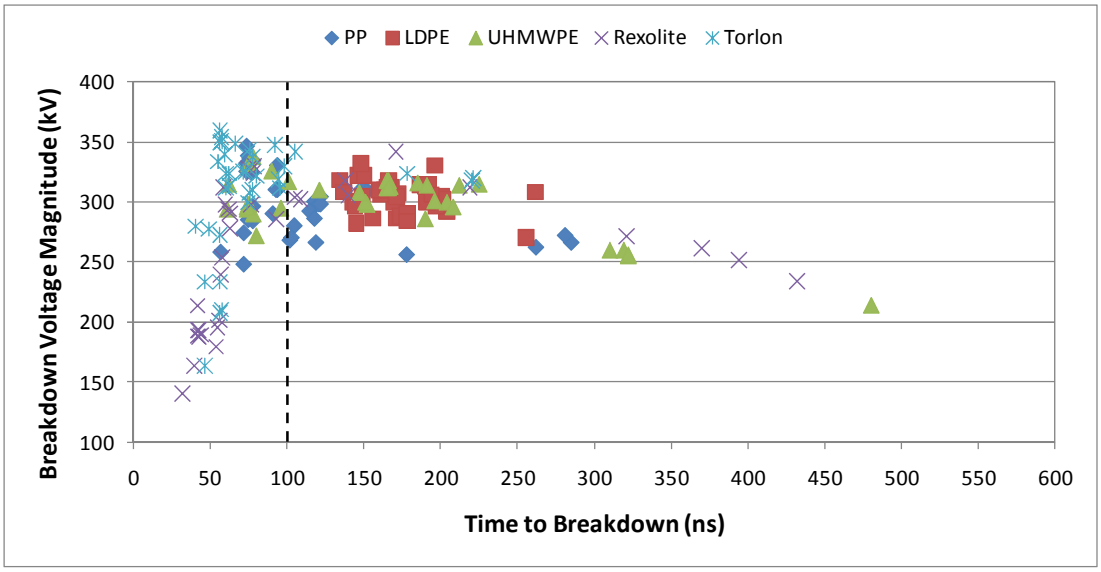

Figure C.1. Volt-time plot for surface flashover along type II (shoulder) samples with high-voltage electrode type A (pin). The dashed line at 100 ns separates the rising edge of the pulse (<100 ns) from the falling edge of the pulse (>100 ns).

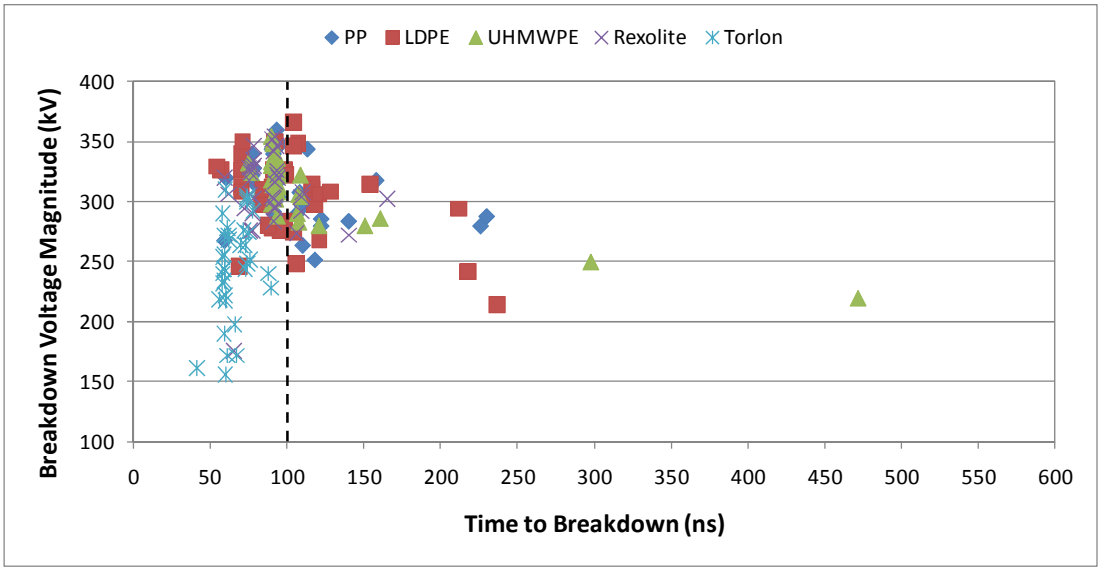

Figure C.2. Volt-time plot for surface flashover along type II (shoulder) samples with high-voltage electrode type B (collar). The dashed line at 100 ns separates the rising edge of the pulse (<100 ns) from the falling edge of the pulse (>100 ns).

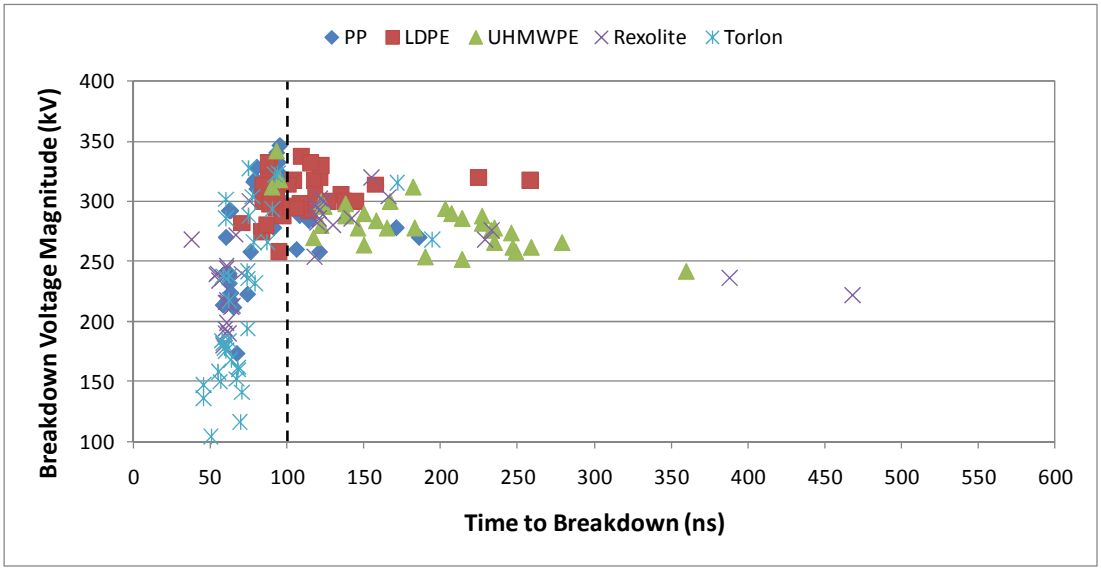

Figure C.3. Volt-time plot for surface flashover along type III (no modifications) samples with high-voltage electrode type B (collar). The dashed line at 100 ns separates the rising edge of the pulse (<100 ns) from the falling edge of the pulse (>100 ns).

Appendix D (reference section 5.3.1)

BREAKDOWN INITIATION

Non-uniform Fields

Presented herein are the graphs of peak applied field, breakdown field, and time to breakdown for pin-plane geometry (configuration AI) referenced in section 5.3.1:

- Figure D.1. average applied field vs. breakdown number
- Figure D.2. average breakdown field vs. breakdown number
- Figure D.3. time to breakdown vs. breakdown number

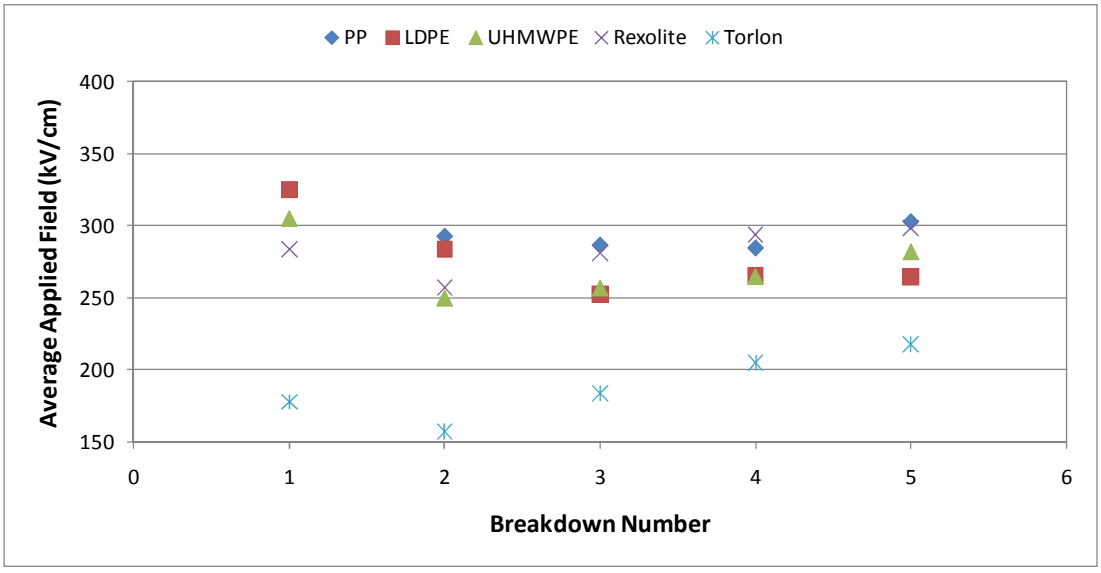

Figure D.1. Average applied fields to cause surface flashover across type I (recess) dielectric samples with high-voltage electrode type A (pin). Each data point represents the mean value from 3 samples.

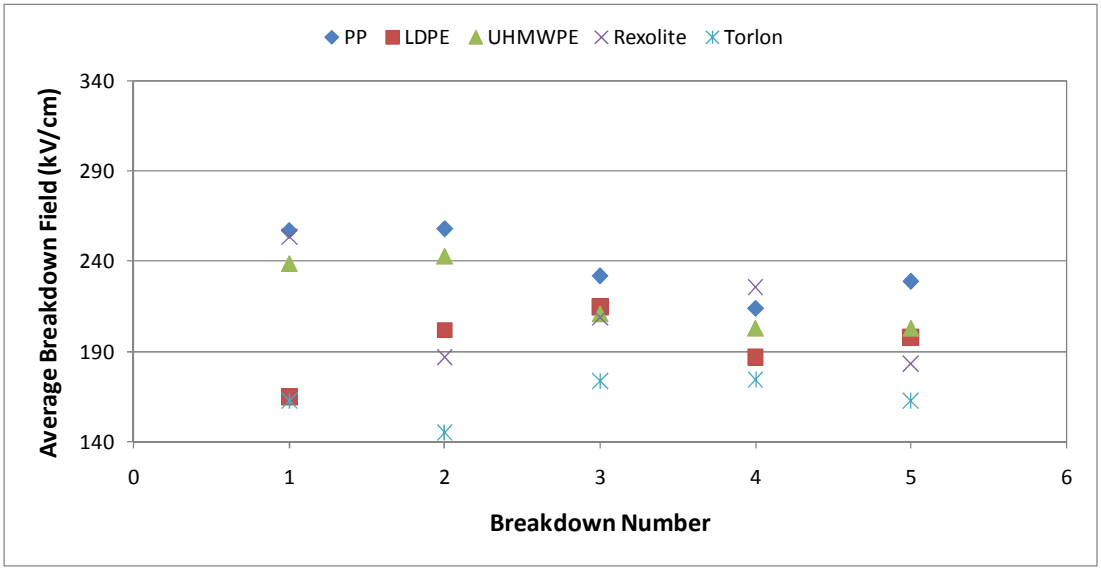

Figure D.2. Average breakdown fields for surface flashover across type I (recess) dielectric samples with high-voltage electrode type A (pin). Each data point represents the mean value from 3 samples.

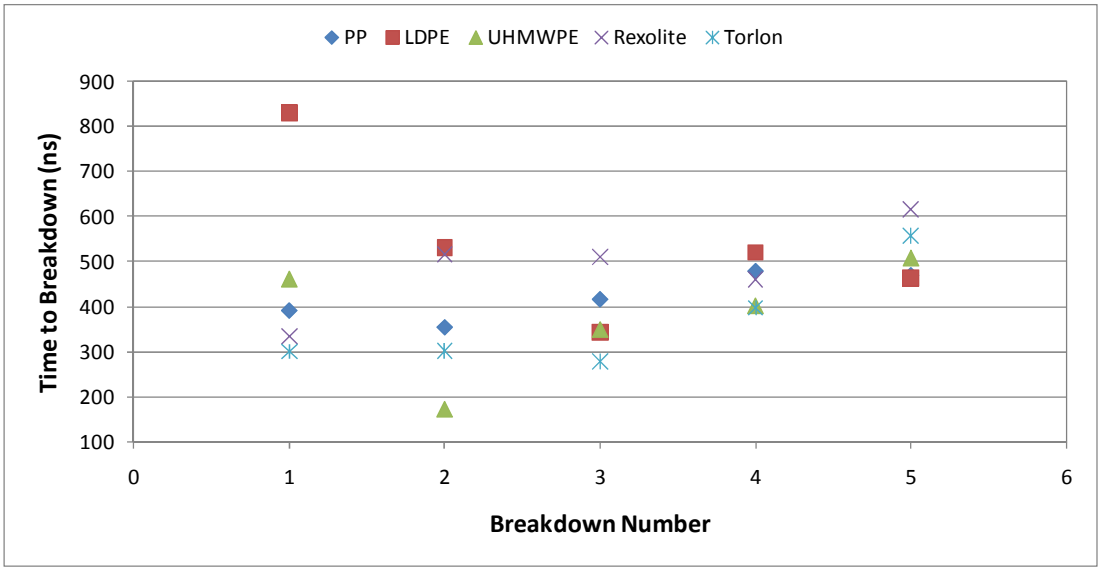

Figure D.3. Times to breakdown for surface flashover across type I (recess) dielectric samples with high-voltage electrode type A (pin). Each data point represents the mean value from 3 samples.

Appendix E (reference section 5.4.1)

WEIBULL STATISTICAL ANALYSIS

Peak Applied Voltage Data

Presented herein are the Weibull plots for the applied voltage data from breakdown initiation measurements, referenced in section 5.4.1:

- Figure E.1. configuration BIII
- Figure E.2. configuration CIII

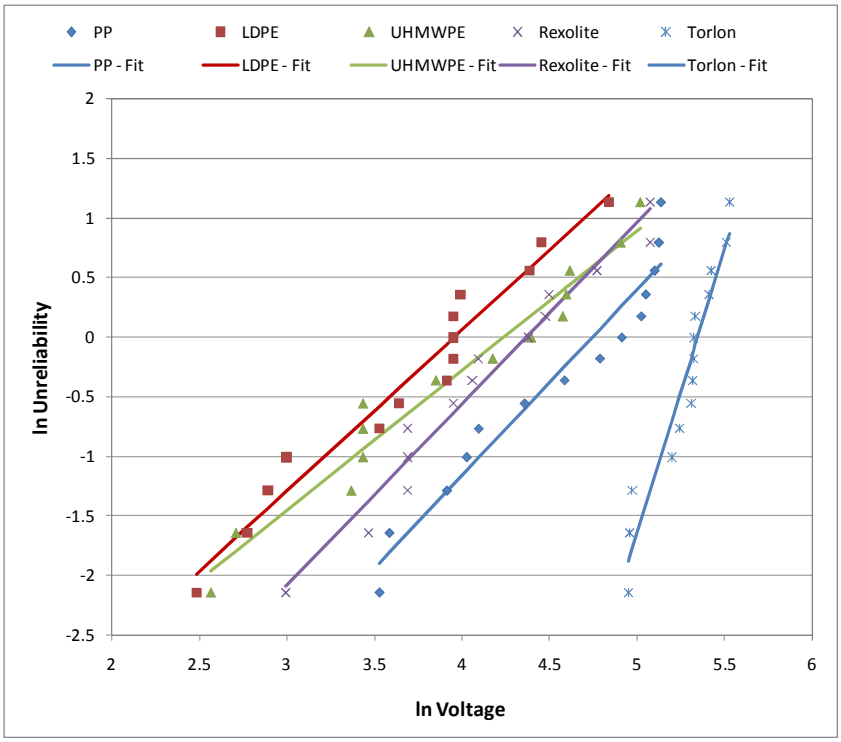

Figure E.1. Weibull plots and curve fits of applied voltage data for type III (no modifications) samples tested with high-voltage electrode type B (collar).

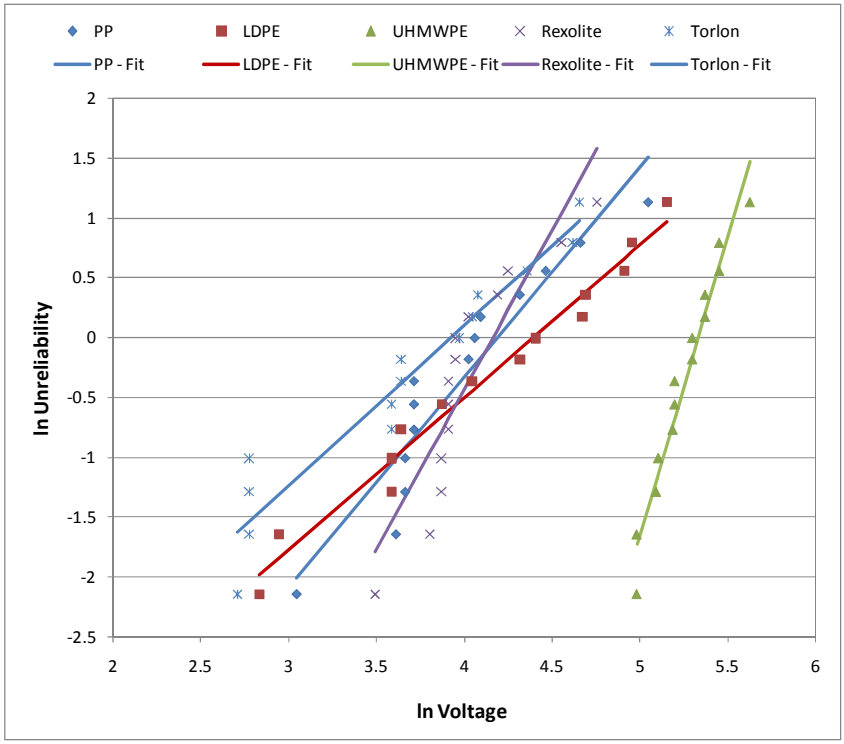

Figure E.2. Weibull plots and curve fits of applied voltage data for type III (no modifications) samples tested with high-voltage electrode type C (plane).

Appendix F (reference section 5.4.2)

WEIBULL STATISTICAL ANALYSIS

Breakdown Voltage Data

Presented herein are the Weibull plots for the breakdown voltage data from breakdown initiation measurements, referenced in section 5.4.2:

- Figure F.1. configuration BIII
- Figure F.2. configuration CIII

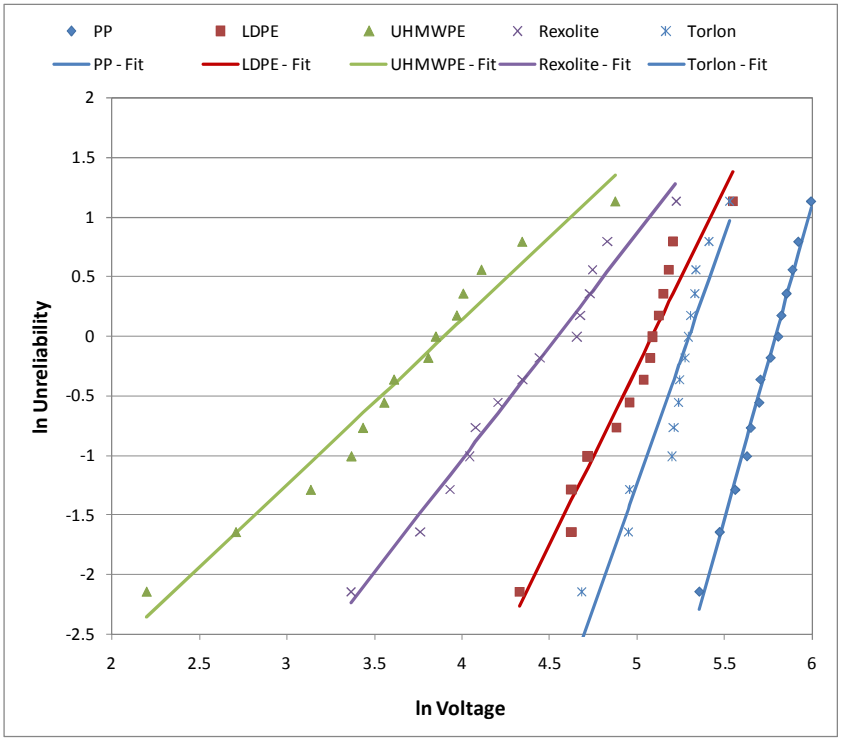

Figure F.1. Weibull plots and curve fits of breakdown voltage data for type III (no modifications) samples tested with high-voltage electrode type B (collar).

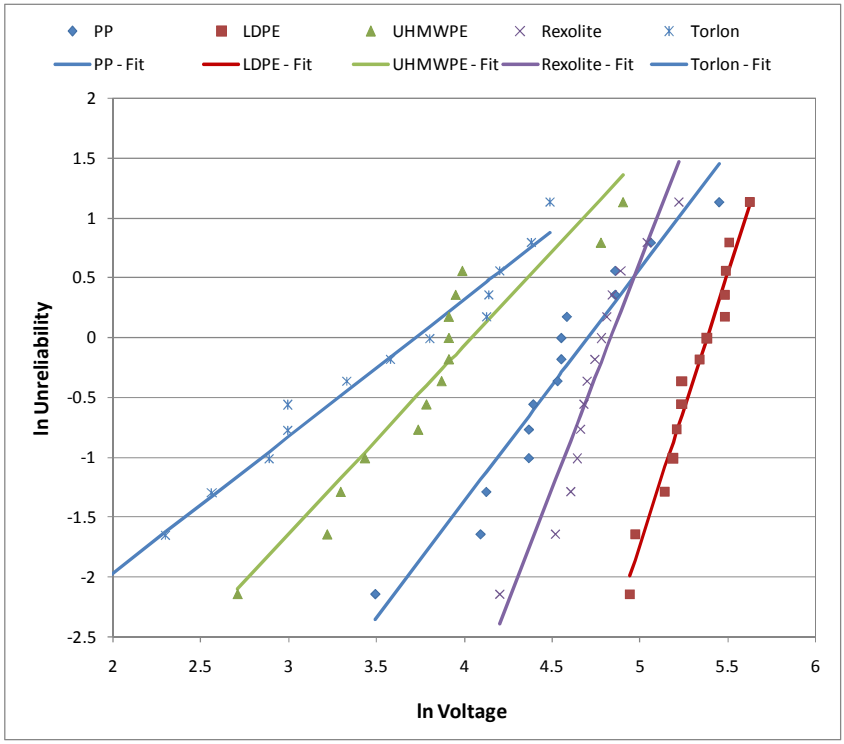

Figure F.2. Weibull plots and curve fits of breakdown voltage data for type III (no modifications) samples tested with high-voltage electrode type C (plane).

Appendix G (reference section 5.4.3)

WEIBULL STATISTICAL ANALYSIS

Material Comparison

Presented herein are the Weibull plots, sorted by material, for both the applied voltage data and the breakdown voltage data associated with breakdown initiation measurements, as referenced in section 5.4.3:

- Figure G.1. LDPE applied voltage data
- Figure G.2. UHMWPE applied voltage data
- Figure G.3. Rexolite applied voltage data
- Figure G.4. Torlon applied voltage data
- Figure G.5. LDPE breakdown voltage data
- Figure G.6. UHMWPE breakdown voltage data
- Figure G.7. Rexolite breakdown voltage data
- Figure G.8. Torlon breakdown voltage data

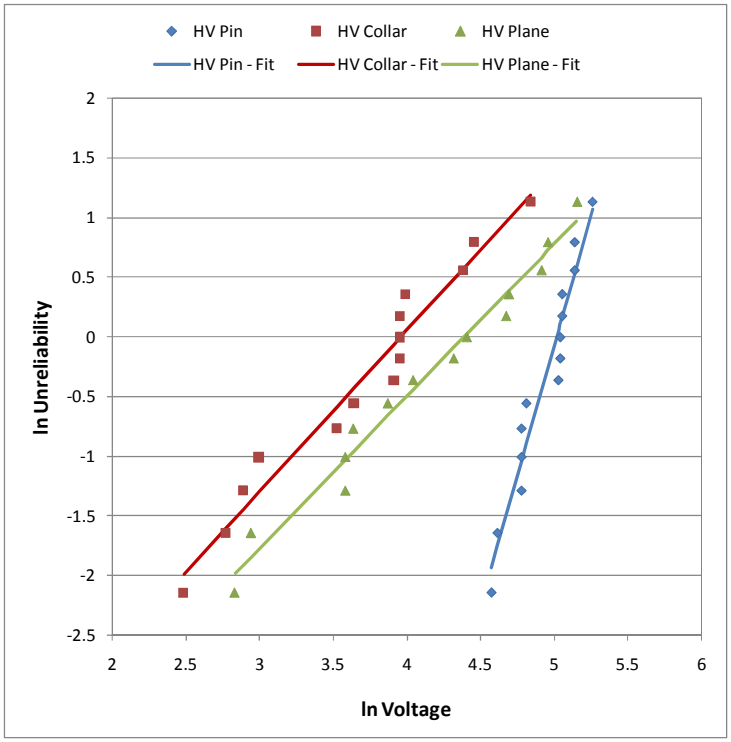

Figure G.1. Weibull plots and curve fits of applied voltage data for LDPE samples.

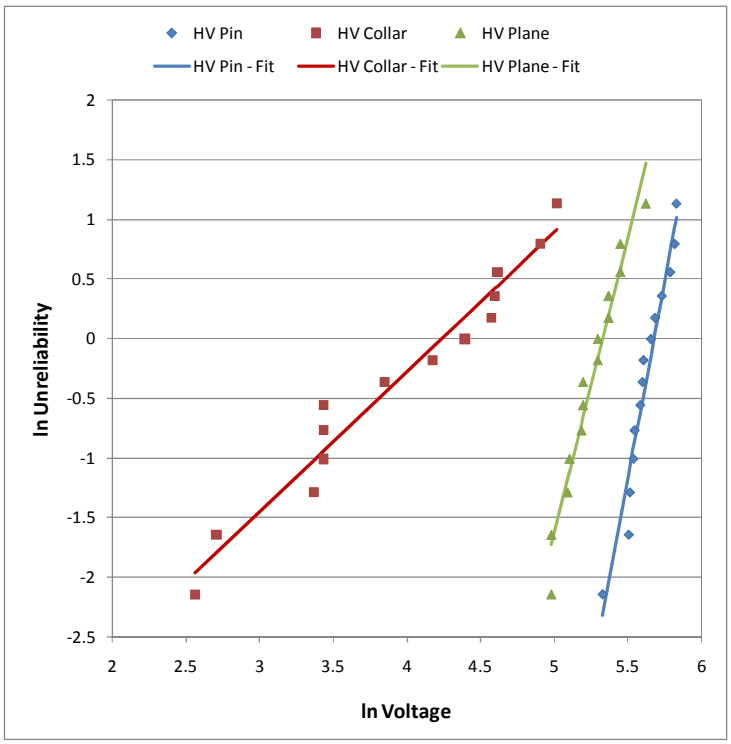

Figure G.2. Weibull plots and curve fits of applied voltage data for UHMWPE samples.

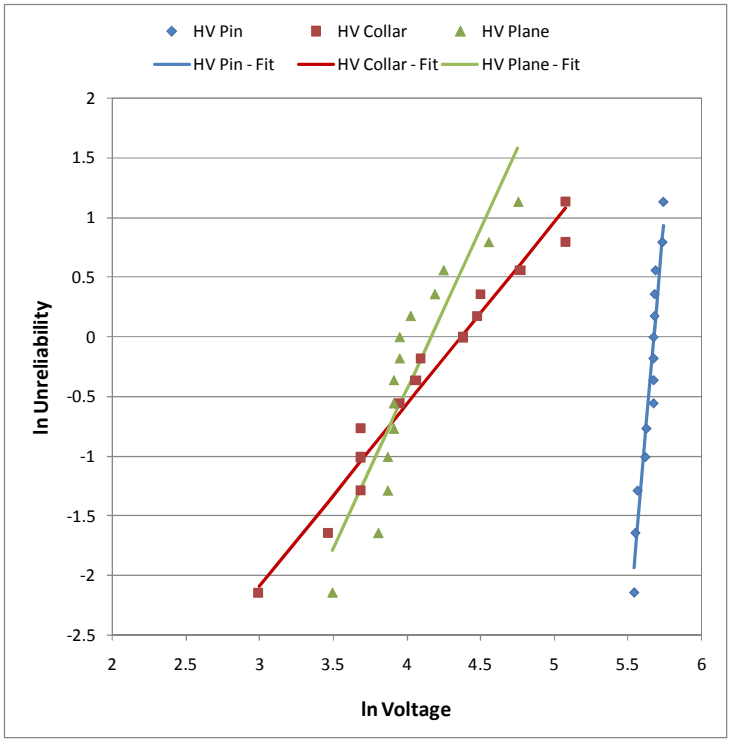

Figure G.3. Weibull plots and curve fits of applied voltage data for Rexolite samples.

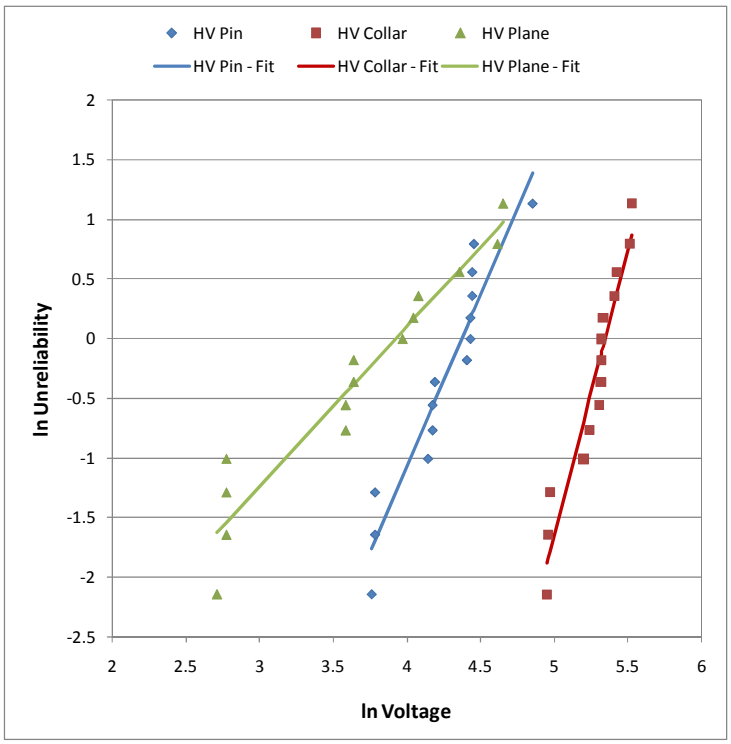

Figure G.4. Weibull plots and curve fits of applied voltage data for Torlon samples.

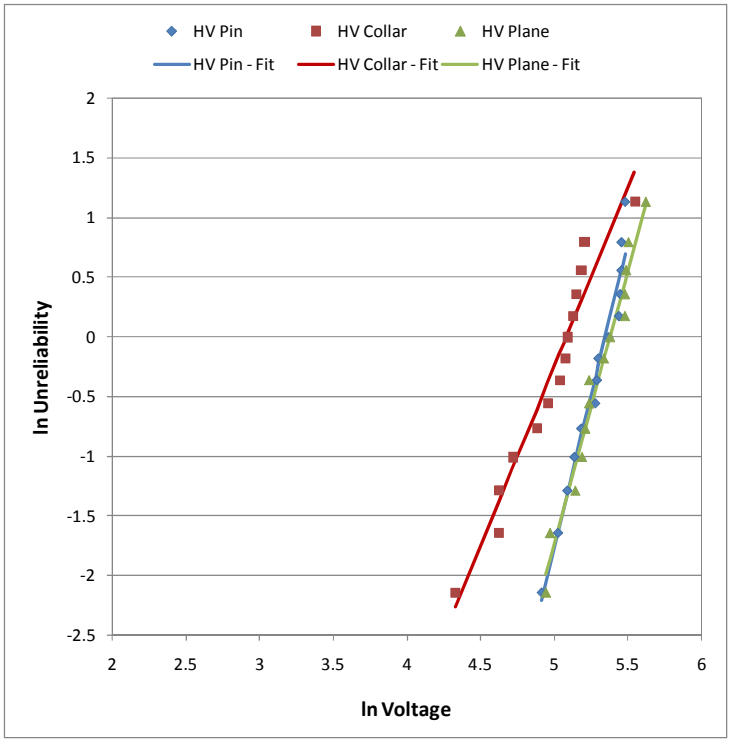

Figure G.5. Weibull plots and curve fits of breakdown voltage data for LDPE samples.

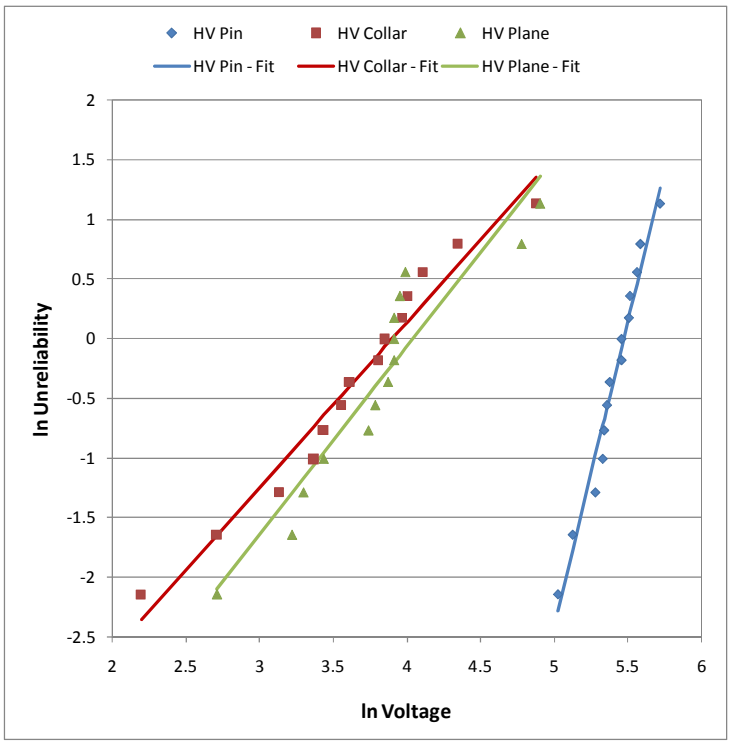

Figure G.6. Weibull plots and curve fits of breakdown voltage data for UHMWPE samples.

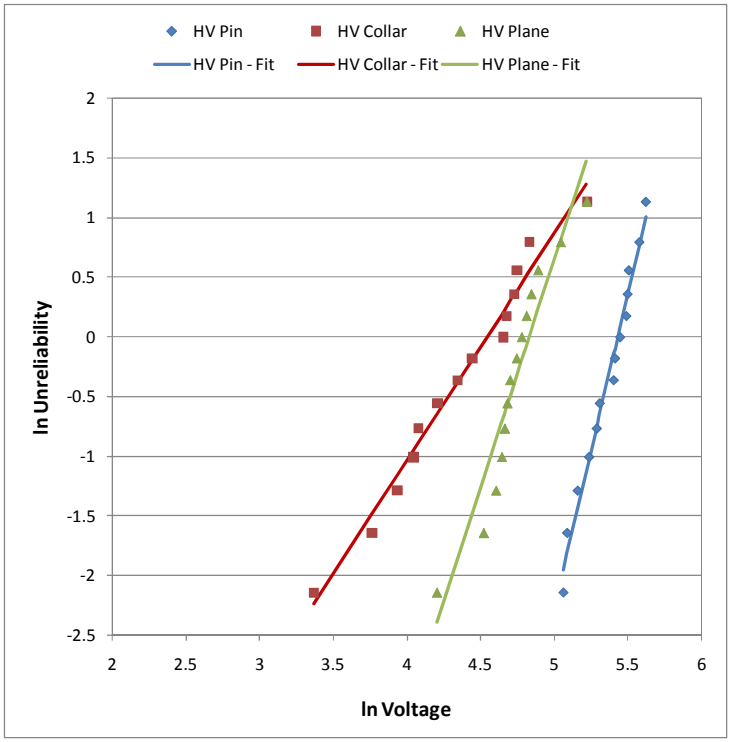

Figure G.7. Weibull plots and curve fits of breakdown voltage data for Rexolite samples.

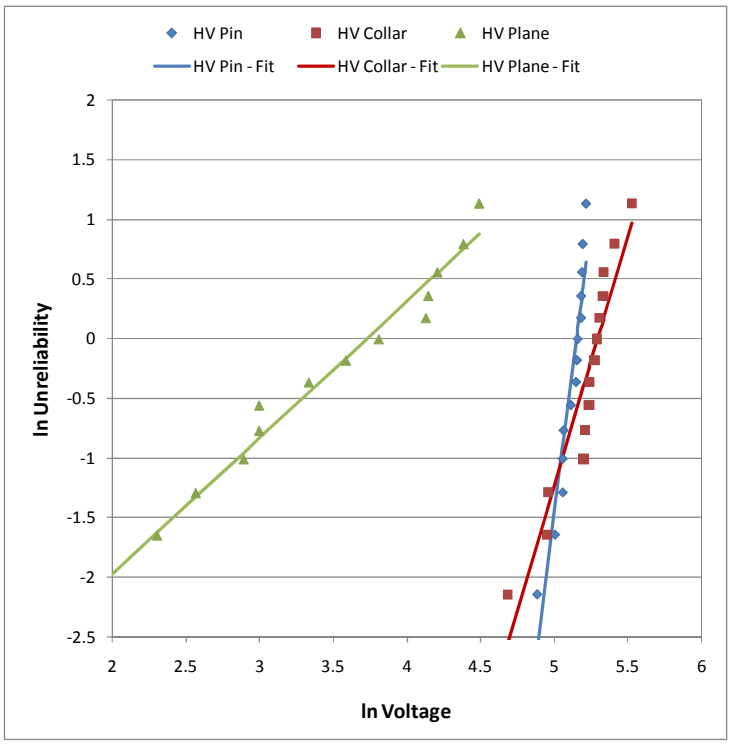

Figure G.8. Weibull plots and curve fits of breakdown voltage data for Torlon samples.

Appendix H (reference section 6.2.1)

NON-UNIFORM FIELDS

Breakdown Voltage

Presented herein are the graphs of breakdown voltage magnitude versus breakdown number referenced in section 6.2.1:

- Figure H.1. configuration AII
- Figure H.2. configuration BII
- Figure H.3. configuration BIII

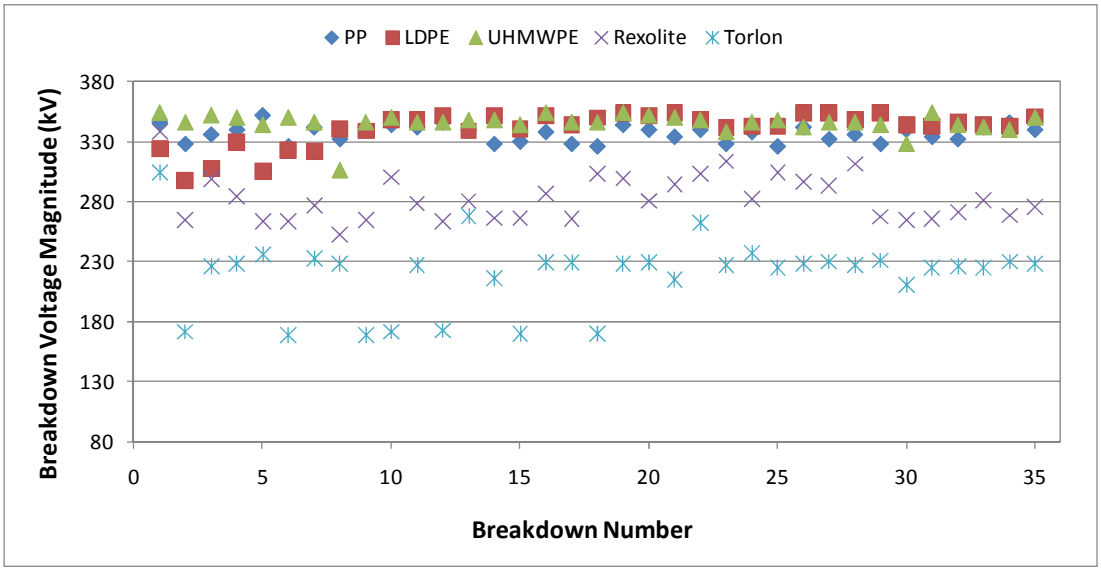

Figure H.1. Breakdown voltage magnitude versus breakdown number for high-voltage electrode type A (pin) and sample type II (shoulder).

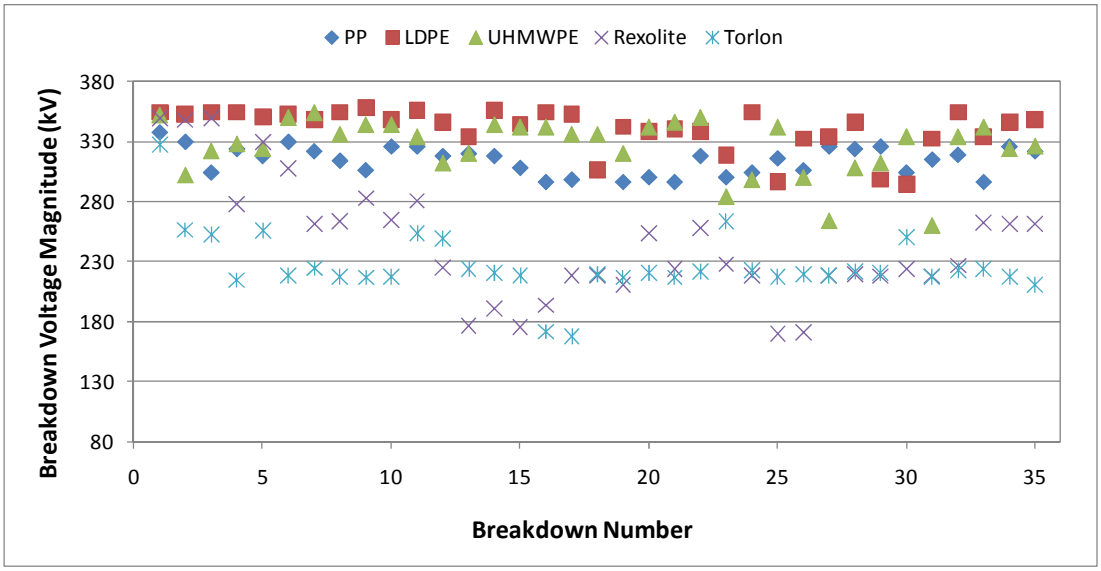

Figure H.2. Breakdown voltage magnitude versus breakdown number for high-voltage electrode type B (collar) and sample type II (shoulder).

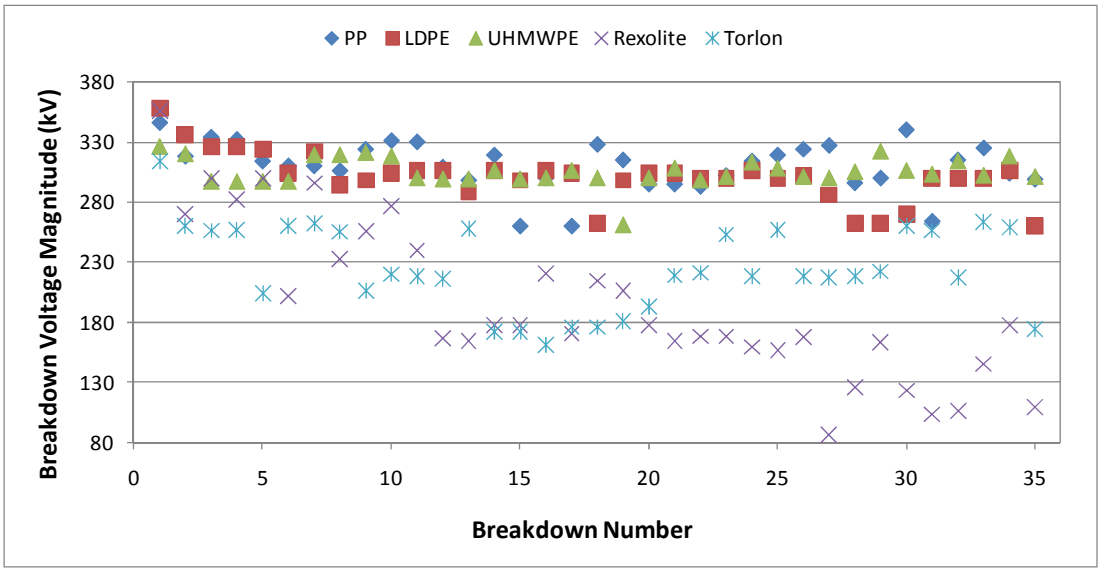

Figure H.3. Breakdown voltage magnitude versus breakdown number for high-voltage electrode type B (collar) and sample type III (no modifications).

Appendix I (reference section 6.2.2)

NON-UNIFORM FIELDS

Time to Breakdown

Presented herein are the graphs of time to breakdown versus breakdown number referenced in section 6.2.2:

- Figure I.1. configuration AII
- Figure I.2. configuration BII
- Figure I.3. configuration BIII

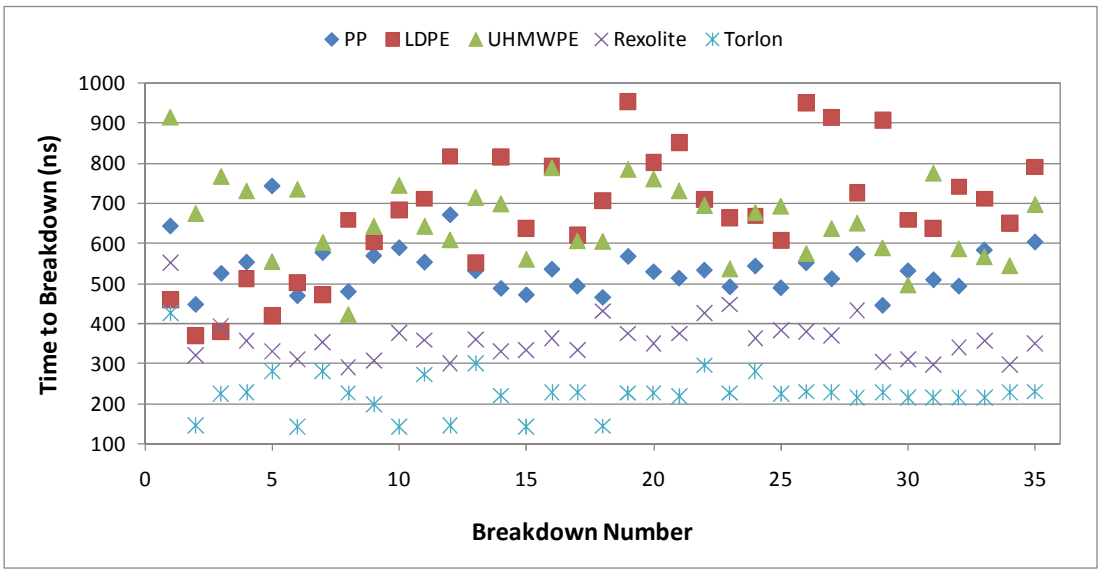

Figure I.1. Time to breakdown versus breakdown number for high-voltage electrode type A (pin) and sample type II (shoulder).

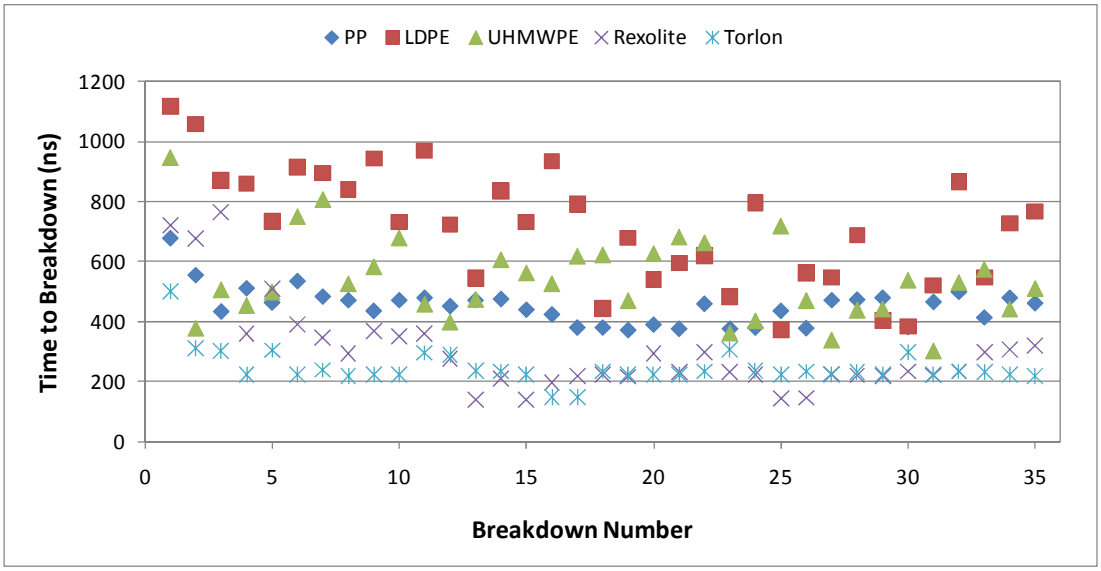

Figure I.2. Time to breakdown versus breakdown number for high-voltage electrode type B (collar) and sample type II (shoulder).

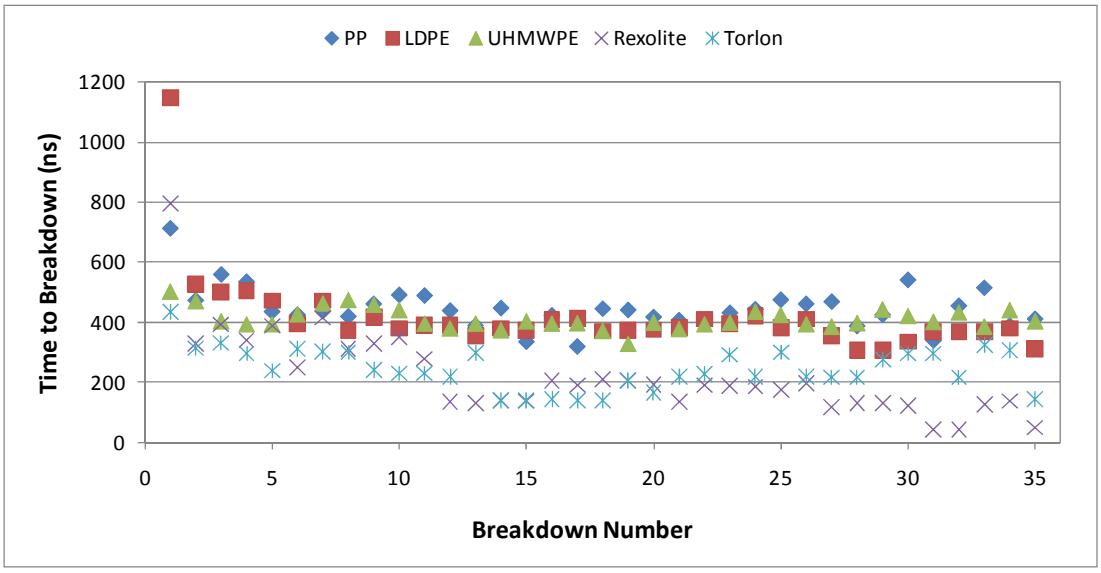

Figure I.3. Time to breakdown versus breakdown number for high-voltage electrode type B (collar) and sample type III (no modifications).

Appendix J (reference section 6.2.3)

NON-UNIFORM FIELDS

Volt-time Plots

Presented herein are the Volt-time (V-t) plots referenced in section 6.2.3:

- Figure J.1. configuration AII
- Figure J.2. configuration BII
- Figure J.3. configuration BIII

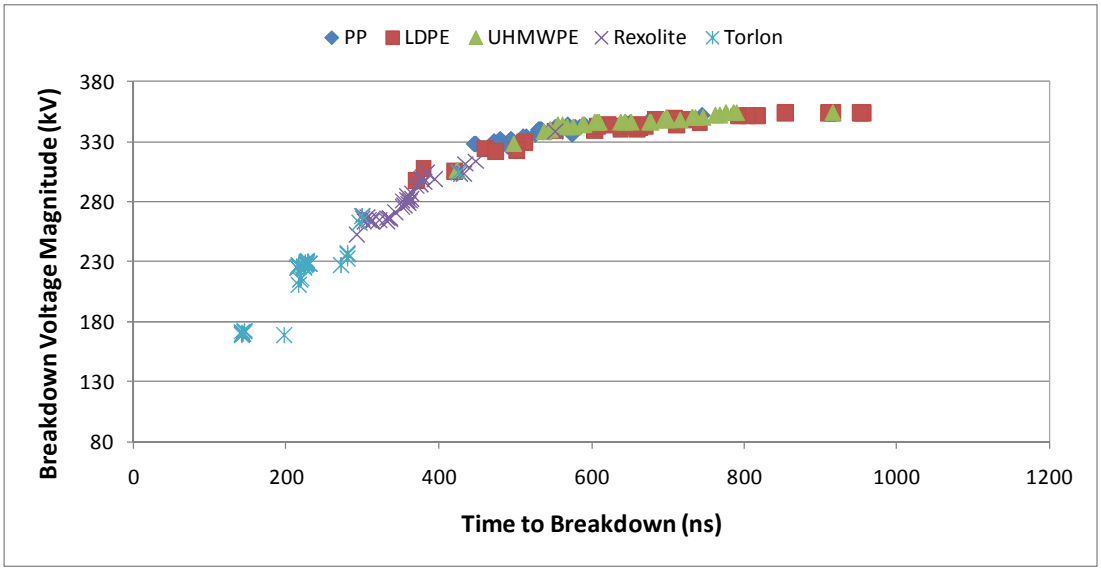

Figure J.1. Volt-time plot for surface flashover along type II (shoulder) samples with high-voltage electrode type A (pin).

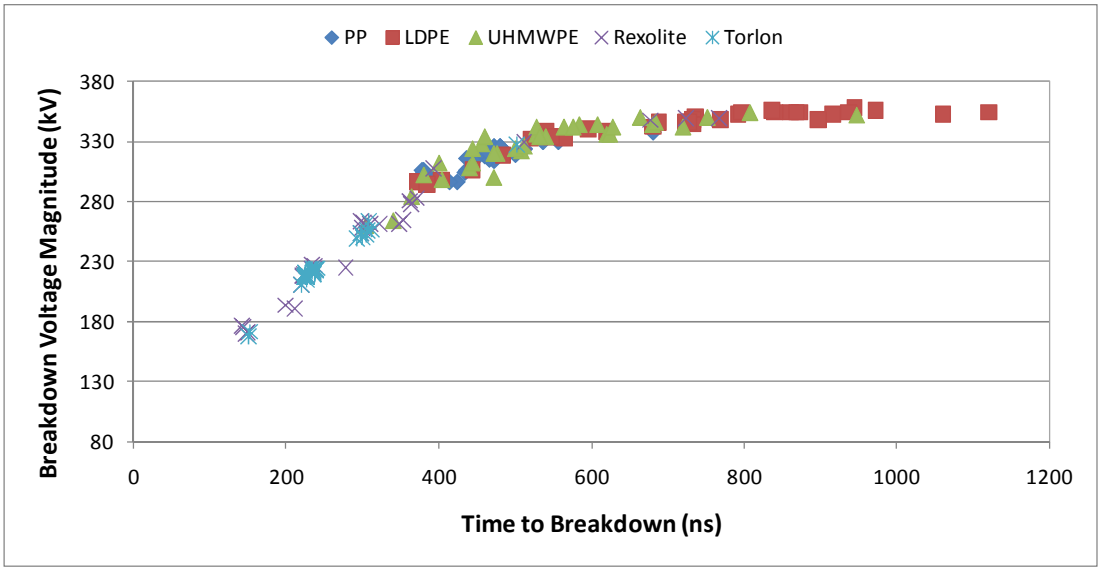

Figure J.2. Volt-time plot for surface flashover along type II (shoulder) samples with high-voltage electrode type B (collar).

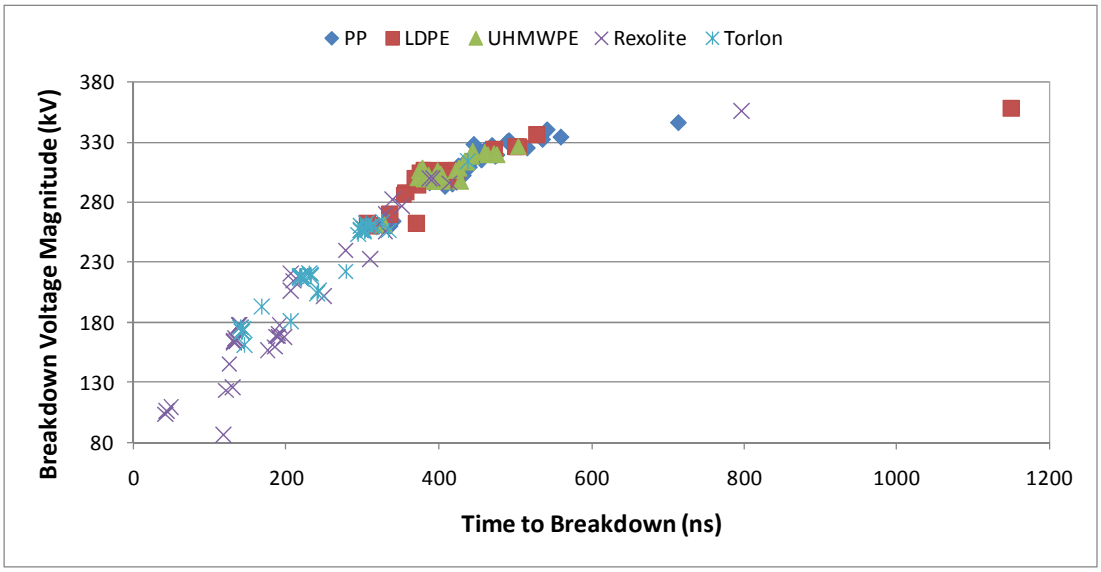

Figure J.3. Volt-time plot for surface flashover along type III (no modifications) samples with high-voltage electrode type B (collar).

Appendix K (reference section 6.4.1)

WEIBULL STATISTICAL ANALYSIS

Breakdown Voltage Data

Presented herein are the Weibull plots for the breakdown voltage data referenced in section 6.4.1:

- Figure K.1. configuration AII
- Figure K.2. configuration BIII

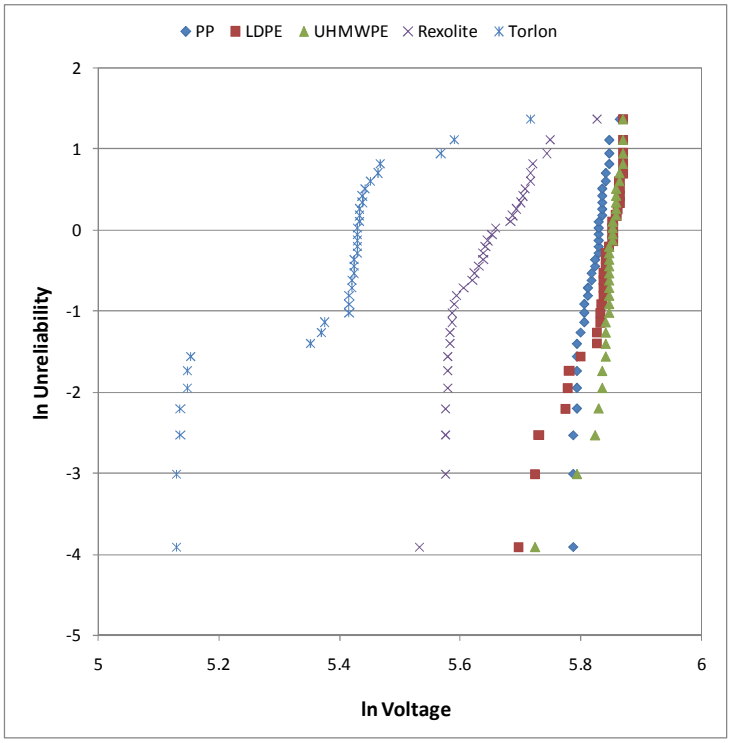

Figure K.1. Weibull plots of breakdown voltage data for type II (shoulder) samples tested with high-voltage electrode type A (pin).

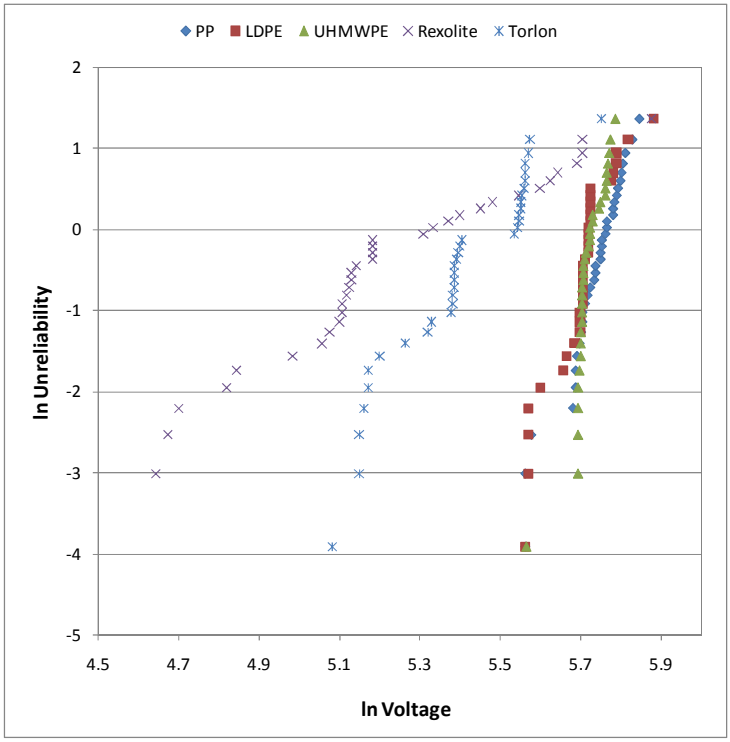

Figure K.2. Weibull plots of breakdown voltage data for type III (no modifications) samples tested with high-voltage electrode type B (collar).

Appendix L (reference section 6.4.2)

WEIBULL STATISTICAL ANALYSIS

Material Comparison

Presented herein are the Weibull plots for the breakdown voltage data referenced in section 6.4.2:

- Figure L.1. PP
- Figure L.2. LDPE
- Figure L.3. Rexolite
- Figure L.4. Torlon

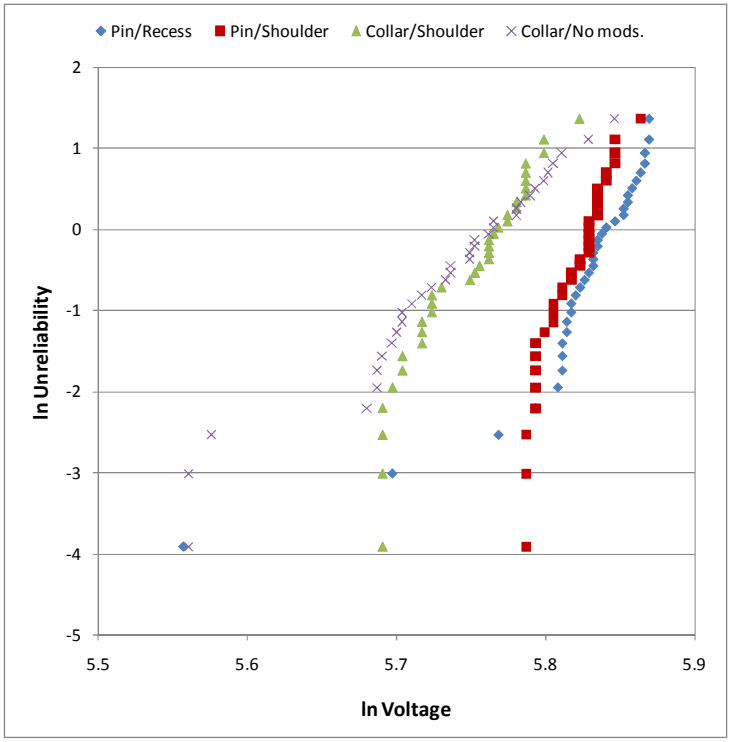

Figure L.1. Weibull plots of PP breakdown voltages for the different experimental geometries.

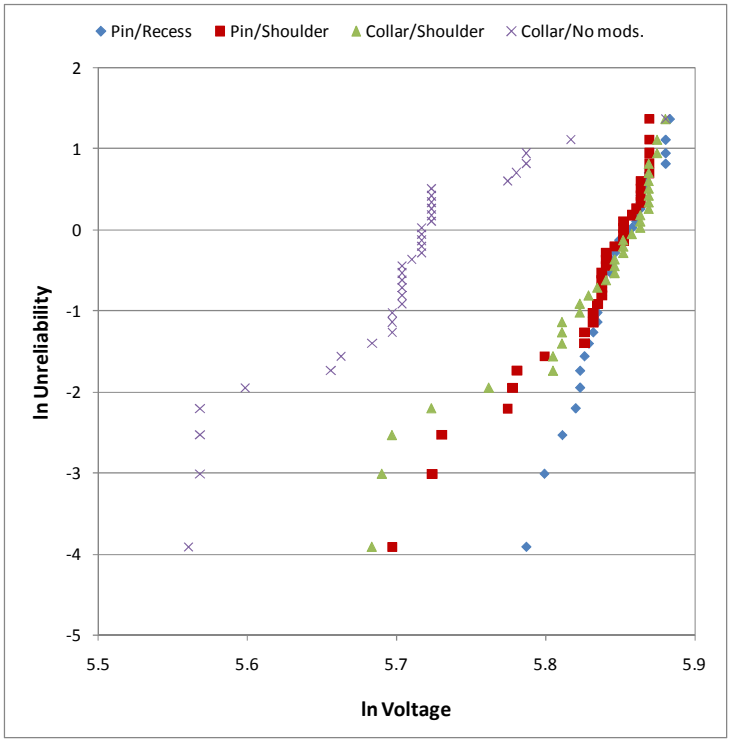

Figure L.2. Weibull plots of LDPE breakdown voltages for the different experimental geometries.

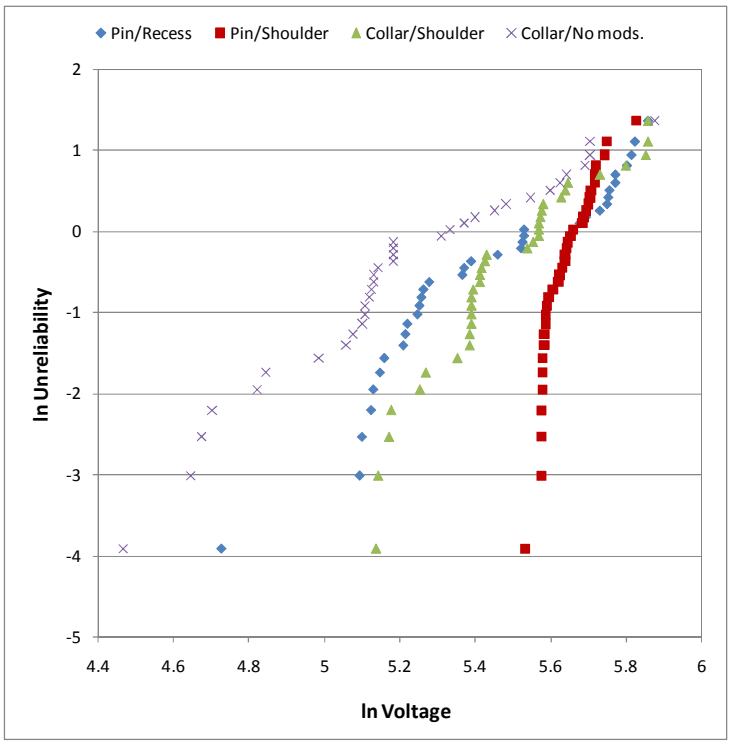

Figure L.3. Weibull plots of Rexolite breakdown voltages for the different experimental geometries.

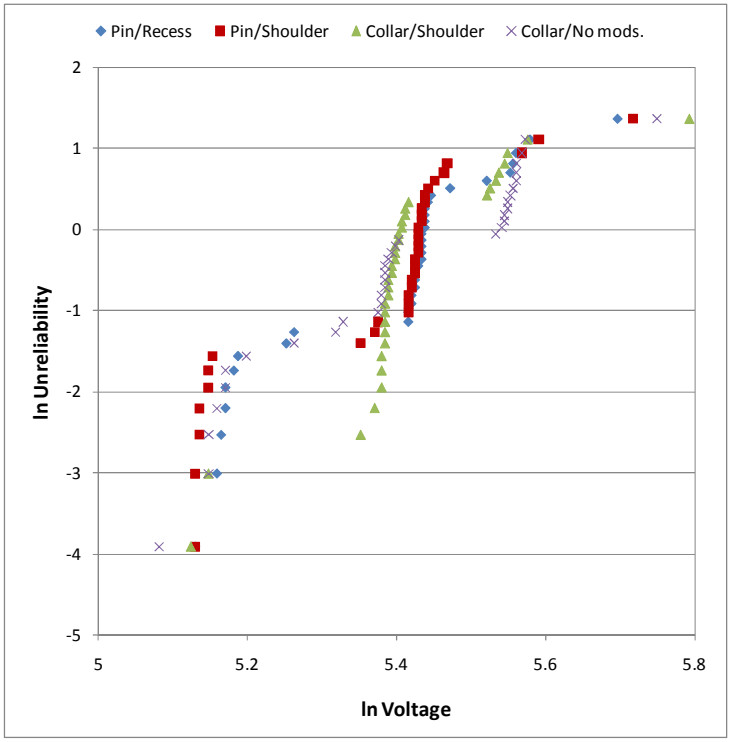

Figure L.4. Weibull plots of Torlon breakdown voltages for the different experimental geometries.

Appendix M

PUBLICATIONS

Throughout the course of this study, work was presented at international conferences and symposiums, including three oral presentations and four poster presentations thus far. This has resulted in the publication of two journal papers and seven conference papers to date, with a further journal paper accepted for publication in the August 2011 issue of the IEEE Transactions on Dielectrics and Electrical Insulation. Two further conference papers have also been accepted for oral presentation at IEEE international conferences in June 2011. The details of these papers are given below.

Journal Papers

1. M.P. Wilson, I.V. Timoshkin, M.J. Given, S.J. MacGregor, M.A. Sinclair, K.J. Thomas, and J.M. Lehr, "Effect of applied field and rate of voltage rise on surface breakdown of oil-immersed polymers," *IEEE Transactions on Dielectrics and Electrical Insulation*, accepted for publication, Aug. 2011 issue.

2. M.P. Wilson, M.J. Given, I.V. Timoshkin, S.J. MacGregor, M.A. Sinclair, K.J. Thomas, and J.M. Lehr, "Impulse-breakdown characteristics of polymers immersed in insulating oil," *IEEE Transactions on Plasma Science*, vol. 38 (10), pp. 2611-2619, 2010.

3. M.P. Wilson, S.J. MacGregor, M.J. Given, I.V. Timoshkin, M.A. Sinclair, K.J. Thomas, and J.M. Lehr, "Surface flashover of oil-immersed dielectric materials in uniform and non-uniform fields," *IEEE Transactions on Dielectrics and Electrical Insulation*, vol. 16 (4), pp. 1028-1036, 2009.

Conference Papers

1. M.P. Wilson, I.V. Timoshkin, M.J. Given, S.J. MacGregor, M.A. Sinclair, K.J. Thomas, and J.M. Lehr, "Effect of electrode geometry and rate of voltage rise on streamer propagation in mineral oil," accepted for presentation at *2011 IEEE International Conference on Dielectric Liquids*, June 2011.

2. M.P. Wilson, M.J. Given, I.V. Timoshkin, S.J. MacGregor, M.A. Sinclair, K.J. Thomas, and J.M. Lehr, "Weibull statistical analysis of impulse-driven surface breakdown data," accepted for presentation at *18th IEEE International Pulsed Conference*, June 2011.

3. M.P. Wilson, M.J. Given, I.V. Timoshkin, S.J. MacGregor, M.A. Sinclair, K.J. Thomas, and J.M. Lehr, "Surface flashover of oil-immersed polymers with varying applied electrical field," *Proc. 2010 IEEE International Power Modulator and High Voltage Conference*, May 2010.

4. M.P. Wilson, M.J. Given, I.V. Timoshkin, S.J. MacGregor, M.A. Sinclair, and K.J. Thomas, "Impulse-driven surface flashover of polymeric dielectric materials immersed in insulating oil," *Proc. 44th International Universities Power Engineering Conference*, 2009.

5. M.P. Wilson, S.J. MacGregor, I.V. Timoshkin, M.J. Given, M.A. Sinclair, K.J. Thomas, and J.M. Lehr, "Impulse breakdown characteristics of dielectric materials immersed in insulating oil," *Proc. 17th IEEE International Pulsed Power Conference*, pp. 455-459, 2009.

6. M.P. Wilson, K.J. Thomas, M.A. Sinclair, R.A. Fouracre, M.J. Given, S.J. MacGregor, and I.V. Timoshkin, "Surface discharges along polymeric insulating materials," *Proc. XVII International Conference on Gas Discharges and Their Applications*, pp. 229-232, 2008.

7. M.P. Wilson, M.J. Given, S.J. MacGregor, I.V. Timoshkin, J.R. Beveridge, K.J. Thomas, M.A. Sinclair, and J.M. Lehr, "Breakdown initiation fields for surface flashover of dielectric materials immersed in transformer oil," *Proc. 2008 IEEE International Power Modulators and High Voltage Conference*, pp. 41-44, 2008.

8. M.P. Wilson, R.A. Fouracre, M.J. Given, S.J. MacGregor, I.V. Timoshkin, K.J. Thomas, and M.A. Sinclair, "Surface flashover of low-density polyethylene in transformer oil," *Proc. 20th IET Symposium on Pulsed Power*, pp. 177-182, 2007.

9. M.P. Wilson, R.A. Fouracre, M.J. Given, S.J. MacGregor, I.V. Timoshkin, K.J. Thomas, M.A. Sinclair, and J.M. Lehr, "Surface flashover of dielectric materials used in pulsed power research," *Proc. 16th IEEE International Pulsed Power Conference*, vol. 2, pp. 1665-1668, 2007.